AUTOMATED UNMANNED SYSTEMS AND DATA ANALYTICS FOR IN-FIELD DIGITAL CROP PHENOTYPING

by

JAVIER RODRIGUEZ SANCHEZ

(Under the Direction of Changying Li and Kyle Johnsen)

ABSTRACT

As the global population approaches nearly 10 billion by mid-century, agricultural production faces unprecedented challenges. Despite advancements in crop breeding, the rate of improvement has proven insufficient to meet the growing demand for food and fiber, necessitating a significant increase in agricultural productivity. Traditional phenotyping methods are labor-intensive and inefficient, creating an urgent need for high-throughput approaches. In-field digital crop phenotyping, empowered by advanced sensing technologies and innovative data discovery methods, has emerged as a promising solution to enhance throughput and accelerate breeding advancements for more productive crops. This work aimed to automate unmanned aerial vehicle (UAV)-based phenotyping pipelines and optimize terrestrial laser scanning (TLS) methodologies for in-field phenotyping through the use of advanced data analytics and the integration of unmanned ground vehicles (UGVs). UAV-based imagery, combined with machine learning algorithms and the Segment Anything foun-

dation model for image segmentation (SAM), enabled precise estimation of yield-related traits in cotton and peanut breeding trials, including cotton boll number, canopy height, growth habit, and main stem prominence, facilitating accurate pre-harvest yield predictions and in-field phenotypic trait assessments. Additionally, novel proximal sensing methods based on TLS with a customized autonomous Husky ground mobile robot were developed to automate field phenotyping and improve in-field crop measurements. A new methodology for spatiotemporal registration of 3D point cloud data obtained through multi-scan TLS enabled continuous monitoring of cotton crop growth dynamics throughout the growing season. Furthermore, an autonomous ground robotic system equipped with a 3D laser scanner demonstrated efficient field navigation and data collection capabilities across different field layouts. By introducing these innovative and optimized methodologies, this research addresses critical challenges in agricultural research and crop breeding. Leveraging advanced remote and proximal sensing technologies with data analytics, this work significantly contributes to the development of digital agriculture and plant phenomics, offering valuable insights and practical solutions for researchers and practitioners interested in advancing sustainable agricultural practices and enhancing crop phenotypes.

INDEX WORDS: Remote Sensing, Proximal sensing, Digital plant phenotyping, High-throughput field phenotyping, Unmanned aerial vehicle, Unmanned ground vehicle, LiDAR, Terrestrial laser scanning, Deep learning, Machine learning, SAM, Field robotics, Crop breeding

AUTOMATED UNMANNED SYSTEMS AND DATA ANALYTICS FOR IN-FIELD DIGITAL CROP PHENOTYPING

by

JAVIER RODRIGUEZ SANCHEZ

B.S., Universidad de Jaén, Spain, 2010

M.S., Universidad de Granada, Spain, 2014

M.S., Universidad de Almería, Spain, 2017

A Dissertation Submitted to the Graduate Faculty of the

University of Georgia in Partial Fulfillment of the Requirements for the Degree.

DOCTOR OF PHILOSOPHY

ATHENS, GEORGIA

2024

AUTOMATED UNMANNED SYSTEMS AND DATA ANALYTICS FOR IN-FIELD DIGITAL CROP PHENOTYPING

by

JAVIER RODRIGUEZ SANCHEZ

Major Professor: Changying Li

Kyle Johnsen

Committee: John L. Snider

Ramviyas Nattanmai Parasuraman

Peter Kner

Electronic Version Approved:

Ron Walcott

Dean of the Graduate School

The University of Georgia

August 2024

DEDICATION

This dissertation is dedicated to my family, to whom I owe the person I have become, and to Nicole, whose support and care have made it possible for me to reach this point.

To perseverance, because nobody can make the effort for you.

ACKNOWLEDGMENTS

I would like to express my special appreciation to my advisor, Dr. Changying Li for his mentoring and support throughout my research. Being accepted to his lab was not easy, but his guidance over the years put the wind in my sails and made this dissertation possible.

I extend my sincere thanks to my co-advisor, Dr. Kyle Johnsen, for his support and guidance, especially during the latter part of this journey. Life's uncertainties can overwhelm us, but being surrounded by the right people makes things a bit easier. Thank you for your support and for allowing me to be a part of the Virtual Experience Laboratory.

I am also grateful to my committee members, Dr. John Snider, Dr. Ramviyas Parasuraman, and Dr. Peter Kner, for their contributions to this dissertation. I appreciate your feedback on focusing my research goals and improving my work. My gratitude extends to my collaborators, Dr. Andrew Paterson, Dr. Peggy Ozias-Akins, Dr. Ye Chu, and Dr. Jing Zhang, for their assistance and willingness to help in our collaborative studies.

Thanks should also go to my lab colleagues and everyone who altruistically provided their time and effort to my research. Special thanks to Dr. Rui Xu for assisting in field testing and debugging robot operations, Dr. Shangpeng Sun for providing the stepping stone for some of the work presented here, and to Mr. Gary Pierce, Dr. Navneet Kaur, Mr. Zhengkun Li, Mr. Daniel

Petti, Mr. Chenjiao Tan, Mr. Tsunghan Han, Mr. Joshua Griffin, and Mr. Jon S. Robertson for their company and assistance, making both field and lab work more manageable.

I also appreciate the funding from the National Science Foundation Growing Convergence Research, NIFA, and the Georgia Cotton Commission, as well as additional funding from the University of Georgia Graduate School, which helped me achieve my research goals and disseminate my results. I would also like to acknowledge the support from the University of Georgia College of Engineering during my time here.

Finally, I extend my deepest thanks to my parents and brothers, who have always supported my decisions and encouraged me to pursue my dreams. To my partner, Nicole, I am truly grateful. I have arrived where I am now largely because of you. Without your support over the last few years, I might have given up long ago. Your love and care have made it possible for me to achieve the most important accomplishment in my career. Thank you, and I love you all.

CONTENTS

LIST OF FIGURES

LIST OF TABLES

CHAPTER 1

INTRODUCTION

1.1 Background

The latest projections by the United Nations suggest that by 2050 the world's population could reach 9.8 billion (United Nations, 2019). In order to meet the growth in demand of food and fiber, agricultural production needs to be increased at a steady pace (Hunter et al., 2017). Crop breeding has helped develop highly productive crop varieties during the past decades, but the high expected demand of agricultural products in the coming years will make necessary additional efforts to substantially increase the rates of genetic improvement (Voss-Fels et al., 2019) and consequently the breeding efficiency (Araus & Cairns, 2014). Plant breeding programs primarily rely on experiments with high genetic diversity, and the recent advances in genetic technologies have accelerated the development of cultivars with desired characteristics (Collard & Mackill, 2008). However, being able to link genes to their expression under different environments is key for the development of adaptable crops with enhanced characteristics of quality, yield, and stress tolerance (Kumar

et al., 2015). Plant phenomics—the formal characterization of phenotypes at large scale—plays an essential role in linking plant traits to the associated genes (Vinces, 2011).

In the past decades, plant phenotyping has become a common practice in breeding programs (Reynolds & Langridge, 2016). Plant phenotyping enables the identification of the phenotypic expression of traits and helps quantify their evolution over time and across different environments, providing a means to better understand the genotype-phenotype relationship (Großkinsky et al., 2015). This information allows breeders to select the most adaptable and productive cultivars for specific production environments (Goggin et al., 2015). However, conventional plant phenotyping based on manual measurements and destructive sampling, is labor-intensive and costly. This usually translates into a reduction of the number of plants that can be effectively quantified and is a limiting factor for scaling up breeding programs (Bowman et al., 2004). In addition, given the spatial and temporal variability of the canopies, field quantification of functional traits of plants is challenging and becomes a bottleneck for breeding progress (Araus & Cairns, 2014), limiting the potential of further improvement in breeding efficiency. Therefore, the development of tools for effectively increase the throughput of plant phenotyping will be vital to accelerate crop improvement as a key pillar for the sustainability of agriculture (Morisse et al., 2022).

Ongoing innovations in proximal and remote sensing technologies have driven the development of advanced methods for high-throughput phenotyping (HTP). Recent review papers comprehensively discussed a myriad of HTP systems designed for analyzing characteristics related to crop growth rate and yield (Atefi et al., 2021; Bao et al., 2021; Xu & Li, 2022b). However, these developments have often been tailored to specific crops, posing challenges in generalizing methods and workflows across different species or field layouts (Fiorani & Schurr, 2013). Current

trends in field-based HTP solutions aim to to address this gap through the use of automated and data-driven methodologies, enabling flexible and efficient assessment of complex traits (Xu & Li, 2022b). Continued progress in process automation and data analytics is essential to enhance digital methodologies and optimize in-field phenotyping tasks, crucial for meeting future food needs in a sustainable manner.

1.2 Objectives

The main objective of this dissertation was to develop automated tools and methodologies to increase the throughput of plant phenotyping under field conditions using robotics and data analytics. To achieve this goal, the research was divided into two thematic lines: the use of remote sensing for HTP of yield-related traits in large breeding trials, and the use of proximal sensing approaches for field-based HTP. Specific objectives were to:

1. Estimate preharvest cotton yield for genotype selection using UAS and machine learning.

2. Develop and validate a data processing pipeline for HTP of yield-related traits in peanut crops using multispectral aerial imagery and deep learning.

3. Analyze and monitor plot-level functional traits over time in cotton breeding fields using time-series terrestrial laser scanning (TLS) data.

4. Automate in-field TLS data acquisition for cotton breeding trials using multi-scan approaches and a mobile robot.

1.3 Research Contributions and Dissemination

This research aimed to enhance plant phenotyping by addressing the challenges of field-based HTP through the integration of advanced imaging technologies, data analytics, and robotics. The main contributions of this dissertation are: an easy-to-implement methodology for estimating pre-harvest cotton yield from aerial imagery, accompanied by a web-based API; a fully automated methodology for processing unmanned aerial systems (UAS)-based multispectral data and estimating agronomic traits in a peanut breeding field; a method to register terrestrial laser scanning (TLS) data over time for efficient monitoring and tracking of morphological traits throughout an entire cotton season; and the development of a ground robot capable of collecting TLS data within breeding fields without human intervention. These methodologies promise to enhance the efficiency, accuracy, and scalability of crop trait analysis, ultimately contributing to the digitalization and automation of in-field phenotyping tasks for crop breeding and the advancement of plant phenomics.

The methods and results of this dissertation have been presented and published in various conferences and scientific journals: one article has been published, one has been accepted and is currently in press, one has been submitted to a peer-reviewed journal and is under review, and the other is to be submitted. The publications that are presented in this dissertation are as follows:

1. **Rodriguez-Sanchez, J.**, Li, C., and Paterson, A.H. (2022). Cotton Yield Estimation from Aerial Imagery using Machine Learning Approaches. *Frontiers in Plant Science*. 13:870181.

2. **Rodriguez-Sanchez, J.**, Chu, Y., Ozias-Akins, P., Zhang, J., Johnsen, K., and Li, C. Leveraging UAS Imagery and the Segment Anything Model for Automated Trait Extraction in Peanut Breeding Fields. To be submitted to *Plant Methods*.

3. **Rodriguez-Sanchez, J.**, Snider, J.L., Johnsen, K., and Li C. Crop Growth Tracking through Spatiotemporal Registration of Terrestrial Laser Scanning Time-Series Data. Accepted by *Frontiers in Plant Science*, 07/04/24.

4. **Rodriguez-Sanchez, J.**, Johnsen, K., and Li, C. A Ground Mobile Robot for Autonomous Terrestrial Laser Scanning-based Field Phenotyping. Submitted to *Journal of Field Robotics*, 07/25/23.

1.4 Overview of the Dissertation Chapters

The dissertation consists of seven chapters, where chapters 3 to 6 represent individual manuscripts presented in a standard format. Chapter 1 outlines the significance, objectives, and main contributions of the dissertation. Chapter 2 contextualizes the dissertation by providing a brief overview of current trends and technologies for field phenotyping.

Chapter 3 introduces a cost-effective method for estimating pre-harvest cotton yield using drone imagery. Using just one annotated RGB plot image extracted from an orthoimage of the field, a supervised SVM classifier was trained to estimate the number of cotton bolls at the plot level and analyze yield differences among cultivars. The classifier was tested across various scenes to assess its robustness.

Chapter 4 explores the automation of aerial imagery data processing for field phenotyping using advanced foundational models for image segmentation. A fully automated data processing pipeline was developed to extract morphological crop traits at the plot level in a peanut breeding field based on the Segment Anything Model (SAM). Convolutional neural network models were developed for morphological traits classification and TSWV infestation level detection.

Chapter 5 presents a novel methodology for enhancing LiDAR-based field phenotyping over time. An optimized two-stage process for spatiotemporal registration of terrestrial laser scanning (TLS) data was developed. Performance evaluation of spatiotemporal alignment of point clouds collected throughout the growing season were carried out. The evolution of canopy height and volume was modeled using time-series TLS data to monitor crop morphological traits evolution and identify significant differences among genotypes.

Chapter 6 introduces an autonomous ground phenotyping platform for in-field TLS. A methodology for optimizing multi-scan TLS data collection in the field, without human involvement, was implemented. The performance of the robotic platform in autonomously navigating and collecting TLS data was tested under real-world conditions.

Chapter 7 offers general research conclusions, highlights limitations, and suggests future research directions.

CHAPTER 2

CURRENT TRENDS IN IN-FIELD DIGITAL PHENOTYPING USING IMAGING TECHNOLOGIES

Plant phenotyping for crop breeding aims to identify superior individuals with desirable traits that can adapt to specific production environments (A. Walter et al., 2015). Field-based plant phenotyping allows for evaluating plant traits in real environments, ensuring adequate throughput for crop breeding (White et al., 2012). Phenotyping methodologies vary based on the crop, growth stage, target traits, and available resources (Chawade et al., 2019). Generally, non-destructive and high-throughput crop phenotyping (HTP) techniques can be categorized into two main groups: remote and proximal sensing (Tao et al., 2022). Remote sensing approaches employ sensors at a distance from the plants, often using satellites, manned aircrafts, or unmanned aerial vehicles (UAVs). Proximal sensing, on the other hand, involves the use of sensors in close proximity to the

plants, typically using ground-based platforms such as tractors, manned platforms, or unmanned ground vehicles (UGVs) to carry sensing devices through the fields. Developing HTP tools and automated methods for both remote and proximal sensing may help accelerate the screening and selection of genotypes (Yoosefzadeh-Najafabadi et al., 2023).

Imaging sensing systems for remote and proximal sensing in precision agriculture typically combine spectral, spatial, and temporal information from a diverse array of devices (J. Liu et al., 2024). Over the past decades, platforms based on RGB (red, green, and blue) cameras, multispectral, hyperspectral, and thermal sensors, as well as spectrometers, have been used for collecting in-field crop data and monitoring large fields (L. Zhu et al., 2018). More recently, the adaptation of technologies like light detection and ranging (LiDAR) from more mature fields to agricultural settings has sparked interest in the plant science community for three-dimensional (3D) crop analysis (Araus et al., 2018). With technological advancements, the throughput of these systems has increased rapidly (Jin, Sun, et al., 2021). Additionally, developments in automating data acquisition methods have been instrumental in discovering new traits indirectly correlated with traits of interest (Rutkoski et al., 2016), ultimately expanding genetic variation in breeding programs (Chawade et al., 2019). These systems have changed the way crop traits are measured and analyzed, providing digital methods to increase the throughput of in-field phenotyping tasks, allowing breeders to increase selection intensity and accuracy by screening a larger number of samples effectively (Araus et al., 2018).

Both aerial-based and ground-based systems have their advantages and disadvantages for plant phenotyping (Pabuayon et al., 2019). Aerial systems are typically cost-effective and capable of quickly gathering information from large areas, allowing for fast and repetitive coverage of exten-

sive fields. They can be adapted to different crops, growth stages, and field layouts (Xu et al., 2019). However, their operation time is often limited by battery constraints (Deery et al., 2014), lower payload capacities, and sensitivity to weather conditions, particularly wind. Additionally, spatial resolution depends significantly on speed and altitude (Yang et al., 2017). Ground-based systems, on the other hand, are generally more stable, can carry multiple and heavier sensors, and typically offer better spatial resolutions and more details due to their closer proximity to the crop (Condorelli et al., 2018; Wang, Singh, et al., 2018), reducing noise and errors during data collection. However, they require more time to cover an entire field and are more challenging to deploy safely due to limited row spacing and soil conditions (Andrade-Sanchez et al., 2014; Araus & Cairns, 2014). There is no single technology that can satisfy all requirements for field phenotyping. Therefore, the selection of the appropriate system depends on the specific task at hand, considering field layout, canopy complexity, throughput requirements, and time constraints for data acquisition.

2.1 Unmanned Aerial Systems for High-Throughput Field Phenotyping

In recent years, the applications of unmanned aerial systems (UAS) in agriculture, particularly in plant breeding, have expanded significantly, offering researchers enhanced capabilities for precise, high-throughput data collection (Bhandari et al., 2023). UAVs are relatively inexpensive and can be equipped with a variety of sensors (Xu et al., 2019), making them a valuable tool for large crop field monitoring. UAV-based remote sensing technologies enable precise data collection at the field

scale with spatial and temporal resolutions not achievable using traditional platforms (Bhandari et al., 2023; Yeom et al., 2018).

Advancements in UAS technologies over the past decades have improved the throughput and accuracy of remote sensing for monitoring crop growth and development (W. Guo et al., 2021). While traditional remote sensing approaches using satellite imagery have allowed breeders to monitor crops (Bellón et al., 2017; Dubovyk et al., 2015; Z. Jiang et al., 2014; M. Zhang et al., 2014), satellite data resolution and availability are often limited, restricting detailed plot-level analysis. In contrast, UASs provide a cost-effective and flexible alternative for collecting high-resolution data periodically (Xie & Yang, 2020). These systems can be easily programmed to navigate predefined paths at specific velocities and distances from crops, enabling frequent and timely data collection at optimal resolutions superior to other airborne systems (Barbedo, 2019).

UAVs can be fitted with a variety of imaging systems for efficient data collection (Gano et al., 2024). The most common imaging systems for UAV-based remote sensing are RGB sensors (Sweet et al., 2022), which are relatively inexpensive, lightweight, and provide high resolution. These sensors have been successfully used in crop breeding for extracting and monitoring phenotypic traits such as plant height (van Iersel et al., 2018; Volpato et al., 2021; Watanabe et al., 2017), canopy morphology (Torres-Sánchez et al., 2015), assessing nutrient levels in field crops (Buchaillot et al., 2019; Lu et al., 2021), and evaluating disease resistance (Sugiura et al., 2016). Additionally, multispectral sensors, which measure red, green, blue, near-infrared, and red-edge bands, and hyperspectral sensors have allowed the computation of various vegetation indices to monitor plant health (Gill et al., 2022) and model yield for genotype selection (X. Zhang et al., 2019).

Although significant advancements have been made, the broader adoption of UAS-based methodologies for plant breeding requires more than just hardware and sensor improvements. Standard operating procedures for UAS data collection, processing, and analysis are critical for ensuring the accuracy and reliability of phenotypic data (Bhandari et al., 2023). A major challenge in remote sensing is obtaining automatic, rapid, and accurate information from the collected data (Osco et al., 2021). Integrating machine learning (ML) and deep learning (DL) into data analysis pipelines provides robust and intelligent methods for improving aerial imagery analysis (Maimaitijiang et al., 2020; Yoosefzadeh-Najafabadi et al., 2023) and has demonstrated the potential to enhance breeding efficiency and selection accuracy (Herr et al., 2023). Recent studies have shown that combining selected multispectral bands with sophisticated ML tools can lead to sensitive approaches for early stress detection and disease monitoring (Nagasubramanian et al., 2018; Tang et al., 2022). However, these approaches rely heavily on high-quality and abundant data that can be expensive and time-consuming to collect, necessitating further research to standardize procedures and fully develop these techniques for plant phenotyping (Gano et al., 2024).

UAS-based phenotyping approaches are particularly suited for analyzing large fields and relatively simple traits or crop structures. However, given the limited spatial resolution and payload of aerial systems, analyzing more complex crops with greater detail and accuracy will benefit from the use of ground-based proximal sensing systems.

2.2 Unmanned Ground Vehicles for LiDAR-based In-field Phenotyping

Ground-based phenotyping platforms offer distinct advantages over aerial systems for imaging-based in-field phenotyping. These systems tend to be modular, allowing for the integration of multiple sensors and configurations tailored to specific needs (Andrade-Sanchez et al., 2014; Bai et al., 2016; Y. Jiang et al., 2018; Qiu et al., 2019; Xu & Li, 2022a). They also provide stability, enabling the mounting of manipulators or heavy equipment for multi-view analysis of targeted plants (Benet et al., 2018; Shafiekhani et al., 2017). Despite their benefits, ground-based systems typically require more time and investment compared to aerial platforms (Wang, Singh, et al., 2018), necessitating efficient phenotyping methodologies that optimize throughput and resource use to meet the demands of breeding programs.

Advancements in imaging sensors and 3D technologies have significantly enhanced in-field plant growth assessment, improving field operations and resource utilization (L. Li et al., 2014). These technologies enable precise extraction of multiple morphological traits that cannot be derived from 2D images due to occlusions and perspective ambiguities (S. Sun et al., 2018), supporting accurate modeling of crop structures and predictions of yields and growth dynamics (Sandhu et al., 2019). These advancements highlight ongoing efforts in adapting mature technologies such as LiDAR from other fields to agricultural applications.

LiDAR technology has accumulated considerable attention for crop phenotyping in recent decades due to its accurate and repeatable measurements (Madec et al., 2017). LiDAR scanners

utilize laser beams capable of penetrating foliage openings, surpassing other technologies in depth sensing capabilities. Moreover, LiDAR systems are less dependent on illumination conditions compared to other sensors (Hosoi & Omasa, 2009), making them well-suited for field operations. Ground-based LiDAR sensors are deployed on stationary or mobile platforms (Tao et al., 2022). While mobile platforms offer flexibility in scanning crops across various locations, traditional setups such as customized pushcarts and tractors typically require operator intervention, increasing costs and potential errors. Emerging field-based high-throughput phenotyping (HTP) approaches integrating automation and robotics aim to enhance operational autonomy (Atefi et al., 2021; Bao et al., 2021). However, adapting these technologies across diverse crops and field layouts remains challenging, often requiring customized solutions that can be time-consuming to deploy and operate efficiently.

Improvements in the methodologies for processing LiDAR data have enabled a progressive increase in the throughput and spatiotemporal resolution of LiDAR-based plant phenotyping systems (Jin, Sun, et al., 2021). In-field LiDAR data has been used to assess traits in multiple crops at diverse scales, from canopy-level (Hosoi & Omasa, 2009, 2012; Jin et al., 2020) to plant-level (Gage et al., 2019). High-resolution LiDAR scanners have also facilitated detailed morphological analysis at the organ level (Jin et al., 2019; Malambo et al., 2019; Paulus et al., 2014; S. Sun et al., 2021). However, the need for robust data acquisition and appropriate data processing methodologies for efficient in-field phenotyping persists (Jin, Sun, et al., 2021).

Despite significant advancements in LiDAR-based phenotyping technologies, several challenges persist. The efficiency of data collection in phenotyping platforms is currently inadequate, especially for large breeding fields (Xu & Li, 2022b). Optimization of data acquisition methods,

including sensor placement and scanning frequency, is essential to enhance efficiency without compromising data quality. Implementing adaptable approaches for automating in-field data collection processes while ensuring accuracy and reliability is paramount. Moreover, the time-consuming nature of current methods for processing close-range field data hampers the throughput of data analysis (Gill et al., 2022). Developing robust algorithms for analyzing diverse and voluminous data from multiple sensors and standardizing protocols and tools across different crop stages and field layouts are critical to ensure consistency and comparability of phenotypic data (Medic et al., 2023). Addressing these challenges comprehensively will be instrumental in advancing LiDAR-based ground phenotyping systems and enhancing their utility in agricultural research and crop improvement programs.

CHAPTER 3

COTTON YIELD ESTIMATION FROM AERIAL IMAGERY USING MACHINE LEARNING APPROACHES[1]

[1]Javier Rodriguez-Sanchez, Changying Li, and Andrew H. Paterson. 2022. *Frontiers in Plant Science*. 13:870181. Reprinted here with permission of the publisher.

Abstract

Estimation of cotton yield before harvest offers many benefits to breeding programs, researchers and producers. Remote sensing enables efficient and consistent estimation of cotton yields, as opposed to traditional field measurements and surveys. The overall goal of this study was to develop a data processing pipeline to perform fast and accurate pre-harvest yield predictions of cotton breeding fields from aerial imagery using machine learning techniques. By using only a single plot image extracted from an orthomosaic map, a Support Vector Machine (SVM) classifier with four selected features was trained to identify the cotton pixels present in each plot image. The SVM classifier achieved an accuracy of 89%, a precision of 86%, a recall of 75%, and an F1-score of 80% at recognizing cotton pixels. After performing morphological image processing operations and applying a connected components algorithm, the classified cotton pixels were clustered to predict the number of cotton bolls at the plot level. Our model fitted the ground truth counts with an R^2 value of 0.93, a normalized root mean squared error of 0.07, and a mean absolute percentage error of 13.7%. This study demonstrates that aerial imagery with machine learning techniques can be a reliable, efficient, and effective tool for pre-harvest cotton yield prediction.

3.1 Introduction

Cotton is a major industrial crop in the United States (U.S.), especially in the southern and western U.S. Cotton fiber is one of the principal natural textile fibers worldwide (Townsend & Sette, 2016), and the U.S. is the third leading cotton producer with an expected production of 22.5 million bales for 2019/20, just after China (27.5 million bales) and India (27 million bales). Cotton is a soft staple

fiber that grows from the surface of seeds, enclosed in pods known as bolls. Primary components of economic yield, cotton boll number and boll weight are agronomic traits that help to define cotton crop performance in its last stages of growth. These traits can be used as indicators of fiber production, which ultimately play a key role in breeding programs and may also provide valuable information for farmers to plan hedging strategies.

Lint yield is one of the most important criteria for selecting new lines in breeding programs (Bourland & Myers, 2015), but it is costly to obtain reliable data. Visual estimation of yield performance is often used by cotton breeders to select promising cotton genotypes, but it can be challenging. Morphological characteristics of cotton plants such as general shape, branch density, or leaf area change during the growth cycle of the crop and they may mislead visual ratings of yield (Bourland & Myers, 2015). Moreover, boll size can vary by year, breeding line, and position on each fruiting branch, which can make it difficult to standardize visual cotton yield quantification methods. Physical harvesting of the bolls, either manually or by using mechanical pickers, to reduce the estimation bias is labor intensive and time-consuming, limiting the number of plots that can be quantified (Bowman et al., 2004). Thus, the development of tools for effectively automating plant phenotyping tasks is of great potential value for breeding programs.

In recent years, the applications of unmanned aerial systems (UAS) in agriculture have grown rapidly and have transformed modern farming. UAS are relatively inexpensive and can be equipped with a variety of sensors, which makes them a valuable tool for large crop field monitoring. These systems can be programmed easily to navigate pre-defined paths with a specific velocity while retaining a specific distance from the crop. This means that they can be used to collect data remotely from the field at optimal resolutions quickly and easily. UAS surveying has been widely

used for monitoring different crops (Barbedo, 2019), but only a few studies have addressed the use of these systems to estimate cotton yield, and only two have investigated their use for cotton genotype selection. The methodologies used to estimate cotton yield from UAS imagery can be classified in two main groups: approaches based on the use of only 3-channel RGB (Red, Green, Blue) color images, and approaches that utilize a combination of different sensor data to indirectly calculate lint yield.

To estimate cotton yield from RGB imagery, one of the main techniques is color thresholding segmentation, which has been applied either to a single color channel or to multiple channels at the same time. For instance, Dodge, 2019 applied a global thresholding method (using a fixed threshold value) to the B channel alone on RGB aerial images to isolate cotton-related pixels. Their methodology achieved an R^2 of 0.817 for the first year's experimental data. However, this relationship was not consistent, and they needed to include additional postprocessing to improve their model generalization for the next year's data (R^2 = 0.736). Yeom et al., 2018 analyzed the spatial and spectral characteristics of open cotton bolls on RGB images during the harvest period. They established a global automatic threshold based on Otsu's method to separate cotton bolls from other non-target objects. They achieved R^2 values of 0.63-0.65 at estimating yield using the cotton boll area as the input variable. However, they assumed that cotton bolls have higher spectral values than the other elements of the crop, which can be a limiting factor with changing illumination conditions when the range of image intensities of the color channels for the cotton bolls can resemble other crop elements. Huang et al., 2016 found that a global RGB threshold could not extract the cotton pixels from the images accurately because the range of image intensities in the R, G, and B channels of the cotton bolls overlapped with that of the soil and other crop elements.

Alternatively, they proposed the application of the thresholding technique on Laplacian images obtained from the divergence of the gradient of each image with respect to pixel intensity. They were able to establish a ratio—cotton unit coverage (CUC)—of the number of cotton boll pixels detected to the number of pixels in a particular area. They achieved their best results ($R^2 = 0.83$) after introducing additional postproessing steps to detect and remove poorly illuminated plot images because their method was affected by shadowing and changing illumination conditions.

Additional approaches based only on RGB images have also been proposed. Maja et al., 2016 estimated cotton yield of small field plots from a cotton breeding program using K-means clustering algorithm with 4 classes. They clustered the cotton pixels on the image based on their color and found a linear relationship ($R^2 = 0.782$) between the ratio of cotton pixels with respect to the total image area and the actual yield. However, they needed to introduce a fixed cluster size constraint to avoid large clusters and reduce misclassification of highly reflective areas of the scene such as the bare soil. This additional constraint can limit the generalization of their methodology for highly dense cotton crops where the cotton bolls tend to form large groups. Chu et al., 2016 estimated additional crop information (plant height and canopy cover) from aerial RGB images and were able to model cotton yield ($R^2 = 0.529$) before maturation and boll opening. However, their study of yield was limited to the stages of the crop before defoliation such that the canopy cover could be computed correctly.

In addition to RGB cameras for lint yield estimation, multispectral and thermal cameras have been used. Huang et al., 2013 used various vegetation indices obtained from multispectral aerial images in conjunction with soil properties to estimate yield variation. Their model based on the ratio of vegetation index (RVI) and soil electrical conductivity (EC) measurements performed well

for non-irrigated fields (R^2 = 0.718) but was unable to estimate yield accurately for irrigated fields (R^2 = 0.033). Feng et al., 2020 modeled cotton yield using multiple features derived from RGB, multispectral, and thermal cameras. They applied a global threshold in all three channels R, G, and NIR (near infrared radiation) to discriminate open cotton bolls from the soil and leaves. They found that the ratio of the number of cotton pixels to the overall number of pixels in a specific area of a multispectral image (cotton fiber index (CFI)) could be used to estimate yield at the pre-harvest stage (R^2 = 0.90). Moreover, by using a combination of plant height, CFI, canopy temperature and the a^* component of the CIELAB color space, they obtained an even better result (R^2 = 0.94). However, this sophisticated approach required the simultaneous use of color, multispectral and thermal cameras, which is costly and may require more computation capacity, time, and labor for data collection and processing.

Methods based on machine learning (ML) techniques have been explored recently. Support vector machines (SVM) are one of the most widely used machine learning algorithms for supervised data classification and regression analysis. Based on statistical learning, SVMs aim to identify a decision boundary to partition data in a high-dimension feature space into two sets. This decision hyperplane can be then used for data classification or regression analysis. There are two basic SVM formulations to perform these tasks. For data classification, support vector classification (SVC) models (Cortes & Vapnik, 1995) try to find the hyperplane to separate input data belonging to two different classes with the maximum margin. The learning process for an SVC aims to maximize that margin and minimize classification errors between the two classes.

These classification models return for each input data a class label and its probability of belonging to each class. The second type of SVM is for regression problems. Support vector regression

(SVR) is a regression function that can predict dependent variable by using independent variables as continuous values instead of class labels. The SVR works with the similar principle as SVM: to find the hyperplane that best fits the data inside a decision boundary delimited by a predefined error margin Drucker et al., 1996; Vapnik et al., 1996. The models can be optimized using the regularization parameter C and the margin of tolerance ε.

During the last decade, SVMs and its variants have been successfully applied in agricultural remote sensing for crop classification (S. Liu & Whitty, 2015; Song et al., 2014) and plant disease identification (Garcia-Ruiz et al., 2013; Raza et al., 2015; Rumpf et al., 2010). For cotton crops, SVMs have been successfully used to identify cotton flowers from multispectral imagery (Xu et al., 2019) and for budding rate monitoring from aerial RGB imagery (Xia et al., 2019). Regarding cotton yield estimation, other ML methods have also been used. By using RGB and multispectral aerial imagery, Ashapure et al., 2020 implemented an artificial neural network (ANN) to estimate cotton yield throughout the season based on crop canopy attributes. They were able to predict cotton yield at early stages of the crop with an average $R^2 = 0.861$ using features that included canopy information, multispectral vegetation indices, cotton boll information (obtained by using a color-based threshold method (Jung et al., 2018)), and crop irrigation status. This advanced methodology required the use of color and multispectral imaging systems, which increases platform costs and would entail additional time and labor for data collection and processing.

Methods for cotton yield estimation based on remote sensing techniques have various limitations. Traditional image processing techniques, such as thresholding, are not flexible enough to adapt to variable conditions present in the scene, resulting in relatively low performance. Some studies rely upon additional sensors to retrieve new features, which ultimately increases platform cost and usage

and processing complexity. In this paper, we present a simple and easy-to-implement methodology for estimating pre-harvest cotton yield at the plot level. By using RGB airborne imagery and a SVM algorithm, this new methodology could benefit cotton breeders by allowing them to acquire accurate information about different crop plots for their selection experiments in a timely manner. Moreover, it also may provide farmers an inexpensive, quick and precise estimation of the yield in their cotton fields before harvesting. The specific objectives of this study were to (1) implement a support vector machine model to classify cotton boll pixels in aerial images; (2) develop a predictor to estimate the number of cotton bolls at the plot level; (3) evaluate the performance of the proposed method against ground truth yield measurements; and (4) apply the proposed method to identify differences between genotypes in a cotton breeding trial.

3.2 Materials and Methods

3.2.1 Experimental Field

The field under study was located at the Iron Horse Farm (IHF) in Greene County, Georgia, U.S. ($33\circ43'01.3"N 83\circ18'29.1"W$) (Figure 3.1). The dimensions of the field were 200m $\times$ 12m (length $\times$ width), and it comprised a total of 488 plots. These plots were arranged into 10 rows with 46 plots per row and 1 additional row of 28 plots. A total of 220 different cotton genotypes were planted in plots of approximately 3-meters wide, with a final plant density dependent on the germination rate of the seeds. Six of the genotypes were commercial cultivars (TAM94L25, Acala1517-98, UA48, FM832, DeltaPine393, and GA230) with 10 replications per cultivar. The rest were 214 breeding lines from 10 different cotton populations (J, K, L, M, N, O, P, Q, R, S) with two replicates.

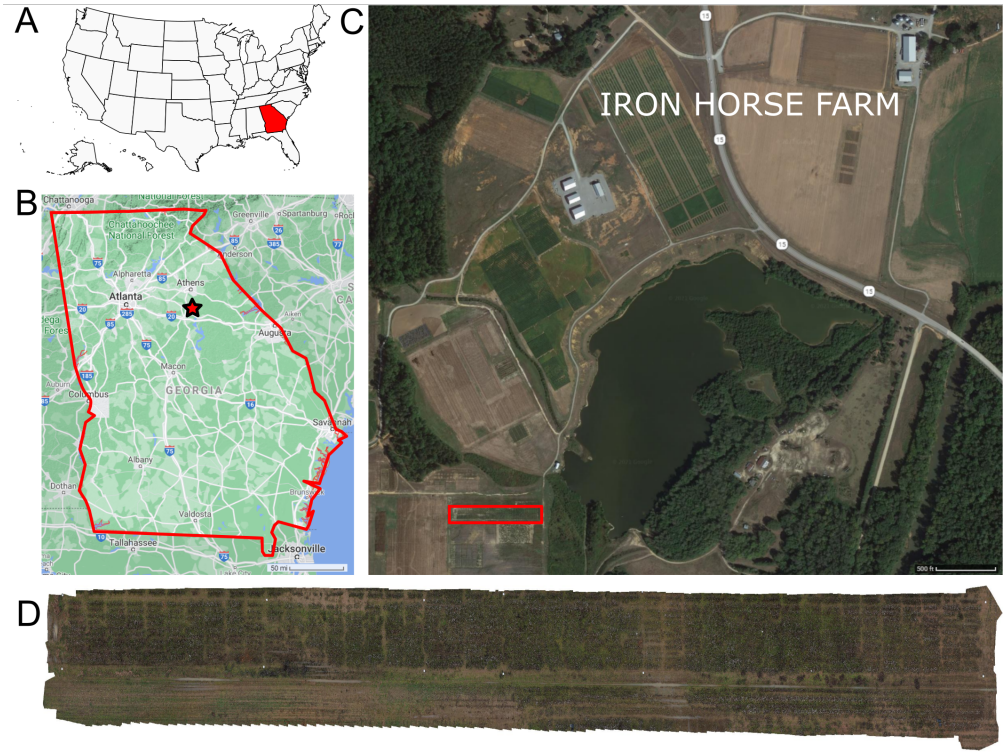

Figure 3.1: Experimental field location. The experiment was conducted in the Iron Horse Farm, Greene County, GA, U.S. A) Location map of Georgia, marked in red, in the U.S., B) General map of Georgia, the experiment location is marked with a red star, C) Iron Horse Farm aerial view (Greene County, GA), the specific location of the experimental field is delimited by a red rectangle, and D) Field layout.

3.2.2 Data Collection

Aerial Imagery

Original RGB color images were captured on February 1, 2020 on a single flight using a quadcopter DJI Matrice M100 (Shenzhen DJI Sciences and Technologies Ltd., Shenzhen, China), equipped with a Lumix G7 digital single-lens reflex (DSLR) camera (Panasonic Corporation, Osaka, Japan). This camera has a 17.3 $\times$ 13 mm CMOS image sensor with 16.0 megapixels (4592 $\times$ 3448 pixels)

resolution and stores captured images using the sRGB color space. The camera was mounted on the bottom of the drone using a custom 3D-printed bracket, which ensured that the camera lens was aligned to a 90 degree angle relative to the ground. Figure 3.2 shows the system used for data collection. The flight was controlled internally by the M100's N1 flight controller and was carried out at a height of 15 m above ground level, and at a speed of 1.9 m/s. With this configuration, the ground pixel size was 0.26 cm/pixel. The camera was configured automatically according to the light conditions of the field. Different white balance configurations were tested for color balancing before the flight, and the "Auto White Balance" compensation (AWB) was found adequate for the weather conditions on the collection day. A Manifold onboard computer (Shenzhen DJI Sciences and Technologies Ltd., Shenzhen, China) was in charge of triggering the camera at a constant rate of 1 frame per second. The forward overlap between images in the same flight line was configured to 80%, while the side-by-side overlap between adjacent flight lines was set to 60%. A total of 447 images were collected during the flight.

A set of 12 ground control points (GCP) with circular patterns were generated using Agisoft Metashape software (Metashape Professional 1.5.5, Agisoft LLC, Russia) and deployed along the field's border for geo-referencing the UAS images (Figure 3.3). The patterns were cut off from matte black adhesive-backed vinyl sheet and pasted onto a white acrylic 60 cm square sheet. The GCPs were surveyed in the field using an RTK-GPS system.

Ground Truth Data

A digital method was used to provide the ground truth data to evaluate the remote sensing predictions. Since manual harvesting of cotton bolls is time consuming, labor intensive, and destructive,

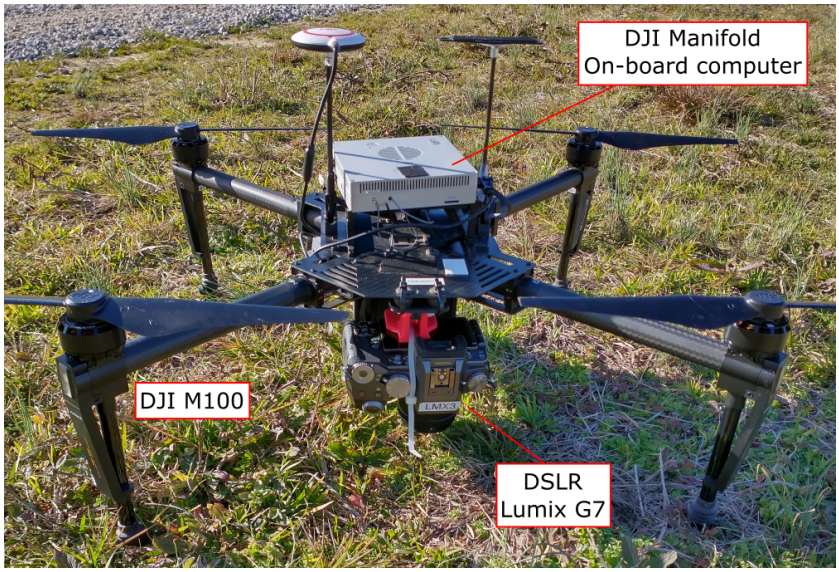

Figure 3.2: Equipment used for image collection. Unmanned Aerial Vehicle, DJI Matrice M100 Pro, equipped with a Manifold onboard computer and a Panasonic Lumix DMC-G7 DSLR camera as imaging device.

we employed high resolution 3D point clouds and a virtual reality (VR) annotation tool to count number of bolls digitally. The field was scanned on February 2^{nd} using terrestrial laser scanning (TLS) techniques. A FARO Focus S70 3D laser scanner (FARO Technologies Inc., Florida, U.S.) was used to collect high resolution 3D point cloud data (PCD) from multiple locations through the field. The scanner was configured to $\frac{1}{2}$ resolution, and $2\times$ quality. With these parameters a full scan can collect up to 174.8 megapoints with a point distance of 3.1 mm in a scan distance of 10 meters. The LiDAR data was captured from the ground at a distance ranging between 1 m and 2 m from the plants, to enable the visual identification and counting of the cotton bolls. Individual scans were registered as a single PCD using FARO SCENE 2019 software (FARO Technologies Inc., Florida, U.S.). A set of 10 coded planar markers obtained from SCENE software were de-

ployed around the field to facilitate the coregistration of multiple PCDs. SCENE was configured to automatically detect the registration markers and align the scans. After registration, individual plots were manually segmented and extracted from the 3D reconstructed PCD as .PTS files using SCENE *clipping box* tool. Each individual plot was then processed using CloudCompare software (version 2.11.2). A statistical outlier removal using 2 points for mean distance estimation and 1.0 as the standard deviation multiplier threshold was applied to the individual point clouds to reduce noise and clean spurious points. From the 488 plots that composed the field, a set of 45 plots (Figure 3.3) were selected for digital ground truth counting. A VR annotation tool developed by the Virtual Experience Laboratory at the University of Georgia was leveraged to count the cotton bolls from the clean PCDs using an Oculus Quest 2 VR set (Facebook Technologies Inc., California, U.S.) and a desktop computer. More details of this VR tool will be covered in a future manuscript. These counts were considered as the ground truth measurements (GT_{VR}) for further analysis.

The plots used as the ground truth included a representative subset of the plots in the field: from plots with a small number of cotton bolls (<20 cotton bolls) to highly dense cotton plots (>350 cotton bolls). A summary of the ground truth values for both the manual and digital sampling is presented in Table 3.1.

Table 3.1: Ground truth data summary. Manual ground truth counts include the cotton boll number measured by destructive sampling of 25 plots randomly selected from the field. Digital ground truth counts include the cotton boll number of 45 ground truth plots measured using digital approaches.

	Samples No.	**Min (boll number)**	**Max (boll number)**	**Mean (boll number)**
Digital ground truth	45	14	362	160.933
Manual ground truth	25	61	367	184.680

To calibrate this approach, the digital ground truth counts were regressed against the actual number of cotton bolls in a subset of manually harvested plots. The manual ground truth subset

was composed of 25 plots that were randomly selected from the 45 plots in the digital ground truth set. In these plots, only the open cotton bolls were harvested, counted, and weighted manually. These manual ground truth measurements (GT_{manual}) were performed in two different batches: 15 plots were harvested on February 3^{rd}, 2020 and 10 plots were harvested on February 27^{th}, 2020 (Figure 3.3). A strong linear relationship ($R^2 = 0.996$) was found between GT_{VR} and GT_{manual} for the 25 manually harvested plots.

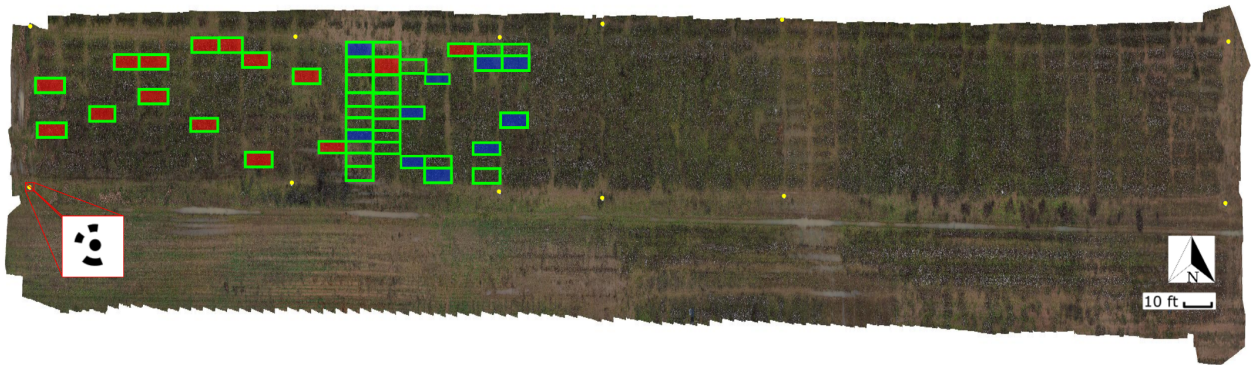

Figure 3.3: General orthomosaic map of the experimental field. Ground Control Points (GCP) used for image geo-referencing are identified as yellow circles; a total of 12 GCPs were used around the field. The red square at the bottom-left corner shows a zoom-in view of one of the 60 cm x 60 cm square GCPs with the 12-bit circular coded pattern. Ground truth plots measured on February 2, 2020 using digital approaches are identified with green boxes (45 plots). Plots harvested on February 3, 2020 are identified with boxes filled in red (15 plots); ground truth plots harvested on February 27, 2020 are identified with boxes filled in blue (10 plots).

3.2.3 Data Processing Pipeline

The data processing pipeline for cotton yield estimation presented in this paper (Figure 3.4) involved four main steps: (A) generation of an orthomosaic map of the entire field from the aerial images collected, (B) individual plot images extraction and pre-processing using image processing tech-

niques, (C) development of an image pixel classifier based on SVM for cotton pixels segmentation at the plot level, and (D) cotton boll number estimation for each individual plot.

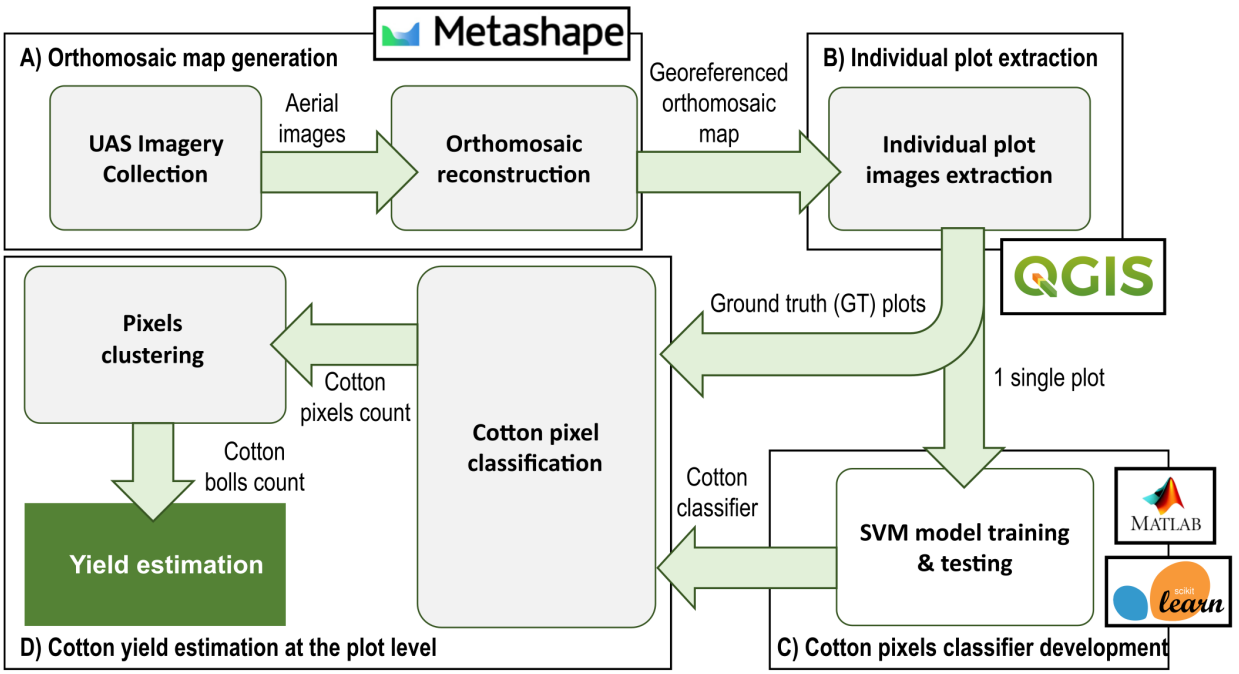

Figure 3.4: Data processing pipeline. The process pipeline includes 4 main steps: A) Orthomosaic map generation, B) Individual plot extraction, C) Image pixel classifier development, and D) Cotton yield estimation at plot level. Green arrows indicate the flow of data/information between processes.

Orthomosaic Map Generation and Individual Plot Image Extraction

An orthomosaic map was created from the RGB images using Agisoft Metashape software. A generic pair preselection with high accuracy setting was selected for photo alignment on Metashape software. By using the *"detect markers"* tool, all GCP markers were identified to georeference the images.

After applying a mild depth filtering and enabling interpolation, a digital elevation model (DEM) was generated using the dense point cloud from the estimated camera positions. Finally, using the DEM and mosaic as the blending mode, the orthomosaic map was obtained.

To extract plot images from the orthomosaic map we used the open-source geographic information system (GIS) software Quantum GIS, version 3.8.2-Zanzibar (Open Source Geospatial Foundation, Beaverton, OR, U.S.). A vector layer with the boundaries of each plot was created manually and then clipped to the orthomosaic map to obtain an individual GeoTIF image file for each plot.

Individual Plot Image Preprocessing

To reduce computation time and speed up the processing of individual plot images, preprocessing was implemented. Each individual plot image contains around 500,000 pixels. However, just a small portion of these pixels are meaningful for yield estimation, i.e., cotton-related pixels. As a general example, an image of a typical cotton crop plot will include plant leaves, weeds, and other plant matter (green to yellow color pixels); soil and other mineral matter with near-neutral hues (gray, brown, and tan color pixels); branches and other woody elements (light brown color pixels); and cotton pixels (shades of white color pixels). Hence, using traditional image processing techniques, all vegetation and soil-related pixels from the images could be potentially removed prior to pixel classification. A modified version of the Excess Green minus Excess Red Index (*ExG-ExR*) (Meyer & Neto, 2008) provided good results for removing vegetation pixels. To compute the modified index $ExGR_{mod}$ for the cotton plots, the following equation was used:

$$ExGR_{\text{mod}} = 2.5 \times G_{\text{norm}} - 3 \times R_{\text{norm}} - B_{\text{norm}} \tag{3.1}$$

where R_{norm}, G_{norm}, and B_{norm} are the normalized R, G, and B color channel values respectively that were computed as in Meyer and Neto, 2008.

Similarly, a new index that we called $Soil_{Idx}$ based on the CIELAB color space was found useful to remove soil pixels without having any visible impact on the pixels associated to the cotton bolls. To compute this index the following equation was used:

$$Soil_{\text{Idx}} = 0.5 \times L_{\text{norm}} - 2 \times a_{\text{norm}} + b_{\text{norm}} \tag{3.2}$$

where L_{norm}, a_{norm}, and b_{norm} are respectively the normalized L^*, a^*, and b^* components of the CIELAB color space.

SVM Classification Model Development

Cotton color is significantly different from most other elements in the field. Hence, pixel color can be used intuitively as a descriptor for cotton pixel segmentation. However, after a preliminary analysis of the RGB color component values of the image pixels, we found that some branches and woody elements in the background were almost indistinguishable from the cotton boll pixels, mainly because of shades and other light-blocking effects. This suggests that RGB color space information alone was not a robust enough descriptor to properly extract the cotton pixels, as previous studies have noted. Other color spaces, in particular HSV and CIELAB color models, increase invariance with respect to luminosity and lighting changes and are more robust than the RGB color space

in relation to the presence of shadows (Hdioud et al., 2018). In this study, we applied an SVM model to classify image pixels using RGB, HSV, and CIELAB color spaces information. This information was used as feature descriptors to discriminate between cotton boll pixels and the rest of background pixels.

The SVM model was developed using the Scikit-learn library (Pedregosa et al., 2011) on the Jupyter Notebook interactive computing platform, version 6.1.4. To reduce the annotation burden, only a single plot image was used to extract features and create the dataset for model training. Initially, an 11-dimensional feature vector was extracted from each pixel. These vectors contained the location of the point in the image (row, col); and the values of the RGB, HSV and CIELAB color space components of the point (R, G, B, H, S, V, L^*, a^*, b^*) for each pixel in the image. The Matlab Image Labeler app (The Math Works Inc., Natick, MA, U.S.) was used to annotate the image. This annotation tool enables the user to interactively draw pixel ROIs to label the boundaries of the visible cotton bolls to classify every image pixel into one of two target classes: cotton and non-cotton. The class of each pixel—1 for cotton pixels, and 0 for non-cotton pixels—was added to the features vector as the target column. To minimize the complexity of the model, a dimension reduction step was introduced to identify the best set of features. A recursive feature elimination (RFE) algorithm was applied for best features selection. The resulting dataset was divided into training and validation subsets with a ratio of 4:1. For model training, a radial basis function (RBF) kernel was used, the hyperparameter C was configured to be 1.0, and the hyperparameter γ was selected as 'scale'.

To evaluate the performance of the SVM model for cotton pixels classification, accuracy, precision, recall, and Type I and Type II error rates were calculated. In addition, to provide a more

comparable metric with other similar studies, the F1 score metric was also computed. The accuracy can be defined as the percentage of correct predicted pixels for the total number of pixels analyzed and can be calculated as follows:

$$Accuracy = \frac{TP + TN}{TP + TN + FP + FN} \times 100 \tag{3.3}$$

where TP and TN—true positives and true negatives, respectively—are the number of pixels correctly classified for each class, and FP and FN—false positives and false negatives, respectively—are the number of misclassified pixels.

The precision metric measured the proportion of pixels classified as cotton pixels that were classified correctly. This metric accounts for the ability of the classifier to not label a pixel that is not cotton as cotton. In contrast, the Type I error rate indicates the probability of misclassifying an non-cotton object as cotton using the classifier. The precision and the Type I error rate can be calculated as follows:

$$Precision = \frac{TP}{TP + FP} \times 100 \tag{3.4}$$

$$Type\ I\ error\ rate = \frac{FP}{TP + FP} \times 100 \tag{3.5}$$

The recall measured the proportion of cotton pixels that were classified correctly by the SVM model among all the actual cotton pixels in the image. This metric describes the ability of the classifier to find all cotton pixels. The Type II rate, in contrast, indicates the probability of misclassifying

a cotton pixel as a non-cotton pixel. These metrics can be calculated as follows:

$$Recall = \frac{TP}{TP+TN} \times 100 \tag{3.6}$$

$$Type\ II\ error\ rate = \frac{TN}{TP+FP} \times 100 \tag{3.7}$$

Finally, F1 score, as a function of precision and recall, conveyed the balance between those two metrics by taking their weighted average. It can be calculated using the following equation:

$$F1\text{-}Score = 2 \times \frac{precision \times recall}{precision + recall} \times 100 \tag{3.8}$$

All these metrics ranged from 0% to 100%, 100% being related to the best performance.

Yield Prediction Model Development and Evaluation Metrics

The developed SVM classifier was used to classify the cotton pixels presented on the unseen 45 plot images corresponding to the ground truth plots. After each image pixel was classified as a cotton or non-cotton point, a morphological erosion operation using a 3×3 elliptic structuring element, followed by a morphological dilation operation with a 5×5 rectangular structuring element were applied to eliminate noisy points and reduce the effect of pixels misclasification. Then, connected components labeling was applied to the binary image to count number of bolls. The connected components were computed using an 8-way pixel connectivity, where pixels are considered connected if they share any of the pixels that compose their respective Moore Neighborhood. These

post-processing operations were performed using the OpenCV library (Bradski, 2000), version 4.5.3.

To evaluate the performance of the cotton yield prediction model, a linear regression analysis was performed between the estimated cotton boll numbers and the ground truth values. The coefficient of determination (R^2) was used to check how closely the estimations mirrored the actual boll number at the individual plot level. Additionally, to facilitate performance comparison with other yield prediction studies that may use different scales, the normalized root mean squared error (NRMSE) was computed over the range of observed values—maximum cotton boll number minus minimum cotton boll number for the ground truth plots. The residuals were also computed to observe the difference between the ground truth data and the predicted values. Furthermore, to validate the performance of the yield prediction algorithm, the mean absolute percentage error (MAPE) was computed between the predicted number of cotton bolls and the ground truth measurements. These performance indices were computed using the following equations:

$$NRMSE = \frac{\sqrt{\frac{1}{N} \times \sum_{i=1}^{N} (y_i - \hat{y}_i)^2}}{y_{max} - y_{min}} \tag{3.9}$$

$$MAPE(\%) = \frac{1}{N} \times \sum_{i=1}^{N} |\frac{y_i - \hat{y}_i}{y_i}| \times 100 \tag{3.10}$$

where N is the total number of data points used for the linear regression analysis (N=45), y_{i} is the actual number of cotton bolls for the i^{th} ground truth plot, $\hat{y}_{\mathrm{i}}$ is the number of cotton bolls predicted by the SVM model for the image plot associated to the i^{th} ground truth plot, and $\overline{y}$ is the average number of cotton bolls per plot calculated from the ground truth values of all the 45 ground truth plots.

3.2.4 Genotype Analysis

The average number of predicted cotton bolls and the standard error (SE) for each genotype and population were calculated to evaluate the statistical accuracy of the yield estimations. To evaluate the effectiveness of the yield estimations, the null hypothesis of equal mean value of yield across all the commercial cultivars and breeding lines was tested using the one-way analysis of variance (ANOVA) at the significance level of 0.05. The statistical computing and graphics software R (R Core Team, 2020), version 4.0.3, was used for this test. After testing the effects due to genotype and its significance, the Fisher's Least Significant Difference (LSD) test was used to judge the likelihood that the observed differences between genotypes and populations comprised non-zero differences in yield performance. The LSD test was performed using the R package *agricolae* (de Mendiburu & Yaseen, 2020), version 1.3-5, to test differences among means of yield for all the genotypes.

3.3 Results

3.3.1 Individual Plot Image Extraction and Preprocessing

A total of 408 valid aerial images were used to generate the orthomosaic map (Figure 3.3). The 45 plots with the associated ground truth data were extracted manually from the orthomosaic map and saved as individual GeoTIF files. Figure 3.5 shows one of the extracted plot images. Specifically, this image was used for training the SVM classifier.

The raw RGB image (Figure 3.5 A) had 523,092 pixels. After removing the vegetation pixels using the $ExGR_{mod}$ index (Eq. 3.1), the new processed image (Figure 3.5 B) had 231,447 pixels, which means that the total number of points to analyze was reduced to 44.25%. Finally, after removing the bare soil pixels using our $Soil_{Idx}$ index (Eq. 3.2), the processed image (Figure 3.5 C) was down to 34,212 pixels, 6.54% of the raw image.

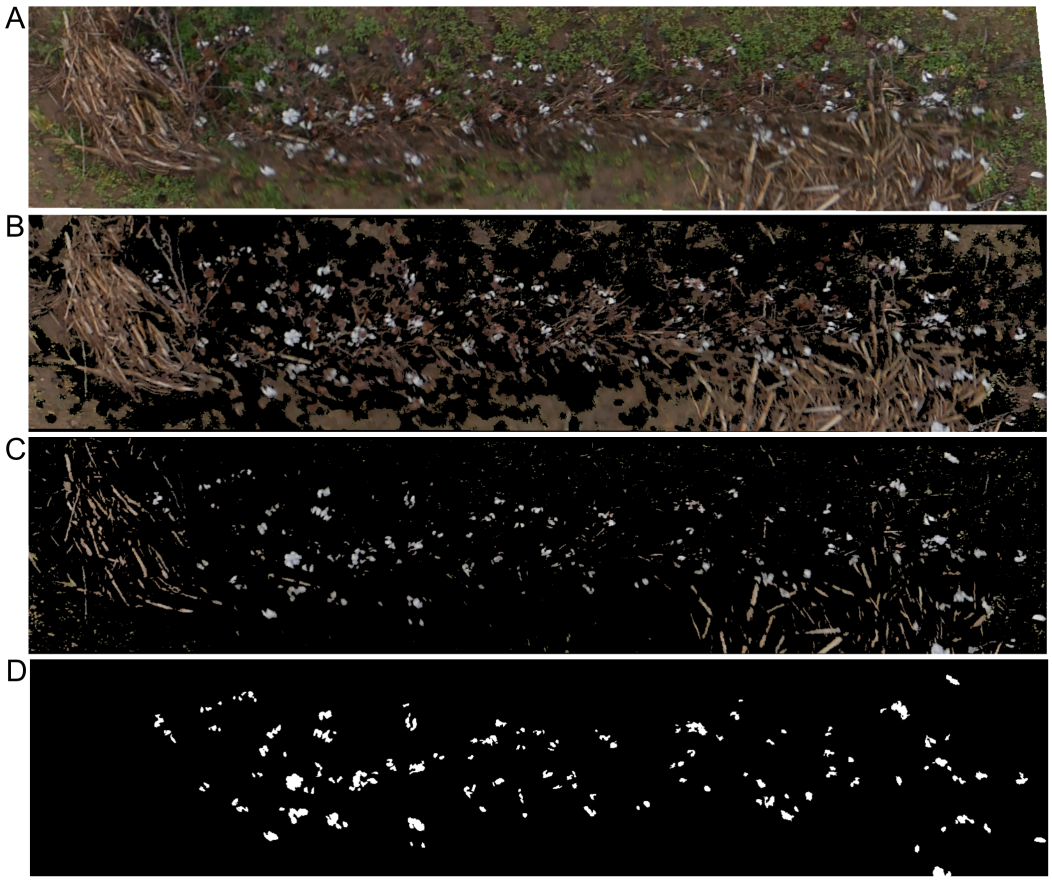

Figure 3.5: Individual plot image preprocessing results. A) Raw RGB image extracted from the orthomosaic map, B) Preprocessing results for the same plot image after removing vegetation pixels using the $ExGR_{mod}$ index (Eq. 3.1), C) Preprocessing results for the same plot image after removing also bare soil pixels using the $Soil_{Idx}$ index (Eq. 3.2), and D) Binary mask used for SVM pixel classifier training. White color identifies cotton pixels. Black color identifies non-cotton pixels.

3.3.2 SVM Classification Model Development

A single image plot was used to train the SVM model. The image selected for developing the classifier included not only the cotton plants and the cotton bolls, but also other objects typically found in the crop such as old branches and other woody objects from previous crops, weeds, and soil (Figure 3.5 A). The result of the annotation process was a binarized image mask in TIF file format (Figure 3.5 D).

For feature selection, just the 9 color channels (R, G, B, H, S, V, L^*, a^*, b^*) were analyzed. The RFE algorithm was configured to select the 4 best features, by removing one feature at each iteration using a Random Forest (RF) classifier as the estimator. Results from the RF classifier (Figure 3.6) showed that the 4 most important features were S, B, b^* and H color components. These features were then used to create the training dataset, implying a reduction from the original 11-dimensional feature vector to a 4-dimensional vector. The resulting dataset, which contained 34,212 pixels of the preprocessed training image, was then split into the training subset (27,369 pixels) and the testing subset (6,843 pixels). By reducing the number of features from 11 to 4, the average time needed to classify the pixels of the training image plot was reduced a 13.3%, from 8.42 seconds to 7.3 seconds.

To analyze qualitatively the results of our cotton pixel classifier, a color code was used to identify image pixels. Figure 3.7 shows the inference results of the cotton classifier on the training plot image compared to the annotated mask. As can be seen, most of the cotton pixels are marked with cyan color, which indicates that they were correctly classified by the SVM model, i.e. true positives (Figure 3.7 B, C, and D). However, the classifier missed some of the cotton pixels presented in

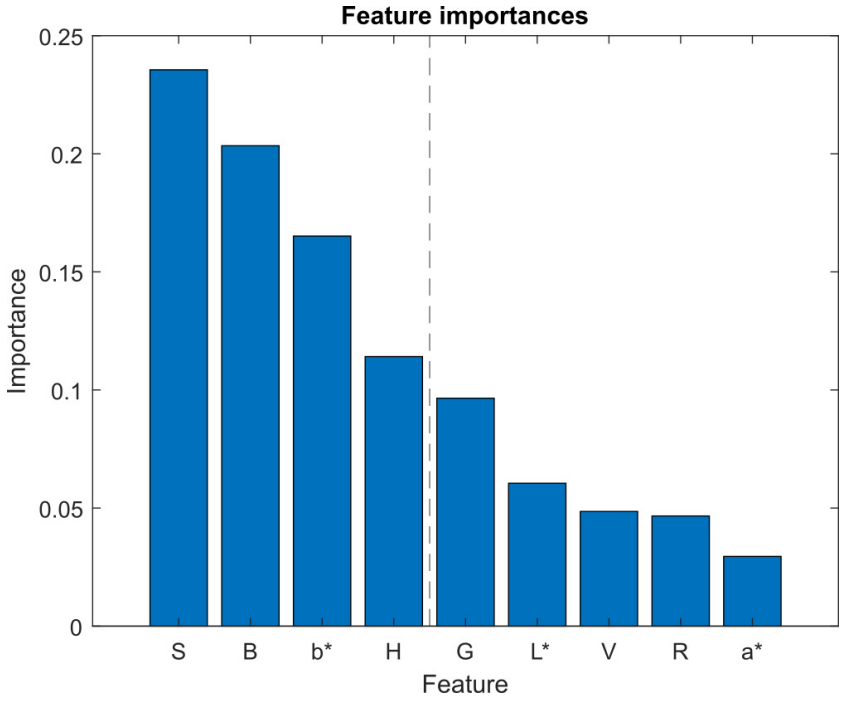

Figure 3.6: Feature selection analysis. Feature importances obtained using random forest algorithm for feature selection. Blue bars represent the importance of each feature in the classifier model. L^*, a^*, and b^* refer to the CIELAB color space components.

the image. A small portion of real cotton pixels were wrongly classified as non-cotton pixels, comprising false negatives or Type II errors and can be seen as pure blue pixels in Figure 3.7 B and D. A smaller portion of non-cotton pixels were misclassified as cotton, comprising false positives or Type I errors and can be identified as pure red pixels in Figure 3.7 A and D.

Quantitatively, the classification results of the trained SVM model on the testing subset are summarized in Figure 3.8. The column and row shown in grey indicate the classifier's overall performance. The cell in the bottom right of the plot shows the overall accuracy—correct predictions—of the pixel classifier. The model achieved an accuracy of 88.7%; 22.9% of the 6843 testing pixels were correctly classified as cotton and 65.8% of all testing pixels were correctly classified as non-

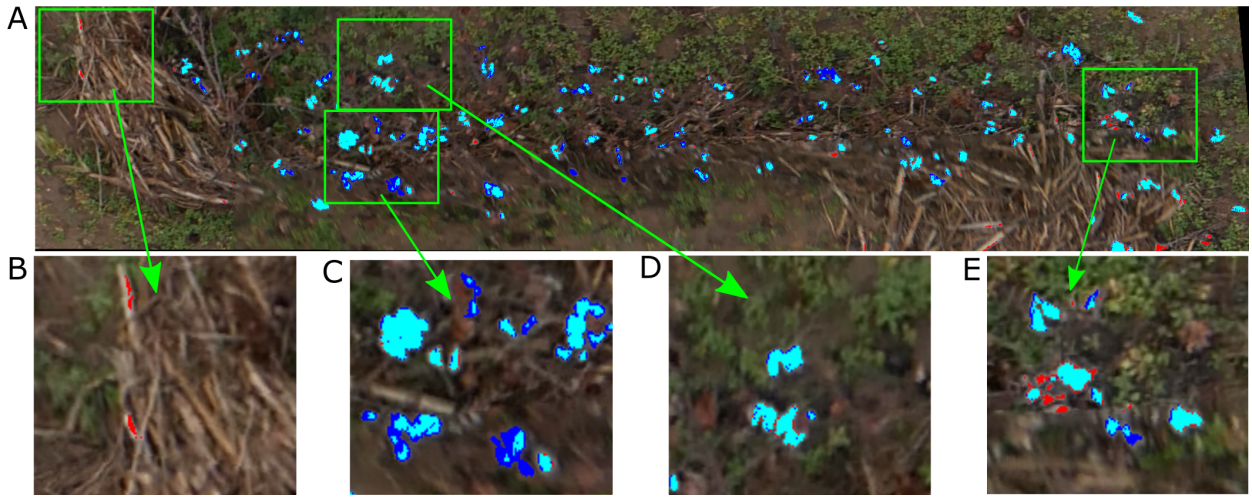

Figure 3.7: Inference results of the SVM classifier on the training plot image. Blue pixels were missed by the classifier (Type II errors); red pixels were misclassified as cotton by the classifier (Type I errors); cyan were correctly classified cotton pixels. A) Training plot image classification results, B) Non-cotton pixels misclassified as cotton (Type I errors), C) Cotton boll pixels not fully detected (Type II errors), D) Cotton boll pixels fully correctly detected, and E) Type I and Type II errors mixed together.

cotton. Only 11.3% of predictions were wrong; 7.5% of the cotton pixels were incorrectly classified as non-cotton and 3.8% of non-cotton pixels were incorrectly classified as cotton. The column on the far right of the plot shows the percentages of all pixels predicted to belong to each class that were correctly and incorrectly classified. Accounting only for the positive class identification, the upper right cell indicates the precision and the rate of Type I errors of our model. With 1564 out of 1821 cotton pixels being correctly predicted, the SVM classifier achieved a precision of 85.8%, and a Type I error rate of 14.2%. The row at the bottom of the plot shows the percentages of all the pixels that belonging to each class were correctly and incorrectly classified. The bottom left cell indicates the recall and the rate of Type II errors of our classifier. Out of 2079 actual cotton pixels,

the model achieved a recall of 75.2% and a Type II error rate of 24.8%. Finally, the image pixel classifier achieved an F1 score of 80.2% at detecting cotton pixels on the testing subset.

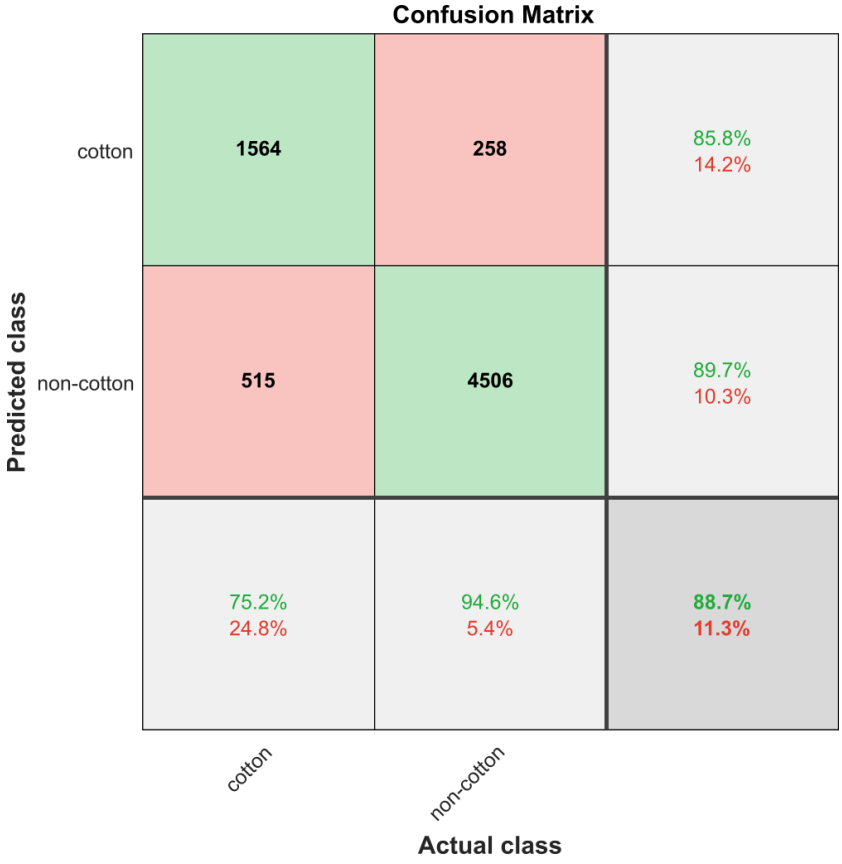

Figure 3.8: Confusion matrix chart. Green cells show the number of correct classifications by the SVM model. Red cells show the number of classification errors. Grey cells show overall performance of the model.

3.3.3 Plot-level Cotton Yield Estimation Model Development

The pixel classifier we developed was then used to extract the cotton pixels from the 45 individual images associated with the digital ground truth plots. It was able to detect subtle color changes, and was robust enough to avoid misclassifying most of the woody elements and the soil (Figure 3.9 A). After applying the image post-processing steps and the clustering algorithm, we obtained an esti-

mation of the number of cotton bolls for each image. Figure 3.9 B shows the clustering results of a sample image plot extracted from the orthomosaic map. A total of 344 different cotton bolls (pixel clusters) were identified on this particular image plot. Each one of these clusters are identified by a unique color to facilitate the visual analysis.

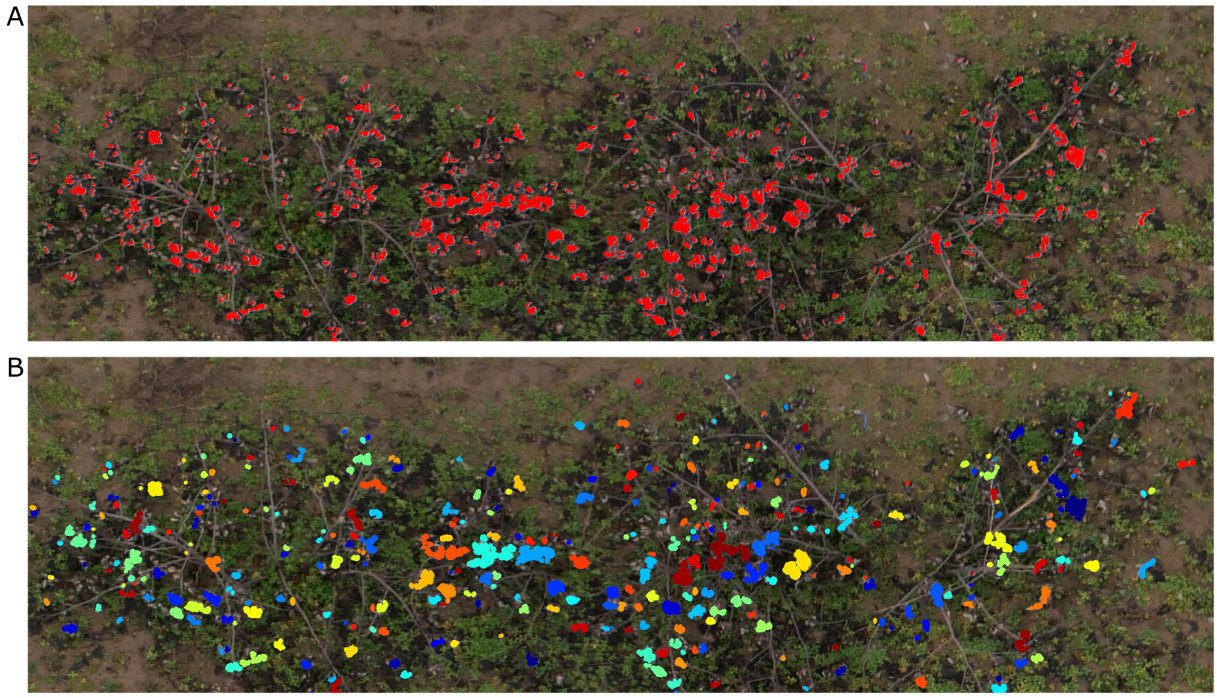

Figure 3.9: Cotton boll inference results. Cotton pixels segmentation and clustering results for a representative plot (Plot ID 45003). A) SVM classifier inference results. Red pixels represent the cotton pixels detected by the SVM classifier as cotton, and B) Cotton boll clustering results. Each cluster is identified by a unique color.

The number of cotton bolls estimated for the 45 individual image plots analyzed was regressed against its ground truth measurement (Figure 3.10). The estimations of number of cotton bolls at the plot level shows a strong linear relationship (R^2 = 0.932) with the ground truth measurements. This trend is consistent at different numbers of cotton bolls, which indicates that our pixel classifier and clustering algorithm adapted to the changing scenes and was able to segment properly the

cotton bolls from both low yielding plots and high yielding plots. The analysis of residuals showed randomly dispersed points around the horizontal axis with no apparent pattern, which indicates that the linear model was a good fit for the input data. Only one data point does not follow the regular distribution (red circled point on Figure 3.10) and given its value is more than three standard deviations from the mean, it was identified as an outlier,. Our model achieved a MAPE of 13.672% at detecting cotton bolls and a normalized RMSE value of 0.066 over the range of observed cotton bolls.

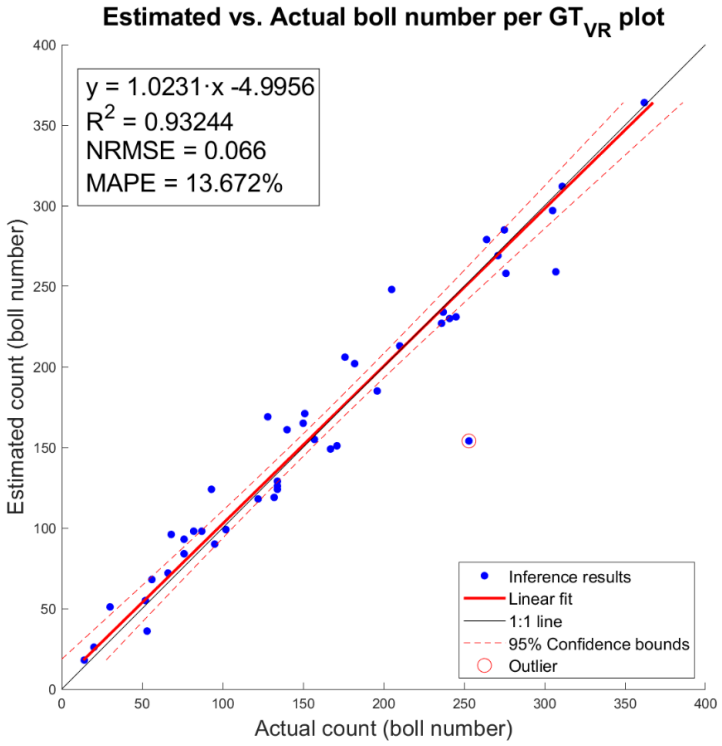

Figure 3.10: Estimated versus actual number of cotton bolls per ground truth plot (GT_{VR}). Blue dots represent inference results of our model. Red line represents the linear fit. Red dotted lines represent the 95% confidence interval for the fit. One outlier is marked with a circle surrounding the data point.

3.3.4 Web API Deployment

A web-based API (web app) was developed to integrate the developed pipeline into a more usable interface with the aim of improving automation and usability (Figure 3.11). The web app consisted of three basic functions to process each input plot image: the preprocessing steps (vegetation and soil pixels removal), the SVM classifier deployment (creation of features and SVM pixel classification), and the final cotton boll number estimation (morphological image processing operations and connected components labeling algorithm). The SVM classifier and the clustering algorithm were deployed using Flask as the core of the API, in a dockerized environment. A Docker container image of the web app is available on Docker Hub in the repository https://hub.docker.com/r/javirodsan/yieldestimation. Additionally, we will provide the code and some sample images for testing at https://github.com/Javi-RS/Cotton_Yield_Estimation.

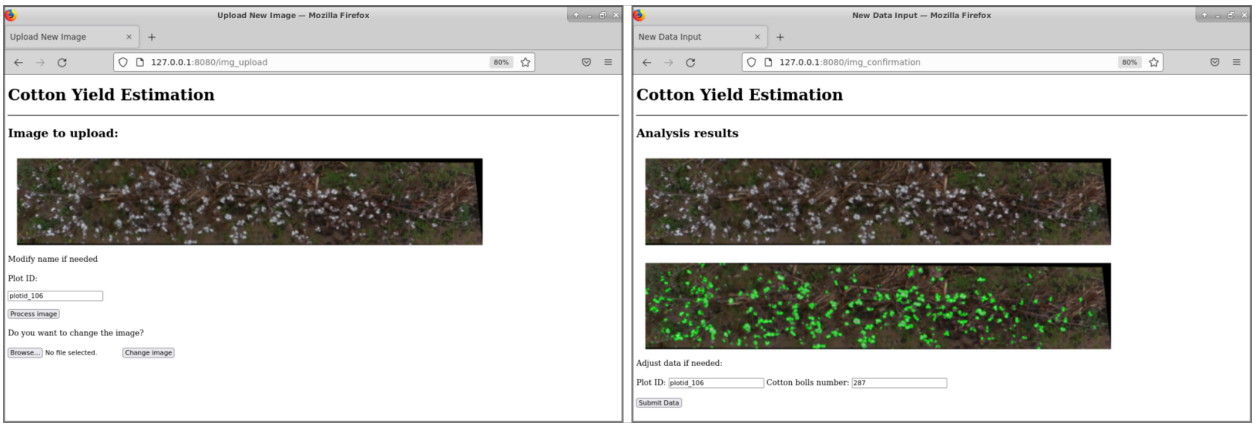

Figure 3.11: Web API for automatic image analysis.

3.3.5 Genotype Analysis Results

The mean number of predicted cotton bolls and the SE for each genotype are summarized in Table 3.2. Results show that the cotton yield estimations produced by the proposed method has relatively low SEs for each cultivar and breeding line, which indicates that the means of the yield for the different genotypes are centered around the population mean, and hence, the sampled plots are representative of the population.

Table 3.2: Statistical analysis summary of predicted yield for commercial cultivars and breeding lines. Data are sorted from higher to lower yield by genotype. Genotypes are grouped according to the probability of means differences and alpha level (0.05). Cultivars and breeding lines with the same letter are not significantly different. † indicates breeding line populations, comprised of samples of progeny from crosses between different mutant lines described in Patel et al., 2014.

Genotype	Sample size	Mean (boll number)	SE	groups
UA48	10	237.300	26.755	a
Acala1517-98	10	211.500	25.937	ab
GA230	10	199.100	21.969	abc
DeltaPine393	10	198.300	23.137	abc
L†	16	179.625	15.264	abcd
N†	20	178.800	32.627	bcd
FM832	10	176.800	19.960	bcd
Q†	40	172.525	11.224	bcd
S†	184	166.576	5.380	bcd
O†	22	163.591	18.585	bcd
M†	8	158.875	32.627	bcd
K†	44	158.364	10.682	cd
TAM94L25	10	156.300	18.049	cd
R†	44	151.614	10.072	cd
J†	18	143.889	14.703	cd
P†	32	137.594	11.275	d

The ANOVA test identified significant differences between the means of estimated yield for cotton genotypes, with $F(15, 472) = 1.874$ and $p < 0.05$. Thus, the null hypothesis of equal mean value of yield across all the genotypes can be rejected, which suggests that our methodology was

effective in identifying differences in yield. The Fisher's LSD test identified statistical differences between the estimation of average yield for the cultivars, with UA48 and Acala1517-98 being significantly higher than TAM94L25, while FM832 being significantly lower than UA48. Regarding the mutant-derived populations, L and N populations had the highest yielding, and P had the lowest yielding, with other groups in-between. While the LSD test was able to identify significant differences of means of yield among the commercial cultivars, individual breeding lines had only two replications which provided insufficient evidence for definitive ranking.

3.4 Discussion

Estimating cotton yield before harvesting would assist breeders to identify highly productive genotypes without incurring the time and cost of actually harvesting the field. Our study demonstrated that the number of cotton bolls present on each individual plot of a field can be estimated accurately by using RGB images captured from a drone flight at a low altitude. This approach can be used to quickly estimate yield at the plot level and would allow cotton breeders analyze large variety trials efficiently, especially with higher levels of replication as were used for the cultivars. However, additional data would be needed to confirm its usability on experimental breeding lines.

3.4.1 Comparison with Other Studies

As opposed to previous methods, our method used a supervised machine learning model to classify the pixels in the image instead of using traditional global thresholding techniques. Approaches for cotton yield estimation based on traditional image processing techniques (Dodge, 2019; Huang

et al., 2016; Yeom et al., 2018) usually assume that cotton has a distinctive spectral response that enables the easy discrimination of cotton bolls from the rest of the elements of the crop just by using a threshold value in one or more of the RGB channels. However, in a real-case scenario the illumination conditions can change considerably during data collection, and often the range of image intensities of the color channels for the cotton bolls are similar to other crop elements. Although some studies have applied adaptive threshold techniques or have included prior preprocessing steps to minimize the limitations of global thresholding techniques (Maja et al., 2016), these approaches are not flexible enough to cope with the variability of reflectance across a field, and hence their accuracy is limited. Our method uses an SVM model based on 4 image channels to segment cotton-related pixels. Machine learning techniques are more flexible than traditional image processing methods at finding patterns on data with non-obvious relationships. A recent study (Ashapure et al., 2020) has already investigated the use of machine learning techniques to estimate cotton yield. However, the focus of their study was to find the relationship between cotton yield and the parameters of the crop during the course of the season, not near harvest. Therefore, the potential of this approach for later growth stages might be limited because it includes crop features related to the canopy status. Our approach was developed to be applied after crop defoliation (which commonly precedes cotton harvest) to reduce the effects of occlusions by leaves and maximize cotton boll visibility. Although this limits the applicability of our method to the pre-harvesting time frame, this is the period during which breeders evaluate the overall performance of new breeding lines, so it can be considered one of the key stages in the selection trials.

3.4.2 Type I and II Errors Analysis

Our SVM classifier was able to segment the cotton pixels accurately from the input images, showing a promising overall performance for the training image (Figure 3.7). As we have commented in section 3.2, the classifier made some Type I errors (false positives), and Type II errors (false negatives). In our context we tried to minimize the Type I errors, i.e. the number of background pixels wrongly classified as cotton pixels. We aimed to detect all the cotton pixels in the image, but we did not want to overestimate them. Usually, the number of cotton boll pixels in a plot image is much lower than the number of pixels from other parts of the plants and background. Hence, the chances of misclassifying non-cotton pixels are higher. Figure 3.12 shows the performance of the SVM classifier model on an unseen plot image. Type I errors were mainly caused by elements of the scene with a spectral response similar to the cotton bolls. As shown in Figure 3.12 B, some branches and other foreign objects in the field were highly reflective and they were misclassified as cotton pixels.

Type II errors were caused primarily by dark cotton pixels in the image that were not properly detected by the classifier. Bolls from the lower parts of the canopy were less reflective than those from the top parts with more light. Therefore, the image pixels were usually darker on these parts, and the SVM classifier was not able to detect completely all the cotton pixels of some cotton bolls (Figure 3.12 B). These zones are usually small, and the image post-processing operations tend to remove them before clustering (Figure 3.12C). Even though there were some obvious classification errors, most of the cotton bolls detected by our algorithms were true cotton bolls. These errors do

not necessarily have a substantial effect on our estimations of yield because it was expected that not all the cotton bolls can be seen from downward images.

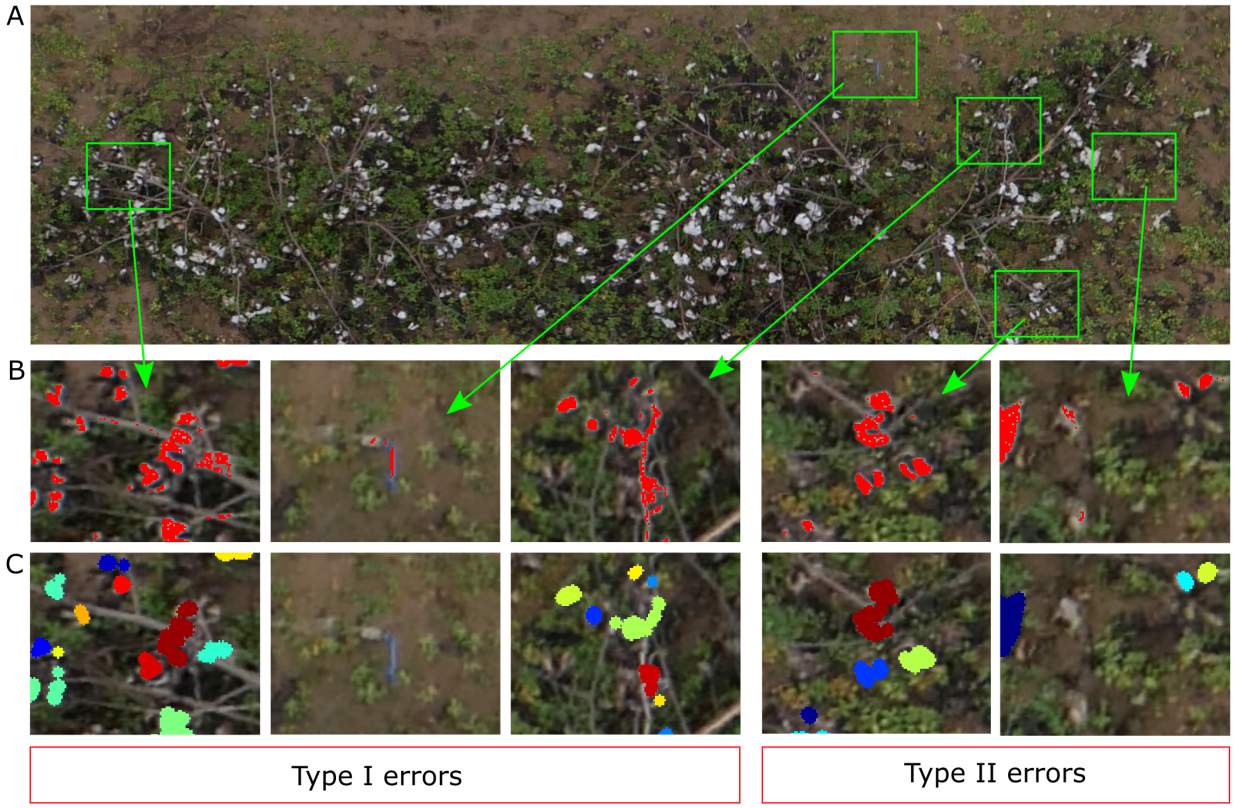

Figure 3.12: Qualitative analysis of the yield estimator. A) Original image plot (Plot ID 45003), B) Zoomed-in view to Type I and Type II errors at segmenting cotton pixels. Red represents the pixels segmented by the SVM classifier as cotton pixels, and C) Zoomed-in view to the same zones as (B) to visualize the clustering results. Different colors identify different clusters (cotton bolls).

The morphological operations enhanced the appearance of the cotton bolls in the binarized images and reduced the influence of the SVM Type I errors on the cotton boll estimation. The small elliptic structuring element used for the erosion operation contributed to removing isolate pixels and small pixel clusters associated to branches and other wrongly classified elements, and hence the pixel clustering step performed relatively well at isolating cotton bolls and correcting Type I

errors (Figure 3.12 C). A larger element for the dilation operation aided to extend the boundaries of the rest of cotton pixels to eliminate gaps between close pixels and consolidate cotton bolls (Figure 3.12 C).

3.4.3 Limitations

We used a digital RGB camera to collect the aerial images, which internally processes the data from the image sensor and performs the JPEG compression to save the image in a removable storage media. These images are stored without a previous radiometric correction. We tried to minimize the effect of the illumination on the data collection day by using an automatic color balance compensation. Although the AWB compensation was adequate for our data analysis, it might not be a universal solution for all the possible illumination conditions in the field. Therefore, the use of our model directly to images collected at different times may be limited if the atmosphere and solar radiation greatly differ from those on our data collection day. However, since the method we proposed is relatively fast and easy to use, retraining the SVM model with new data from the specific collection day can be feasible.

Additionally, as we noted in section 3.3, one of the points in the data set was identified as an outlier during the linear regression analysis (red circled point in Figure 3.10). By further analyzing this particular data point and the associated plot (Figure 3.13), we can determine that these kind of errors are caused by one of the main limitations of 2D image analysis: lose of depth information. The SVM classifier detected the cotton pixels in the orthomosaic image fairly well. Moreover, the clustering algorithm was able to find and segment properly some of the cotton bolls (Figure 3.13 B). However, the high density of cotton bolls in this plot made the cotton pixels to appear close together

on the 2D aerial image (Figure 3.13 A), which prevented our clustering algorithm from segmenting all the cotton bolls properly. Therefore, the estimation of number of cotton bolls for this plot was not accurate—only 154 out of 253 cotton bolls were detected. If we compare this image with its 3D point cloud counterpart, we can see that a substantial number of the cotton bolls were located in almost vertical branches (Figure 3.13 D), which made the lower cotton bolls to be heavily occluded by the rest when looking from the top (Figure 3.13 C). In a 2D image all the pixels are contained in the same plane. This lack of depth information impeded our algorithm to identify cotton pixels at different height levels and led to underestimating the number of cotton bolls.

3.4.4 Future Work

Most of the image processing can be performed automatically without any supervision. However, the extraction of plot images from the orthomosaic map was carried out manually. A future research direction could investigate the feasibility of automatically separating the plots from the orthomosaic map using only geographic information. This would improve the efficiency of this methodology and would contribute to improving the throughput for breeding purposes. Additional research could also be performed to improve cotton pixel classification, including the use of more advanced deep learning methods such as convolutional neural networks (CNN) that could discriminate cotton pixels from the rest of elements by automatically integrating spatial and morphological information as additional features without needing to design them manually. Even though the methodology presented here was developed and tested using individual plot images, it could be modified easily to perform yield estimations on production fields because of its ease of use. Some minor modifications on the processing pipeline would make it suitable for production fields. Instead of extracting entire

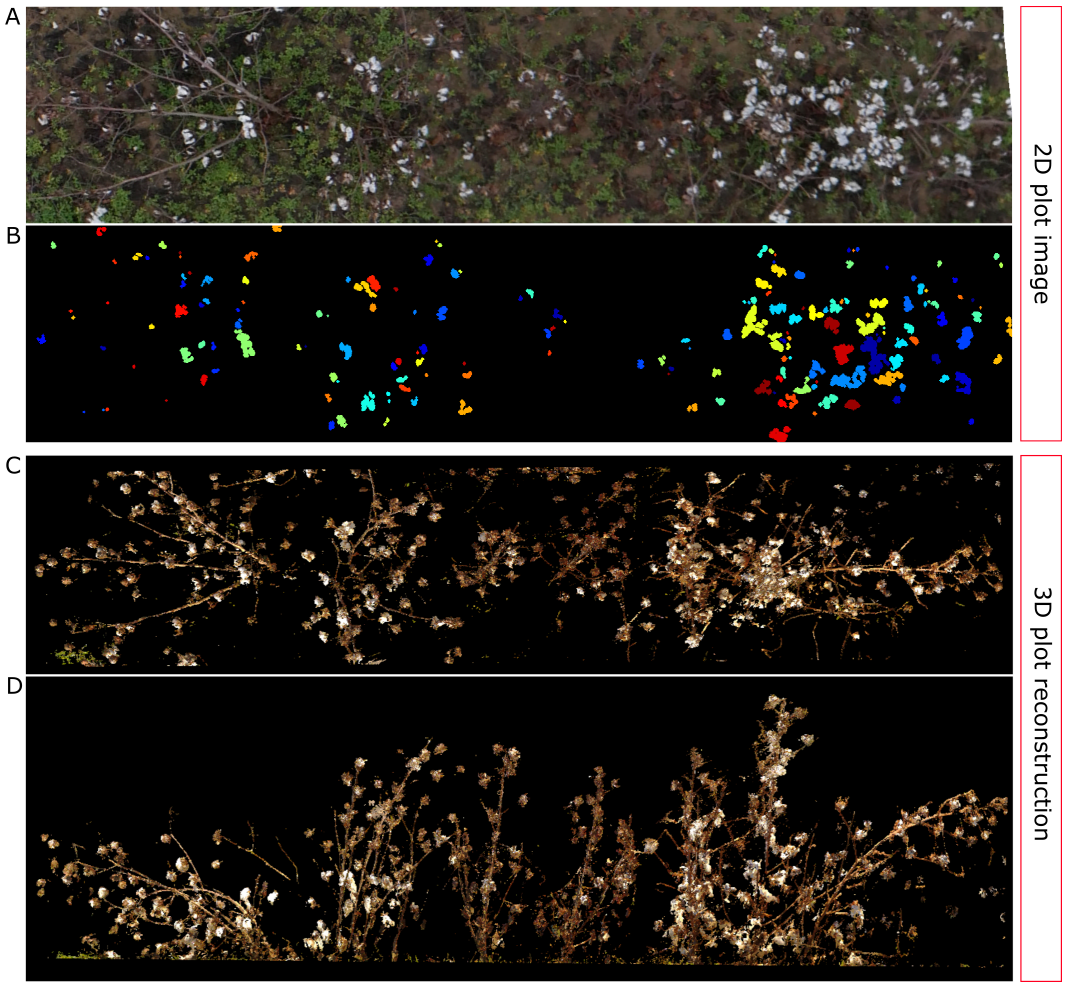

Figure 3.13: Outlier analysis: 2D versus 3D comparison. A) Original image plot (Plot ID 41028), B) Cotton boll clustering results; each cluster is identified by a unique color, C) TLS reconstructed 3D point cloud: Top view, and D) TLS reconstructed 3D point cloud: Frontal view.

plots, the orthomosaic map could be divided into several sections or cells using grids with fixed dimensions. Then, our method could be used to estimate the yield from each cell and then aggregate the estimations to have an estimation of the total production of the entire field. However, further studies will need to be carried out to validate this approach on different crop densities. Additionally, our model was able to detect cotton bolls consistently from almost all the plots of the field. However,

we didn't correct the images atmospherically, which may affect the direct application of our model to images collected under different conditions. We will investigate how to further improve our pipeline by including a preprocessing step to correct radiometrically the images and make our method agnostic to illumination lighting conditions and imaging sensors. Finally, we were able to use digital ground truth techniques based on 3D information to demonstrate some of the limitations of 2D approaches for estimating yield from aerial imagery. We will investigate the feasibility of using 3D crop analysis to overcome these limitations and its viability to estimate other crop traits.

3.5 Conclusions

This study presents a cost-effective approach for estimating cotton yield production from images collected using a drone and a conventional RGB camera. A supervised machine learning classifier based on an SVM model was trained using only a single plot image. Since this approach requires the annotation of only one RGB image, it reduces the complexity and time needed for model deployment. The classifier demonstrated to be robust to changing scenes and discriminated accurately the cotton pixels in individual plot images with different number of cotton bolls. Consequently, reliable cotton boll counting was obtained. In addition, the methodology was found to be effective in identifying the differences in yield among different commercial cultivars and breeding lines. Overall, the proposed method can help improve the efficiency of decision making for breeding programs and optimize the use of resources by speeding up the analysis of entire field trials. Future work will focus on automating the extraction of plot images, as well as on the application of 3D-based approaches and more advanced machine learning methods to improve cotton boll detection.

CHAPTER 4

LEVERAGING UAS IMAGERY AND THE SEGMENT ANYTHING MODEL FOR AUTOMATED TRAIT EXTRACTION IN PEANUT BREEDING FIELDS. [1]

[1] Javier Rodriguez-Sanchez, Ye Chu, Peggy Ozias-Akins, Jing Zhang, Kyle Johnsen, and Changying Li. To be submitted to *Plant Methods*

Abstract

The increasing demand for efficient agricultural practices necessitates advancements in high-throughput phenotyping (HTP) tools. Unmanned aerial systems (UASs) have transformed data collection for field phenotyping. This study developed and validated a data processing pipeline integrating computer vision and deep learning techniques to automate UAS-based phenotyping for yield-related traits in peanut breeding fields. The Segment Anything Model (SAM) auto-mask generator was used to identify the breeding field and its geographic orientation without user input, while multi-point prompts initialized SAM for precise individual plot segmentation masks. This approach reduced over-segmentation and improved plot boundary delineation compared to the traditional watershed segmentation method, especially with overlapping canopies. Correlation between field measurements and canopy height was derived using linear regression, achieving an R^2 value of 0.78, an RMSE of 3 cm, and an MAPE of 10%. Convolutional Neural Network (CNN) models estimated growth habit and main stem prominence with accuracies of 84% and 81%, respectively. The use of multispectral imagery further enabled the detection of tomato spotted wilt virus (TSWV), being able to classify plots into three infestation levels with an accuracy of 66%. This pipeline significantly enhances phenotyping efficiency and accuracy for peanut breeders, reducing manual labor and providing a scalable solution for large-scale breeding programs.

4.1 Introduction

Plant phenotyping under field conditions is crucial to enhance breeding efforts and disease resistance evaluation in peanut crops. Many traits related to plant architecture influencing cultivation practices

and productivity of peanut crops have been studied, including main stem height, reproductive branch length, and branching pattern (L. Li et al., 2019; Nigam, 2014). These traits are important for breeders seeking to improve yield gains. However, current methods for assessing these traits in the field often rely on labor-intensive manual techniques or visual ratings, which are prone to errors. The complexity of plant architecture further complicates accurate trait differentiation and digitization, highlighting the need for more precise and efficient phenotyping techniques.

Handheld sensors has shown promise in replacing visual scores for disease resistance selection in peanut breeding programs (Chapu et al., 2022). These sensors enable more accurate and efficient assessment of disease resistance traits compared to manual methods, although analyzing large fields manually remains cumbersome. To overcome these challenges, there is a critical need for rapid and accurate phenotyping methods that can efficiently predict traits under varying field conditions (Bagherian et al., 2023; Wood et al., 2023). Integrating high-throughput phenotyping (HTP) approaches can significantly enhance breeding efforts by enabling improved selection of breeding lines and rapid screening of genotypes with enhanced characteristics of yield and stress tolerance.

The advent of unmanned aerial systems (UAS) and advanced imaging technologies has transformed precision agriculture. These systems offer cost-effective, high-throughput crop data collection capabilities, with diverse sensor options such as red-blue-green (RGB), multispectral, hyperspectral, thermal, and ligth detection and ranging (LiDAR), making them adaptable to complex field environments (W. Guo et al., 2021; Xie & Yang, 2020). UAS-based phenotyping promises large-scale, rapid, and non-destructive data collection for crop breeding (Gano et al., 2024). However, challenges such as limited data resolution, data processing speeds, and the need for robust

models to handle complex traits under varying environmental conditions persist (P. Hu et al., 2019; Yang et al., 2017).

Different approaches based on UASs have enabled efficient assessment of agronomic traits of peanut crops under field conditions. RGB aerial imagery has been used for estimating canopy height (Brown et al., 2022; Sarkar et al., 2020), while multispectral imaging has facilitated early disease detection (Patrick et al., 2017), peanut maturity assessment (Abd-El Monsef et al., 2019), leaf area index monitoring (Qi et al., 2020), and chlorophyll content analysis (Qi et al., 2021). Advanced methods incorporating machine learning and artificial neural networks have further enhanced crop trait estimation (Bagherian et al., 2023; Santos et al., 2021; Sarkar, Cazenave, & Oakes, 2021), increasing the throughput of phenotyping tasks. However, despite these advancements, challenges such as lack of standardized processing techniques, accuracy of trait prediction models, and validation across diverse conditions remain significant concerns (Abd-El Monsef et al., 2019; Patrick et al., 2017; Santos et al., 2021; Sarkar, Ramsey, et al., 2021; Souza et al., 2022; Sweet et al., 2022).

Automation in UAS-based data processing is essential for achieving the required throughput in field crop breeding. Initial efforts in UAS-enabled large-field analysis (Hearst & Cherkauer, 2015) have evolved into sophisticated, automated algorithms (Mardanisamani & Eramian, 2022). However, no universal solutions have been developed yet. Recent advancements in plot extraction automation using UAV imagery have significantly improved phenotypic data analysis efficiency and accuracy. Machine learning algorithms and software tools and functions such as Easy MPE (Tresch et al., 2019), GRID (C.-J. Chen & Zhang, 2020), FIELDimageR (Matias et al., 2020; Pawar & Matias, 2023), R/UAStools::plotshpcreate (Anderson & Murray, 2020), or AirMeasurer (G. Sun et al., 2022) have reduced manual effort in segmenting field plots, but some kind of input

in the form of initial parameters or manual pre-processing are still required for most of these current developments. Despite these advancementes, challenges such as image resolution trade-offs, plot alignment variability and overlapping, and adaptability to non-homogeneity within fields still persist in recent studies (Ahmed et al., 2019; Ha et al., 2021; Tresch et al., 2019). Attempts to reduce even more the need for manual input have been implemented (Bruce et al., 2020; Ha et al., 2021, 2022; Khan & Miklavcic, 2019; Mardanisamani et al., 2021; Robb et al., 2020), but still some parameters need to be pre-selected for optimal performance or the methods are dependent on external equipment or software that may limit its usability.

Recent advancements in deep learning, particularly the development of vision foundation models show significant promise in addressing limitations in data processing automation for agricultural applications (J. Li et al., 2024). Specifically, the Segment Anything Model (SAM) (Kirillov et al., 2023) has demonstrated its performance at classifying pixels into different semantic categories without additional training, showing potential in outlining cultivated land from remote sensing images (Gui et al., 2024; Gurav et al., 2023; J. Sun et al., 2024). However, the quality of the provided masks is influenced by image resolution, with a tendency of over-segmenting cluttered scenes (Carraro et al., 2023). To address this, agricultural-specific adapters have been explored (Y. Li, Wang, et al., 2023), yet precise segmentation remains challenging due to complex backgrounds and low contrast between targets and surroundings. While SAM scales well for regular objects, segmenting irregular agricultural objects in complex scenes requires prior knowledge for successful segmentation (Ji et al., 2024), emphasizing the need for appropriate prompt selection to enhancing SAM in challenging environments (J. Hu et al., 2024). Additionally, detailed segmentation masks for phenotyping may require post-processing for improving its quality (D. Williams et al., 2023).

Solving these challenges to fully exploit SAM's ability to generalize across various data types and conditions, might enable fully automation of plot extraction from UAV imagery in agricultural fields, reducing human intervention and improving efficiency for large-scale plant phenotyping applications.

This study presents a fully automated methodology for processing aerial imagery, addressing current challenges in data processing to streamline the extraction of plot-level trait data and facilitate high-throughput phenotyping in breeding trials. Our main contribution involves leveraging SAM's generalization capabilities to identify and segment individual plots from orthorectified field image maps without additional training. This method significantly reduces manual labor in post-processing and optimizes the data processing pipeline, providing an advanced solution for the automated assessment of traits in breeding fields. This approach can significantly reduce the burden of annotating plot fields during the analysis of multiplot breeding fields. The aim of this study was to develop and validate a data processing pipeline for high-throughput phenotyping (HTP) of yield-related traits in peanut breeding using multispectral aerial imagery and deep learning. The specific objectives were to: (1) develop a fully automated pipeline based on SAM models for aerial data processing, encompassing field identification, individual plot segmentation, and canopy height normalization; (2) develop and validate CNN-based models for estimating morphological traits such as canopy height, growth habit, and main stem prominence using RGB imagery; and (3) explore the feasibility of detecting tomato spotted wilt virus (TSWV) crop infestation using multispectral imagery and deep learning.

4.2 Materials and Methods

4.2.1 Experimental Field and Trait Field Measurements

The current study was conducted at the University of Georgia research station in Gibbs Farm, Tifton, GA (Figure 4.1). Plant material was planted in early June 2022. The experiments were arranged in a randomized complete block design with three field replicates per line. Three peanut populations——GT, C1803, and IF——were hand-planted in two-row plots. Three seeds of each line were sowed on both sides of the plot with a 15 cm distance between seeds. A total of 1350 plots were planted in raised beds, separated by two-meter alleys of bare soil.

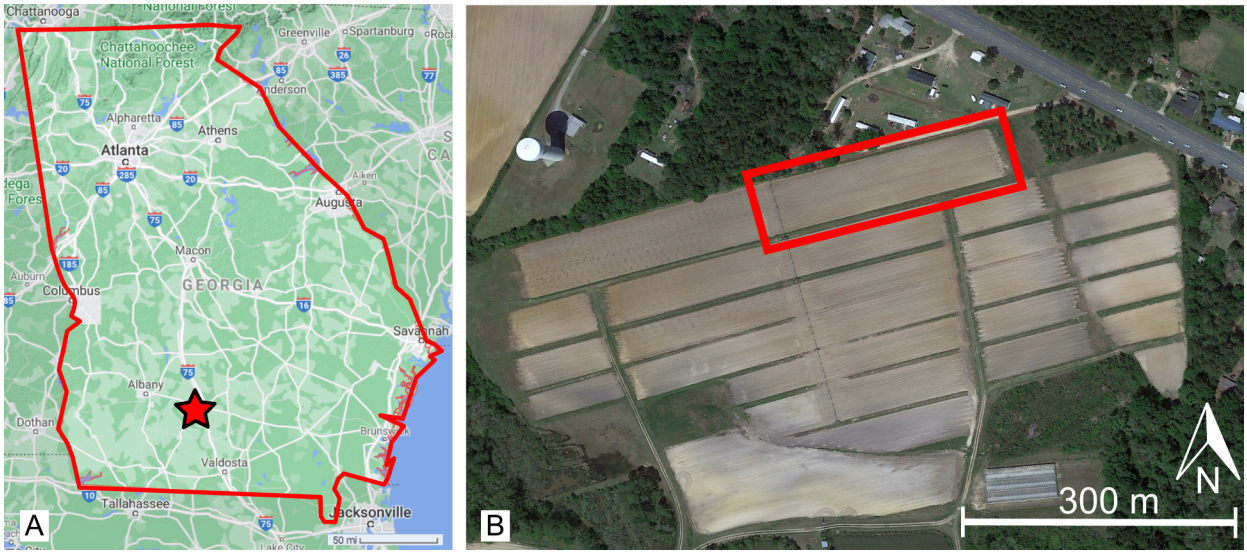

Figure 4.1: Experimental field location. The experiments were conducted in the Gibbs Farm research station, Tifton, GA, US. A) General map of Georgia, the experiment location is marked with a red star; B) Gibbs Farm aerial view (Tifton, GA, US), the specific location of the experimental field is delimited by a red rectangle.

Morphological trait measurements were manually collected 90 days after planting (DAP). Canopy height (CH) was determined by measuring the distance between the ground and the top of

the canopy using a measuring tape. CH measurements were taken from 50 randomly selected plots, with two measurements per plot, averaged to obtain the final CH value. The CH measurements ranged between 16 cm and 40 cm, with an average value of 24.8 cm and a standard deviation (SD) of 6.37 cm.

Main stem prominence (MP) and growth habit (GH) were visually rated following standard peanut trait categorization (Pittman, 1995). MP was rated on a scale from 1 to 3 based on the visibility of the main stem (1: not apparent, 2: somewhat apparent, 3: apparent). GH was rated on a scale from 1 to 6 (1: prostrate, 2: spreading, 3: spreading and bunch, 4: bunch, 5: erect, 6: mixed). A plant with a prostrate growth habit exhibits an erect main stem with branches close to the ground. A spreading growth habit shows branches partially on the ground with tips curved upward, and a slightly taller main stem. A bunch growth habit displays a semi-erect shape with branches curving upward from the base, and the main stem tends to be slightly more prominent than other branches. An erect growth habit features straight branches that ascend from the base at angles of 45° or less from vertical, with the main stem typically taller than that of bunch-type plants. The distribution of MP and GH classes across the plots is summarized in Tables 4.1 and 4.2.

Table 4.1: Visual ratings summary for main stem prominence. Number of samples per main stem prominence (MP) class for all plots in the field.

	Number of samples			
MP class	**GT**	**C1803**	**IF**	**Total**
Not apparent	266	255	168	689
Somewhat apparent	13	13	60	86
Apparent	145	168	192	550

Table 4.2: Visual ratings summary for growth habit. Number of samples per growth habit (GH) class for all plots in the field.

	Number of samples			
GH class	**GT**	**C1803**	**IF**	**Total**
Prostate	0	1	3	4
Spreading	207	262	216	685
Spreading&Bunch	19	8	36	63
Bunch	192	166	170	528
Erect	0	0	0	0
Mixed	13	7	0	20

Visual ratings of Tomato Spotted Wilt Virus (TSWV) were also conducted in all plots of the field, accounting for the percentage of the canopy exhibiting TSWV symptoms. The infestation level ranged from 0% (no visible symptoms) to 100% (totally symptomatic canopies).

4.2.2 Data Processing Pipeline

The data processing pipeline for peanut crop phenotyping developed in this study involved three main steps: aerial data collection and pre-processing, orthoimage processing, and agronomic traits estimation (Figure 4.2). Our main contributions were focused on automating the post-processing pipeline after aerial data collection and pre-processing. The data processing pipeline was developed in Python using the PyTorch as the machine learning framework. All experiments were conducted on a desktop computer equipped with an 8-Core Intel(R) Core(TM) i7-9700K CPU running at 3.60 GHz, with 64 GB of RAM, and an NVIDIA GeForce GTX 1080 8GB GPU card.

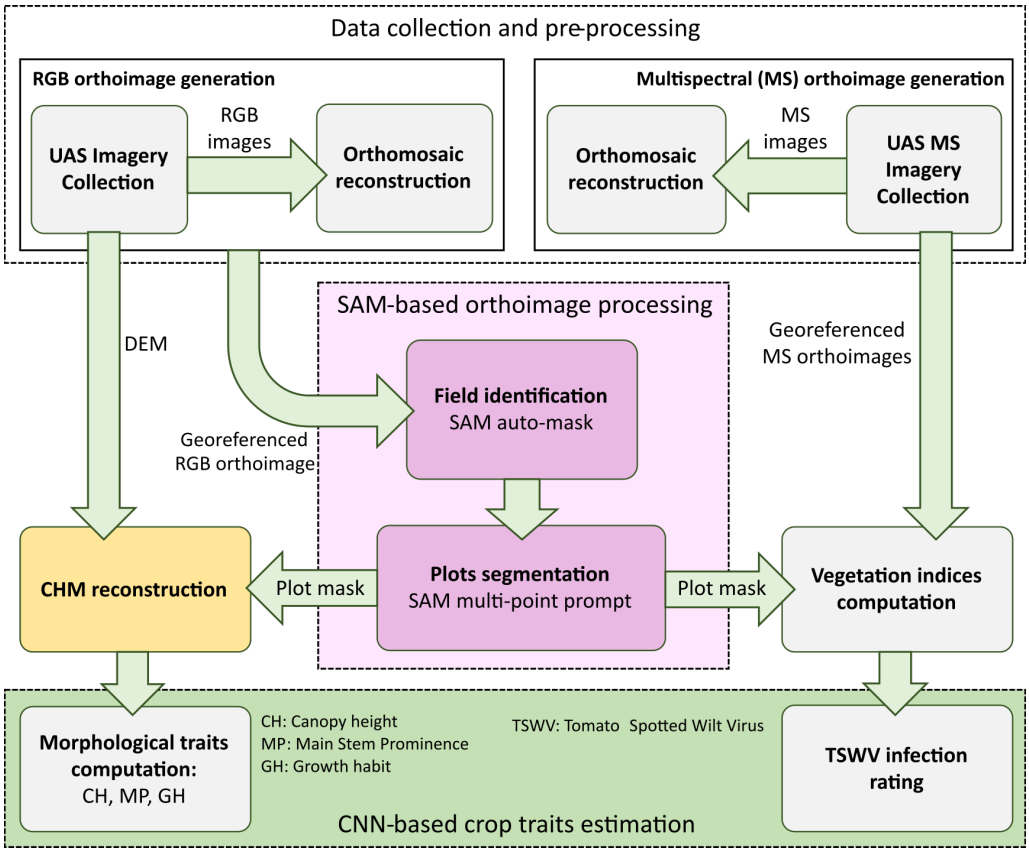

Figure 4.2: Data processing pipeline for peanut phenotyping. Processing workflow for automated extraction of phenotypic information from red-green-blue (RGB) and multispectral (MS) aerial imagery. Green arrows indicate the flow of data/information between processes. Colored boxes indicate the main contributions of this study.

Data Collection and Pre-Processing

Red-green-blue (RGB) and multispectral (MS) aerial imagery were captured on the same day during two separate flights. RGB imagery was collected using a Phantom 4 Pro V2 quadcopter (Shenzhen DJI Sciences and Technologies Ltd., Shenzhen, China) with an integrated color camera. The drone was flown at an altitude of 30 m above ground level, maintaining an 80% overlap for both front and side images. For MS imagery collection, a DJI Matrice M200 quadcopter (Shenzhen DJI Sciences

and Technologies Ltd., Shenzhen, China) equipped with a Slantrange 3p MS sensor (Slantrange Inc., California, US) was used. This sensor collects four spectral bands with peak wavelengths at approximately 550 nm (Green), 650 nm (Red), 710 nm (RedEdge), and 850 nm (NIR). The MS sensor was mounted on the bottom of the drone facing downward, and the flight was performed at an altitude of 50 m above ground level, ensuring a ground sample distance (GSD) of approximately 2.5 cm per pixel. All flights were conducted within 2 hours of solar noon, following pre-programmed flight paths using DroneDeploy (DroneDeploy, Inc., California, US).

Collected imagery was pre-processed to obtain orthorectified images of the field using Agisoft Metashape software (Metashape Professional 1.5.5, Agisoft LLC, Russia). Both image sources—RGB and MS—were processed in individual chunks within the same project, following the methodology described in (Rodriguez-Sanchez & Li, 2022). For each chunk, camera positions were estimated using a generic pair preselection with high accuracy for photo alignment. A digital elevation model (DEM) was then generated from the dense point cloud created using the estimated camera positions. Finally, the orthomosaic map was produced from the DEM with mosaic blending mode. After orthomosaic reconstruction, both chunks were aligned using the ground control points deployed in the field.

4.2.3 SAM-based Automated Orthoimage Processing

The Segment Anything Model (SAM) by Meta AI includes two main operation modes: automatic and interactive. The automatic mode uses an auto-mask generator to identify and generate segmentation masks for all objects in an input image. The interactive mode allows users to guide the segmentation process by providing foreground and background points. We leveraged both of

them sequentially to achieve full process automation. From the vision transformer (ViT) backbones available for SAM, we chose the largest, ViT-H (Huge), which excels in capturing intricate details and long-range dependencies in images, making it ideal for high-resolution images or complex datasets.

Experimental Field Identification

In the SAM Auto-Mask Generator mode, a dense grid of points is created across the image, with each point serving as a potential starting point for object detection. SAM evaluates these points to detect and generate masks for all distinct objects, effectively segmenting every identified object without requiring user input. This mode is particularly useful for comprehensive segmentation in fully automated workflows.

SAM uses several parameters to achieve accurate segmentation, including thresholds for object detection, which help distinguish significant objects from noise. Initially, we found that the default settings impeded the effective detection of our field. To address this, we adjusted the mask quality settings thresholds, allowing for less perfect masks to be retrieved. Specifically, we reduced the predicted Intersection over Union (IOU) threshold from 0.88 to 0.5 and the stability score threshold from 0.95 to 0.5. Additionally, we scaled the image so that the longest dimension equaled 1024 pixels to speed up the process, similar to the procedure used in the original SAM paper.

Individual Plot Segmentation

After identifying the field extents and its geographic orientation, we proceeded to identify each individual plot. Our approach for plot segmentation was based on the SAM multi-point prompts

mode, which allows users to interactively guide the segmentation process by providing foreground and background points. Users select one or several points on the object to segment (foreground) and points on areas to be excluded (background). Based on these user-specified points, SAM refines its segmentation to accurately include the object and exclude the background, generating a customized segmentation mask.

To automate the selection of point prompts and avoid manual interaction, we used computer vision techniques to identify potential points that could guide SAM (Figure 4.3). First, the Excess Green minus Excess Red Index (ExG-ExR) (Meyer & Neto, 2008) allowed us to roughly segment the vegetation pixels in the image. These pixels were accumulated vertically, resulting in a graph with peaks (maxima) and valleys (minima). The valleys indicated vertical areas with less vegetation, and the middle point of each valley was considered as the X-coordinate separating contiguous crop ranges (columns of plots) in the field (Figure 4.3A).

Each range was then processed individually (Figure 4.3B). By accumulating the vegetation pixels horizontally, we identified the horizontal lines with more accumulated vegetation, approximating the rows where the plants were planted (blue dashdotted lines in Figure 4.3B). The central points of the vegetation along these lines were used as plot centroids.

The detected centroids were used as prompts for the interactive SAM mode on the full image. For a specific plot in the current range, its centroid was used as a foreground point, while the rest of the centroids in the range were used as background points. The resulting SAM segmentation mask was associated with the plot ID for further processing.

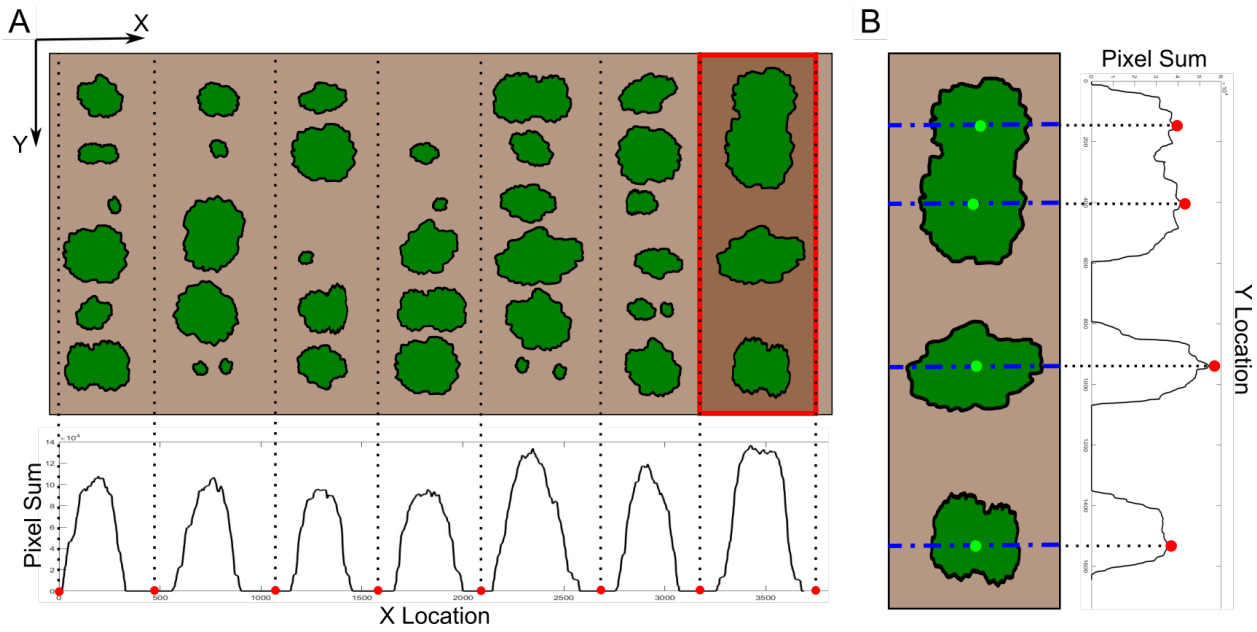

Figure 4.3: SAM point prompts identification. A) Detection of crop ranges by adding vegetation pixels vertically. Red circles indicate middle points of areas with minimum vegetation (alleys). B) Zoomed-in view of the range enclosed in the red rectangle in (A). Red circles indicate maxima values for the accumulated vegetation pixels. Blue dashdotted lines indicate the identified rows for the specific range. Green circles indicate individual plot centroids.

4.2.4 Canopy Height Model Reconstruction

The reconstruction of the canopy height model (CHM) is a crucial step in UAV-based field crop analysis. CHM represents the height of the crop canopy above ground level, providing valuable insights into the vertical structure of crops, essential for understanding plant health, growth, and field conditions.

CHMs digitize the crop height above ground level and normalize it with respect to the underlying terrain. CHM is closely related to the digital elevation model (DEM) obtained as a byproduct during the image orthorectification process of aerial imagery. DEMs, also known as digital surface models

(DSMs), represent the elevation of the field's surface, including both the terrain and any vegetation present. To derive an accurate CHM, it is crucial to separate the canopy height from the mixed surface data provided by the DEM.

To create the DTM, two sampling points, one located on each side of the SAM segmentation masks, were used to rasterize the terrain local to each plot (Figure 4.4. Subsequently, using the *'startinpy'* Python library, a Delaunay triangulation algorithm linked all the sampling points for the entire field, creating a triangulated surface mesh resembling the terrain. The CHM was obtained by subtracting DTM values from the DEM.

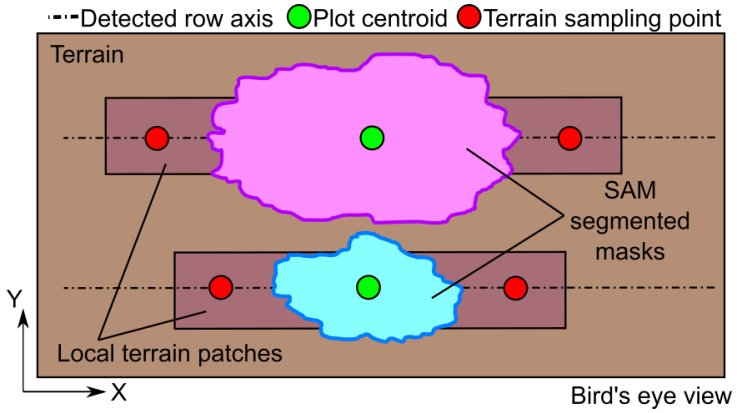

Figure 4.4: Terrain points sampling for CHM reconstruction. Bird's eye view of a two-row plot depicting the distribution of sampling points for local terrain estimation. Segment anything model (SAM) masks for single-row plots are depicted in pink and turquoise colors.

4.2.5 Agronomic Traits Estimation

To extract agronomic traits at the plot level from the crop, we needed to segment each two-row plot. We observed that due to poor germination or disease, some plots had only one row. To establish the two-row limits without manual checking, we leveraged the fact that the tractor tracks were below the reconstructed DTM. Since the crop was planted on raised beds, the reference DTM obtained

using our methodology was established at the raised bed surface level, and areas of the field below this reference level appeared as negative elevation values in the CHM. Using the Hough transform (Hough, 1962) on the negative CHM values, we detected the horizontal lines that separate each bed. These lines, together with the range limits identified previously, defined the boundaries for each two-row plot in the field. Subsequently, by computing the center of mass for each plot mask pair within each plot's limits, we determined the center of each plot. A bounding box of 112 pixels by 112 pixels encompassing the crop masks within each specific plot was then automatically drawn.

To estimate CH at the individual plot level, we analyzed CHM values within the bounding boxes. The CHM data contained in each box was transformed into a 2D numpy array with dimensions 112 by 112 and associated with each plot. We then extracted the maximum value from each array (CH_{max}).

To estimate other agronomic traits, we implemented convolutional neural network (CNN) architectures based on the LeNet model (Lecun et al., 1998). The CNN models were developed under the Pytorch framework. The Adam optimizer and the negative log likelihood loss (NLL) function was used for the models. To estimate MP and GH, the numpy arrays obtained during the CH estimation process were used to create the datasets for CNN model development. These data were split between training and testing subsets following a 4:1 ratio. For estimating TSWV infestation levels, previous studies have found that the Normalized Difference Red Edge (NDRE) was the best vegetation index to identify TSWV symptomatic canopies in peanut crops (Patrick et al., 2017). Therefore, we constructed an NDRE orthomosaic map using the formula $NDRE = (NIR - RedEdge)/(NIR + RedEdge)$ and the respective spectral orthoimages (i.e., 710 nm for RedEdge, and 850 nm for NIR). We then applied the bounding boxes to the NDRE ortho-

mosaic map and stored this information into 2D numpy arrays. These data were also split between training and testing subsets following a 4:1 ratio for CNN model development.

CNN Models Architecture

The best CNN architecture as well as the optimal learning parameters—learning rate, batch size, and number of epochs—for estimating each trait were selected through a 5-fold cross-validation process by using the training and testing subsets and repeating the analysis across different folds. This procedure ensured consistent performance of the model cross different subsets of data, avoiding specific data points biases.

The cross-validation process found optimal CNN architectures slightly different for each trait (Figure 4.5). The best model for MP estimation, resulted in an 11-layer architecture (Figure 4.5A). This network comprising 4 pairs of convolutional (Conv) and max-pooling (Pool) layers, followed by 3 fully connected (Dense) layers. Each pair of Conv and Pool layers was followed by batch normalization and a rectified linear unit (ReLU) activation function. For GH estimation, a deeper 13-layer architecture provided better results during training (Figure 4.5B). This architecture consisted of 5 pairs of Conv and Pool layers, also followed by 3 Dense layers. Similar to the MP architecture, each Conv and Pool pair was followed by batch normalization and a ReLU activation. In both architectures, the multi-dimensional output from the last Pool layer was flattened before being fed into the Dense layers, with a ReLU activations between each Dense layer. Additionally, for GH estimation, we introduced a regularization factor by applying a 50% dropout between the last two Dense layers. At the output of the last Dense layer, a logSoftMax activation function was used to convert the network's final layer logits into probability distributions and provide the most probable

class. The CNN architecture for TSWV classification was a shallower network with 9 layers (4.5C), including 3 pairs of Conv and Pool layers and 3 Dense layers. In this case, we dropped the batch normalization between Conv and Pool pairs and applied only a ReLU activation. For MP, a batch size of 8 and 14 epochs provided the best results. For GH, a batch size of 16 and 14 epochs were optimal. For TSWV estimation, a batch size of 16 and 10 epochs were optimal.

Figure 4.5: CNN model architectures for trait classification. A) Architecture for main stem prominence classification. B) Architecture for growth habit classification. C) Optimal architecture for TSWV infection level classification.

4.2.6 Performance Evaluation

To evaluate the performance of our proposed segmentation and trait estimation process, we conducted a series of tests to assess accuracy, precision, recall, and computational efficiency. The primary objectives were to ensure the robustness and reliability of the segmentation process and the accuracy of the derived agronomic traits.

For the SAM-based field identification, we tested the robustness of the segmentation under varying orthoimage orientations, simulating the different geographic orientations that a field can have. We rotated the RGB orthoimage in 0.5° increments from 0° (North orientation) to 180° (South orientation). At each rotation angle, we applied the SAM auto-mask generator to retrieve the detected mask for the field, its boundary (minimum oriented bounding rectangle), and the center of this bounding rectangle. This test allowed us to evaluate the consistency and accuracy of the field segmentation across different field orientations.

To quantify segmentation stability and accuracy, and ensure that our segmentation method was robust to field orientation changes, we measured the Intersection over Union (IoU) between the bounding rectangle obtained at different rotations and a manually annotated ground truth rectangle encompassing the extent of the field. The IoU metric, which can be computed using Equation 4.1, provided a clear indication of the overlap between the predicted field boundaries and the ground truth.

$$IoU = \frac{\text{area of intersection}}{\text{area of union}} = \frac{}{} = \frac{TP}{TP+FP+FN} \tag{4.1}$$

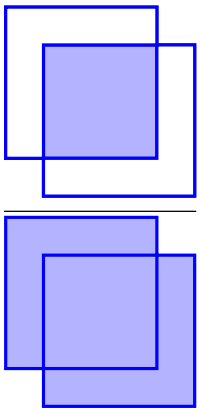

For the segmentation accuracy of individual plots, we compared the automated segmentation results against manually annotated ground truth data. We annotated one third of the field plots (approximately 900 single plots) using the LabelMe interactive tool (Wada, 2018). These annotated masks were used to calculate the IoU metric (Equation 4.1) for each segmented plot, measuring the overlap between the predicted segmentation masks and the ground truth masks. Additionally, we computed *Recall* (Equation 4.6), *Specificity* (Equation 4.7), and *Accuracy* (Equation 4.5) to evaluate the ability of the segmentation process to correctly identify plot boundaries and distinguish between different plots.

To assess the accuracy of the CHM reconstruction and the agronomic traits estimation, we conducted a comparative analysis with ground truth measurements. The CH values derived from the CHM were compared to the manual height measurements conducted in the field. To facilitate performance comparison with other studies, was computed. To validate the performance of the CH estimations, the root *Mean Squared Error* (RMSE), the *Normalized Mean Squared Error* (NRMSE), and the *Mean Absolute Percentage Error* (MAPE) were computed between the predicted CH and the actual measurements. These performance indices were computed using the following equations:

$$RMSE = \sqrt{\frac{1}{N} \times \sum_{i=1}^{N} (y_i - \hat{y}_i)^2} \tag{4.2}$$

$$\tag{4.3}$$

$$MAPE(\%) = \frac{1}{N} \times \sum_{i=1}^{N} |\frac{y_i - \hat{y}_i}{y_i}| \times 100 \tag{4.4}$$

where N is the total number of data points used for the linear regression analysis (N=50), y_{i} is the actual CH value for the i^{th} ground truth plot, and $\hat{y}_{\mathrm{i}}$ is the estimated CH for the i^{th} plot.

To evaluate the CNN models' generalization capabilities for MP, GH, and TSWV classification, we computed average *Accuracy* 4.5, *Precision* 4.8, *Recall* 4.6, and *F1 score* (4.9) to evaluate the ability of each model to classify morphological traits and disease levels. The different metrics used to evaluate our method are summarized as follows:

$$Accuracy = \frac{TP + TN}{TP + TN + FP + FN} \times 100 \tag{4.5}$$

$$Recall = \frac{TP}{TP + FN} \times 100 \tag{4.6}$$

$$Specificity = \frac{TN}{TN + FP} \times 100 \tag{4.7}$$

$$Precision = \frac{TP}{TP + FP} \times 100 \tag{4.8}$$

$$F1\text{-}Score = 2 \times \frac{Precision \times Recall}{Precision + Recall} \times 100 \tag{4.9}$$

where TP and TN—true positives and true negatives, respectively—are the number of pixels correctly classified for each class, and FP and FN—false positives and false negatives, respectively—are the number of misclassified pixels. All these metrics ranged from 0% to 100%, 100% being related to the best performance.

4.3 Results and Discussion

4.3.1 Field Identification

The SAM auto-mask generator successfully identified the breeding field boundaries without any manual intervention (Figure 4.6). Using the SAM auto-mask generator and our methodology provided a robust framework for analyzing crop fields. The initial broad segmentation (Figure 4.6A) ensured that all potential regions of interest were identified. The subsequent refinement process (Figure 4.6B) allowed for filtering out most of the detected masks to focus on the specific area of the experimental field. Finally, the metric-based selection of the most stable and accurate mask (Figure 4.6C) ensured the reliability of the results. This automatic identification was consistently accurate, ensuring that the entire field was correctly delineated in the UAV imagery.

The initial set of masks produced by the SAM auto-mask generator encompassed various regions within and around the crop field, including the plants, pathways, and adjacent field in the surrounding area. In total 3072 masks were generated (3 masks per sampling point). SAM was

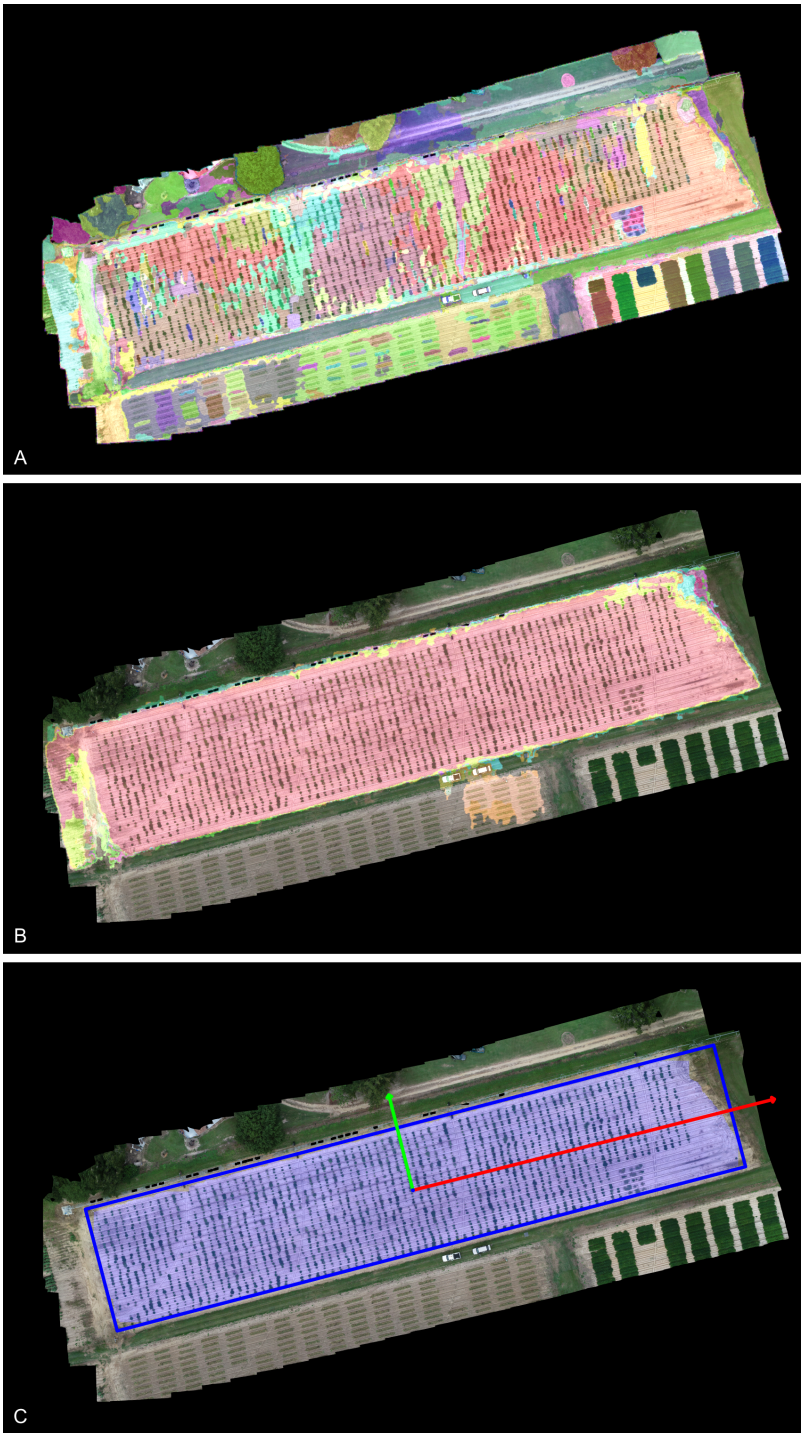

Figure 4.6: Field masks from SAM auto-mask generator. A) Full set of masks automatically generated by SAM. B) Filtered masks centered in the experimental field. C) Best field mask with minimum area rectangle enclosing the experimental field. Different colors indicate different segmented image masks. Red and green arrows indicate the orientation of the first and second principal components.

able to delineate distinct features across the entire field image. However, there was visible some oversegmentation, as some previous studies have already discovered (Carraro et al., 2023). Nevertheless, this initial step of our pipeline demonstrated SAM's broad application in identifying various components within a complex agricultural landscape, contributing to recent discoveries in agricultural fields delineation (Gui et al., 2024; Gurav et al., 2023; J. Sun et al., 2024).

Our post-processing methodology to isolate the relevant masks from the entire set produced by SAM, based on mask location and quality helped refine the set of mask centered specifically on the crop field under study. Non-relevant segments such as pathways and peripheral vegetation are excluded, focusing solely on the main area of interest—the crop field. This step highlights the ability to tailor the mask selection process to target specific areas within a larger dataset, enhancing the precision of the analysis by incorporating previous knowledge about the specific application (Ji et al., 2024).

By averaging the stability score and predicted IoU metrics provided by SAM, we were able to further refine the set of masks and select the best one that represented the field. The stability score measures the consistency of the mask under different conditions, while the predicted IoU metric assesses the accuracy of the predicted segment compared to the ground truth. By combining these metrics, we ensured that the final masks were both robust and accurate, representing reliably the crop field, which is a key step for detailed and reliable phenotypic assessments.

Field Identification Stability

Field identification performance was robust at field orientation (Figure 4.7). The distribution of errors followed a normal distribution centered at approximately -0.2°, with a maximum absolute

error of less than 0.8°. This demonstrates the high accuracy of our automated process at identifying the orientation of the field.

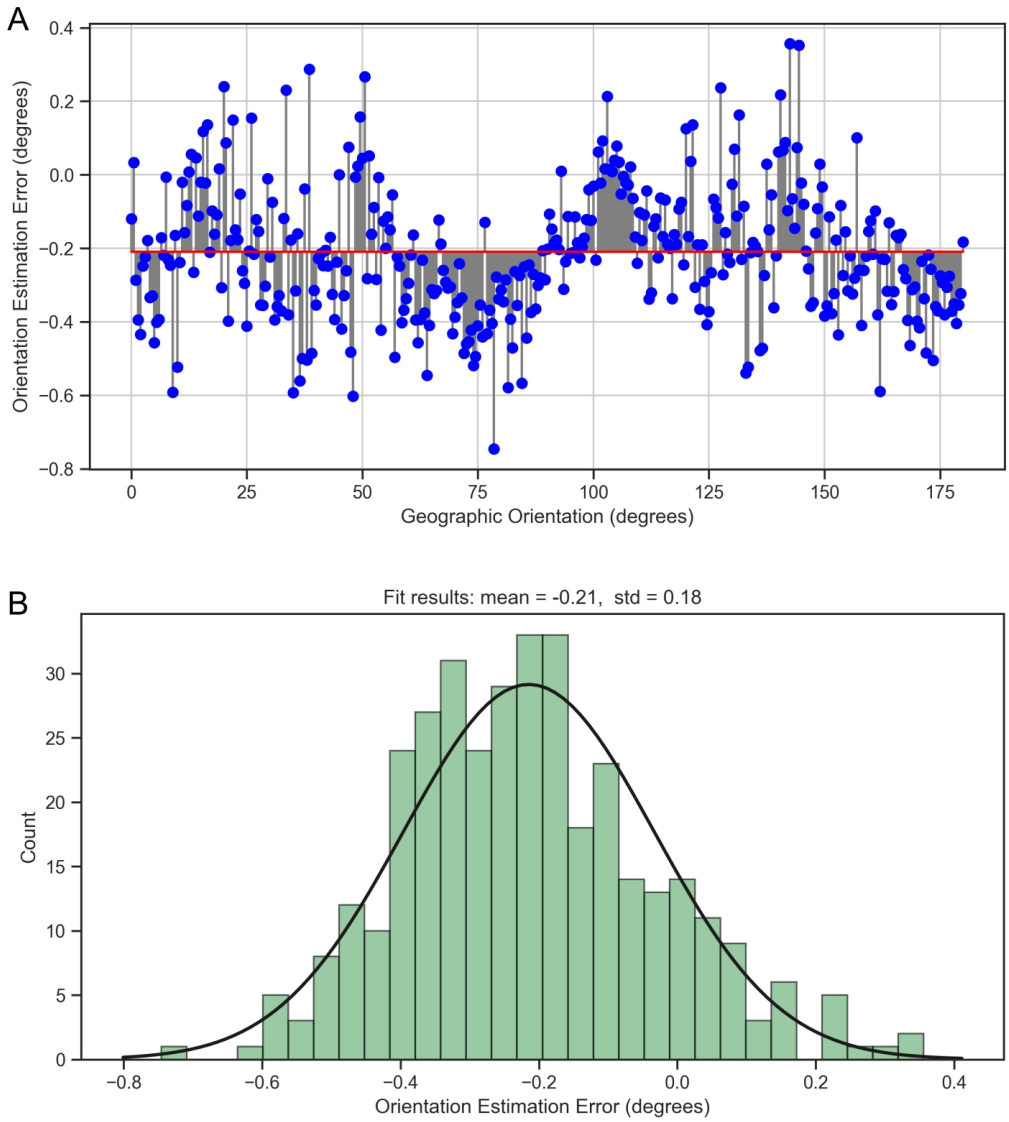

Figure 4.7: Field orientation estimation differences. A) Differences between SAM-based estimations of field orientation versus actual orientation for each tested angle. B) Histogram of orientation angle differences.

Regarding the quality of the masks for field identification, our analysis showed high overlap between the manual annotations and the estimated field extends (Figure 4.8. All calculated field boundaries showed an IoU greater than 0.85, with most of the masks centered around 0.95. The

mean IoU from our analysis reached 0.93, indicating the robustness of our method at different field orientations.

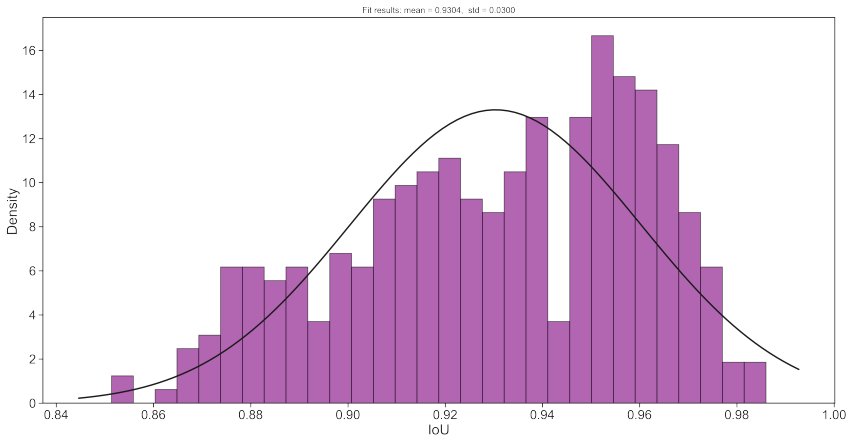

Figure 4.8: Field orientation estimation differences. Differences between SAM-based estimations of field orientation versus actual orientation.

4.3.2 Individual Plots Automatic Delineation

The segmentation of individual plots using the Segment Anything Model (SAM) with multi-point prompts resulted in precise plot segmentation (Figure 4.9). The boundaries of most plots in the field were correctly identified using our approach to guide the interactive mode for SAM segmentation.

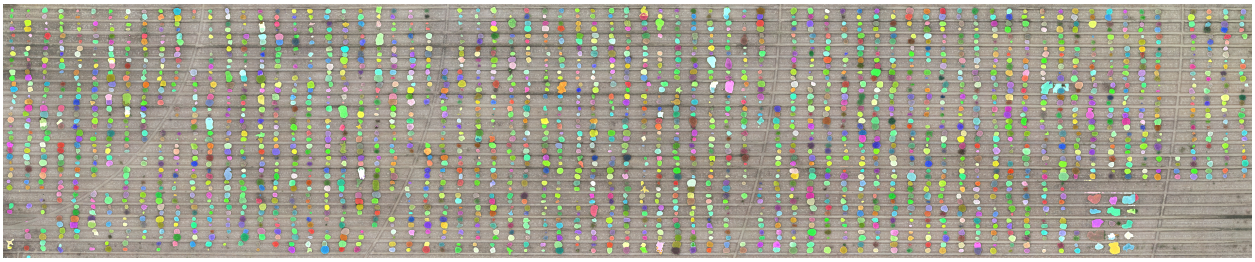

Figure 4.9: Individual plot masks from SAM multi-point prompt. Different colors indicate individual plot masks.

Despite the overall good performance, an analysis of individual plot segmentation errors revealed specific areas where the methodology did not perform as expected (Figure 4.10). When we compare the individual plot masks provided by SAM, most of the annotated pixels are correctly identified by our methodology. However, some pixels belonging to the plots were clearly missed by the segmentation process. Those missed pixels were primarily located at the external borders of the plots (Figure 4.10A and C), indicating the at extracting precise details. In other cases, entire plots were left unsegmented (Figure 4.10B, C, and D) Other pixels were misclassified as part of the plots, when they were not part of them. This case was mainly due to wrongly classifying dead parts of the plots. These dead parts might present different coloration, but they usually continued the shape of the plots, which challenged SAM generalization. There were also a few instances of terrain pixels being wrongly segmented as part of the plots. Although there were minor cases of this, these instances were hard to analyze. These errors might be due to the fact that the plots associated were much smaller than the rest, partially dead, and presented an odd shape (Figure 4.10D). Therefore, the multiple points used as prompts to guide the SAM segmentation might have picked similar textures as the surrounding terrain. Despite these spurious segmentation masks can affect the phenotyping process down the road, they could be easily removed by applying some morphological post-process based on the expected location of the masks with respect to the rest.

The performance of crop segmentation algorithms can be affected by several aspects. Many existing methods for crop segmentation are sensitive to varying environmental conditions such as lighting, shadows, and soil background, impacting their robustness and accuracy (Y. Li et al., 2020). SAM could help reduce the overhead associated with these challenges by providing more reliable and adaptable segmentation capabilities. However, the selection of the appropriate prompts for

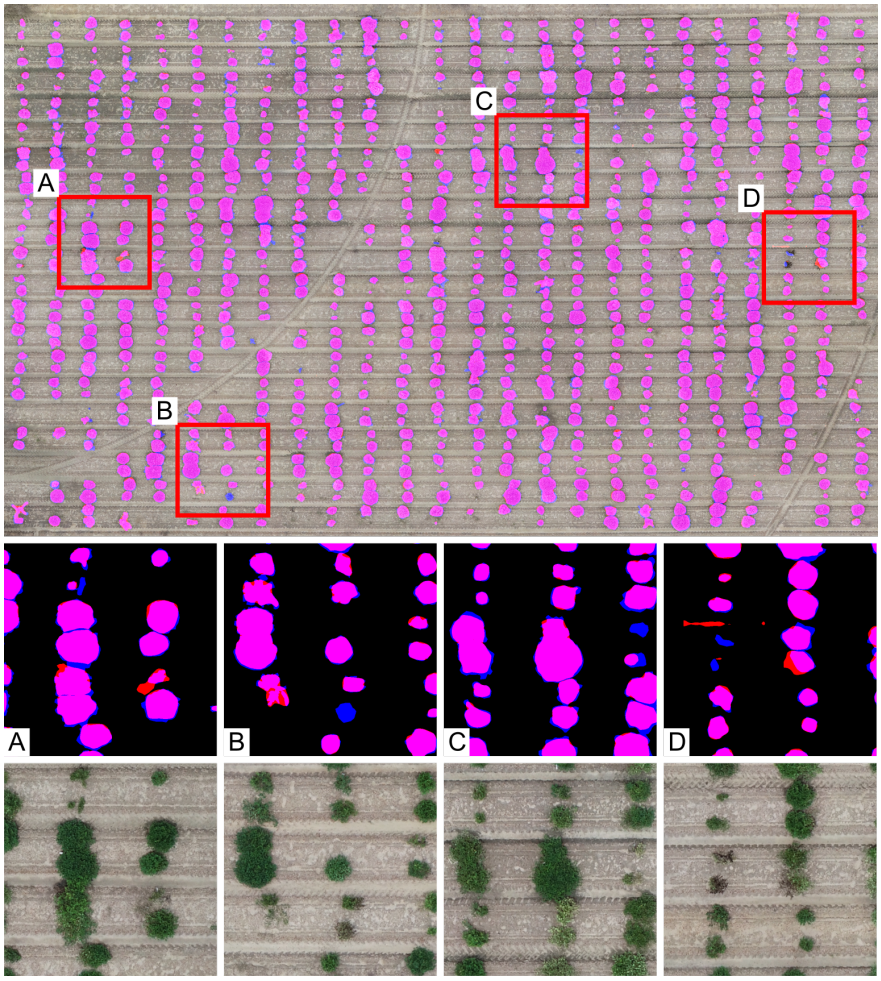

Figure 4.10: Analysis of individual plot segmentation errors. Blue pixels indicate areas missed by our methodology; red pixels denote areas misclassified as part of the plots; fuchsia pixels represent correctly classified plot pixels. The bottom images are zoom-ins corresponding to the red squares in the top image, providing detailed views of the primary segmentation errors identified. A) shows that some shadows and dead plants were wrongly segmented. B) highlights plots that were missed by our method. C) shows that missed pixels are primarily located at the external borders of the plots. D) indicates instances where spurious terrain pixels were misclassified as plots.

challenging environments should be carefully analyzed (J. Hu et al., 2024). Our approach based on the previous segmentation of vegetation pixels from the orthomosaic allowed the efficient creation of point prompts automatically without user intervention. However, a more advanced method to detect plots centroids could help reduce the segmentation errors. In the same way, further refinement in the mask provided by SAM can be beneficial for solving some of the errors encountered, as it has already been identified in recent works (D. Williams et al., 2023).

Accurate field phenotyping is essential for monitoring crop health, growth, and yield. Precise plot segmentation allows for detailed analysis of individual plots, facilitating targeted interventions and better management practices. The use of advanced segmentation models like SAM can significantly improve the efficiency and accuracy of phenotyping processes, ultimately contributing to more effective agricultural research and production strategies. By understanding and addressing the specific segmentation errors, researchers can optimize SAM's application, leading to more accurate and reliable phenotyping results in diverse field conditions.

Segmentation Masks Details

SAM-based masks are less detailed than the manually annotated ones. If the resources available are scarce, the selection of a saller backbone for SAM segmentation can help reduce the overload. SAM provides three different backbones based on visions transformers (ViTs): ViT-S, ViT-L, and ViT-H. These backbones differ primarily in their depth and computational complexity. ViT-S (Small) is the most lightweight version, characterized by fewer transformer layers and a smaller number of attention heads. This makes ViT-S faster to train and less resource-intensive, suitable for scenarios where computational efficiency is crucial without sacrificing too much on performance. ViT-L

(Large) increases both the depth of transformer layers and the number of attention heads compared to ViT-S, offering a more powerful feature extraction capability. It strikes a balance between computational cost and performance, making it a versatile choice for various image analysis tasks. ViT-H (Huge) is the most advanced and resource-demanding variant, featuring a significantly larger number of transformer layers and attention heads. ViT-H excels in capturing intricate details and long-range dependencies in images, making it ideal for high-resolution images or complex datasets where utmost accuracy is required, albeit at the expense of increased computational resources and training time. Each variant of ViT offers a spectrum of choices tailored to different trade-offs between computational efficiency and model capability, catering to diverse needs in image processing and computer vision applications.

If more details are required, other parameters can be tweaked. One key parameter is the point grid density. This parameter determines the spacing and number of points generated across the image. By default, SAM uses a dense grid to maximize coverage, ensuring that even small or closely packed objects are detected. A higher grid density results in more points being evaluated, leading to finer and more detailed segmentation at the cost of increased computational resources. This grid needs to be calibrated to balance between computational efficiency and segmentation accuracy.

4.3.3 Canopy Height Estimation

The terrain sampling method for CHM reconstruction showed to be effective in reconstructing the underlying terrain (Figure 4.4). The use of points close to each plot allowed us to get a detailed terrain that facilitated the process of normalization of plant heights.

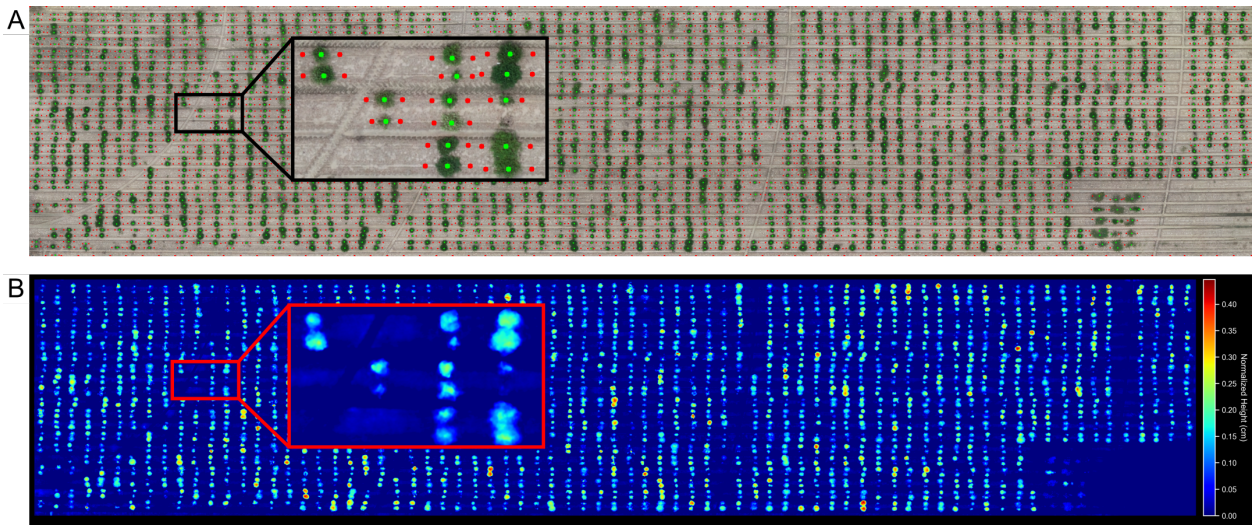

Figure 4.11: Terrain sampling points for CHM reconstruction. A) Sampling points details for terrain modeling. B) Canopy height model (CHM) after height normalization.

Several methods have been developed for DTM reconstruction from UAV imagery (Sweet et al., 2022). However, the need for robust image processing techniques that can accommodate to varied crop conditions is key to fully automate the phenotyping process. The crop under study was planted in raised beds, which can introduce further challenging at estimating the terrain accurately (Brown et al., 2022). Our approach takes advantage of the detected canopy to sample terrain points next to the plants, ensuring that the terrain local to each plot is accurately modeled. This limits the impact of wheel furrows on the estimation of CH. Nevertheless, terrain alterations caused by other field alterations close to the plant, such as the central pivot for irrigation (inset in Figure 4.4), still can have an impact on the CH estimations.

Our methodology demonstrated a strong correlation between estimated and measured canopy heights (Figure 4.12). Approximately 78% of the variability in the estimated canopy height can be explained by the measured canopy height, highlighting a strong relationship between the two

variables. The low RMSE and NRMSE values, with just under 3 cm and 11%, respectively, suggest good model performance ((C. Guo et al., 2022). In addition, the low MAPE value obtained implys that the predicted CH values were, on average, close to the actual values.

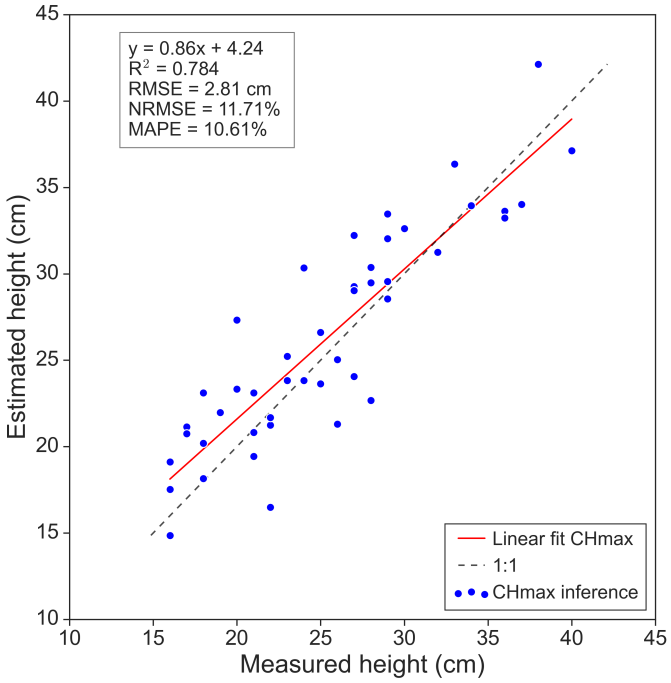

Figure 4.12: Measured versus Estimated Height.

The model provided accurate estimates of CH. However, the slope of the regression line indicates a slight underestimation at higher canopy heights. Nevertheless, this can have a limited impact on phenotyping studies where crops with compact canopies are prefered for mechanization (Kunta et al., 2021) Analyzing the regression line, our model tended to underestimate CH slightly as the actual height increased. Similarly, the positive intercept of approximately 4 cm suggests that at lower canopy heights, the model estimates are slightly higher than the measured values, possibly due to limitations in UAV-based estimations due to sensor resolution.

The strong correlation and low error metrics support the feasibility of our methodology for automated canopy height estimation in field phenotyping. This approach could significantly reduce the labor and time required for manual measurements, leading to more efficient and scalable phenotyping practices.

4.3.4 Performance of the CNN Models for Trait Estimation

Our results indicated that both CNN models for trait estimation achieved high accuracy and were effective in classifying MP and GH traits (Table 4.3). While the GH model showed strong potential for practical use, the MP model performed moderately well. The TSWV model, however, showed relatively poor performance at estimating the level of infestation of the crop.

Table 4.3: Performance metrics for CNN models

Model	Accuracy	Precision	Recall	F1 Score
MP	0.77	0.75	0.77	0.75
GH	0.81	0.78	0.81	0.78
TSWV	0.66	0.69	0.66	0.67

For the MP model, the average accuracy was 77%, suggesting that the model performed reasonably well in identifying the prominence of the main stem for this field. The precision and recall values were balanced, indicating that the model is consistent in identifying true positives and minimizing false positives. However, there is still room for improvement, especially in enhancing the precision to ensure fewer false positives.

The GH model showed the highest performance among the three models, with average accuracy of approximately 80%, indicating a strong performance, with the model effectively identifying the growth habits of the plants. The relatively high accuracy and balanced precision and recall

values suggest that the model was both reliable and consistent. This implies that the GH model can be effectively used in practical applications for phenotyping growth habits in the field, providing accurate and dependable results.

The TSWV infection model, in contrast, demonstrated lower performance, with an accuracy of just 66% at classifying three level of infestation. These results indicate that the model struggled with accurately identifying TSWV infection compared to the other traits. The lower accuracy and recall suggest that the model may miss a significant number of true positives, leading to underestimation of the infection rates. In addition, the precision being slightly higher than the recall indicates that when the model predicted an infection, it was more likely to be correct, but it still missed many actual cases. This highlights the need for further refinement of the model, possibly through improved training data, more sophisticated architectures, or enhanced feature extraction methods.

While the developed CNN-based models hold promise for automating phenotyping processes, the complexity of certain traits necessitates ongoing development and refinement to consistently achieve accurate results. The performance variations observed across different traits highlight the challenges in modeling intricate biological characteristics. While the GH model demonstrates robust performance, the low performance of the TSWV infection model revealed significant room for improvement. These findings emphasize the need for enhanced training data quality, optimization of model architectures, and advancement in feature extraction techniques to effectively capture and classify the nuances of complex traits. Achieving consistent and precise results across all traits will be crucial for leveraging CNN models in real-world phenotyping scenarios effectively.

Morphological Traits Classifiers Performance

Focusing on the specific classification results for each model, our approach showed strong performance in predicting the MP and GH traits, with high accuracy and low misclassification rates (Figure 4.13). The MP classifier demonstrated strong performance with an accuracy of 81% for correctly predicting the "Not apparent" class and 85% for the "Apparent" class. Misclassifications were relatively low, with around 16% of "Not apparent" instances being incorrectly classified as "Apparent" and 10% of "Apparent" instances being predicted as "Not apparent". Analyzing the performance per class, the classifier achieved an accuracy of 88% for the "Spreading" class and 89% for the "Bunch" class. Misclassifications were below 12% for "Spreading" being predicted as "Bunch" and approximately 10% for "Bunch" being predicted as "Spreading." These results suggest that the classifier is highly effective in distinguishing between the two growth habits, with slightly higher accuracy compared to the MP classifier. The low misclassification rates reinforce the robustness of this model for predicting growth habits in peanut plants.

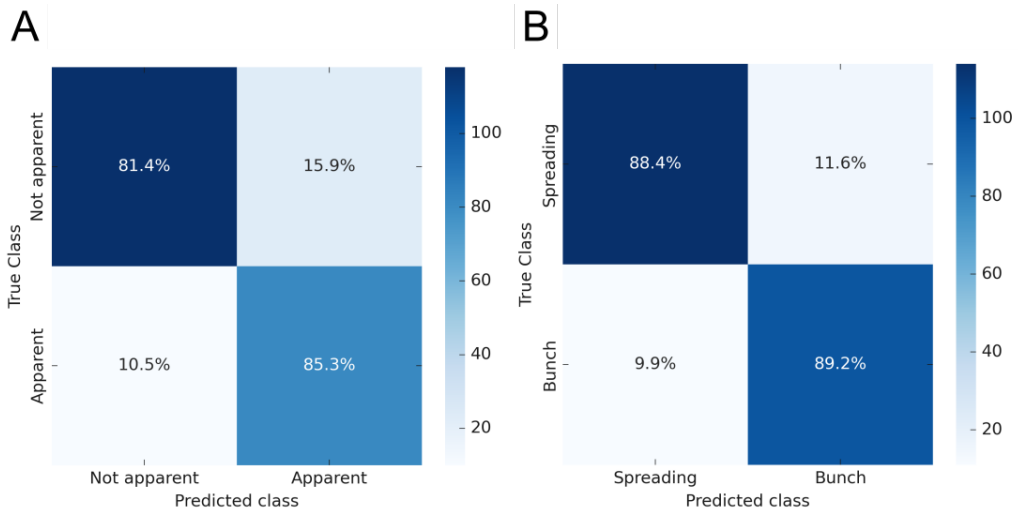

Figure 4.13: Confusion matrices for traits classification. A) Main stem prominence classification results. B) Growth Habit classification results.

The CNN classifiers for predicting the GH of peanut plants showed high performance, yet several factors might have influenced their accuracy. The primary challenge was the inherent variability of the morphological traits and the subtlety in the differences between traits categories for the analyzed traits. These categories, although distinct, may present overlapping features, especially if environmental conditions influence the plants' appearance. This overlap can cause the classifier to misinterpret features that are not strictly indicative of one class over the other. These distinctions may not always be stark, particularly in intermediate cases where the prominence of the main stem is not clear-cut. This can challenge the classifier's ability to consistently differentiate between the two classes.

Data imbalance can similarly affect performance when there are considerably more examples of one class over another in the training set. Our training dataset exhibited a notable class imbalance, with a significantly higher number of examples for one growth habit compared to the other. Preliminary results indicated that our models became biased towards the more frequent class, thus impacting its ability to correctly identify the less represented class. This imbalance can lead to a model bias, making it more accurate in predicting the more frequent class at the expense of the less common one.

Addressing this challenge is difficult due to limited options for increasing instances from the minority class. From a breeder's perspective, if we aimed to enhance the models' performance in classifying these specific classes, we could plant more genotypes that exhibit the minority class phenotypes. Additionally, the quality and consistency of the labels used for training are crucial. The categorization between growth habits and the prominence of the main stem in the field is subject

to human interpretation and may vary among different annotators. This variation introduces noise into the training data, affecting the classifier's accuracy.

Environmental factors can further complicate the classification task due to the complex genotype-environment interactions. Morphological traits such as GH and MP can be influenced by external factors such as soil type, water availability, and climate, which can cause variations in plant appearance that are not solely attributable to genetic traits. This variability needs to be captured adequately in the training data to ensure the model can generalize well across different conditions.

Furthermore, the CNN's architecture and hyperparameters need to be finely tuned to capture the subtle differences in growth habits effectively. A more sophisticated model or better-tuned hyperparameters might enhance the classifier's ability to distinguish between these habits accurately. Lastly, the CNN architecture and its hyperparameters were carefully chosen and optimized. Our test using more complex architectures and pre-trained model such as ResNet or VGG-16, did not provide improvements in traits classification, and only increased the utilization of computing resources. In addition, we tested augmentation techniques for the minority classes to try ot improve the performance. However, the subtle differences in growth habits and main stem prominence made further improvements challenging.

This indicates that the CNN-based classifier is reliable for a preliminary screening of traits, to this trait, but there is still a small room for improvement in reducing the misclassification rates. Even if the model is not able to distinguish the minor classes of growth habit, it will be useful to plant breeders since we can use these platforms to screen the easily identified classes and use manual observations for the plants/lines that the model struggles to classify.

TSWV Estimation Performance

The classifier for TSWV virus infection showed some overlap between infection level predictions (Figure 4.14). The classifier showed moderate performance with 64% accuracy for "low" infection, 65% for "moderate" infection, and just below 71% for "high" infection. Misclassification rates were more notable here: 27% of "low" infection instances were classified as "moderate", and 9% as "high". For "moderate" infection, 12% were misclassified as "low", and 22% as "high". Notably, the "high" infection class showed a misclassification rate of 29% as "moderate." While the classifier performed reasonably well, it struggled with distinguishing between the infection levels compared to the other two traits. The overlap in predictions, particularly between "low" and "moderate" or "moderate" and "high" infection levels, suggests the need for further refinement in the classifier to improve its discrimination capability for TSWV virus infection.

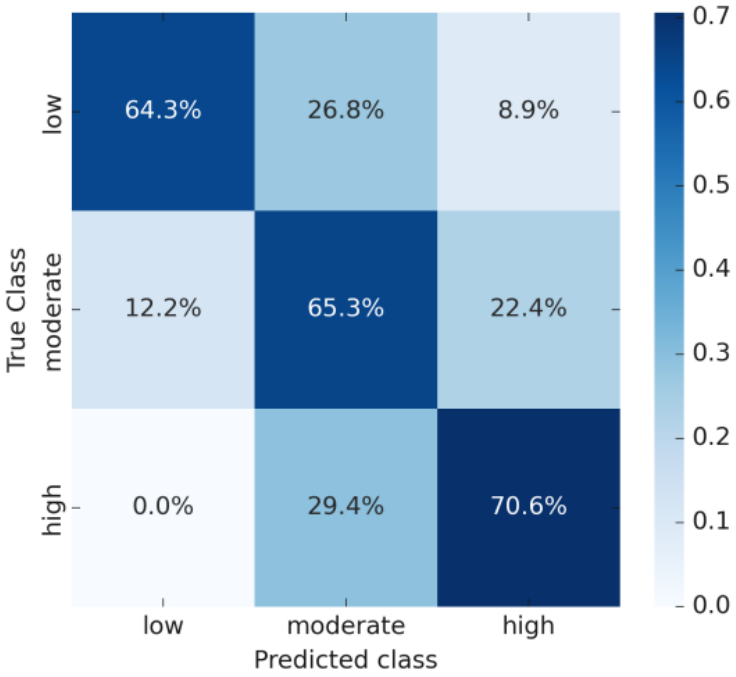

Figure 4.14: Confusion matrix for TSWV estimation.

The third confusion matrix evaluates the classifier's performance in predicting the presence of TSWV virus infection, categorized into "low," "moderate," and "high" infection levels.

The lower performance of the TSWV virus infection model can be attributed to several interrelated factors. One significant challenge is the complexity and variability of TSWV symptoms, which can overlap considerably between different infection levels (low, moderate, high). Unlike the better defined binary traits such as MP and GH, the gradation in symptoms for TSWV infection adds a layer of complexity that makes it harder for the CNN to accurately distinguish between the classes. Additionally, the imbalance in the training dataset could exacerbate this issue. There were, in general, fewer examples of "moderate" or "high" infection cases compared to "low" infection cases, and hence the model might not learn to perform well on these underrepresented classes, leading to higher misclassification rates. Feature similarity also plays a key role; the visual features of peanut plants at different TSWV infection levels were very similar, particularly between adjacent classes. This similarity made it challenging for the CNN to learn distinct features that effectively separate each class, resulting in misclassification. Environmental variability introduced another layer of complexity, as factors such as soil quality, water availability, and climatic conditions can influence the symptoms of TSWV infection, introducing noise into the dataset. This variability made it harder for the model to generalize well across different conditions and accurately classify the infection levels.

The cause of the lower performance with respect to the morphological traits estimation might be due to the lower resolution of multispectral images. In addition, given the field layout, the visual ratings were performed at the individual plants rather than at the plot level, which might have caused that in plots with much variation visible between two plants within a plot but low TSWV rating.

Furthermore, other factors like soil or plant to plant variation could have affected the performance of the model.

4.4 Limitations and Future Works

We thoroughly tested our approach in a real-world peanut breeding field, showing great potential for automating the extraction of digital data from the field at the plot level. While our results are promising, it is important to validate the performance of our methodology under various field layouts, specific field conditions, crop types, and environmental factors. To comprehensively assess the adaptability and generalizability of our methodology, we will perform further experimentation across different peanut field layouts, including larger plots, different crops such as cotton, and fields with higher weed pressure.

We demonstrated that SAM segmentation can be guided using basic information that is readily accessible in an autonomous manner, achieving great results in generalizing. However, the quality of the points provided as prompts is critical. We will investigate more advanced methods for roughly estimating plot locations using advanced machine learning techniques to enhance SAM segmentation masks. Future work should also focus on fine-tuning SAM to effectively segment challenging crop fields with complex backgrounds, as demonstrated by the work of MedSAM in the medical field (Ma et al., 2024).

Field data from breeding crops for traits classification often result in unbalanced datasets as we cannot control the number of instances for each class in the field. This imbalance can compromise the performance of trained machine learning models, as consistent and precise labeling is essential

for effective training. To address this issue, we will investigate ways to accelerate the annotation process of crop traits and provide labels for underrepresented classes by using advanced data augmentation techniques, including the generation of synthetic data. These approaches will help balance the dataset and improve the robustness and accuracy of our machine learning models. Additionally, the architecture and hyperparameters selected for the CNN models might need further improvement for this specific classification task, especially for TSWV estimation. The model may require a more sophisticated architecture or different hyperparameters to better capture the nuances in TSWV infection symptoms. We will explore the use of pre-trained models and additional data, with a more balanced distribution, to enhance the model's ability to distinguish between different levels of TSWV virus infection.

4.5 Conclusions

This study showcased the integration of the Segment Anything Model (SAM) for automating plot extraction and trait estimation using UAV-based multispectral imagery in plant phenotyping. The SAM-based pipeline significantly reduced manual labor and enhanced the accuracy of plot boundary delineation. This approach can be particularly beneficial for automating the digital crop phenotyping process, helping reduce the manual effort required to segment and analyze individual plots from large agricultural fields. We showed the performance of this methodology at ensuring high precision and consistency in trait measurement, including canopy height, growth habit, and main stem prominence. Furthermore, the detection of tomato spotted wilt virus (TSWV) using multispectral

imagery highlights the potential of UAVs and deep learning for early disease detection, facilitating the rapid screening of genotypes in breeding programs.

CHAPTER 5

COTTON MORPHOLOGICAL TRAITS TRACKING THROUGH SPATIOTEMPORAL REGISTRATION OF TERRESTRIAL LASER SCANNING TIME-SERIES DATA[1]

[1]Javier Rodriguez-Sanchez, Kyle Johnsen, and Changying Li. Submitted to *Frontiers in Plant Science*, 05/21/24.

Abstract

Understanding the complex interactions between genotype-environment dynamics is fundamental for optimizing crop improvement. However, traditional phenotyping methods limit assessments to the end of the growing season, restricting continuous crop monitoring. To address this limitation, we developed a methodology for spatiotemporal registration of time-series 3D point cloud data, enabling field phenotyping over time for accurate crop growth tracking. Leveraging multi-scan terrestrial laser scanning (TLS), we captured high-resolution 3D LiDAR data in a cotton breeding field across various stages of the growing season to generate four-dimensional (4D) crop models, seamlessly integrating spatial and temporal dimensions. Our registration procedure involved an initial pairwise terrain-based matching for rough alignment, followed by a bird's-eye view adjustment for fine registration. Point clouds collected throughout nine sessions across the growing season were successfully registered both spatially and temporally, with average registration errors of approximately 3 cm. We used the generated 4D models to monitor canopy height (CH) and volume (CV) for eleven cotton genotypes over two months. The consistent height reference established via our spatiotemporal registration process enabled precise estimations of CH (R^2 = 0.95, RMSE = 7.6 cm). Additionally, we analyzed the relationship between CV and the interception of photosynthetically active radiation ($IPAR_f$), finding that it followed a curve with exponential saturation, consistent with theoretical models, with a standard error of regression (SER) of 11%. In addition, we compared mathematical models from the Richards family of sigmoid curves for crop growth modeling, finding that the logistic model effectively captured CH and CV evolution, aiding in identifying significant genotype differences. Our novel TLS-based digital phenotyping methodology enhances preci-

sion and efficiency in field phenotyping over time, advancing plant phenomics and empowering efficient decision-making for crop improvement efforts.

5.1 Introduction

The increasing demand for agricultural products has emphasized the need for more efficient methods to accelerate crop productivity (Voss-Fels et al., 2019). Field-based plant phenotyping, key for evaluating plant traits in distinct environmental conditions, has become integral in crop breeding (Großkinsky et al., 2015). However, conventional techniques are laborious and time-consuming, often restricting assessments of traits to the end of the growing season and creating bottlenecks in breeding programs (Furbank & Tester, 2011). Recent advancements in remote and proximal sensing have increased the throughput and precision of field-based phenotyping (Singh et al., 2016). Nevertheless, persistent challenges in data processing and automation impede further progress in plant phenomics (Chawade et al., 2019; Kim, 2020). Therefore, novel strategies are imperative to streamline procedures and enable enhanced trait monitoring for crop growth tracking.

Integrating temporal data analysis into phenotyping pipelines can unveil plant development patterns and cyclic phenomena in growth. Continuous monitoring of plant growth is key for understanding plant behavior and responses to external factors (Miao et al., 2020). Recent studies have demonstrated the potential of continuous plant growth monitoring to identify specific genotypes contributing to particular traits (D. Li et al., 2022; Wang, Singh, et al., 2018; Xavier et al., 2017; Zhou et al., 2020). However, the variability in crop growth within fields makes it challenging to establish standardized and consistent monitoring systems, hindering uniform trait tracking over time

for large-scale fields (Tao et al., 2022). Exploring innovative and adaptable solutions for in-field trait assessment is key to overcoming these challenges and improving field phenotyping efficiency.

Advancements in three-dimensional (3D) imaging have expanded the application of plant modeling for the purpose of predicting crop traits over time. Detailed plant 3D models obtained from imaging data through photogrammetry methods (Gelard et al., 2018; Hui et al., 2018; Paproki et al., 2012), structured light scanning (Y. Li et al., 2013), and active laser triangulation (Paulus et al., 2014) have been applied to track individual organs and monitor canopy growth of potted plants. However, these methods have proved labor-intensive and may lack scalability for larger field experiments. At the field scale, photogrammetry methods have also been proposed to gather 3D information from the crop over time using 2D imagery from ground (Carlone et al., 2015; Dong et al., 2017) or aerial systems (Chebrolu et al., 2018; Malambo et al., 2018). Despite their potential for large field coverage, these methods face constraints in capturing complex canopies due to RGB sensor limitations in handling occlusions, repetitive patterns, and changing light conditions.

In recent years, advanced methods using light detection and ranging (LiDAR) technologies for crop phenotyping have gained prominence. LiDAR scanners can mitigate some of the limitations associated with traditional 2D image sensors (Y. Lin, 2015). Notably, employing a linear LiDAR scanning approach, mobile laser scanning (MLS) techniques have found application in field crop monitoring using moving ground vehicles (Jiménez-Berni et al., 2018; S. Sun et al., 2018) or specialized rail-based phenotyping platforms (Y. Li, Wen, et al., 2023). However, these methodologies involve analyzing crops from a fixed top-to-bottom orientation, potentially limiting the capture of lower canopy layers in dense crops with complex architectures, as certain parts of the crop may be shadowed or obscured from the sensor's perspective.

Terrestrial laser scanning (TLS) techniques based on stand-alone 3D LiDAR scanners offer reliable solutions for overcoming occlusion issues and simplifying field-based crop phenotyping. Those scanners have demonstrated effectiveness in monitoring seasonal crop changes in small-scale breeding fields (Hosoi & Omasa, 2009, 2012) as well as daily canopy alterations in both individual plants (Herrero-Huerta et al., 2018) and large field trials (Jin, Su, et al., 2021). Their consistent performance under various lighting conditions and superior depth-sensing capabilities make them particularly well-suited for precise crop canopy measurements in field-based plant monitoring (Jin, Sun, et al., 2021; Madec et al., 2017). However, the adoption of TLS techniques for plant phenotyping may be hindered by the absence of standardized and automated data processing methodologies (Medic et al., 2023), making continuous monitoring challenging. Simplifying LiDAR data processing and extraction of information can enhance plant trait analysis over time and promote broader usage in field phenotyping.

To ensure consistent crop growth modeling and plant traits monitoring using TLS, a fundamental step is to precisely associate spatial information from data collected over time into the same geospatial context. However, the complex transformations that crops undergo during the growing season complicate the registration of point clouds collected at different time points. The most straightforward technique for TLS-based crop growth tracking involves scanning the field from a fixed location at different points in time (Eitel et al., 2016). This single-position scanning approach introduces challenges such as laser shadows obscuring parts of the crop and variations in point density, particularly for plants closer to the laser scanner, that can impact subsequent data analysis (Malambo et al., 2019). An alternative approach involves scanning the field from multiple locations (e.g., multi-scan TLS). A study successfully employed this method to track wheat height over the

growing season (T. Guo et al., 2019). Despite its advantages in reducing occlusions, this approach relied on precise geolocation of point cloud data, requiring accurate positioning systems that increase costs and processing time for data analysis (Crommelinck & Höfle, 2016). Another proposed method involves using a motorized gantry-type phenotyping platform to mount the LiDAR scanner and collect TLS data (Jin, Su, et al., 2021). While effective for accurate trait monitoring, this approach requires a dedicated structure and highly accurate position sensors for real-time scanner location, introducing complexities to the phenotyping process.

To further enhance the precision and consistency of TLS-based time-series field phenotyping, the alignment of point clouds collected over time into a common coordinate system—4D registration—becomes fundamental. Traditionally, registering point clouds for crop growth monitoring has relied on the use of registration targets. This approach involves installing registration targets throughout the field to assist in aligning successive point clouds and has proven effective in monitoring crop growth in large breeding fields (Friedli et al., 2016; Tilly et al., 2014), as well as individual plants evolution under field conditions (Su et al., 2019). However, it can be labor-intensive and error-prone. Deviations in the target placement between surveys can impact the temporal alignment accuracy, and hence the estimation of traits over time. Ensuring that the registration targets are placed consistently in the same exact location in agricultural fields, where machinery needs to operate or other experiments need to be executed, can be challenging. More adaptable approaches used crop distribution to improve the alignment of remotely sensed data (Chebrolu et al., 2018; Günder et al., 2022). Although these studies were limited to aerial imagery, the concept could enhance spatiotemporal alignment of TLS data, facilitating its application for field phenotyping.

Alternative methods for 4D registration of point clouds have also been implemented to accommodate changes in plant structures, albeit with limitations for large-scale fields. Recent studies have proposed non-rigid registration methods to align point clouds at the organ-level during the growing season (Chebrolu et al., 2020, 2021; Magistri et al., 2020). In contrast to rigid-body transformations (Besl & McKay, 1992), which assume a fixed relationship between the point clouds, non-rigid registration allows for more flexible and adaptive alignment, enabling more accurate tracking of plant growth and structural changes over time. However, these approaches require highly-detailed plant models, which can hinder their practicality for field crops where segregating individual plants might not be feasible. The development of methodologies for spatiotemporal registration of large-scale LiDAR data can significantly broaden the application of these technologies in field phenotyping, enabling efficient crop growth modeling and trait monitoring over time for enhanced crop development.

In this study, we present a novel methodology for automating the registration of field-based time-series TLS point clouds, addressing critical challenges in data registration and processing to facilitate consistent crop phenotyping and growth tracking. Our primary technical contribution lies in the development of a two-phase TLS data registration approach, which exploits terrain morphology and crop row distribution to minimize alignment errors between point clouds collected over time. This innovative method reduces dependence on fixed registration targets and streamlines the data processing pipeline, offering breeders a robust solution to acquire accurate phenotypic traits from the same physical locations at different time points. From a crop science perspective, our work introduces an efficient approach to track the evolution of crop traits throughout the season, enhancing our understanding of cotton plant development and trait variations. The specific objec-

tives of the study were to: (1) develop a robust methodology for precise spatiotemporal registration of field-acquired point clouds; (2) validate the effectiveness of the methodology in reducing point cloud alignment errors throughout the growing season; (3) investigate the utility of registered time-series TLS data for extracting key morphological traits and facilitating precise monitoring of cotton crop growth dynamics; and (4) assess the applicability of the developed methodology in informing crop modeling efforts, with a focus on its potential to deepen our understanding of cotton plant growth and genotype-specific trait variations.

5.2 Materials and Methods

5.2.1 Experimental Field

The field research site used in this study was located at the University of Georgia's Iron Horse research farm in Greene County, GA, USA (33°43'01.6"N 83°18'1.8"W). The field contained 11 different genotypes, arranged in a randomized complete block design with 8 replications. These genotypes included conventional Upland cotton varieties from public breeding programs (Acala Maxxa, DES 56, Tamcot Sphinx, UA 48), exotic genotypes (T0018MDN, T0246BC3MDN, and MDN0101 (GH191)), commercial Upland cultivars (DG 3615, DP 1646, and ST5020), and a Pima cotton cultivar (DP 314). A more detailed description of the included cultivars can be found in (Kaur et al., 2023).

The field's layout consisted of single-row plots, each measuring 3.05 meters in length, with an inter-row spacing of 1.83 meters (Figure 5.1). A 1.52-meter wide bare soil alley separated each range of plots. The field was organized into 88 plots, distributed across 8 rows, with 11 plots per

row, resulting in approximate dimensions of 52 meters in length and 14 meters in width. A total of 15 seeds were sowed in each plot on June 18, 2021 (planting date), and the final plant density in each plot varied based on germination and survival rates.

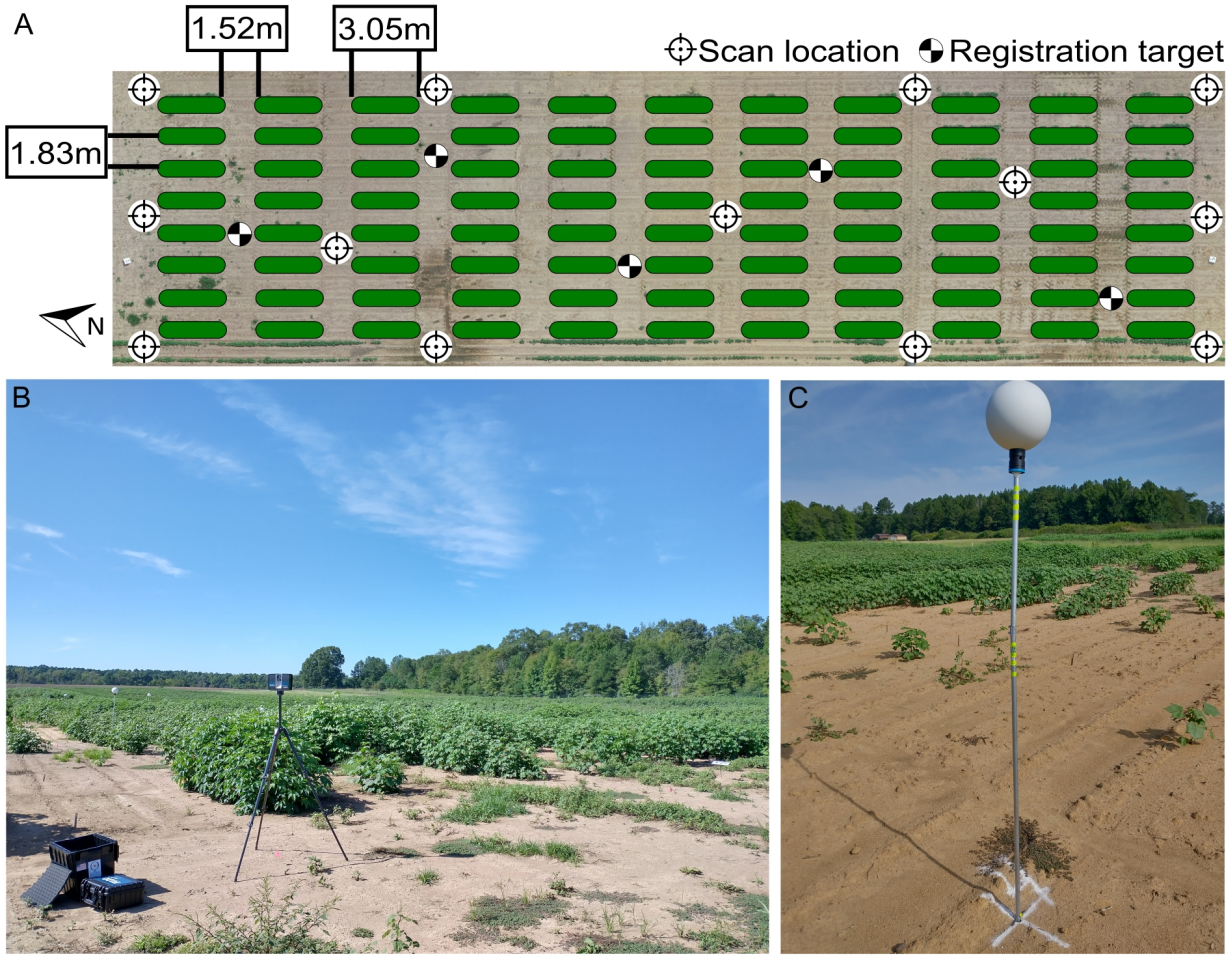

Figure 5.1: Experimental field layout. A) Distribution of plots (green ovals), scan locations (circular target icons), and registration targets (checkered circles) for LiDAR-based phenotyping. B) LiDAR scanner performing TLS scan at a scan location. C) Registration target deployed in the field.

5.2.2 Field Data Collection

A FARO Focus 3D S70 laser scanner (FARO Technologies, Florida, US) was used for terrestrial laser scanning (TLS). To reduce occlusions and collect as much information from the crop as

possible, a multi-scan methodology was adopted to scan the field. Between nine and thirteen scan locations, depending on the growth status of the crop, were used to ensure an adequate coverage of the crop during the different growth stages. The LiDAR was mounted on an elevating tripod (Figure 5.1 B), whose height was adjusted *in situ* during each data collection session in accordance with crop height. At the beginning of the season, the height of the scanner was configured to 1.25 m. When the plants reached the canopy closure stage, the scanner height was adjusted to 1.8 m. The quality parameter for the LiDAR scanner was set to 2x, while the angular resolution was set to 1/2 (angular step of 0.18°) for both the vertical and horizontal angles, which is equivalent to a point distance of 3.05 mm over 10 m. The collected point clouds were colorized using information gathered from the color camera integrated in the LiDAR scanner. Additionally, global positioning system (GPS) and inclinometer information from the scanner's internal sensors were also saved during the scan. For each scan location, raw point cloud data were stored in an SD card as FARO Laser Scan (.FLS) files for further processing.

Nine data collection sessions were conducted to monitor canopy development from crop establishment to canopy closure. The LiDAR scanner was used to survey the cotton field approximately at 35, 42, 49, 56, 62, 70, 77, 84, and 98 days after planting (DAP). During each session, five spherical targets with a diameter of 200 mm (Koppa Target Spheres, California, USA) were strategically placed throughout the field to facilitate the spatial co-registration of point clouds from different scan locations into a common coordinate system. These targets were mounted on aluminum rods with heights ranging from 1.4 m to 2 m (Figure 5.1 A). The spherical targets were deployed before each TLS survey session. A mallet was used to drive the aluminum rods into the ground, ensuring each one of them went in straight and deep enough to provide stability during the survey. Since

permanent structures in the field were not feasible due to ongoing experiments, the aluminum rods were taken down and stored between data collection sessions. Therefore, the position of the spheres was not necessarily consistent across different data collection sessions.

Manual measurements of key plant traits were conducted directly in the field at three different stages of crop development and served as ground truth data for validation purposes. The first session took place immediately after the onset of the blooming stage, approximately at 60 DAP. The second ground truth session occurred during the peak blooming period, at around 80 DAP. The final session was performed at the canopy closure stage, 90 just before the first open cotton bolls became visible. The field measurements included the height of the canopy and the quantity of light intercepted by the canopy, which is directly proportional to crop growth (Baker & Meyer, 1966) and plays a key role in modeling crop evolution and yield (Loomis & Williams, 2015). Canopy height (CH) was determined by measuring the distance between the ground and the top of the canopy (the plant terminal) using a measuring tape. Two to five different plants within each plot were measured following established methods commonly used in cotton breeding. The final CH value was calculated by averaging these measurements. Light interception was estimated by the fraction of photosynthetically active radiation (PAR) intercepted by the canopy (IPAR_f), using Equation 5.1. Two IPAR_f readings were taken per plot and then averaged. Light interception measurements were taken using an AccuPAR LP-80 ceptometer (METER Environment, Pullman, WA) under cloudless conditions between 1100 and 1300 h. Both the below-canopy photosynthetically active radiation (PAR_{below}) and the above-canopy irradiance (PAR_{above}) were measured simultaneously.

$$IPAR_f = \frac{PAR_{above} - PAR_{below}}{PAR_{above}} \tag{5.1}$$

5.2.3 Data Processing Pipeline for Spatiotemporal Alignment

Our TLS-based 4D field phenotyping methodology involved a sequential series of data processing steps (Figure 5.2). Initially, intra-session data processing helped co-register multi-scan point clouds into a common coordinate system and prepared the data collected in each data collection for subsequent analysis. Inter-session processing aligned consecutive point clouds in both space and time, facilitating the extraction of crop traits to analyze growth trends over the season.

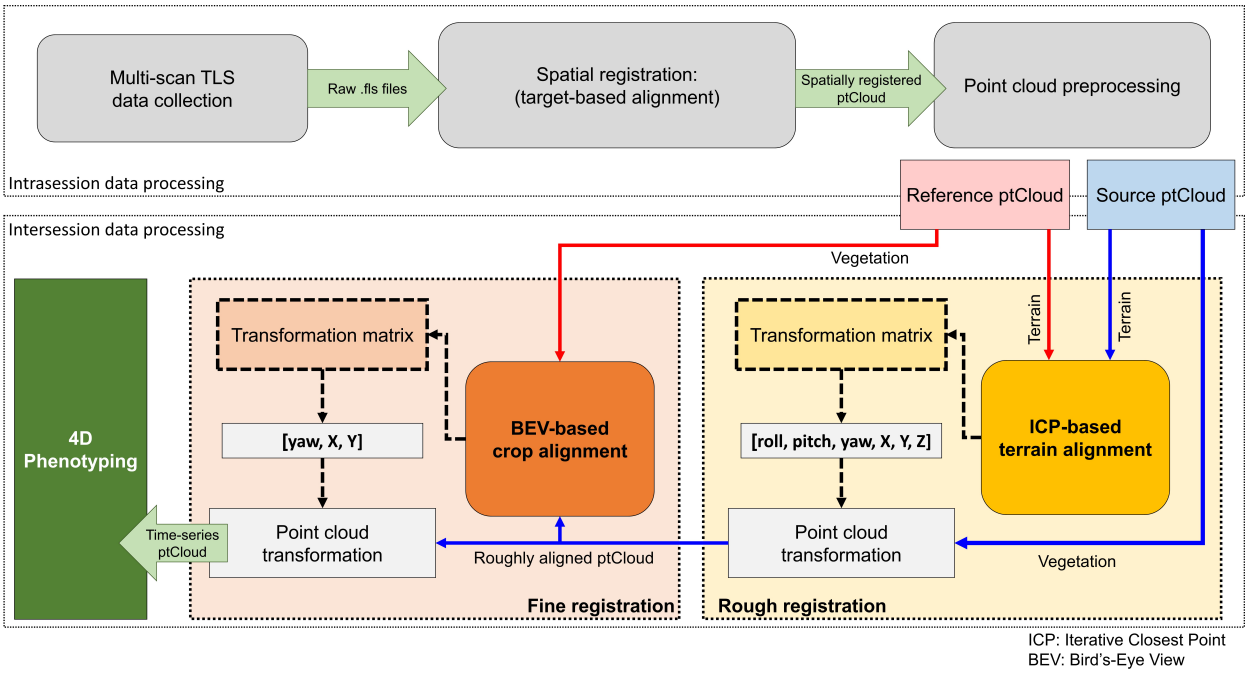

Figure 5.2: Data processing pipeline overview. Proposed methodology for in-field LiDAR-based time-series phenotyping.

The data processing pipeline was designed to run on Windows systems, using only CPU resources. All experiments were conducted on a desktop computer equipped with an 8-Core Intel(R) Core(TM) i7-9700K CPU running at 3.60 GHz and 64 GB of RAM.

Intra-session Data Processing

After each data collection session, point clouds from multiple scan locations were co-registered using SCENE software (FARO Technologies, Florida, US), version 2019.2. The raw .FLS files were imported into SCENE and preprocessed using the *'Edge artifact'* filter. Point clouds were automatically registered using the *'Target Based'* method. Registration results were validated through target-based and mean point error statistics. Then, SCENE's *'Clipping box'* tool was used to isolate and extract 3D points within designated field boundaries. Points within the clipping box were saved in the LASer (.LAS) file format.

Co-registered point clouds underwent denoising using a statistical outlier removal (SOR) filter with parameters $N = 20$ and ± 2.5 standard deviations as outliers boundaries. Then, a subsampling step based on a 5 mm point-to-point distance threshold reduced the point clouds size while maintaining spatial information, reducing computational demands. After subsampling, point cloud height was normalized with respect to a local digital terrain model (DTM) ensured consistency in elevation data across the field. For a more detailed description, please refer to the Supplementary Materials.

Inter-session Data Processing

The terrain's elevation profiles and slopes are generally stable in the short term, and the arrangement of crop rows remains consistent despite canopy growth. Leveraging this stability, we introduced a two-phase alignment process for temporally registering successive point clouds: one as the fixed reference and the other as the source undergoing alignment.

In the initial phase, we conducted a preliminary alignment using the reconstructed terrain models to establish a rough correspondence between pairs of point clouds. We used the iterative closest point (ICP) pairwise matching algorithm (Besl & McKay, 1992) to align the DTM points. The ICP algorithm seeks to find the best-fitting transformation that minimizes the distance between points in two point clouds, in our case the terrain points. This iterative process continues until a satisfactory alignment with minimum root mean squared deviation (RMS) is achieved. The resulting transformation matrix, including full rotation and translation components (i.e., roll, pitch, yaw, X, Y, and Z), was applied to the source point cloud, providing an initial spatial alignment.

To further refine the alignment and minimize errors, we implemented a second phase based on bird's-eye view (BEV) alignment (Figure 5.3). This approach used the distribution of crop rows and plots, automatically identified from the point clouds, to match the orientation and position of both point clouds from a top-down perspective. This refinement step ensured greater accuracy in aligning the point clouds collected over time.

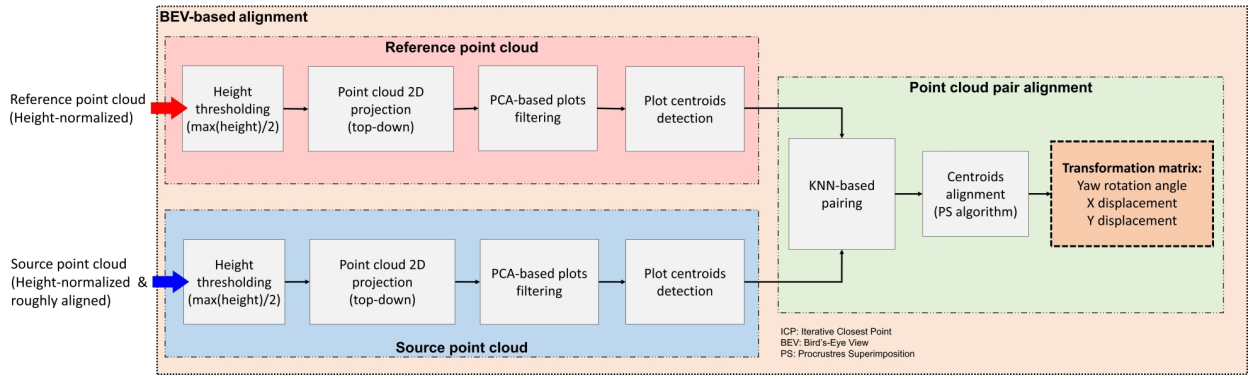

Figure 5.3: Bird's-eye view (BEV) alignment steps. Refinement of the alignment process for multi-temporal point cloud pairs registration.

The BEV alignment process started with the identification of plots centroids in both point clouds. A height threshold, set at half the maximum height value within each plot, was applied to

separate points belonging to the upper canopy section. After thresholding, the canopy points were projected onto the X-Y plane, resembling a 2D top-down orthographic view of the field. Using contour detection, points corresponding to each plot were clustered and filtered using Principal Components Analysis (PCA) to eliminate incomplete plots or noisy point clusters. We leveraged the typical growth pattern observed in field crops planted in plots, where the length along the row axis generally exceeds the width. Any clusters deviating from this expected growth pattern were identified as noise and excluded from subsequent processing stages. The pixel coordinates corresponding to the centroid of each validated cluster were retained for further analysis.

The detected centroids served to improve the alignment between the point clouds. However, certain plots may not appear in the 2D projection in the XY plane during specific growth stages. To address this issue, a k-Nearest Neighbor (KNN) algorithm (Fix & Hodges, 1951) identified pairs of points common to both point clouds, excluding any missing centroids from the BEV alignment process. The rigid transformation between the source and reference point clouds was formulated as a Procrustes superimposition (PS) problem (Rohlf & Slice, 1990). This method involves determining the transformation needed to optimally align two sets of points, effectively overlaying one onto the other. Using a custom implementation of Sneath's method (Sneath, 1967) (Algorithm 1), we calculated the translation and rotation required to align the centroids from the source point cloud with those from the reference point cloud.

Given a reference set R of m pairs of coordinates (x, y) representing the plot centroids detected in the reference point cloud, and a source set S of n pairs of coordinates (x, y) representing the plot centroids detected in the source point cloud, the PS algorithm returns the optimal translation and rotation angle that minimize the sum of the squared distances between corresponding points.

Algorithm 1 Procrustes superimposition algorithm for plot centroids alignment

Input:
Reference set's centroids coordinates $R = [(x_1, y_1), \ldots, (x_j, y_j)];\ j = 1, 2, \ldots, m$
Source set's centroids coordinates $S = [(x_1, y_1), \ldots, (x_l, y_l)];\ l = 1, 2, \ldots, n$
Output:
Optimal translation T
Optimal rotation angle θ

Initialization:

$R' = [\,]$ ▷ Initialize data set to store neighbor points from reference set
$S' = [\,]$ ▷ Initialize data set to store neighbor points from source set
$T = (0, 0)$ ▷ Initialize translation components on X and Y axes (T_x, T_y)
$\theta = 0$

$[R', S'] = KNN(R, S)$ ▷ Compute k-nearest neighbors
$(\bar{x}_{R'}, \bar{y}_{R'}) = (\frac{\sum_{i=1}^{k} x_{R'i}}{k}, \frac{\sum_{i=1}^{k} y_{R'i}}{k})$ ▷ Compute center of gravity for neighbors in reference set
$(\bar{x}_{S'}, \bar{y}_{S'}) = (\frac{\sum_{i=1}^{k} x_{S'i}}{k}, \frac{\sum_{i=1}^{k} y_{S'i}}{k})$ ▷ Compute center of gravity for neighbors in source set

$T \leftarrow (\bar{x}_{R'} - \bar{x}_{S'}, \bar{y}_{R'} - \bar{y}_{S'})$ ▷ Store translation components (T_x, T_y)
for $i = 1, 2, \ldots, k$ **do**
    $R'(k) \leftarrow (x_{R'i} - \bar{x}_{R'}, y_{R'i} - \bar{y}_{R'})$ ▷ Translate reference set to the origin
    $S'(k) \leftarrow (x_{S'i} - \bar{x}_{S'}, y_{S'i} - \bar{y}_{S'})$ ▷ Translate source set to the origin
end for
$\theta = \arctan\left(-\frac{\sum_{i=1}^{k} (x_{S'i} \cdot y_{R'i} - y_{S'i} \cdot x_{R'i})}{\sum_{i=1}^{k} (x_{S'i} \cdot x_{R'i} - y_{S'i} \cdot y_{R'i})} \right)$ ▷ Compute optimal rotation angle
return T, θ

First, k pairs of points common to both point clouds were identified using the KNN algorithm (Algorithm 1, line 5). Then, the center of gravity (i.e., mean or average point) for these matched points was computed for each point cloud (Algorithm 1, lines 6 and 7). The distance between centers of gravity coordinates in the X and Y axes was used to compute the components of the optimal translation (T_x, T_y) (Algorithm 1, line 8). Then, both sets of points were translated to the origin (Algorithm 1, lines 9 to 12). Finally, the rotation angle was calculate using the sums of the cross products between x and y components for both sets to minimize the distances between corresponding points (Algorithm 1, line 13).

After fine registration, all point clouds were aligned under a common coordinate system. It is important to note that the initial normalization conducted in the previous section was performed locally for each data collection session. Discrepancies in DEM quality across different growth stages may introduce height errors between sessions, potentially impacting crop growth analysis. To mitigate these errors and minimize bias in trait estimation, height values for every data collection were renormalized using a common reference plane across all collected point clouds. The terrain mesh derived from the reference point cloud served as the global reference ground level (Z = 0 meters) for all subsequent point clouds. This approach ensured that traits measured relative to each plot's unique characteristics had a consistent reference, enabling an unbiased assessment of crop growth over time.

Performance Analysis for Spatiotemporal Registration

To evaluate our methodology's effectiveness in aligning point clouds over time, we needed accurately aligned reference models for each data collection session. We achieved this by manually

aligning each point cloud dataset with the baseline reference, which was the initial point cloud collected at 35 DAP. Working in pairs and using the CloudCompare tool *'Align (point pairs picking)'*, we selected 12 key points common to both point clouds. We then refined the alignment using the *'Translate/Rotate'* tool until we achieved a root mean square (RMS) error of approximately 3 mm. The resulting transformation matrix served as the basis for comparing the temporal registration performance of our method.

To measure the performance of our registration process, we compared each point cloud spatiotemporally registered by our data processing pipeline with its manually aligned counterpart from each data collection session. The Hausdorff distance (Rote, 1991) was considered as performance metric to measure the dissimilarity between both point sets. Given two different point sets $PC_A = a_1, a_2, \ldots, a_n$ and $PC_B = b_1, b_2, \ldots, b_n$, the Hausdorff distance from PC_A to PC_B can be computed as follows:

$$d_H(PC_A, PC_B) = \max_{a \in PC_A} \min_{b \in PC_B} (d(a,b)) \tag{5.2}$$

where a and b are points belonging to the point clouds PC_A and PC_B respectively, and $d(a, b)$ is the Euclidean distance between a and b.

5.2.4 Crop Traits Estimation

Individual-plot Point Clouds Preparation

To isolate individual plots within the registered point clouds, we initially generated a polygon grid covering the entire field area and saved it using the ESRI shapefile (.shp) spatial data format. A

region of interest (ROI) was manually defined for the first plot, then replicated and uniformly spaced to create a grid pattern aligning with crop rows and plots. The shapefile grid was used as the spatial guide to segment individual plots from each data collection session. As the point clouds were spatially and temporally co-registered with the reference point cloud from the first session, this grid generation was a one-time task applied throughout the growing season

Plot-level Traits Extraction

After segmenting individual plots, key morphological traits, including canopy height (CH) and canopy volume (CV), were extracted using the *'laspy'* and *OpenCV* libraries in Python. In addition, we evaluated the use of CV estimations as a proxy for estimating light interception under field conditions, which has been identified as a key input for process-based growth and yield models in cotton (Ermanis et al., 2020; Pokhrel et al., 2023). This indirect approach for estimating light interception has been explored previously in almond orchards (X. Zhang et al., 2021).

To estimate CH at the individual plot level, we analyzed normalized height values within each plot point cloud. We explored two percentile values, 95^{th} (CH95) and 99^{th} (CH99), as well as the maximum height (CH_{max}) derived from the histogram of Z-coordinates. We also compared CH estimations post-4D registration and those from individual point clouds before temporal registration.

For CV estimation, we initially calculated the per-plot projected canopy area (CA). Vegetation points were differentiated from terrain points based on a 5 cm threshold for Z-values. The identified vegetation points were then projected onto the XY plane, generating a 2D binary image mask for each plot. CA was determined by counting the number of pixels per unit area within the projected vegetation points. Subsequently, CV was estimated by multiplying the projected area by

the corresponding CH values using the equation:

$$CV_{projArea} = CA \cdot CH = numPixels \cdot \frac{shapeSize_m}{shapeSize_{px}} \cdot CH \tag{5.3}$$

where $shapeSize_m$ represents the shapefile area for the plot in m^2, and $shapeSize_{px}$ represents the area in pixels.

Crop Trait Estimation Performance Metrics

The overall performance of our methodology at estimating crop traits for field phenotyping was assessed by comparing trait values estimated from TLS data with ground truth values. The selection of the optimal height percentile for CH estimations was based in three metrics: the coefficient of determination (R^2), the root mean squared error (RMSE), and the mean absolute percentage error (MAPE), as defined in Equations 5.4, 5.5, and 5.6, respectively. Higher values of R^2 approaching 1 and lower RMSE and MAPE values indicated more accurate estimations.

$$R^2 = 1 - \frac{\sum_{i=1}^{n}(y_i - \hat{y}_i)^2}{\sum_{i=1}^{n}(y_i - \overline{y})^2} \tag{5.4}$$

$$RMSE = \sqrt{\frac{1}{n} \cdot \sum_{i=1}^{n}(y_i - \hat{y}_i)^2} \tag{5.5}$$

$$MAPE(\%) = \frac{1}{n}\sum_{i=1}^{n}\left|\frac{y_i - \hat{y}_i}{y_i}\right| \cdot 100 \tag{5.6}$$

where n is the total number of data points used for regression analysis, y_i is the actual value of CH for the i^{th} ground truth plot, $\hat{y}_i$ is the predicted CH value obtained from the LiDAR point cloud associated with the i^{th} ground truth plot, and $\overline{y}$ is the mean CH value calculated from the total of ground truth measurements.

To assess the use of CV estimations as a proxy for estimating canopy light interception, a nonlinear regression analysis was performed. This analysis compared the estimated CV values with field ground truth measurements of IPAR_f, using nonlinear least-squares fitting with the *'curve_fit'* function from the *'scipy'* Python library. The standard error of regression (*SER*) was calculated to evaluate the goodness of fit, accounting for the number of independent variables.

$$SER = \sqrt{\frac{1}{n-(p+1)} \cdot \sum_{i=1}^{n} (y_i - \hat{y}_i)^2} \tag{5.7}$$

Here, y_i and $\hat{y}_i$ are the actual and predicted values of IPAR_f for the i^{th} ground truth plot, respectively, n is the total number of data points used for nonlinear regression, and p is the number of coefficients in the model not counting the intercept.

Growth Modeling and Parameters Estimation

The growth cycle of cotton plants follows an S-shaped curve, with lower and upper bounds indicating the period of growth equilibrium (Snider et al., 2021). Among the mathematical models for growth modeling, the three most commonly used for asymptotic growth are the logistic model, the Gompertz model, and the Richards growth model (Tjørve & Tjørve, 2010) (Supplementary Table A.1). These models capture plant growth trajectories with different levels of asymmetry and flexibility. We defined W as the trait value at a given time t, A as the maximum value for the trait

(upper asymptote), k as the growth rate, and T_i as the time at inflection when the maximum growth rate occurs.

The three sigmoid growth models were used to analyze the estimated trait data and reveal the underlying dynamics of CH and CV evolution over time. Nonlinear mixed-effect models (NLME) were employed to capture trait evolution, considering *time* and *genotype* as fixed effects, while *replicate* was treated as a random effect. For the model fitting process, we used the statistical computing and graphics software R (R Core Team, 2023), version 4.2.3, and the *'nlme'* package (Pinheiro & Bates, 2000). For the sake of simplicity and to ensure convergence, we assumed that the growth rate parameter k remained constant and independent of genotype, without showing any random variability across replicates.

The likelihood ratio test (*'anova.lme'*) from the *'nlme'* package was used to identify the most suitable model based on the Akaike information criterion (AIC) (Akaike, 1992) and the Bayesian information criterion (BIC) (Schwarz, 1978) metrics. The model with the highest AIC and BIC support was fitted to the trait data, estimating growth curve parameters. This comprehensive approach enabled us to discern significant variations in growth characteristics across different genotypes.

5.3 Results

5.3.1 Development of the 4D Field Model for Validation

We successfully reconstructed detailed point clouds for each data collection session using multi-scan TLS approaches and automatic registration (Figure 5.4). The average mean point distance

between matched target pairs was 1.6 mm, with a maximum error of 3.2 mm across all sessions. On the whole, the average mean scan point error remained consistently below 6 mm, peaking at 8.5 mm for data collected at 84 DAP. After point cloud preprocessing, the point cloud density was reduced by 8 to 18 times (Supplementary Table A.2), significantly decreasing LAS file sizes to approximately 0.5 GB each and facilitating subsequent processing. This reduction also enabled simultaneous processing of all point clouds in a single CloudCompare session.

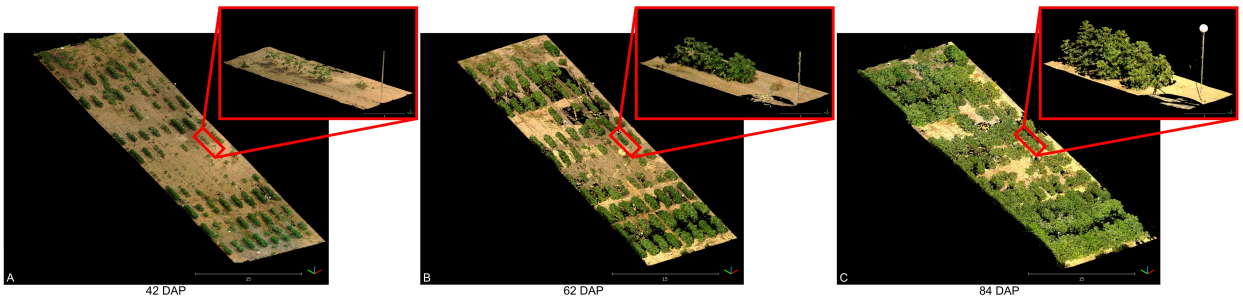

Figure 5.4: 3D representation of the field at three different growth stages. A) data collected 42 days after planting (DAP). B) data collected 62 DAP. C) data collected 84 DAP. Point clouds were colorized using information from the sensor's camera. Black areas represent spaces without 3D point information. Insets show a close-up of the same plot in each point cloud.

The presence of consistent and distinguishable 3D features across all collected point clouds allowed for the creation of an accurate 4D field model (Figure 5.5). This model integrated individually reconstructed 3D point clouds from each session, aligning them to the reference point cloud under a unified coordinate system. As a result, we obtained almost perfectly aligned point clouds for each session that served as a crucial reference for validating the accuracy of our registration process. By comparing the individual point clouds after alignment using our methodology to the reference model, we were able to assess the performance of our registration method.

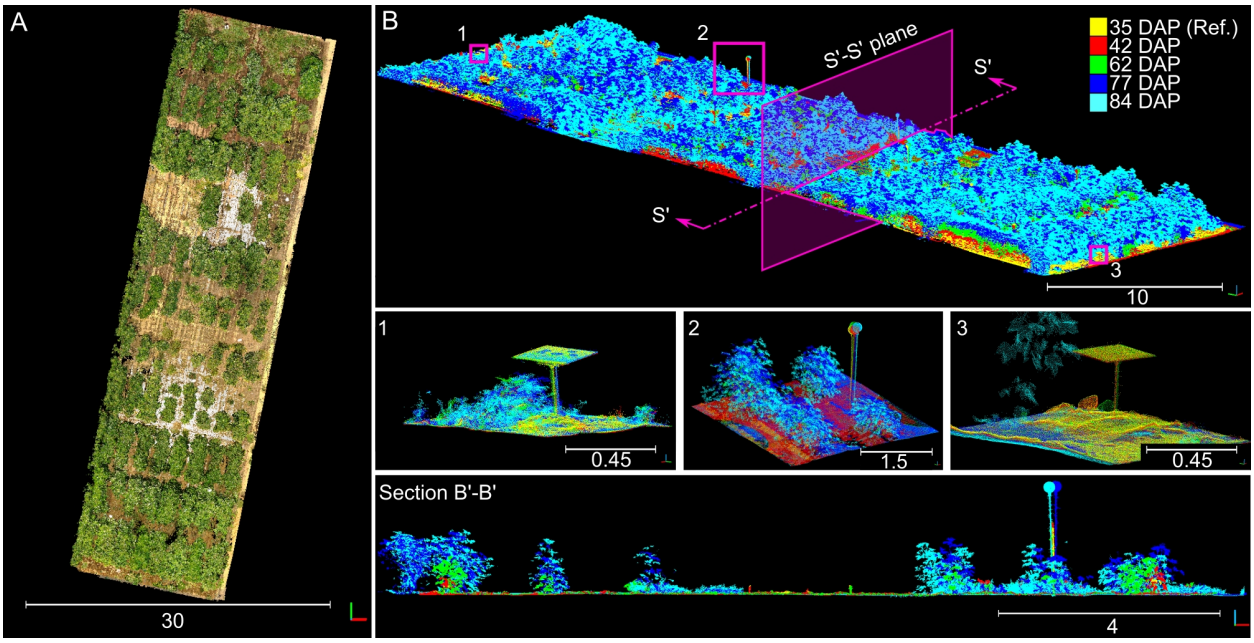

Figure 5.5: Manually aligned time-series point cloud used for benchmarking. A) overhead view of the reconstructed time-series point cloud; 3D points were colorized using information from the sensor's camera. B) perspective view of the point cloud colorized by data collection session; numbered insets show close-up views for the distinctive objects enclosed in pink boxes. Section B'-B' shows a slice of the point cloud taken from the direction indicated by the pink arrows. Different solid colors denote point clouds collected at different dates.

5.3.2 Terrain-based Registration of Point Clouds

The rasterization of terrain points and the posterior meshing process allowed us to obtain consistent DTM models for each data collection session during the growing season (Figure 5.6). However, the reconstruction process tended to overestimate terrain elevation in areas with excessive vegetative growth and denser canopies. As the growing season progressed and plant canopies began to overlap with neighboring plots, the number of terrain points collected by the LiDAR scanner notably decreased, leading to data gaps in the rasterized point clouds (Figure 5.6 C and D). These gaps presented a challenge in accurately modeling the terrain. Notably, when comparing the initial terrain model from the first data collection session (Figure 5.6 A) to the final session (Figure 5.6 D), disparities in elevation reached nearly 37 cm in regions with dense vegetation. Despite these challenges, our method consistently produced accurate terrain morphology results up to 84 DAP when all plots in the field effectively reached the canopy closure stage.

Leveraging internal sensors data gathered during LiDAR data collection allowed us to position consecutive point clouds in close proximity to each other and facilitated convergence of the ICP algorithm, minimizing its risk of getting trapped in local minima (Supplementary Figure S2). The resulting RMS values for ICP registration between the DTM for each data collection session and the reference DTM were consistently less than 10 mm.

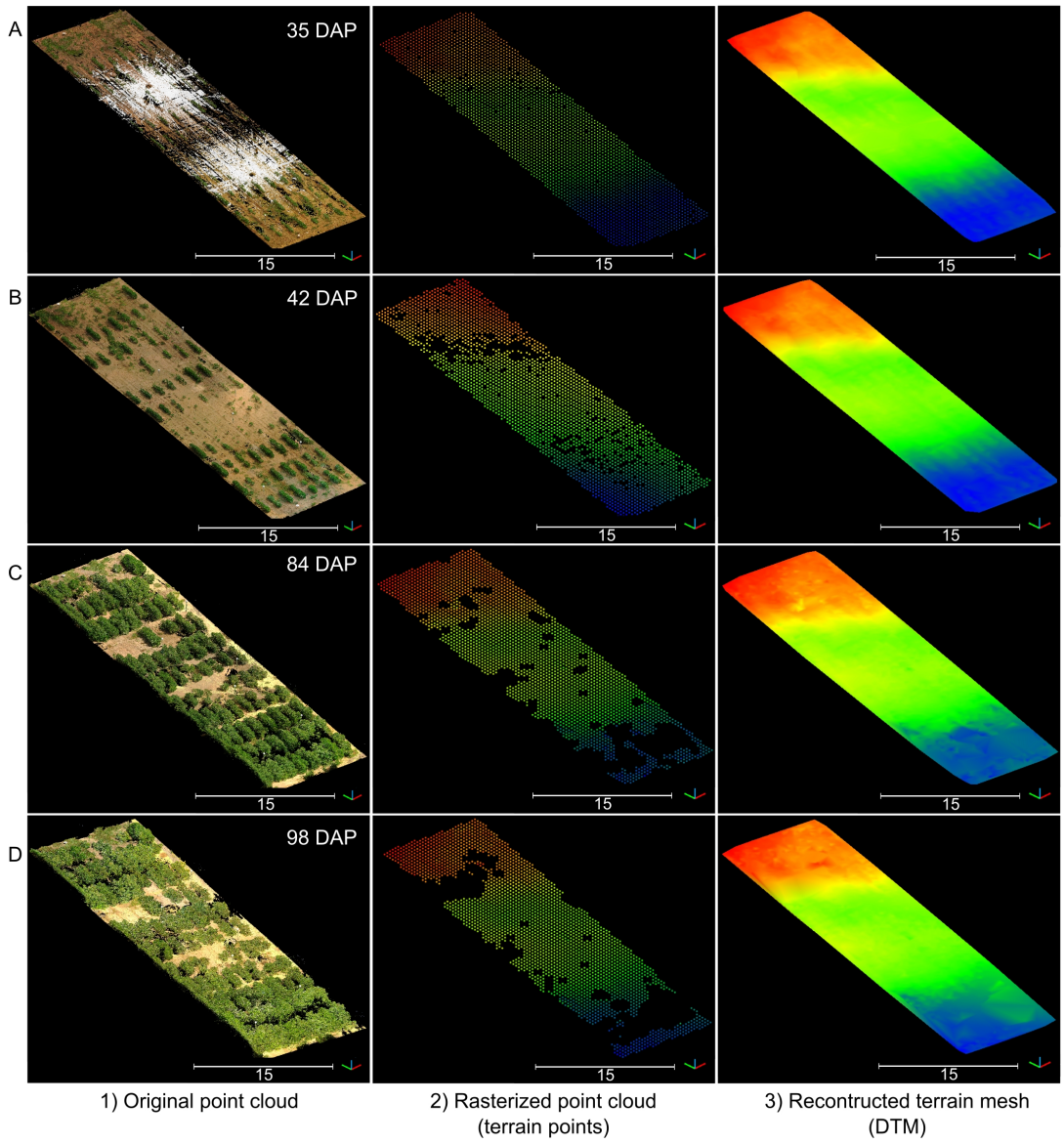

Figure 5.6: Reconstructed digital terrain model (DTM). DTM for four data collection sessions during the vegetative growth stage. Rows A) to D) correspond to data collected at 35 days after planting (DAP), 42 DAP, 84 DAP, and 98 DAP, respectively. For each row, from left to right: 1) RGB point cloud, 2) Rasterized point cloud colorized by elevation, and 3) Reconstructed DTM colorized by elevation. Elevation is represented using a color map ranging from blue (the lowest point) to red (the highest point).

5.3.3 Bird's-Eye View-based Alignment for Spatiotemporal Registration Refinement

The developed process enabled the isolation of prominent plots in the field, allowing for an accurate identification of their centroids (Figure 5.7). Through local height normalization and thresholding, only the upper section of the canopy was retained (Figure 5.7 A), revealing the distinct pattern of crop rows by focusing solely on vegetation points (Figure 5.7 B). Following plot clustering, PCA-based filtering reduced the potential impact of spurious points or poorly defined plots, such as noise, small plots, or tall weeds, thereby enhancing the consistency and robustness of plot centroid identification (Figure 5.7 C and D). For a comprehensive visualization of the BEV alignment process for two point clouds, refer to Supplementary Figure S3.

The BEV alignment step consistently enhanced the accuracy of point cloud registration for data collected during the vegetative crop growth stage (Figure 5.8). Initially, errors ranging between 10 cm and 35 cm with respect to the reference point cloud were observed after the first alignment step (Figure 5.8 A, inset 1). However, after the second alignment step, errors for points above the terrain plane notably decreased to values around 2 to 3 centimeters (Figure 5.8 B, inset 1). Examination of alignment results at terrain level revealed that registration errors in the Z direction remained relatively constant, increasing slightly from 2.2 cm for the initial DTM-based alignment step (Figure 5.8 A, inset 2) to 2.3 cm for the refinement step based on BEV (Figure 5.8 B, inset 2).

In general, the alignment of point clouds remained consistent throughout the growing season, with final alignment errors comparable to those achieved by manual alignment of the point cloud pairs. In the manually aligned point clouds, the distance between point clouds at the overall level

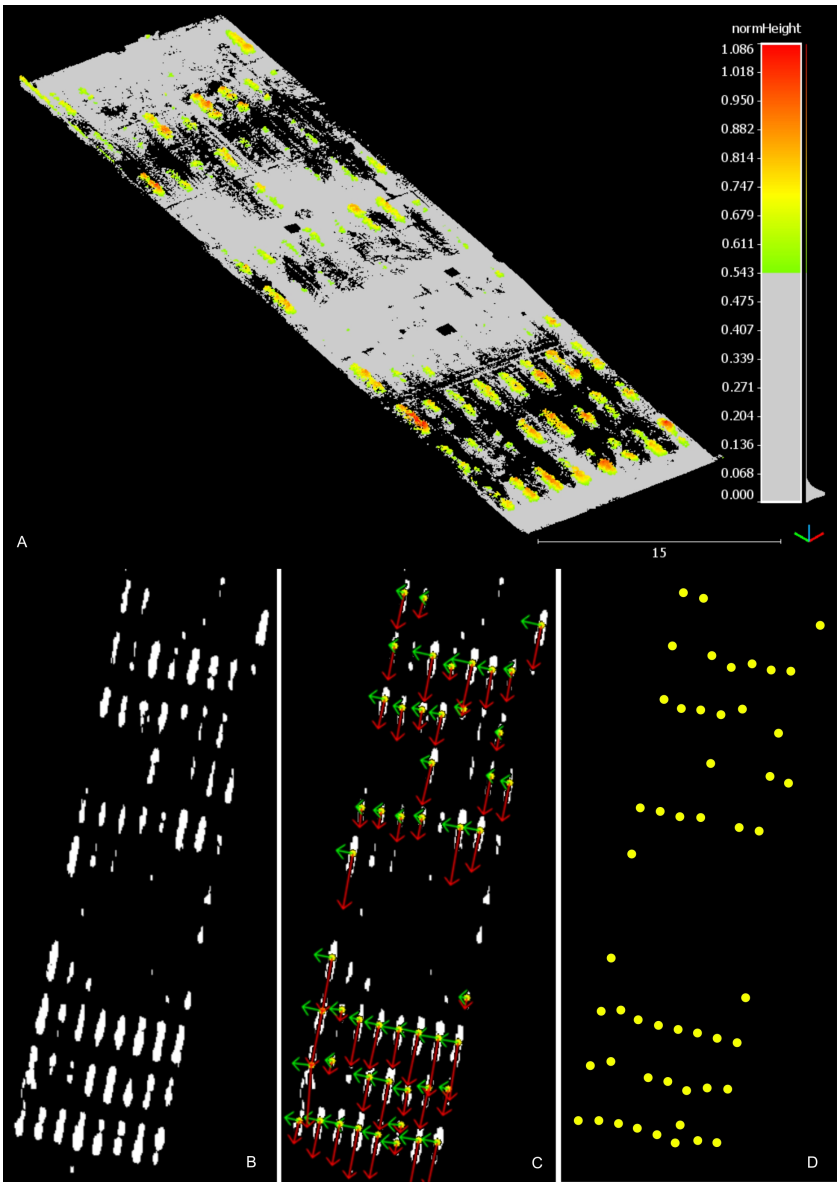

Figure 5.7: Intermediate results of bird's-eye view alignment process. A) canopy points isolated after height thresholding. B) canopy points projected onto the X-Y plane in 2D. C) identified pixel clusters and principal component analysis results. D) visual depiction of identified plot centroids. Red arrows indicate the first principal component's direction, while green arrows illustrate the second principal component's direction.

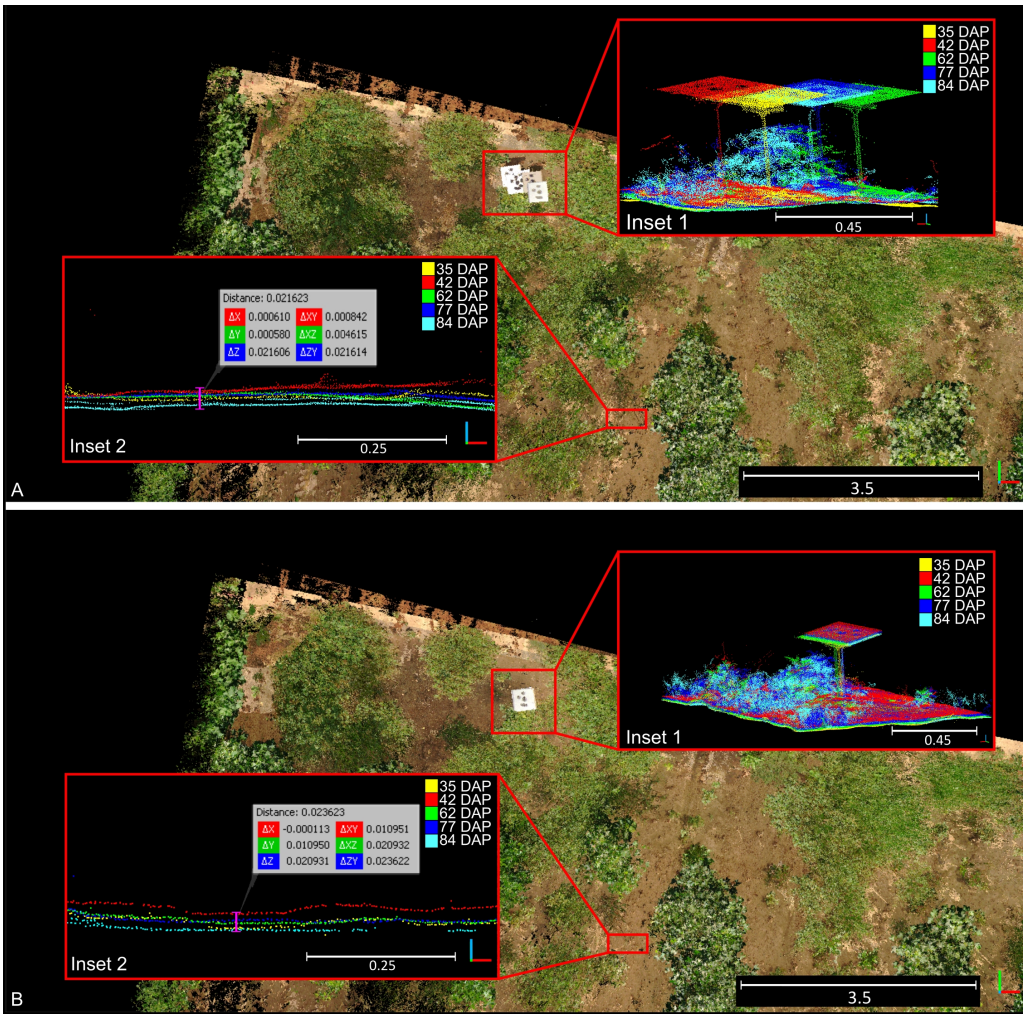

Figure 5.8: Qualitative results of two-step registration. Qualitative results for the alignment of point clouds collected over time using our two-step process. A) initial alignment results following the first step, utilizing digital terrain model matching. B) Ultimate alignment obtained after bird's-eye view refinement. Insets 1) exhibit generalized alignment discrepancies. Insets 2) emphasize errors in the Z direction at the terrain level. Diverse solid colors indicate point clouds gathered at various timestamps.

ranged between 0.5 and 1 cm, while at the ground level, the distance in the Z axis between point clouds reached approximately 6 mm. To see a detailed visual comparison between the manually aligned point clouds and those registered using our methodology, refer to Supplementary Figure S4.

5.3.4 Quantitative Analysis of Errors for Spatiotemporal Registration

Our quantitative analysis confirmed significant reductions in the main distances between point clouds registered using our methodology and their manually aligned counterparts (Table 5.1). After the initial alignment based on DTM matching, the average Hausdorff distance between point clouds was approximately 31 cm, consistent with our previous qualitative analysis (Figure 5.8). With the second alignment step, the average Hausdorff distance was reduced to 5.5 cm, representing an 83% reduction from the initial alignment errors. However, despite this improvement, the alignment error for the final data collection session remained relatively high, reaching 13.5 cm even after the refinement step, in contrast to the approximately 3 cm observed for the other point clouds. This difference can be attributed to the limitations of the initial alignment based on the DTM in advanced growth stages. The denser and taller canopy obstructed the laser beam during the survey more frequently, resulting in limited terrain data for ICP registration. This contributed to larger initial errors that the refinement step, based on the BEV alignment approach, was not able to completely rectify.

A deeper analysis of registration errors revealed a clear trend: as the cotton canopy grew and became denser, the registration errors increased both in magnitude and variability (Figure 5.9). Early stages showed relatively low and uniform errors, while later stages exhibited higher errors due to the complexity of the mature canopy. This progression of errors from the early to

Table 5.1: Spatiotemporal registration errors. Alignment errors in centimeters after each alignment step.

	Step 1 Terrain model-based alignment								**Step 2** Bird's-eye view-based alignment							
			d_{H_X}		d_{H_Y}		d_{H_Z}				d_{H_X}		d_{H_Y}		d_{H_Z}	
DAP	RMS↓ (std)	$\overline{d_H}$	max	min	max	min	max	min	RMS↓ (std)	$\overline{d_H}$	max	min	max	min	max	min
42	2.1 (1.9)	19.3	18.3	-16.9	16.1	-18.3	17.6	-15.8	1.2 (0.6)	3.2	3.0	-3.1	3.0	-3.1	3.2	-3.1
62	4.9 (6.5)	32.5	32.0	-32.3	31.0	-30.0	31.8	-29.4	0.5 (0.3)	2.4	2.1	-2.1	2.1	-2.1	2.1	-2.1
84	3.6 (3.6)	24.2	22.3	-24.0	21.8	-22.6	23.0	-22.4	0.8 (0.5)	3.5	3.2	-3.0	3.0	-3.1	3.2	-3.0
98	5.7 (5.7)	46.8	36.3	-46.1	43.5	-36.9	39.7	-40.1	2.5 (1.8)	13.5	11.7	-12.5	12.2	-11.4	12.3	-11.3

maturity stages demonstrated the increasing difficulty in point cloud registration as the crop canopy developed, highlighting the importance of robust registration methodologies to handle increased canopy density and complexity.

At 42 DAP, during the early-stage canopy development with minimal plant overlap, distance errors peaked at 3.24 cm, with most errors being moderate. The majority of errors ranged between 0.38 cm and 1.13 cm, suggesting a low error spread. At 62 DAP, with increased canopy coverage and uniform growth, the maximum error reached 2.20 cm, with errors more uniformly distributed across the field compared to the earlier stage. Errors were primarily concentrated between 0.25 cm and 0.75 cm, reflecting improved registration accuracy during this stage. This improvement could be attributed to better performance of the BEV refinement step, where increased canopy density provided more information to identify plot centroids, enhancing alignment accuracy. Additionally, as the crop grew taller, interference from weeds diminished, aiding in more accurate plot identification.

By 84 DAP, when the crop already reached canopy closure stage, the maximum error increased to 3.49 cm, with higher variability in areas of dense canopy growth. Errors ranged more broadly,

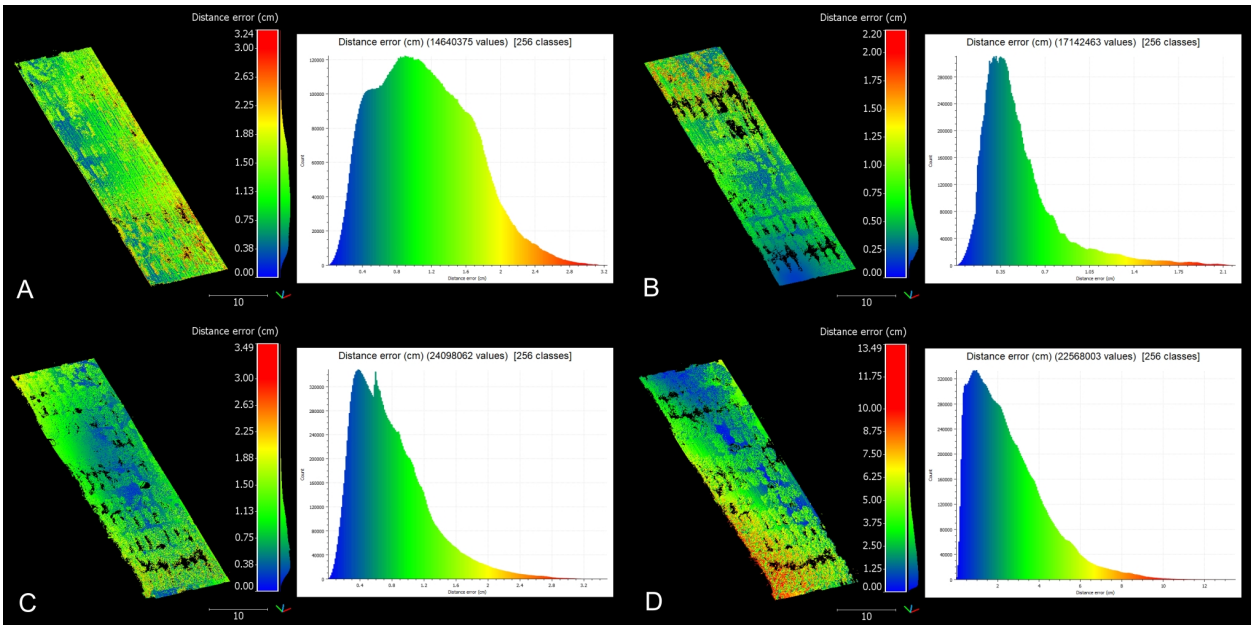

Figure 5.9: Distribution of registration errors across data collection sessions. Comprehensive analysis of registration errors showcasing both the spatial distribution of distance errors and their respective histograms. **(A)** 42 days after planting (DAP). **(B)** 62 DAP. **(C)** 84 DAP. **(D)** 98 DAP. The distribution of distance errors is visualized with a color gradient ranging from blue (low error) to red (high error).

with a significant portion between 0.75 cm and 2.63 cm, highlighting the challenges of maintaining accuracy as the canopy became denser. This stage reflected the increasing complexity of the registration process as the canopy structure became more intricate and plots overlapped, posing significant challenges to maintaining low error rates. At 98 DAP, errors reached a maximum of 13.49 cm, demonstrating significant challenges due to dense and overlapping canopies. A wide distribution of errors, clustering between 2 cm and 10 cm, indicated substantial variability and the presence of outliers caused by canopy occlusion and overlapping. At this point, the refinement step was no able to reduce alignment errors and optimize registration.

5.3.5 Phenotypic Traits Estimation

Our spatiotemporal registration methodology significantly enhanced CH estimations compared to conventional TLS data analysis without temporal registration (Table A.3). All analyzed percentiles for CH estimation—95^{th}, 99^{th}, and maximum height—exhibited a strong relationship with actual measurements for both methods. However, after the two-step spatiotemporal registration process, CH estimations consistently demonstrated stronger correlations with ground truth measurements and reduced errors compared to estimating CH from individual point clouds without temporal co-registration.

Estimations of CH using the maximum height value consistently exhibited the strongest correlation with actual CH values, explaining almost 95% of the total variance. While CH95 and CH99 also demonstrated strong correlations with ground truth measurements, CH_{max} consistently outperformed them across various evaluation metrics. Notably, CH_{max} showed reduced average deviation from the actual values and lower errors compared to CH95 and CH99, with an RMSE below 8 cm and average deviation of about 5%. These results are in line with findings from previous LiDAR-based studies in cotton (S. Sun et al., 2017, 2021), indicating the reliability of CH_{max} for estimating canopy height in cotton crops from multi-scan TLS, particularly in the context of time-series data analysis. CH_{max} captures the tallest point in the canopy, akin to manual field measurements, making it less susceptible to variability in canopy structure compared to percentile-based estimations, especially after denoising the point clouds.

Overall Performance Analysis

Our methodology for processing and analyzing in-field time-series TLS data demonstrated robust performance in estimating key traits versus ground truth measurements (Figure 5.10). The regression analysis showed a strong agreement between estimated values and ground truth measurements for both CH and IPAR_f. Despite the complex and evolving nature of the crop, our methodology allowed for the precise estimation of these traits, accurately capturing the dynamic changes in crop traits over time.

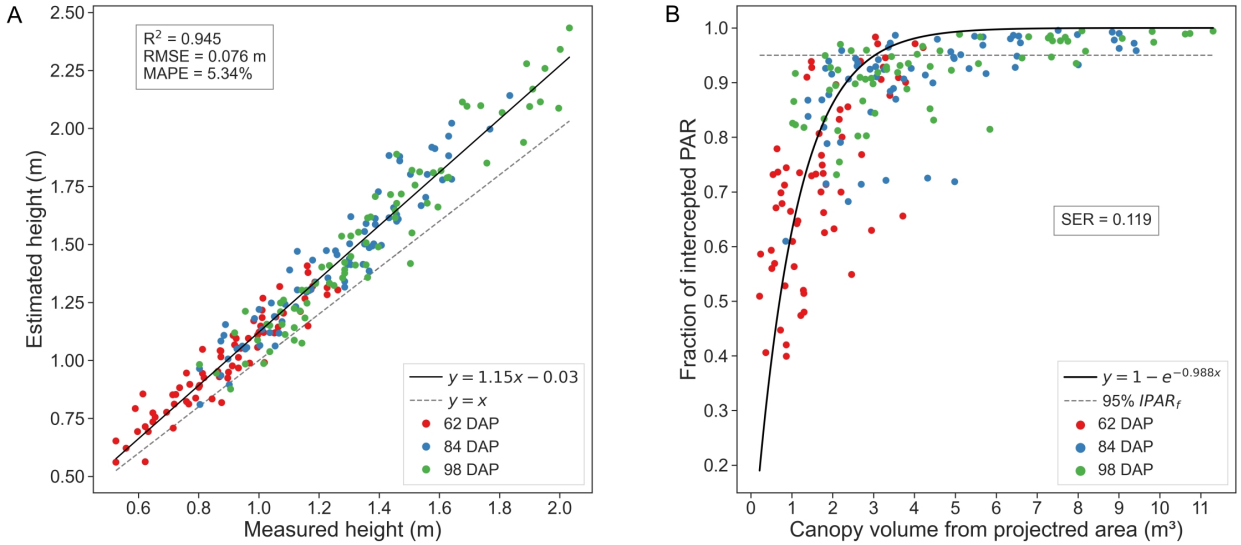

Figure 5.10: Phenotypic traits estimation results. A) canopy height estimations computed using the maximum height value versus ground truth measurements. B) canopy volume estimations versus ground truth measurements of fraction of intercepted PAR.

Regarding CH estimations, we observed a general slight overestimation of canopy height compared to the actual values, which became more pronounced as the crop matured (Figure 5.10 A). The linear regression model displayed a slight deviation from the 1:1 line, a trend consistent across other percentiles, albeit with slight variations. For instance, analysis of the 95^{th} percentile revealed

a more pronounced tendency to overestimate canopy height during early growth stages, suggesting it may be less reliable for estimating in-field cotton plots height.

Analyzing the results for each data collection session individually, error values showed an increasing trend with crop development, leading in more dispersed CH estimations for larger canopies during later growth stages. RMSE values varied approximately 2 cm from the initial session to the last. At 62 DAP, the RMSE surpassed 6 cm, increasing to approximately 7 cm at 84 DAP and 8 cm at 98 DAP. This trend may be attributed to diverse canopy development of plants amongst plots or plant lodging during the season. Other potential causes of errors included underestimation in terrain elevation in regions with dense vegetative growth, as discussed previously (Section 5.3.2), or potential human error, given the challenges of measuring tall (reaching more than 2 m) and dense crops in the field. Nevertheless, examination of MAPE values revealed a consistent performance of our methodology, with only a 1.42% difference between the maximum and minimum MAPE values. Specifically, at 62 DAP, MAPE reached 6.17%, at 84 DAP it was 4.76%, and at 98 DAP, 5.11%. This suggests that, despite the observed increase in RMSE, our estimations remained relatively close to the actual values across different growth stages.

Upon examining the estimated CV in relation to field measurements of IPAR_f, we observed a pattern of exponential saturation with a distinct asymptote as the crop canopy approached its maximum volume (Figure 5.10 B). This pattern aligns with the classical Beer-Lambert's law of attenuation of light through the canopy, offering a straightforward approach for predictive crop physiological traits estimation. Notably, the critical leaf area index at which 95% of radiation is intercepted was reached at canopies volumes between 3 and 4 m^3. The crop attained these volumes in a generalized manner between the first and second ground truth data collection dates, suggesting

the likely canopy closure between 62 DAP and 84 DAP, a timeframe consistent with bibliography on cotton crop physiology (Snider et al., 2021). These findings provide valuable insights into the dynamic interplay between canopy structure and light interception efficiency, key for optimizing crop productivity.

Validation of CH Estimates Over Time

Our spatiotemporal registration of TLS data provided reliable estimations of CH over time (Figure 5.11). The comparison between TLS-based estimates and ground truth measurements indicated that the temporal variation of predicted and observed data was generally within 7 cm for most genotypes and data collection sessions. This agreement was particularly strong for canopies under 1.5 meters, where CH estimations closely matched actual values. However, for canopies exceeding 1.5 meters, our estimations tended to slightly overestimate CH, which is consistent with our previous regression analysis.

The proximity of our estimated values to actual measurements indicated the accuracy of our methodology. CH estimations generally followed trends of steady growth, maintaining close alignment with ground truth values. In several cases, such as UA 48 or ST5020, the estimated CH closely matches the ground truth, demonstrating the reliability of our scanning technique. However, we found some discrepancies between estimated and ground truth values for certain genotypes, such as T0018MDN or MDN0101, highlighting areas for potential refinement in our scanning process. These discrepancies can be attributed to two main factors. Firstly, these two genotypes showed the highest growth rate, and as the canopies grew taller and denser, measuring their height in the field became more challenging and error-prone, introducing noisy points that could mask the

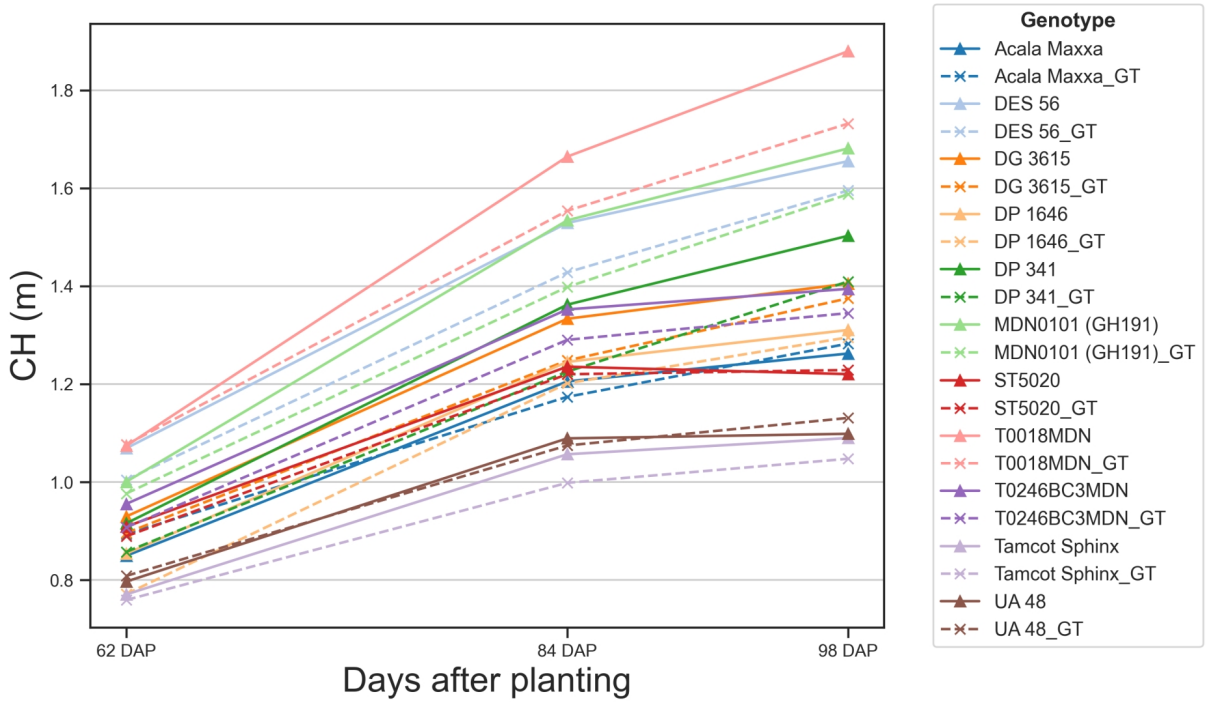

Figure 5.11: Temporal variation of predicted and observed canopy height. Solid lines represent canopy height (CH) values estimated using our methodology. Dashed lines represent ground truth (GT) CH values measured manually in the field. Each color and symbol combination represents a different genotype, with corresponding pairs (e.g., Acala Maxxa and Acala Maxxa_GT) for each genotype.

performance of our methodology. Secondly, the increased complexity of the canopy structure at later growth stages might have affected the accuracy of the TLS data registration, leading to slight overestimations in CH.

Our methodology effectively captured the variations in CH among different genotypes over time. Some genotypes exhibited considerable growth, and our methodology tracked this evolution relatively accurately. At 62 DAP, CH among genotypes showed minimal variation, mostly clustered between 0.8 and 1.0 meters, and our estimation errors were below 5 cm. However, as the crop

matured, our CH estimates began to slightly diverge from the actual values. By 98 DAP, there was greater diversity in CH, ranging from nearly 1.8 meters for some genotypes to around 1.2 meters for others. At this stage, TLS estimates tended to be higher than the actual measurements, with estimation errors reaching approximately 20 cm for certain genotypes. These observations were consistent when analyzed at the individual plot level (Supplementary Figure S5). For genotypes such as DES 56 or DG 3615, average estimation errors remained under 7 cm. However, in plots of genotypes like T0018MDN, errors approached 25 cm at later DAP, indicating challenges in accurately measuring CH as canopies became taller and denser.

5.3.6 Analysis of Phenotypic Traits Over Time

Our methodology for collecting time-series TLS data provided highly detailed 3D information, enabling clear tracking of canopy evolution at the plot level across the distinct crop growth phases (Figure 5.12). The application of multi-scan TLS proved to be a robust technique for crop trait modeling over time, facilitating the reconstruction of detailed 4D models to successfully identify the primary growth phases leading up to crop maturity. The progression of canopy expansion is illustrated in Supplementary Figure S6, which shows a detailed profile of the distribution of canopy area per height layer over time for all genotypes. In general, during the initial growth stages, steady stem elongation and leaf area expansion were observed. With increasing resource availability, plant canopy expanded significantly both vertically and horizontally, resulting in exponential leaf area growth for almost all genotypes between 40 and 70 DAP. As the crop approached canopy closure, the canopy height tended to peak, yet vegetative branches continued to develop, significantly increasing lateral growth and the overall occupied volume until reaching canopy closure, where the

canopy nears its upper size limit. This approach facilitated the extraction of morphological traits at the plot level and enabled comparative analysis across different genotypes throughout the growing season.

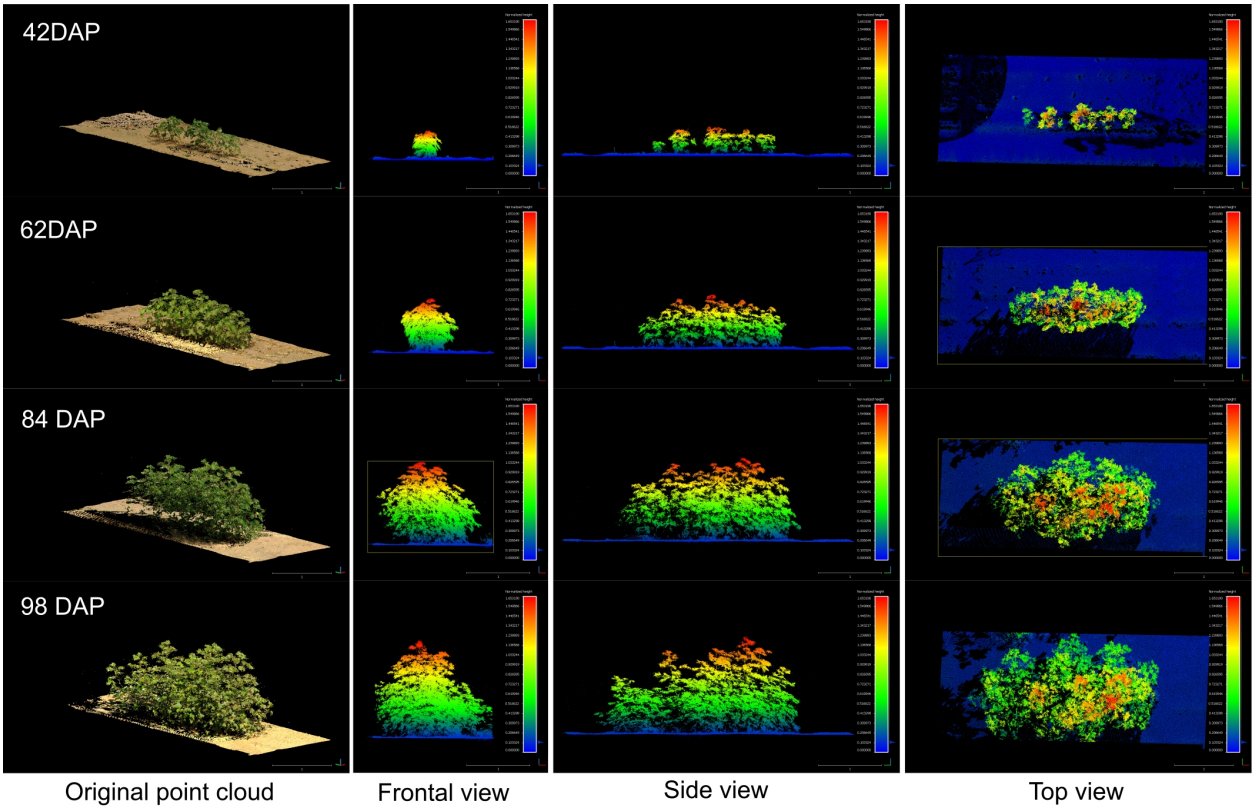

Figure 5.12: Growth comparison for a sample plot during the vegetative crop growth. The left column shows the original RGB point cloud. The rest of columns show the frontal view, side view, and top view for each respective data collection session colorized by plant height. The figure is color-coded based on plant height, normalized with respect to the terrain (DTM), with blue tones indicating points closer to the ground.

Crop Growth Model Selection

The logistic model consistently emerged as the best-performing model across the analyzed traits, exhibiting the lowest AIC and BIC scores for modeling CH and CV evolution (Table A.4). Notably, the variations in performance among the models were relatively modest, indicating that all selected

models provided a reasonably good fit to the data. The ΔAIC and ΔBIC values, which represent the differences in Akaike Information Criterion and Bayesian Information Criterion values, respectively, offer a comparative perspective on each model's performance relative to the best-fitting model.

In our study, the logistic and 3P-Richards models excelled in estimating CH growth parameters. For CH estimations, the logistic model was closely followed by the 3P-Richards model, with only a 4-point difference. The Gompertz model performed notably worse, with differences exceeding 50 points in both AIC and BIC scores. Conversely, the logistic model outperformed the others in CV growth modeling. Here, the 3P-Richards model had the worst AIC and BIC scores, while the Gompertz model's performance was intermediate, with AIC and BIC scores 10 points higher than those of the logistic model.

Traits Evolution Modeling

Our findings revealed significant variability in CH growth parameters across different cotton genotypes, including both maximum CH value and inflection point (Table 5.2). In order to ensure the convergence of the mathematical model and facilitate the estimation of other growth parameters using the available data, we assumed a constant logistic growth rate (k) across all genotypes.

The maximum value in a sigmoidal growth curve represents the upper limit or saturation point of growth for the crop. In our analysis, genotype T0018MDN exhibited the highest maximum CH among all genotypes, reaching nearly 2 meters. Genotypes MDN0101 (GH191) and DES 56 closely followed, with a maximum CH of approximately 1.8 meters. In contrast, genotypes Tamcot Sphinx and UA48 were significantly smaller, with maximum CH values around 1.2 meters. The remaining

Table 5.2: Comparison of logistic growth parameters for canopy height per genotype. Means and standard error (SE) for maximum height (A_{CH}) in meters and inflection point (T_{iCH}) in days after planting. The logistic growth rate (k_{CH}) was assumed constant for all the genotypes. †Means not sharing any letter are significantly different by the Tukey-test at the 5% level of significance.

Genotype	k_{CH}	$A_{CH}{}^{\dagger}$	SE	$T_{iCH}{}^{\dagger}$	SE
Tamcot Sphinx	0.06	1.24^{a}	0.112	53.3^{abcd}	1.153
UA 48	0.06	1.26^{a}	0.097	51.2^{ab}	0.875
ST5020	0.06	1.40^{ab}	0.097	49.1^{a}	0.792
Acala Maxxa	0.06	1.40^{ab}	0.104	53.2^{abc}	1.049
DP 1646	0.06	1.48^{ab}	0.104	55.7^{cde}	0.918
T0246BC3MDN	0.06	1.58^{abc}	0.136	53.3^{bcd}	1.028
DG 3615	0.06	1.59^{ab}	0.104	52.5^{abc}	0.941
DP 341	0.06	1.62^{abc}	0.105	56.1^{cde}	1.145
DES 56	0.06	1.81^{bc}	0.104	54.4^{bcd}	0.804
MDN0101 (GH191)	0.06	1.84^{bc}	0.099	57.7^{de}	0.909
T0018MDN	0.06	2.06^{c}	0.100	59.3^{e}	0.871

genotypes fell in between, with CH values ranging from 1.4 to 1.6 meters. Notably, ST5020, Acala Maxxa, DP 1646, and DG 3615 had significantly shorter canopies compared to T0018MDN.

The inflection point is a critical feature that marks the change in crop growth dynamics. This point, where the curve's slope is at its maximum, represents the stage where the rate of growth transitions from being exponential to linear, signifying the phase of most rapid change in the growth rate. In our experiment, T0018MDN genotype was the last in reaching maximum growth rate, occurring after 59 DAP (T_i = 59.3 DAP). This was significantly later than the other genotypes, except for MDN0101 (GH191), DP 341, and DP 1646. In contrast, ST5020 and UA48 took around 50 days to reach their maximum growth rates. The rest of the genotypes exhibited inflection points of 53 DAP or more. Notably, MDN0101 (GH191) was significantly more slowly in reaching its peak than DG 3625, Acala Maxxa, UA48, and ST5020, taking approximately 54 DAP.

Our analysis of CV estimations over time revealed substantial genotype-dependent differences in CV growth (Table 5.3). Similar to the CH analysis, we assumed a constant logistic growth rate (k) for all genotypes to ensure model convergence. Among the genotypes assessed, T0018MDN exhibited the highest plant volume, surpassing 7 m^3. Following closely were genotypes DG 3615, DES 56, and DP 341, each with volumes exceeding 6 m^3. In contrast, Tamcot Sphinx attained a maximum volume of less than 3 m^3, significantly smaller than T0018MDN. The remaining genotypes displayed CV values ranging between 3 and 7 m^3. Regarding the inflection point for CV growth modeling, genotype DP 1646 demonstrated the highest value among all genotypes, occurring at approximately 70 DAP. Most other genotypes exhibited inflection points between 64 and 68 DAP. MDN0101 (GH191) emerged as the most precocious in reaching its maximum growth rate, at around 63 DAP, indicating a significant earlier maturation compared to genotypes T0018MDN, DG 3615, and DP 341.

Table 5.3: Comparison of logistic growth parameters for canopy volume per genotype. Means and standard error (SE) for maximum canopy volume (A_{CV}) in cubic meters and inflection point (T_{iCV}) in days after planting. The logistic growth rate (k_{CV}) was assumed constant for all the genotypes. †Means not sharing any letter are significantly different by the Tukey-test at the 5% level of significance.

Genotype	k_{CV}	$A_{CV}{}^{\dagger}$	SE	$T_{iCV}{}^{\dagger}$	SE
Tamcot Sphinx	0.106	2.76^{a}	0.92	64.4^{abc}	1.435
UA 48	0.106	3.68^{ab}	0.80	64.8^{ab}	1.058
Acala Maxxa	0.106	4.28^{ab}	0.86	64.0^{ab}	1.116
ST5020	0.106	4.28^{ab}	0.80	65.3^{abc}	1.139
DP 1646	0.106	4.77^{ab}	0.85	70.1^{c}	1.157
T0246BC3MDN	0.106	4.84^{ab}	1.12	66.1^{abc}	1.308
MDN0101 (GH191)	0.106	5.40^{ab}	0.80	62.6^{a}	0.846
DP 341	0.106	6.45^{ab}	0.85	68.3^{bc}	1.218
DES 56	0.106	6.49^{ab}	0.85	66.7^{abc}	0.962
DG 3615	0.106	6.67^{ab}	0.85	67.4^{bc}	1.087
T0018MDN	0.106	7.25^{b}	0.79	67.0^{bc}	0.849

The complex interplay between genotype, environment, and crop development is evident in the diverse morphological traits analyzed and the corresponding evolution curves of CH (Figure 5.13) and CV (Figure 5.14). The evolution of both CH and CV reflects the gradual pace of growth of the crop during the initial stages. As the season progressed and resources become more available, plant canopy expanded both in height and laterally, resulting in exponential CV growth across all genotypes between 40 and 70 DAP. This period of rapid development indicated the crop's increasing capacity to capture light energy. Around 75 DAP, a visible slowdown in stem elongation is observed across nearly all genotypes, signaling the approach to canopy closure. This phenomenon suggests that the crop is nearing its upper size limit, with further CH growth becoming increasingly constrained. Tracking growth traits over time provides valuable insights into the dynamic evolution of cotton crop development, including genotype-specific responses to environmental cues and management practices. These insights can guide breeders and researchers in selecting genotypes with desired traits to improve yield, enhance pest resistance, and ensure adaptability to diverse growing conditions.

5.4 Discussion

5.4.1 Time-Series TLS Data for Field Phenotyping

Using time-related data in plant phenotyping represents a valuable approach to gaining a deeper understanding of the temporal dynamics of plant growth. Plants respond to changing environmental conditions, and field data collected over time can capture these variations, providing continuous insights into trait evolution during the course of a growing season. This can allow for a better under-

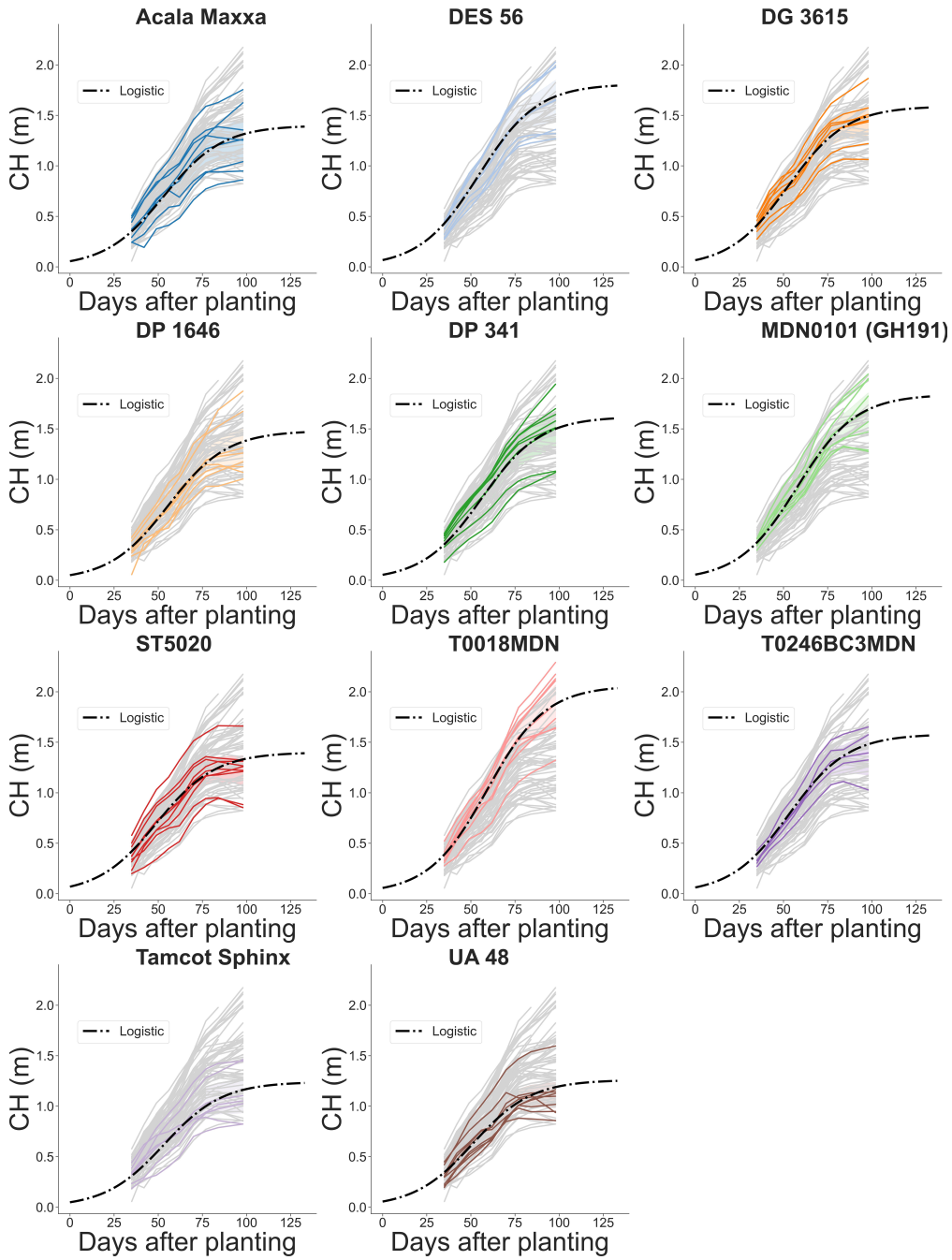

Figure 5.13: Temporal evolution of plot-level canopy height during the growing season. Grey lines indicate estimated canopy height (CH) values for all plots in the field. Colored solid lines highlight the estimated CH for a specific genotype (11 genotypes in total). Dash-dotted lines depict fitted logistic growth curves.

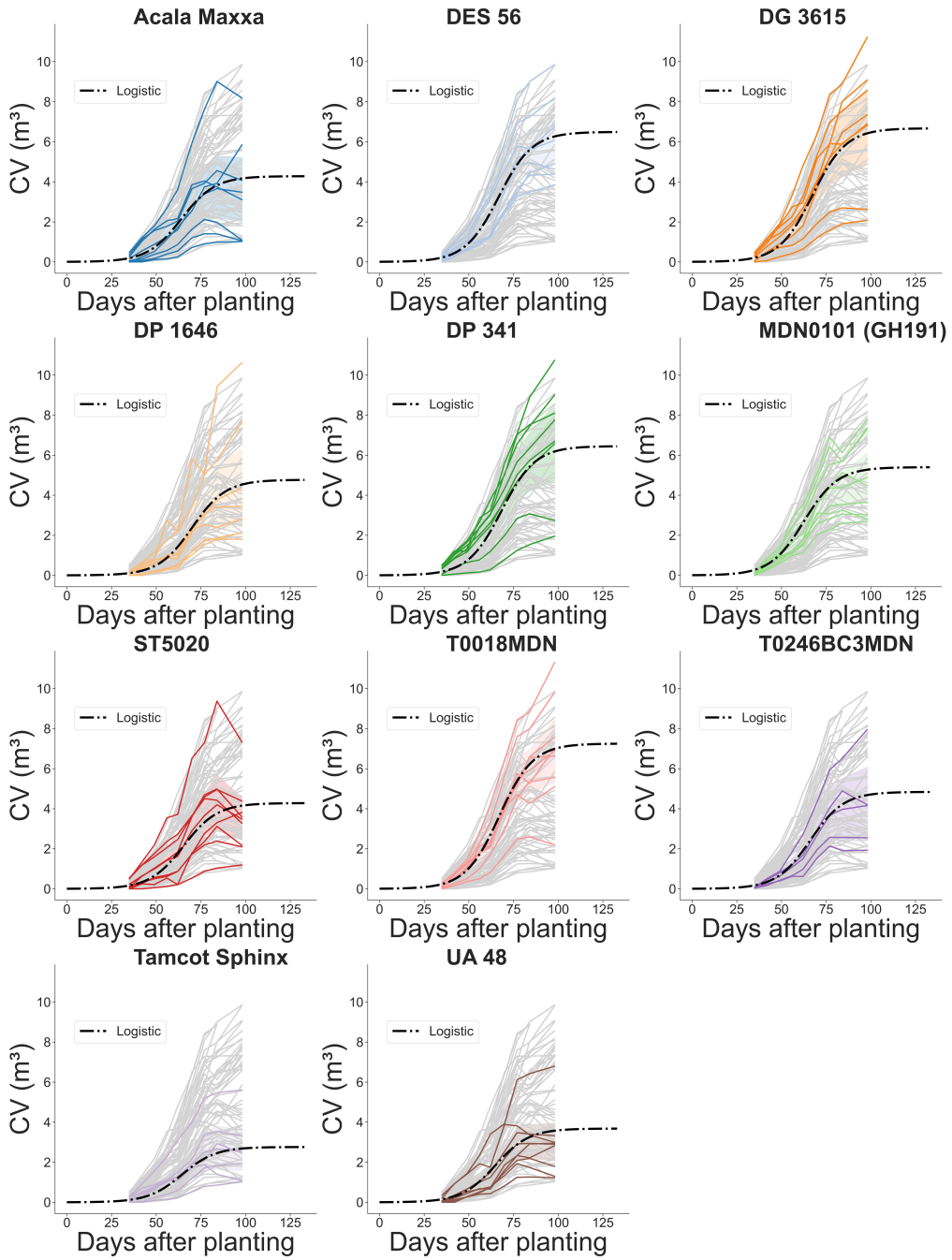

Figure 5.14: Temporal evolution of plot-level canopy volume during the growing season. Grey lines represent estimated canopy volume (CV) values for every plot computed using the method based on projected area. Colored solid lines highlight the estimated CV of individual plots for a specific genotype (11 genotypes in total). Dash-dotted lines depict fitted logistic growth curves.

standing of crop development (Pauli et al., 2016), holding promise for advancing our knowledge of plant biology and supporting the development of crops adapted to varying environmental conditions (Miao et al., 2020). In plant breeding, this information can be key to support genotype selection based on new traits that allow for a more efficient use of resources (D. Li et al., 2022).

Traditional plant phenotyping methods often limit analysis to a single time point, potentially overlooking vital changes and interactions between the crop and its environment during critical developmental stages (Tardieu et al., 2017). Unlike conventional static measurements, time-series data are composed of a sequence of data collected at different timestamps. This temporal context facilitates the identification of key stages of development and growth patterns, offering valuable information about the rate of growth, periods of stability, and potential stress responses (D. Chen et al., 2014).

Integrating time-series data with advanced 3D technologies like LiDAR enhances phenotyping for precision agriculture. LiDAR technology has contributed to the advancement of field phenotyping, offering direct access to complex 3D morphological trait information and allowing for detailed reconstructions of plant structures (Q. Guo et al., 2018). Time-series TLS data can improve the accuracy of growth models by capturing intricate details of plant development during the whole growing season (Jin, Sun, et al., 2021). Our work demonstrated that TLS time-series data can provide consistent information on traits such as canopy height and volume, enabling precise crop traits tracking. This information can increase our understanding of critical growth parameters to optimize management strategies and make more informed decisions in crop breeding.

5.4.2 Importance of 4D Registration of TLS Data for Crop Growth Tracking

Detailed 4D models, incorporating the temporal dimension into 3D spatial data from TLS scans, provide a powerful tool for analyzing and tracking morphological traits across the growing season. However, generating these models poses unique challenges, primarily from the need to align repeated measurements over time. The complex transformations that crops undergo during the growing season complicate the registration of point clouds collected at different time points. Ensuring the consistency and reliability of TLS data collection and processing becomes essential in field conditions (Pieruschka & Schurr, 2019).

Accurate data alignment is crucial for tracking changes in plant structure. While some methods use fixed targets to aid co-registration (Friedli et al., 2016; Su et al., 2019; Tilly et al., 2014), this approach can be labor-intensive and error-prone. The consistent positioning of targets in agricultural fields, where machinery needs to operate or other experiments need to be executed, can be problematic. Deviations in the target placement between surveys can impact the temporal alignment accuracy, and hence the estimation of traits over time.

Inspired by the positive results from a previous study in maize, soybean, and wheat using semi-permanent targets (Friedli et al., 2016), we initially adopted this concept to benchmark our methodology. This study reported deviations in the positions of spherical targets between 2.5 mm and 10 mm. However, after preliminary processing of data from our initial collection sessions, we found deviations in target locations exceeding 20 mm. These larger deviations were not due to the registration process itself but were likely caused by external factors beyond our control. Our experimental field was also used for other studies involving autonomous robot navigation, and

areas with heavy foot and tractor traffic seemed to impact the soil around the spheres, causing the structures to shift.

To address this issue, we proposed an innovative approach that relies solely on the collected data for registration, reducing dependence on artificial targets and minimizing the impact of such external factors. By not relying on physical markers that can be displaced, our approach maintains accuracy over long periods and in environments subject to change. This flexibility makes it especially suitable for dynamic field conditions where traditional fixed targets might fail to provide consistent accuracy. This streamlines field setups and ensures consistent and reproducible results.

Our approach has demonstrated effectiveness in overcoming these challenges, offering an accessible and robust methodology for TLS-based phenotyping in dynamic field environments. Unlike approaches requiring continuous acquisition for ensuring common features for registration (Y. Li, Wen, et al., 2023), our multi-step TLS data alignment leveraged invariant elements naturally present in the collected point clouds to roughly align them. This allowed us to decouple the registration process from changing elements such as the crop, facilitating the registration of point clouds collected at distant time intervals. The observed registration errors, comparable to expected errors in rigid registration at the organ level (Chebrolu et al., 2021) and falling within the range of RMSE values for height estimation, indicate the accuracy of our approach in capturing time-series TLS data. This highlights the potential of our method for LiDAR-based crop phenotyping under dynamic field conditions.

5.4.3 Challenges in Growth Modeling for Crop Breeding

Understanding the growth patterns of cotton plants is essential for effective crop management and informed breeding strategies (Ritchie et al., 2007). Cotton plant development typically follows a sigmoid function, characterized by slow initial growth during establishment, followed by exponential vegetative growth that gradually slows as the crop approaches canopy closure (Snider et al., 2021). Growth modeling plays a key role in estimating key parameters defining these growth curves (Gregorczyk, 1998), providing a systematic approach to incorporate insights into crop phenotyping (Costa et al., 2019).

Growth modeling from field data can be challenging, and many of the growth parameters extracted with our methodology could not be obtained any other way on a large scale. Focused on the analysis of three key morphological traits, CH, CA, and CV, across diverse cotton genotypes, our study unraveled the dynamics of cotton growth and the relationships between growth parameters, providing valuable insights for genotype selection tailored to specific requirements. However, fitting maximal models with all random effects may fail to converge because the random effects structure has a complexity not supported by the underlying data (Barr et al., 2013). Simplification of the random effects structure can help the model to converge (Bates et al., 2015).

Trade-offs are often necessary due to computational limitations and the need for efficient model fitting (McCrea et al., 2023). Challenges may arise across the data analysis pipeline, including processing, model development, and information extraction. Fitting maximal models that include all random effects in growth parameters can face convergence challenges due to the complexity of the random effects structure (Barr et al., 2013). Our study revealed that growth rate could be one

of the most complex parts of the random effects structure for crop growth modeling. Primarily, we dropped covariance terms for some of the random effects, as suggested in one paper (Seedorff et al., 2019) to try to achieve convergence. However, it was not sufficient for our model to converge, and we opted for a more drastic approach of fixing the growth rate for all the genotypes, removing the slope entirely, in order to reduce the complexity of our model. This led us to simplify the model by fixing the growth rate for all genotypes, emphasizing the importance of balancing model complexity and convergence (Bates et al., 2015).

5.4.4 Limitations and Future Works

The adaptability of TLS technology to capture 3D structural information makes it inherently suitable for studying a wide range of plant species. While our methodology has demonstrated effectiveness in a cotton breeding field, highlighting its potential application in similar agricultural contexts, its generalizability across diverse crops and environmental conditions remains to be fully explored.

Additionally, uncertainties in the use of estimated CV as a proxy for estimating canopy light interception should be acknowledged. Variability in environmental conditions can affect the accuracy of IPAR_f measurements and validating its relationship with our CV estimation method warrants further research. Understanding these uncertainties is key for enhancing the reliability and applicability of our methodology across different agricultural settings.

Further experimentation across different field settings is imperative to comprehensively assess the adaptability and generalizability of our methodology. Expanding these efforts to accommodate various research environments will be key to establishing a scalable methodology for consistent field phenotyping over time. Understanding how factors such as canopy structure, plant density,

and environmental influences interact with our methodology is crucial for evaluating its scalability and robustness across different crop types and field conditions. Our initial findings indicated that our methodology could create accurate 4D crop models under conditions of minimal plant overlap. However, maintaining model accuracy became challenging as canopy density increased. Different crop types may require tailored strategies for BEV-based alignment due to their unique growth characteristics. For example, maize plants, which are individually planted and in early stages may project only a small footprint, may require a more precise clustering process. Similarly, densely planted crops like wheat can introduce additional complexities in data interpretation and analysis.

Despite the effectiveness and accuracy achieved in our cotton field, challenges such as laser beam shadowing and occlusions were not entirely eliminated, particularly in advanced growth stages. These issues are common in many remote and proximal sensing studies conducted in the field, demanding further research for resolution. The complex structure of crops like cotton poses a challenge, where increasing the number of scan locations for multi-scan TLS-based field analysis may not completely eliminate occlusion effects. Striking a balance between the need for more scans and efficient resource utilization, including time and computing power, necessitates thorough site studies for TLS site planning to optimize data collection. We are actively exploring the potential of physics-based simulators for knowledge-guided TLS site planning. These simulations can provide valuable insights into the optimal distribution of scan locations, especially in complex field environments, enhancing the efficiency of TLS-based field phenotyping.

Moreover, the increased number of scan locations introduces new challenges, particularly in terms of time consumption and logistics. Traditional practices for LiDAR-based scanning involve manually moving the scanner from one scan location to another, contributing to the time-intensive

nature of data collection. In a prior study, we demonstrated the potential use of a ground robot to automate TLS data acquisition in a breeding field (Rodriguez-Sanchez & Li, 2022). We are working on improving this system to autonomously determine the number of scans and their distribution throughout the field, thereby fully automating the TLS-based phenotyping process. This work is currently under review in a reputed journal, and a preprint is available on arXiv (Rodriguez-Sanchez et al., 2024). This innovative approach aims to enhance the efficiency of TLS data collection for plant breeding, streamlining the phenotyping workflow and aligning with broader trends in automation and robotics within the field of agriculture.

5.5 Conclusions

In this study, we introduced an innovative methodology for precisely registering point clouds collected under field conditions, enabling LiDAR-based crop phenotyping over time. This work emphasizes the critical importance of precise point cloud data collection, accurate registration, and precise modeling for TLS-based field phenotyping. Our two-phase TLS data registration approach has demonstrated its effectiveness in aligning point clouds captured up to two months apart during the vegetative growth season, significantly reducing alignment errors. By leveraging terrain points and crop row distribution, our method provides a reliable and efficient solution for monitoring crop morphological growth, enabling breeders to consistently acquire accurate phenotypic traits from the same physical locations at different time points.

As digital technologies advance, the refinement of current procedures for in-field data collection and processing will strengthen our ability to enhance crop improvement in a more efficient manner.

Despite challenges such as late-season occlusions, our approach presents a promising solution to enhance cotton breeding programs by offering a reliable digital approach to monitor traits over time. It provides a foundation for informed decision-making and genotype selection based on desirable growth characteristics. The findings of this study can contribute significantly to understanding cotton plant growth and genotype variations, offering valuable insights for optimizing cotton crop management and advancing plant phenomics.

CHAPTER 6

A GROUND MOBILE ROBOT FOR AUTONOMOUS TERRESTRIAL LASER SCANNING-BASED FIELD PHENOTYPING[1]

[1]Javier Rodriguez-Sanchez, Kyle Johnsen, and Changying Li. Submitted to *Journal of Field Robotics*, 07/25/23.

Abstract

Traditional field phenotyping methods are often manual, time-consuming, and destructive, posing a challenge for breeding progress. To address this bottleneck, robotics and automation technologies offer efficient sensing tools to monitor field evolution and crop development throughout the season. This study aimed to develop an autonomous ground robotic system for LiDAR-based field phenotyping in plant breeding trials. A Husky platform was equipped with a high-resolution three-dimensional (3D) laser scanner to collect in-field terrestrial laser scanning (TLS) data without human intervention. To automate the TLS process, a 3D ray casting analysis was implemented for optimal TLS site planning, and a route optimization algorithm was utilized to minimize travel distance during data collection. The platform was deployed in two cotton breeding fields for evaluation, where it autonomously collected TLS data. The system provided accurate pose information through RTK-GNSS positioning and sensor fusion techniques, with average errors of less than 0.6 cm for location and 0.38° for heading. The achieved localization accuracy allowed point cloud registration with mean point errors of approximately 2 cm, comparable to traditional TLS methods that rely on artificial targets and manual sensor deployment. This work presents an autonomous phenotyping platform that facilitates the quantitative assessment of plant traits under field conditions of both large agricultural fields and small breeding trials to contribute to the advancement of plant phenomics and breeding programs.

6.1 Introduction

Plant phenotyping has become a pivotal practice in breeding programs, enabling breeders to assess plant traits across diverse environments and over extended periods (Großkinsky et al., 2015). Field

evaluation of these traits plays an important role in developing varieties with enhanced quality, yield, and stress tolerance for targeted locations (Goggin et al., 2015). However, traditional methods for quantifying plant functional traits under field conditions rely on labor-intensive manual measurements and destructive sampling. This not only limits the number of plants that can be assessed but also impedes the scalability of breeding programs (Bowman et al., 2004), presenting a significant bottleneck for breeding progress (Araus & Cairns, 2014). The development of innovative methodologies to automate in-field phenotyping tasks holds the potential to significantly streamline the process and accelerate crop improvement.

Over the past few decades, progress in remote and proximal sensing has significantly contributed to the development of state-of-the-art methods for collecting and processing in-field crop data. These modern techniques, incorporating imaging sensors and three-dimensional (3D) technologies, allow the creation of realistic crop models, enabling the extraction of precise morphological traits to estimate crop growth and productivity (Su et al., 2019). Among the numerous 3D imaging technologies available, light detection and ranging (LiDAR) scanners have emerged as widely utilized tools for field-based phenotyping. LiDAR scanners employ laser beams that can pass through openings in the foliage, surpassing the capabilities of alternative technologies at sensing depth. The measurements obtained from LiDAR scanners exhibit remarkable accuracy and repeatability (Madec et al., 2017). Moreover, LiDARs demonstrate reduced reliance on illumination conditions compared to other sensor types (Hosoi & Omasa, 2009), making them particularly well-suited for field operations.

Terrestrial Laser Scanning (TLS), a technique that utilizes ground-based laser scanners to capture highly accurate and comprehensive 3D data, stands as one of the most prominent LiDAR-based

methods for vegetation monitoring (Jin, Sun, et al., 2021). To mitigate occlusions and improve laser coverage, LiDAR scans are typically performed from multiple locations across the field, known as multi-scan TLS (Fang et al., 2020). However, the implementation of multi-scan TLS can be both time-consuming and labor-intensive. Traditionally, operators manually carry the LiDAR scanner between different scan locations. Furthermore, to achieve precise co-registration of individual scans, the deployment of artificial targets as common reference points is necessary (Friedli et al., 2016). Depending on the field dimensions and the scanner's specifications (e.g., angular resolution and range), a considerable number of scan locations and artificial targets may be required (S. Sun et al., 2021). This can significantly hamper the efficiency of the phenotyping process and impose restrictions on the number of plants that can be scanned in each session. Therefore, strategic approaches for survey planning are essential to ensure the execution of efficient field phenotyping tasks, particularly in breeding fields where occlusions can have a substantial impact.

Site planning plays a crucial role in ensuring an effective TLS survey. The planning process for a TLS survey involves identifying the optimal set of scan locations and strategically distributing them throughout the field to acquire comprehensive and accurate crop information. For field phenotyping, recent studies have implemented empirical strategies based on trial and error to determine the most suitable scan locations (T. Guo et al., 2019). While these methods can be effective in relatively small and straightforward scenarios with minimal anticipated changes in the crop, they prove impractical and inefficient for a typical breeding field with hundreds or thousands of crop plots. Informed decisions based on analytical methods are necessary to optimize the distribution of scan locations, overcoming limitations and ensuring the generalizability of the approach across various field layouts. The integration of robotic technologies with optimized TLS methods offers a promising solution

to standardize field phenotyping procedures, reduce dependence on human labor, and improve the throughput of in-field phenotyping tasks, contributing to the advance the field of plant phenomics.

The primary goal of this study was to develop an autonomous robotic system for TLS-based field phenotyping. The study aimed to accomplish the following specific objectives: (1) integrate a high-resolution 3D LiDAR with a ground robot for autonomous data collection in the field; (2) develop a computer-based approach to optimize the distribution of scan locations for TLS site planning; (3) implement an optimal route planning algorithm for efficient field navigation between scan locations; and (4) conduct field experiments to evaluate the system's performance in multi-plot cotton breeding fields.

The paper is structured as follows: Section 2 provides an extensive review of the various approaches employed in LiDAR-based field phenotyping over the past decade. Section 3 covers the design of the robotic system, addressing both hardware and software aspects. Section 4 delves into the automation of TLS-based field scanning for plant phenotyping. Section 5 presents the experimental plan and details the fields that were utilized for field testing. Section 6 provides a detailed analysis of the results obtained using the developed system. Finally, Section 7 and Section 8 present future research directions and the main conclusions derived from this study.

6.2 Related Work

The emergence of applications based on 3D imaging technologies for plant phenotyping has contributed to increasing the understanding of plant-environment interactions. Canopy architecture is closely related to crop growth rate and yield (Nobel et al., 1993) and investigating of this trait is key

to identifying those genotypes that ultimately generate a substantial gain in commercially valuable traits (Kumar et al., 2015). However, canopy architecture shows complex spatial and temporal relations that are difficult to estimate (Jin, Sun, et al., 2021). 3D technologies allow the creation of realistic crop models that can be used to extract morphological characteristics of plants over the season for the estimation of crop growth and productivity.

6.2.1 Use of LiDAR for Field Phenotyping

In recent years, there has been a significant increase in the application of 3D imaging approaches to analyze plant architecture. This growth can be attributed to the continuous improvement of optical sensors and advanced data processing pipelines. Techniques like structure from motion and laser scanning, originally used in more mature fields such as architecture and engineering, have now been adapted to agricultural settings, sparking interest in 3D crop analysis within the plant science community (Paulus, 2019).

LiDAR has become an important technology for plant phenotyping, offering accurate models of crop structures and enabling the extraction of plant traits related to growth and yield. Operating on the principle of lasers emitting pulses, LiDAR scanners acquire spatial information from the environment in the form of point clouds—a discrete set of data points in 3D space (Vosselman & Maas, 2010). Over time, laser sensors have evolved, becoming more affordable, and the methodologies for processing the point clouds have improved, leading to a progressive increase in the throughput and spatiotemporal resolution of LiDAR-based plant phenotyping systems (Jin, Sun, et al., 2021). LiDAR data has been used to estimate canopy-level information for crops like wheat and rice (Hosoi & Omasa, 2009, 2012), determine biomass at the plot level for maize (Jin et al., 2020),

and extract plant-level architectural traits under field conditions (Gage et al., 2019). Additionally, high-resolution LiDAR scanners have enabled detailed morphological analysis at the organ level for various plant species, including barley (Paulus et al., 2014), maize (Jin et al., 2019), sorghum (Malambo et al., 2019), and cotton (S. Sun et al., 2021). However, challenges for LiDAR-based field phenotyping persist, including the need for high-quality data and appropriate data processing methodologies (Jin, Sun, et al., 2021).

Different deployment methodologies have been implemented for LiDAR-based field phenotyping. The most widely used approaches include mobile laser scanning (MLS) and terrestrial laser scanning (TLS) techniques. MLS approaches involve carrying the LiDAR sensor through the field to capture laser data. These systems have been implemented using various carrier platforms such as backpacks or wearable devices (Y. Jiang et al., 2019; Y. Zhu et al., 2021); gantry systems (Beauchêne et al., 2019; Q. Guo et al., 2018; Virlet et al., 2016), or cable-driven platforms (Bai et al., 2019); as well as mobile vehicles, including self-propelled machines (Ehlert et al., 2010; Llorens et al., 2011; Rosell Polo et al., 2009; Saeys et al., 2009; S. Sun et al., 2018; Wang, Singh, et al., 2018), or custom-made buggies and Phenomobiles (Deery et al., 2014; Jiménez-Berni et al., 2018; S. Liu et al., 2017; Madec et al., 2017; J. Walter et al., 2019; Yuan et al., 2019). However, MLS faces challenges associated with capturing data while in motion, which can result in limited accuracy and resolution. Robust and precise location information is crucial to ensure proper registration and alignment of the collected point clouds. Additionally, the potential influence of vehicle vibrations can affect the quality of the collected data (Xu & Li, 2022b), particularly when capturing fine details or objects with small-scale features.

TLS-based approaches, on the other hand, rely on the stationary position of the LiDAR scanner during the scanning process. TLS systems excel in providing detailed and accurate point cloud data, capturing fine-scale details of plant structures with high resolution. In addition, the portable nature of TLS scanners allows for relatively easy movement between scan positions, enabling *in situ* surveys without the need for specialized platforms. Although the throughput of TLS systems can be lower than MLS approaches, their capabilities make TLS a valuable approach for vegetation monitoring (Calders et al., 2020).

6.2.2 Current Methods for Terrestrial Laser Scanning in Field Phenotyping

While TLS has been widely used in forestry in the last two decades (Calders et al., 2020), its application for crop phenotyping under field conditions is relatively recent. Some studies have successfully applied TLS from only one fixed location (single-scan mode) to estimate height estimation and tracking crop growth (Crommelinck & Höfle, 2016; Eitel et al., 2016; Malambo et al., 2019). However, the most widely used methodology for TLS-based surveying in agriculture is collecting point clouds from different locations across the field (multi-scan mode) to improve point coverage. Multi-scan mode provides more detailed data and can compensate for occlusion-induced shadowed regions. This mode has been employed to measure growth patterns for various crops (Eitel et al., 2014; El-Naggar et al., 2021; Fang et al., 2020; Friedli et al., 2016; T. Guo et al., 2019; Hämmerle & Höfle, 2014; Hoffmeister et al., 2013; Jin et al., 2018, 2019, 2020; Kirchgessner et al., 2016; Koenig et al., 2015; P. Li et al., 2020; C. Lin et al., 2022; Qiu et al., 2019; Su et al., 2019; S. Sun et al., 2021; Tilly et al., 2015). However, the lack of efficient methodologies for in-field data

collection may be delaying the adoption of these kinds of technologies to its full potential for plant phenotyping (Watt et al., 2020).

The use of robotics for automating TLS data collection in plant phenotyping is an area that has received limited attention in research. Only a couple of studies have investigated this topic. Qiu et al., 2019 conducted a study using a custom-made robotic platform to collect multi-scan TLS data autonomously in a maize field. However, the choice of scan locations was constrained to a paved road running parallel to the field. This limitation led to a restricted field of view for the scanner, resulting in occlusions and subsequent inaccuracies. In one of our previous studies (Rodriguez-Sanchez & Li, 2022), we demonstrated an autonomous robot for multi-scan TLS under field conditions. Although we were able to mitigate the occlusion problem, our study highlighted certain limitations on the placement of scan locations to maximize field coverage that can be further improved.

The findings highlight the importance of strategically planning scan point locations in TLS surveys for effective plant phenotyping, particularly in breeding fields characterized by significant occlusion due to adjacent rows of plots. Overcoming these challenges and enhancing survey efficiency require further advancements in optimizing scan locations to maximize field coverage and address occlusion-related issues. The integration of robotic systems for TLS data collection together with strategic site planning algorithms holds promising potential for improving the accuracy and efficiency of plant phenotyping tasks, ultimately contributing to advancements in plant breeding.

6.2.3 TLS Site Planning Approaches for In-field Phenotyping

Before conducting a TLS survey in the field, a series of steps must be undertaken to ensure its success. These steps involve studying the project area needs to identify factors that may cause loss of information, such as obstructions or limited range that can result in shadows or voids in the point clouds. This process can be time-consuming, necessitating prior survey planning to optimize TLS operations.

The planning of a TLS survey involves identifying the optimal set of scan locations and their distribution within the scene to capture complete information from the target objects. Two methodologies can be found in the literature to determine the best set of scan locations: empirical approaches and computational and data-driven approaches. Empirical approaches involve using real laser scanners to collect TLS data from predefined locations. For example, O'Banion and Olsen, 2019 proposed an empirical TLS planning tool for earth surface modeling. The tool provided estimates of the minimum number of scans and optimal resolution needed, based on a database of previously collected point clouds. Similarly, T. Guo et al., 2019 employed an empirical approach for field phenotyping, comparing different scanning strategies to determine the optimal TLS layout for plant height estimation in a wheat crop. Their results suggested that surveying the field from the four corners was the optimal configuration. However, these findings might not generalize easily to other more complex crops or field layouts. Empirical methods can be useful in relatively small and simple scenarios with stable target objects, but they become inefficient for large breeding fields with numerous crop plots or when tall and dense crops increase the risk of occlusions.

Computational and data-driven methods utilize digital models of the scene and computational techniques like ray casting (Amanatides & Woo, 1987) to evaluate visibility from every possible scan position. For instance, Mozaffar and Varshosaz, 2016 presented an iterative algorithm that employed ray tracing for line-of-sight analysis to minimize the number of TLS survey points needed to cover an outdoor area. Starek et al., 2020 used a similar approach for terrain mapping in an agricultural field, utilizing a simulated annealing algorithm to maximize coverage with the minimum number of scan locations. Computational methods provide efficient computations of visibility but require prior models of the scene, and they may face challenges when significant changes occur during the growing season.

In recent developments, more advanced techniques based on computer-aided design (CAD) models have emerged, aiming to calculate ray-environment interactions in complex 3D environments. These techniques leverage the concept of 'slabs' to define the bounding volumes of objects within the scene. A 'slab' is a space bounded by two parallel planes (Kay & Kajiya, 1986), and the intersection of sets of bounding slabs allows for the efficient definition of any bounding volume. Building upon this idea, Smits, 1998 proposed a method to effectively reduce computation resources and improve scene rendering using the slab formulation. Despite the potential advantages, these techniques have seen limited application in TLS layout analysis and, to the best of our knowledge, have not yet been employed in the context of TLS site planning for high-throughput phenotyping.

In this study, we report the first fully autonomous phenotyping platform capable of conducting multi-scan TLS from various locations around and inside the crop for field phenotyping purposes. We employed advanced computational approaches using slab formulation to identify the optimal set of scan locations that ensure an adequate LiDAR coverage of the crop. By integrating this

information into the decision-making pipeline for field data collection, we were able to identify the optimal navigation path for field scanning, thereby increasing the efficiency and autonomy of the TLS data acquisition platform in the field.

6.3 Robotic Platform

In the envisioned autonomous system for LiDAR-based field phenotyping, a robotic platform is in charge of positioning the laser scanner on sufficient scan locations through the field to collect point clouds efficiently. The autonomous phenotyping platform was subdivided into three main constructive blocks: a control module to manage the global operation of the platform, a plant phenotyping module to collect 3D LiDAR data from the crop canopy, and a localization and navigation module to acquire location information and guide the platform to planned scan locations during the mission. Figure 6.1 shows a block diagram with the main hardware components. The system was integrated under the robotic operating system (ROS) framework to allow for the standardization of methodologies and reduce downtime when different phenotyping tasks are required.

6.3.1 Control Module

The control module integrated a series of off-the-shelf hardware devices and software modules to manage the operation of the phenotyping system. This module was composed of a Husky A200 robotic platform (Clearpath Robotics Inc., Ontario, Canada). This robotic platform is a rugged four wheeled skid-steering unmanned ground vehicle (UGV) with dimensions of 990 $\times$ 670 $\times$ 390 mm (L $\times$ W $\times$ H) and a weight of 50 kg. The platform can carry up to 75 kg and has a maximum speed

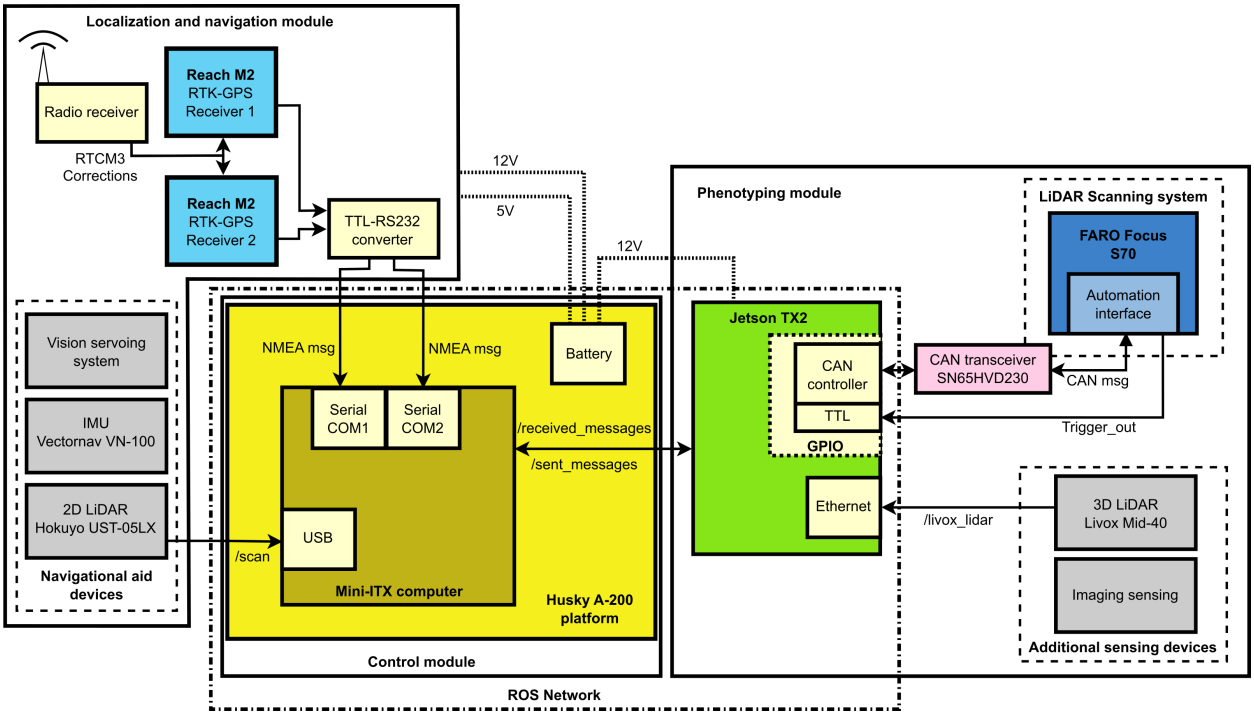

Figure 6.1: Modular block design for the autonomous phenotyping platform. Colored boxes indicate the main components of each module. Gray boxes indicate additional equipment that could be added to the platform.

of 1.0 m/s. At the software level, the control module is hosted by a mini-ITX Singleboard Computer System, 2.7 GHz Intel i5-4570TE, with 8 GB RAM and 120 GB SATA2 SSD drive. The control interface, controller manager, and hardware interfaces were integrated under the ROS framework to ensure the interoperability of all its components and the integrity and availability of the data at any given time. The Husky ran ROS Kinetic Kame as the ROS master and included the common ROS packages available at https://github.com/husky/husky.

6.3.2 Phenotyping Module

The phenotyping module was composed of a FARO Focus 3D S70 laser scanner (FARO Technologies, Florida, US). This device is a high-resolution 3D LiDAR scanner with a detection range between 0.6 meters and 70 meters and a field of view of 300° vertically and 360° horizontally. The angular resolution is configurable between step sizes of 0.009° and 0.288°, which is equivalent to a point distance of 1.5 mm and 49.1 mm over 10 m, respectively. This scanner has built-in sensors, such as a dual axis compensator (inclinometer), that can provide additional information for data post-processing. An automation interface adapter (part number: ACCSS8004) was attached to the laser scanner and provided a Controller Area Network (CAN) interface for remote control.

To control the scanner under the CAN protocol, predefined messages were used. The CAN message format followed the CAN 2.0A standard with an 11 bit identifier (CAN ID) and up to 8 bytes of data. The CAN ID field is used as a command key and the data field is used to set the associated parameters for each command key. By complying with the CAN bus specification, the scan data recording can be enabled by the predefined CAN message "Initiate Scan Operation." The scan data recording can be paused and stopped by the messages "Record/Pause" and "End Scan Operation," respectively. Under CAN control mode, the scanner returns general acknowledgment messages (ACK) after the reception of each command (FARO Technologies, 2020). In addition, the automation interface provides two real-time capable transistor-transistor logic (TTL) signals for synchronization, identified as $trigger_{in}$ and $trigger_{out}$. The $trigger_{in}$ signal supports the integration of time stamps into the CAN messages and the enabling or pausing of the scan data stream recording.

The $trigger_{out}$ signal triggers outgoing CAN messages, emits synchronization pulses during mirror rotation, and can be used to check the current automation status by the signal level.

The FARO LiDAR was interfaced with the ROS network using CAN bus through a Jetson TX2 Developer Kit module (Nvidia Corporation, California, US) that was integrated under the ROS network and was used as the CAN interface controller. The Jetson TX2 module had Ubuntu Bionic Beaver (18.04) installed and ran ROS Melodic Morenia as a slave machine. A CAN board (Waveshare Electronics, Shenzhen, China) based on the SN65HVD230 CAN transceiver was used to interface the single-ended logic used by the CAN controllers at both ends of the bus with the differential signal transmitted over the CAN bus. The components were integrated into ROS using the *socketcan_brige* ROS package and *CANopen* communication protocol. The Jetson TX2 received actuation orders from the control module and published the CAN messages to actuate the laser scanner. The robotic platform was able to autonomously start the scanning operation of the LiDAR, stop the current scanning, and monitor the status of the scanning process during data collection. This allowed the robot to fully automate the LiDAR data collection process and control the timings for navigating between scan locations.

6.3.3 Localization and Navigation Module

For field navigation, the robotic system used real-time kinematic (RTK) positioning based on the global navigation satellite system (GNSS) to obtain robot's location information. RTK-GNSS provides readings with centimeter-level accuracy in both horizontal and vertical dimensions, with the vertical accuracy typically less precise than the horizontal accuracy. This high precision is achieved through the transmission of positioning corrections from a fixed base station to a mobile

rover. To estimate the orientation of the platform during navigation, a GNSS compass technique was implemented using two GNSS receivers (i.e., rovers). This technique uses information from two receivers rigidly mounted at a fixed distance with respect to each other (i.e., compass baseline) to determine the platform heading. The use of two GNSS antennas providing absolute positioning information allows the estimation of the heading angle (ψ) that defines the direction of movement of the platform at any given time.

The GNSS receivers provided absolute location information in the form of geographic coordinates (longitude, latitude, and altitude). These global coordinates can be transformed to local coordinates such as the LiDAR scanner or the rovers, by applying the adequate homogeneous transformation matrix (i.e., rotation and translation). In a general form, on a 3D Euclidean space, transformations between a global coordinate system (G) and any arbitrary local coordinate system (L) can be computed using homogeneous transformations to account for the translation and rotation of the coordinate systems as follows:

$$\begin{bmatrix} X_G \\ Y_G \\ Z_G \end{bmatrix} = \begin{bmatrix} \Delta_x \\ \Delta_y \\ \Delta_z \end{bmatrix}_{G \to L} + R_L^G(\phi, \theta, \psi) \times \begin{bmatrix} X_L \\ Y_L \\ Z_L \\ 1 \end{bmatrix} \tag{6.1}$$

where X_G, Y_G, and Z_G are the coordinates of the point in the global coordinate system; X_L, Y_L, and Z_L are the coordinates of the origin of the local coordinate system in the global frame; R represents a 3D rotation matrix expressed by the basic rotations about each one of the axes (x-,

y-, z-axis) of the coordinate system; and $[\Delta_x, \Delta_y, \Delta_z]$ is a vector that represents the displacement between the origins of both coordinate systems.

Figure 6.2 shows the different coordinate systems involved during robot navigation and the relationship of the angles that define the platform's 3D orientation with their respective axes under an ENU (East-North-Up) coordinate system. X_R, Y_R, and Z_R are the coordinates of the platform in the global coordinate system, which are coincident with the center of rotation of the robot. X_1, Y_1, and Z_1, and X_2, Y_2, Z_2 are the coordinates of the GNSS antennas ($Rover_1$ and $Rover_2$) in the global frame, respectively.

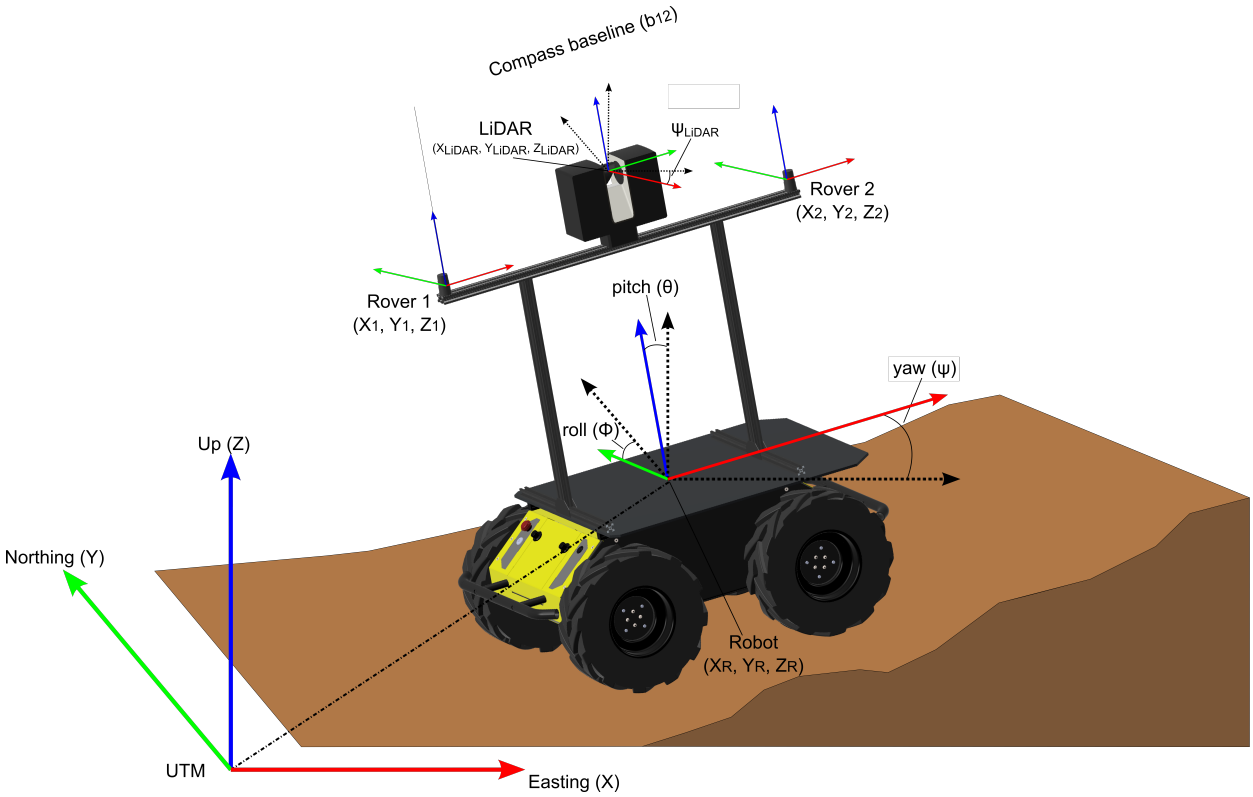

Figure 6.2: Coordinate systems for the phenotyping platform. Global (UTM) and local coordinate systems representation for major components of the robotic platform under an ENU (East-North-Up) coordinate system. Coordinate systems orientations on x-, y-,and z-axis are identified by red, green, and blue arrows, respectively. Dotted vectors indicate orientation of the global coordinate system at robot's origin.

Under this coordinate system, the heading angle of the platform will be given by the relationship between rover's X and Y coordinates as follows:

$$\psi = \arctan\left(\frac{Y_2 - Y_1}{X_2 - X_1}\right), \tag{6.2}$$

where $\psi \in [-\pi, \pi]$. It is worth noting that the signs of the numerator and the denominator in Equation (6.2) must be taken into account to place the heading angle in the right quadrant.

6.3.4 Phenotyping Robot Implementation

Hardware Components Integration

For our experiments, a GNSS antenna Smart6-L (Novatel Inc., Calgary, AB, Canada) was used as the base station (i.e., base). A FGR2-C radio receiver (FreeWave Technologies, Boulder, CO, USA) was in charge of broadcasting the RTK corrections from the base station. Both the GNSS and the radio antennas for the base station were placed on top of a 6 m post in an open space at approximately 400 meters from the fields under study. The rovers were configured to receive positioning corrections from the base using a shared FGR2-C radio receiver that was connected to a dual-channel MAX3232 RS232 to TTL transceiver breakout board (SparkFun Electronics, Boulder, Colorado) installed on the platform. The positioning system was configured to provide GPS-based pose readings at a rate of 10 Hz.

The robotic system mounted two RTK-GNSS antennas (*GNSS Ant.*$_1$ and *GNSS Ant.* $_2$) that were placed longitudinally on the platform in such a way that the baseline vector (i.e., the vector between the two antennas) was oriented towards the moving direction of the robot (Figure 6.3).

Each GNSS antenna receiver was composed of a Reach M2 multi-band RTK GNSS module (Emlid, Budapest, Hungary) that were attached rigidly to the robotic platform frame on the longitudinal axis. The GNSS receivers were installed at a height of 110 cm above ground, with the same physical orientation relative to each other. The baseline between antennas was fixed to 95 cm. Figure 6.3 shows the physical integration of all components of the phenotyping platform.

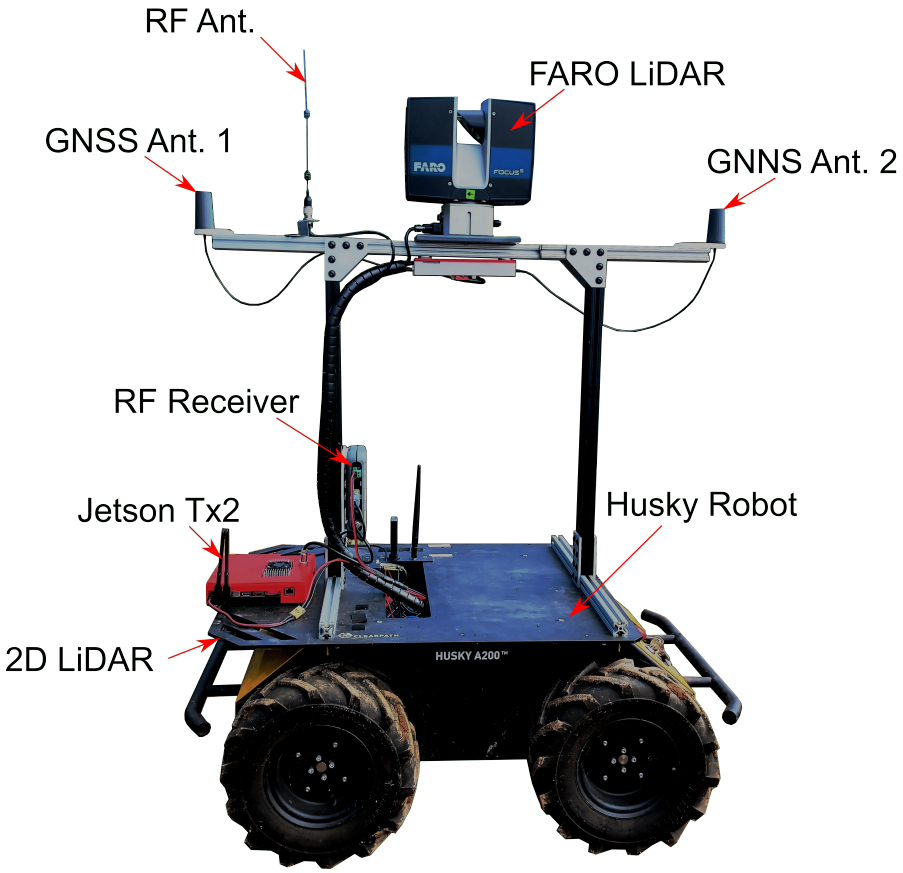

Figure 6.3: Autonomous phenotyping platform integration.

Navigation Stack

Path tracking involves the control problem that deals with the constraints of the robot movements and the timing during field navigation. Its solution provides actuation commands to follow the

adequate trajectory to reach each waypoint satisfactorily. The control module was in charge of reading the list of waypoints, computing the navigation path between waypoint pairs, and sending the adequate velocity commands to the actuators to follow the path. Our implementation of the ROS *navstack* (Figure 6.4) was based on the *robot_localization* package (Moore & Stouch, 2014). A single extended Kalman filter (EKF) instance was used to compute state estimates by fusing the odometry information provided by the wheel encoders together with the GNSS compass information provided by the dual RTK-GPS antenna system. In order to provide additional information to the navigation stack and to improve the in-field autonomous navigation, a Hokuyo UST-05LX 2D laser scanner (Hokuyo Automatic Co. Ltd., Osaka, Japan) was installed on the platform for obstacle avoidance. This sensor was integrated into ROS using the *urg_node* ROS wrapper for the Hokuyo *urg_c* library. This node supplied an obstacle layer to the navigation stack that was used to avoid colliding with elements placed directly in the robot's trajectory.

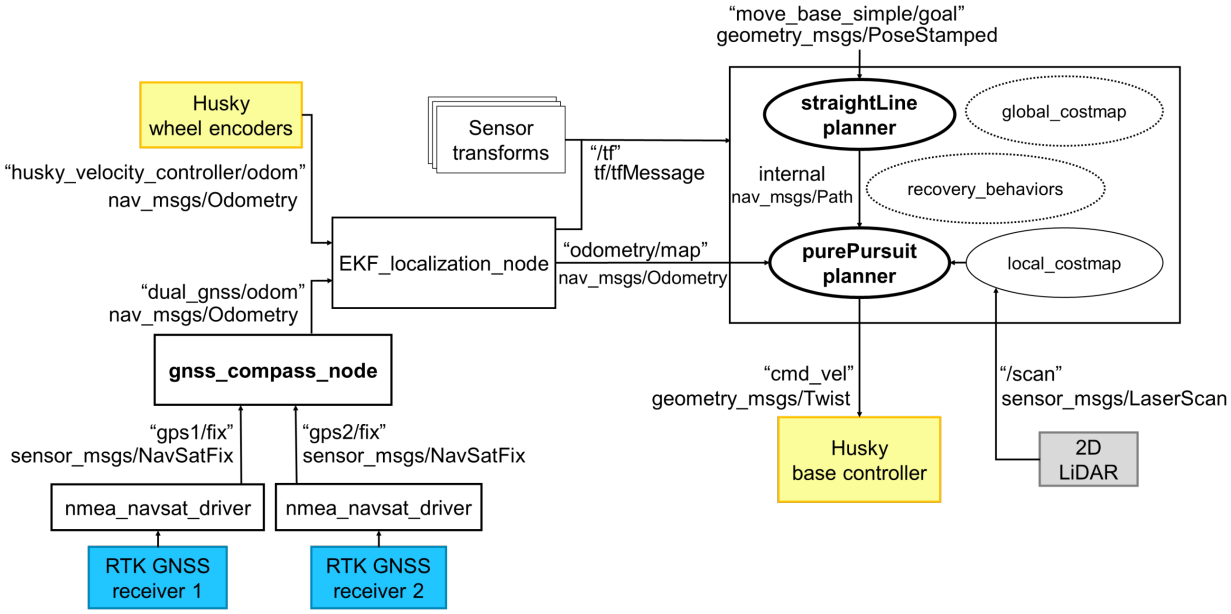

Figure 6.4: Navigation stack for the autonomous phenotyping platform.

6.4 Automation Workflow

To ensure that the data collected by the LiDAR scanner are suitable for plant breeding purposes, the system must guarantee that the point clouds of the crop are acquired with the adequate data quality, and within time limits. Unfortunately, there are still no standards that help define the minimum quality required for specific phenotyping tasks, and current TLS-based phenotyping studies base their survey planning on personal experience. Robotics and automation technologies can help standardize LiDAR-based field phenotyping tasks by performing efficient TLS surveys without human intervention. Our methodology to automate the TLS process using ground robots is composed of three main steps (Figure 6.5). First, the set of scan locations must be optimized to reduce the time needed to perform the TLS survey without losing important information from the crop. Second, the optimized set of scan locations needs to be converted to waypoints for the robot to be able to follow them during field navigation. Finally, the robotic platform needs to navigate the field in a reliable and efficient manner.

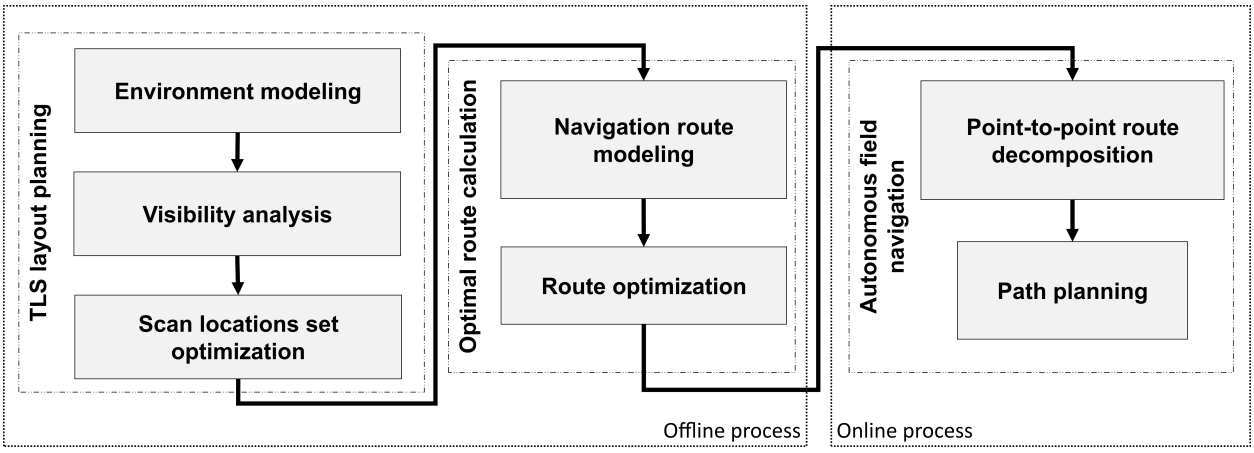

Figure 6.5: Terrestrial laser scanning automation pipeline. Overview of the proposed methodology for automating field-based plant phenotyping using TLS and robotics

6.4.1 TLS Layout Planning

Planning a TLS survey can be both challenging and time-consuming, especially when applied to plant phenotyping tasks, which introduces additional limitations. One important aspect to consider is that the accuracy of laser sensors tends to decrease as the distance to the target objects increases, potentially affecting the quality of the point clouds used for plant phenotyping. Furthermore, not all field locations where the scanner can be placed will provide the same level of detailed information about the crop due to occlusions. As a result, site planning becomes a key step for conducting an efficient TLS field survey. Identifying the most suitable set of locations for field scanning will significantly enhance the overall efficiency of the TLS survey, leading to more effective data collection and analysis.

Environment Modeling

The first step in identifying the optimal set of scan locations is to determine which positions in the field are suitable for placing the LiDAR scanner. Achieving this requires creating a model of the scene based on basic information about the field layout. Typically, in a breeding field, plots are planted in straight lines using agricultural machinery, forming long rows separated by alleys to divide blocks of different treatments (Figure 6.6). Additionally, the outer edges of the field (headlands) are left unplanted to ensure safe turns for farm equipment during field operations. Both the distance between rows (row spacing) and the alley width are configured according to breeders' specific needs, ultimately determining the arrangement of the plots in the field.

To model the crop, each plot in the field can be replaced by the imaginary rectangular parallelepiped that encloses its volume (i.e., bounding volume or bounding box) in such a way that they are oriented towards the row direction. This plot representation resembles the oriented bounding boxes (OBB) representation (Gottschalk et al., 1996). An OBB is a rectangular bounding box oriented arbitrarily in space. By choosing the coordinate system for the field in such a way that its axes are parallel to the faces of the bounding boxes, the field can be then modeled using the simplified axis-aligned bounding box (AABB) representation (Schneider & Eberly, 2002). An AABB is a subclass of OBB whose main axes are parallel to the basis vectors of the frame in which they're defined. Using this representation, each plot in the field will be represented by an AABB that can potentially intercept the LiDAR's laser beams (green rectangles in Figure 6.6).

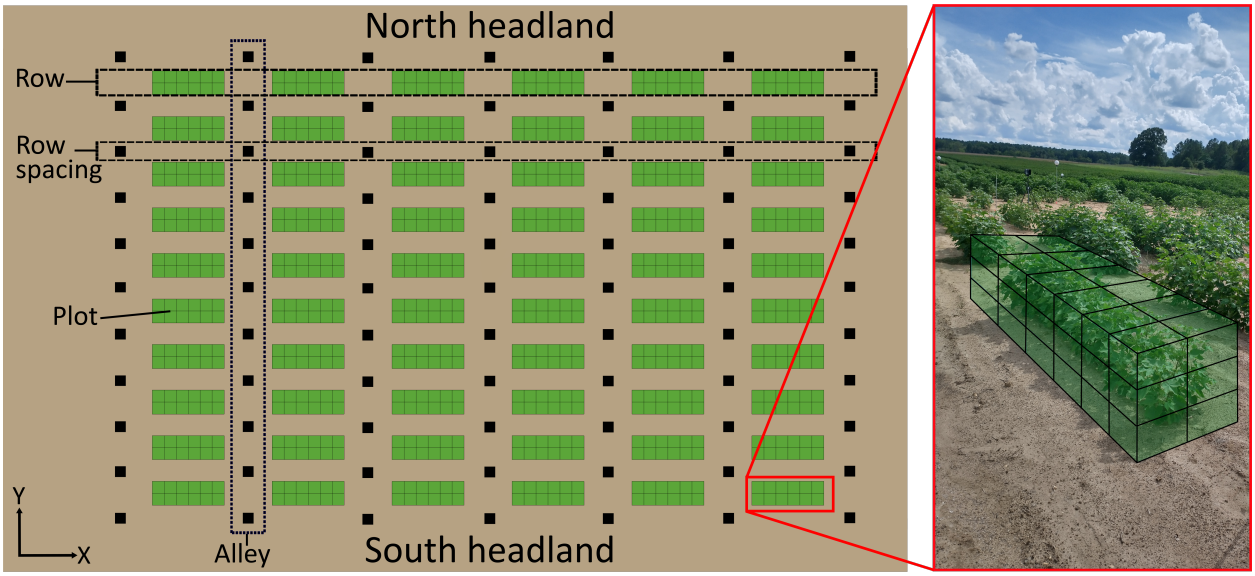

Figure 6.6: Layout of a typical plot-based breeding field. Green rectangles represent each plot in the field. Black squares represent potential scan locations. The zoomed-in inset on the right shows an example of discretization of one of the plots in the field.

The simple substitution of each plot on the field for its AABB will not allow us to accurately model the interaction of the laser beams with the crop. The footprint of these laser beams is usually small (in the order of mm), so the same plot will be potentially hit multiple times by a great number of different rays. Thus, a finer representation of the plots would be beneficial for modeling ray-crop interactions. Each bounding box can be further discretized using smaller cells or voxels. After some tests, we found that voxels of $0.5 \times 0.5 \times 0.33$ meters (length $\times$ width $\times$ height) for discretizing each AABB provided the best tradeoff between resolution and modeling time. For example, for a $3 \times 1 \times 1$ plot the mentioned cell division will translate into six cells on the longitudinal axis, two cells on the lateral axis, and three on the vertical axis. In total, each plot will be composed of 36 cells that can intercept rays (Figure 6.6 (inset)).

For TLS surveying for field phenotyping, any space not occupied by plants is deemed obstacle-free. While any unoccupied position in the field may appear suitable for scanner placement, certain considerations must be taken into account. Laser scanners have a minimum scan distance (typically ranging from 0.5 to 1 meter) below which accurate distance computation becomes challenging. Thus, the scanner must be positioned at a distance greater than this minimum from any adjacent plots to avoid measurement errors, especially beyond the seedling or first leaf growth stages. Due to this constraint, the space between neighboring rows cannot be considered as potential scan locations. Only alleys and headlands will meet the necessary distance requirement to enable precise LiDAR data collection. Therefore, only these areas should be regarded as obstacle-free spaces for scanner placement to ensure accurate TLS surveys in a breeding field.

Moreover, the use of a ground robot as the carrier for the LiDAR scanner imposes further limitations on the space that can be effectively used for in-field navigation. For a ground robot

to navigate the field safely, a minimum clearance with obstacles equivalent to its footprint (the effective area occupied by the robot platform while stationary) is needed. In breeding fields with a grid-like distribution of rows, alleys, and headlands, intersections between row spacing and alleys offer ample space for the robot to maneuver, allowing for smooth directional changes without causing damage to the crop. As a result, only these locations (black squares in Figure 6.6) will be used as potential positions for TLS placement without affecting the crops.

Visibility Analysis

The second step to optimize the TLS layout is to identify which parts of the crop are visible from each potential scan position. Following a line-of-sight (LOS) problem formulation (Koranne, 2009) with the LiDAR scanner being considered as the observer, we can identify which parts of the digitized crop are visible from each specific location using ray casting analysis (Appel, 1968).

The utilization of the slab method, as proposed by Smits, 1998, presents an efficient approach for calculating ray-box intersections within complex 3D environments. Unlike the general case where a ray might intersect all six planes defining the box, the slab method streamlines the computations to just three intersections: X, Y, and Z slabs. By taking advantage of the specific characteristics of the AABB representation, this reduction significantly speeds up the intersection tests. Figure 6.7 (a) shows the application of the slab method for two different rays on the XY plane.

Following the notation in A. Williams et al., 2005, the ray will intersect the bounding volume if both of the following conditions are met: $t_X min < t_Y max$ and $t_Y min < t_X max$. Here, $t_{i_{min}}$ and $t_{i_{max}}$ represent the closest and farthest points of intersection with the i-slab from the origin of the ray,

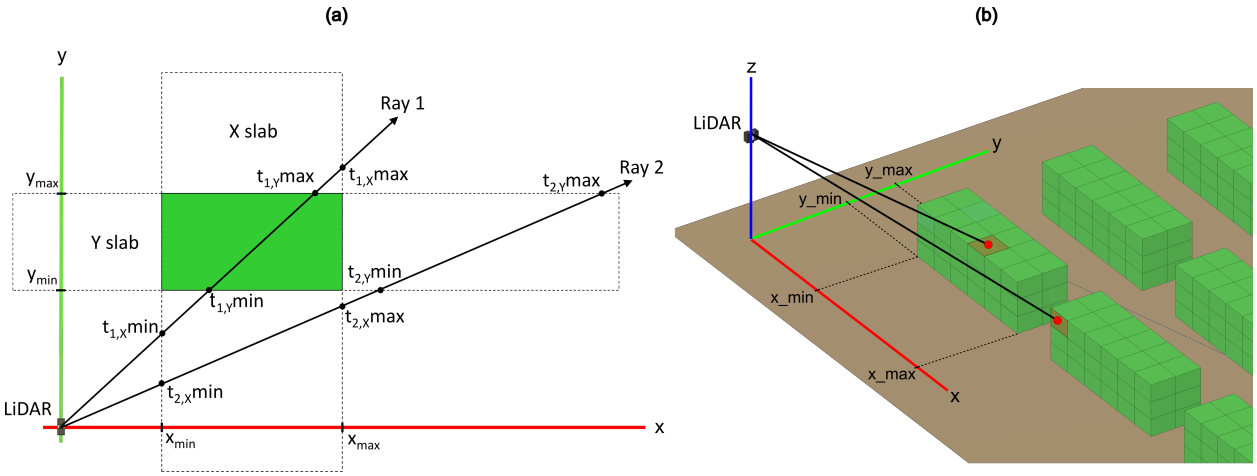

Figure 6.7: Computation of ray-AABB intersection using the slab method. (a) computation example on the XY plane for two rays. (b) cell visibility in the 3D space. Red dots show the impact point of each ray. Darker cells indicate cells visible from the scan location (visibility=1) for the specific ray.

respectively. Failure to satisfy any of these conditions will result in the ray not intersecting the slab and consequently missing the bounding volume.

If the ray intersects all three slabs, it also successfully intersects the box, leading to two intersection points——the entry and exit points of the ray. However, for visibility analysis, only the entry point is essential, as it determines which cell of the plot is visible from the current scan location (see Figure 6.7 (b)). To further optimize computation time, we also considered the hierarchical distribution of bounding boxes and cells. First, we evaluate whether the ray hits the plot level, and only if it does, we proceed to calculate the specific cell intercepted by the ray within the plot.

To conduct the visibility analysis for the entire field, from each scan location a set of laser beams is created according to the parameters of the scanner such as start and end angles, and vertical and horizontal angle steps (i.e., angular resolution). The start angle will determine the first ray direction. At every angle step, the ray casting algorithm will cast new rays and compute the intersections with

the bounding boxes in the digitized field. The ray casting algorithm will stop when the end angle is reached. This process is executed in an iterative fashion until all the scan locations in the field are visited.

By iterating over all the rays emitted from a particular scan location, we will obtain the entire field of view for said scan location. This field of view determines the cells' visibility from each specific scan location in the field. The visibility of a cell can be defined as the direct line of sight from a scan location, in such a way that a cell will be considered visible (visibility = 1) if it can be reached by any rays emitted from the scan location, or invisible (visibility = 0) if it is occluded and cannot be reached by any rays. Repeating this step for all scan locations, a visibility score table for the entire field can be created. This visibility score table will include a row for each scan location and a column for each plot cell on the field. For each iteration of the ray-box intersection algorithm, the table will be updated with the number of cells hit by the current laser beam.

Scan Locations Set Optimization

After computing the visibility score table, a greedy algorithm (Chvatal, 1979) was implemented to iteratively select the optimal or near optimal set of scan locations. The greedy algorithm is a polynomial time algorithm with several variants commonly used to approximate set-covering problems (Slavík, 1997). Algorithm 2 shows a basic pseudocode to implement the original variant.

Given a set U of m cells to be covered, a set V of n candidate scan locations or viewpoints, and a set C of p cells covered per each scan location, a visibility score list is created by aggregating the number of visible cells per scan location (Algorithm 2, lines 13 to 16). Then, the list is sorted in descending order according to the total number of visible cells per scan location to find the

viewpoint with maximum visibility (Algorithm 2, line 17). The first scan location of the list covers the largest number of elements in the scene, and the greedy algorithm chooses this viewpoint as one of the scan locations of the optimal set (Algorithm 2, line 18). Then, this viewpoint is removed from the table together with all the associated cells that are visible from it (Algorithm 2, lines 19 and 20). This process is iterated until all cells are covered.

Algorithm 2 Greedy selection of TLS scan locations.

1: **Input:**
2: Cells to be covered $U = \{U_k;\ k = 1,2,...,m\}$
3: Candidate scan locations $V = \{V_j;\ j = 1,2,...,n\}$
4: Cells covered per scan locations $C = \{U_{j,l};\ l = 1,2,...,p;\ p \leq m\}$
5: **Output:**
6: Optimal set of scan locations $S = \{S_i,\ i = 1,2,...,q;\ q \leq n\}$
7: Initialization:
8: $S = [\,]$
9: $V_{temp} = [\,]$
10: $U_{temp} = U$
11: $i = 1$
12: **while** $U_{temp} \neq [\,]$ **do**
13: **for** $j = 1,2,\ldots,n$ **do**
14: $vis(V(j)) = \sum_{l=1}^{m} C(j,l)$ ▷ calculate visibility score per scan location
15: $V_{temp}(j) \leftarrow [V(j), vis(V(j))]$ ▷ populate visibility list
16: **end for**
17: $V_{temp} \leftarrow sort(V_{temp})|_{Vis(V_{temp}))}$ ▷ sort list in descending order by visibility score
18: $S(i) \leftarrow V_{temp}(1)$ ▷ store first scan location
19: $U_{temp}(C(V_{temp}(1))) \leftarrow [\,]$ ▷ remove cells covered by the scan location
20: $V_{temp}(1) \leftarrow [\,]$ ▷ remove scan location from list
21: $i \leftarrow i + 1$
22: **end while**
23: return S

6.4.2 Optimal Route Calculation

Navigation Route Modeling

Once the optimal set of scan locations is determined, the robotic platform must visit each scan location to perform the TLS survey. In order to achieve that, the autonomous system needs to find a valid route to join scan location pairs by using the free space in the field. Using graph theory (Thulasiraman et al., 2016), the navigation problem can be modeled as a weighted connected undirected graph $G = (V, E)$ (Figure 6.8), where V is the set of vertices or nodes representing the scan locations, and E is the set of edges that connect the nodes, whose weight $w(e)$ is given by the distance between scan locations.

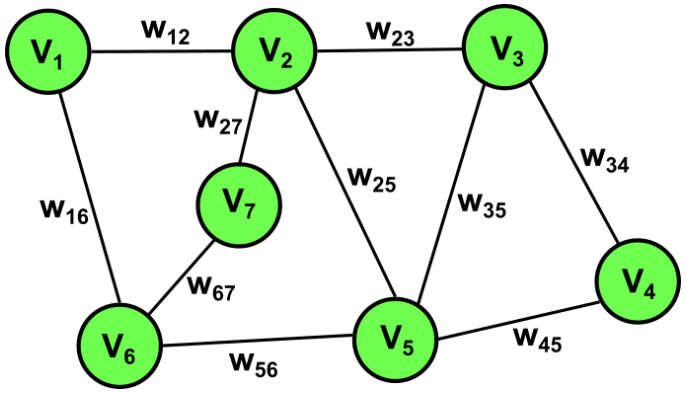

Figure 6.8: Weighted undirected graph for scanning route optimization. Vertices $(V_1, ..., V_7)$ represent the set of scan locations to visit. Edges weight $(w_{12}, ..., w_{67})$ represent the distance between scan location pairs.

The parameters of the crop such as plot length and width, row spacing, and alley width were used for field digitization. This information can also be used to calculate the weight of the edges of the graph for the routing problem. Assuming a perfectly flat field where the robot platform moves only on a two-dimensional plane, the distance *d(a,b)* between any two points *a* and *b* on this plane

located at coordinates $a = (a_x, a_y)$ and $b = (b_x, b_y)$ respectively, can be computed in a general form using the Minkowski distance:

$$d(a,b) = (|a_x - b_x|^p + |a_y - b_y|^p)^{1/p} \tag{6.3}$$

where p represents the order of the norm and determines the type of distance to be calculated.

Navigation in a crop field will be restricted to the free space (i.e., row spacing, alleys, and headlands). This free space will change through the season as plants grow and the crop evolves. Specifically, the row spacing is limited and may not be completely available during the entire season for robot navigation. That is specially the case when the crop reaches the canopy closure stage, where the space between rows will disappear. According to the growth stage of the crop, two different approaches can be used to calculate the distance between location pairs and give numerical values to each section of the route (Figure 6.9).

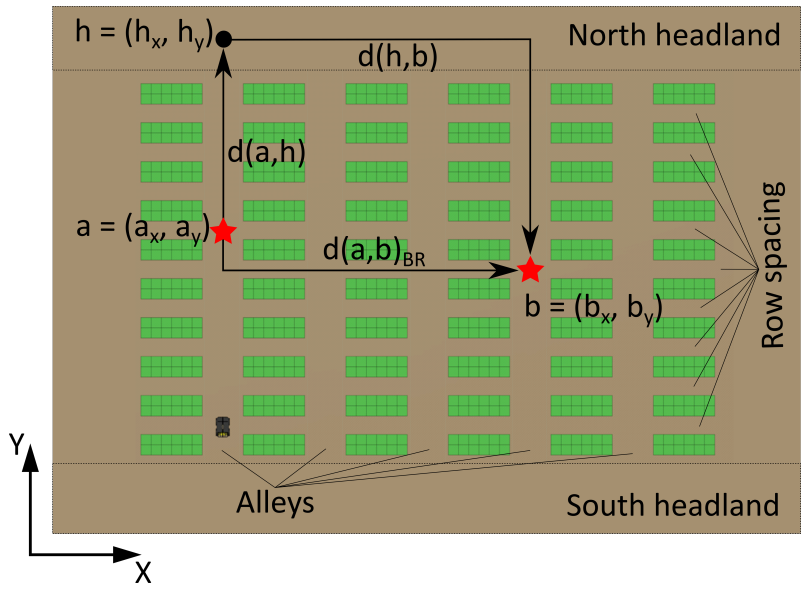

Figure 6.9: Approaches for computing distances between scan location pairs. Red stars indicate consecutive scan locations. Black arrows show the direction of the route for each approach.

In early crop growth stages, row spacing would potentially be accessible, and the robotic platform could safely navigate between rows (i.e., between-rows (BR_{nav}) navigation). Under this approach, the distance between scan location pairs can be computed as the L1 norm ($p = 1$) or Manhattan distance, sometimes also denoted as taxicab distance (Krause, 1986). This distance is equivalent to the distance measured along axes at right angles. Using Equation 6.3 with $p = 1$, the distance between two scan locations a and b at coordinates $a = (a_x, a_y)$ and $b = (b_x, b_y)$ will be given by:

$$d(a,b)_{BR_{nav}} = |a_x - b_x| + |a_y - b_y| \tag{6.4}$$

When the crop gets close to the canopy closure stage, robot navigability between the rows will be greatly impacted. Passing through the field using the row spacing without damaging the crop will not be possible. In this stage, only alleys and headlands will be available for the robot to navigate the field. Therefore, an alley-headland-alley (AHA_{nav}) approach must be used for navigation. Under this approach, the distance between scan location pairs can be computed by combining the L2 distance (Euclidean distance) to the nearest headland, and the Manhattan distance from the headland position to the next scan location. If we define an intermediate waypoint $h = (h_x, h_y)$ located at the headland in such a way that $a_x = h_x$, the distance between two scan locations a and b at coordinates $a = (a_x, a_y)$ and $b = (b_x, b_y)$ for the AHA_{nav} approach can be computed using the following equation:

$$d(a,b)_{AHA_{nav}} = d(a,h) + d(h,b) = \sqrt{(a_y - h_y)^2} + |h_x - b_x| + |h_y - b_y| \tag{6.5}$$

Navigation Route Optimization

In general, to effectively automate the TLS survey we seek a continuous route that connects all scan locations for the robot platform to follow. A simple nearest neighbor algorithm, where from every scan location the platform always moves to the nearest unvisited location, could be used to obtain a feasible route. However, while the selection of the nearest location at each step may be optimal, it doesn't guarantee that the global solution is the most optimal route for the entire survey. This algorithm may lead to suboptimal paths that do not produce the shortest overall distance. If we further constrain the route to be the route that visits all scan locations using the minimum distance, the problem can be formulated as a traveling salesman problem (TSP): given a list of scan locations and the distance between each pair of scan locations, the mobile platform must visit all of them and return to the starting location using the shortest route.

The TSP problem can be modeled using a linear function in which the decision variables are constrained to take integer values (Dantzig et al., 1954; Miller et al., 1960). Therefore, integer programming can be used to get an approximation to the solution for these kinds of problems. Given a connected undirected graph $G = (V, E)$, with edge weights $w(e) = w_{ij}$ as the distance from location i to location j, and defining x_{ij} as a binary variable with value of 1 if the edge E_{ij} is included in the path, the solution to the TSP problem aims to find the closed cycle that contains all nodes n with minimal length such as:

$$min \sum_{i} \sum_{j} w_{ij} x_{ij};\ i = 1, \ldots, n,\ j = 1, \ldots, n \tag{6.6}$$

constrained by the requirements that each scan location can be left behind exactly once (i.e., from each node in the graph only one outgoing edge is allowed):

$$\sum_{j} x_{ij} = 1;\ i = 1,\ldots,n \tag{6.7}$$

and that each scan location can be visited exactly once from one other scan location (i.e., at each node only one incoming edge is allowed):

$$\sum_{i} x_{ij} = 1;\ j = 1,\ldots,n \tag{6.8}$$

These two constraints, however, do not prevent the presence of closed routes that do not include all the vertices of the graph (i.e., subtours). Having into account that for any given subtour the sum of edges will be equal to the number of vertices in it, a third constraint can be added to ensure that the solution to the problem is a fully connected tour and not the union of smaller subtours. Using the Dantzig–Fulkerson–Johnson formulation (Dantzig et al., 1954), we can impose the condition that the sum over all edges in a subset of the graph be less than the number of vertices in the subset. In this way, the subset cannot form a proper subtour, and hence the solution to the problem will be a fully connected tour and not the union of smaller subtours.

Being V the set of all nodes in the graph, and S a subset of V, the subtour elimination constraint can be expressed as follows:

$$\sum_{i \in S} \sum_{j \in S} x_{ij} \leq |S| - 1;\ S \subset V,\ |S| \geq 2 \tag{6.9}$$

The solution to this problem will provide the optimal sequence of scan locations that minimizes the distance traveled by the robotic platform during the in-field TLS data collection.

6.4.3 Autonomous Field Navigation

To conduct the TLS survey autonomously, the robot must navigate the field visiting all the scan locations in the optimal set without requiring any input from humans. Robot navigation refers to the problem of moving a mobile platform in the environment following a path free of obstacles. It involves tasks related to mapping, path planning, and path tracking. For ensuring the success of the TLS operation, once the optimal sequence of scan locations has been identified, valid navigation paths connecting consecutive scan locations needs to be created and efficiently followed by the robotic platform.

Point-to-Point Route Decomposition

The navigable space through the field (see Section 6.4.1) will provide a grid-like structure of obstacle-free paths that the phenotyping platform can leverage to navigate efficiently. Taking advantage of this grid distribution of navigable paths, the route between two consecutive scan locations can be decomposed into a set of straight paths parallel to both the horizontal and vertical axis in such a way that only straight trajectories and in-place rotations will be needed for field navigation.

In Section 6.4.2 two different approaches to calculate the distance of the paths between scan locations were introduced. In both approaches, alleys and headlands were considered usable for the robot to navigate. However, the use of row spacing differs between approaches. The BR_{nav}

(between-rows) approach allows calculating navigation paths using the row spacing, while the AHA_{nav} (alley-headland-alley) approach will forbid it. These two approaches will lead to two ways of decomposing the navigation route (Figure 6.10), but both will be agnostic to the robot planner used for robot navigation.

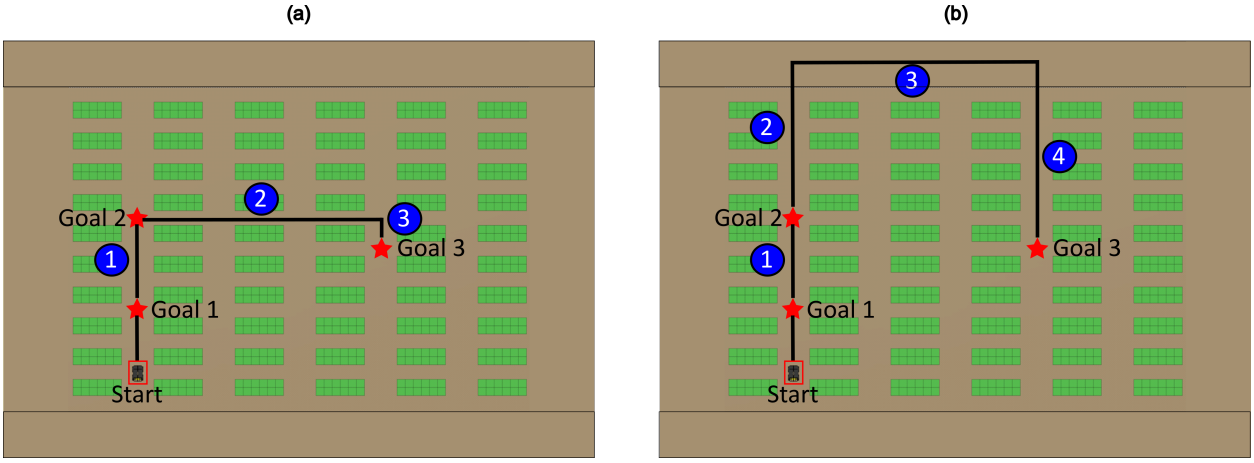

Figure 6.10: Route decomposition approaches. (a) between-rows navigation (BR_{nav}) steps: 1- goals in same alley; 2- row navigation to change alleys; 3- navigation to goal. (b) alley-headland-alley navigation (AHA_{nav}) steps: 1- goals in same alley; 2- navigation to the nearest headland to change alleys; 3- headland navigation to change alleys; 4- navigation to goal.

In general, two different situations can be identified regarding the position of consecutive scan locations for field navigation: scan locations located in the same alley and scan locations in different alleys. When the scan locations are placed in the same alley, the robot will be able to navigate directly from one location to the next using the current alley. This can be observed in step number 1 in both Figure 6.10 (a) and Figure 6.10 (b). On the other hand, when the next scan location is located in a different alley, the robotic platform will need to perform a change of alleys. For the BR_{nav} approach, the platform will use the closest space between rows to navigate to the alley where the next scan location is located (step number 2 in Figure 6.10 (a)). Finally, the robot will reach the goal using the current alley (step number 3 in Figure 6.10 (a)). For the AHA_{nav} approach, the

robot will navigate to the closest headland first (step 2 in Figure 6.10 (b)). Then, the robot will move to the alley where the next scan location is located using the headland as a corridor (step 3 in Figure 6.10 (b)). Finally, the platform will move from this position to the goal location using the current alley (step 4 in Figure 6.10 (b)).

Path Planning

Path planning aims to solving the problem of finding a collision-free path for the robot to navigate from one location in the field to another. Given the robot dimensions and the obstacles in the navigation space, the solution to this problem provides a sequence of positions that joins the initial and goal locations. Our approach for field navigation implemented a point-to-point navigation based on waypoints. Following the approach introduced in Section 6.4.3, the route between scan location pairs can be decomposed in more basic straight paths (i.e. subpath). Each subpath of the navigation route will consist of a straight path between a starting waypoint and a goal waypoint that the robot needs to visit.

In general, path planning for robot navigation involves two main tasks: global planning and local planning. The global planner is responsible for finding, at a high level, the optimal path for the navigation stack to follow based on prior knowledge of the environment. The local planner tracks the global path and, if needed, recalculates the robot trajectory locally based on additional information provided by the navigation sensors. To implement autonomous navigation between waypoints, we used the ROS Navigation Stack (ROS *navstack*) depicted in Figure 6.4. The ROS *navstack* uses the *move_base* package to compute the actions needed to fulfill the mission. This package interconnects the global and local path planners to reach the waypoint goals efficiently.

Global Path Planning

The global path planning seeks to construct a valid path between locations based on global information of the environment. For the global planner, we implemented a straight line planner for the *move_base* package. The straight line planner, which adhered to the *nav_core::BaseGlobalPlanner* interface, computed a straight trajectory to connect the starting and the goal waypoints of each subpath. The final heading at the goal waypoint was calculated as the direction of the vector that links the current goal location and the goal location for the next subpath. That way, when the robot successfully reached the current goal it rotated on the spot to face the next goal.

Local Path Planning

The local path planning aims to generate a trajectory to guide the robot through the global navigation path based on current information about the state of the platform and the environment. The local planner was in charge of enabling the robot to follow the global path between waypoints. The local planning control was achieved using a planner based on the pure pursuit path tracking algorithm (Coulter, 1992). The pure pursuit algorithm calculates the arc trajectory needed for the robot to move from the current position to a virtual goal position on the global path located some distance ahead (i.e., look-ahead point). The look-ahead point (X_{LD}, Y_{LD}) can be computed by finding the intersection point of the circle of radius look-ahead distance (L_D) centered at the robot's location in the global coordinate system (X_R,Y_R), and the global path (Figure 6.11).

The pure pursuit planner computes the radius R of the arc trajectory that joins the current robot's location with the look-ahead point located on the global path. Applying the law of sines to

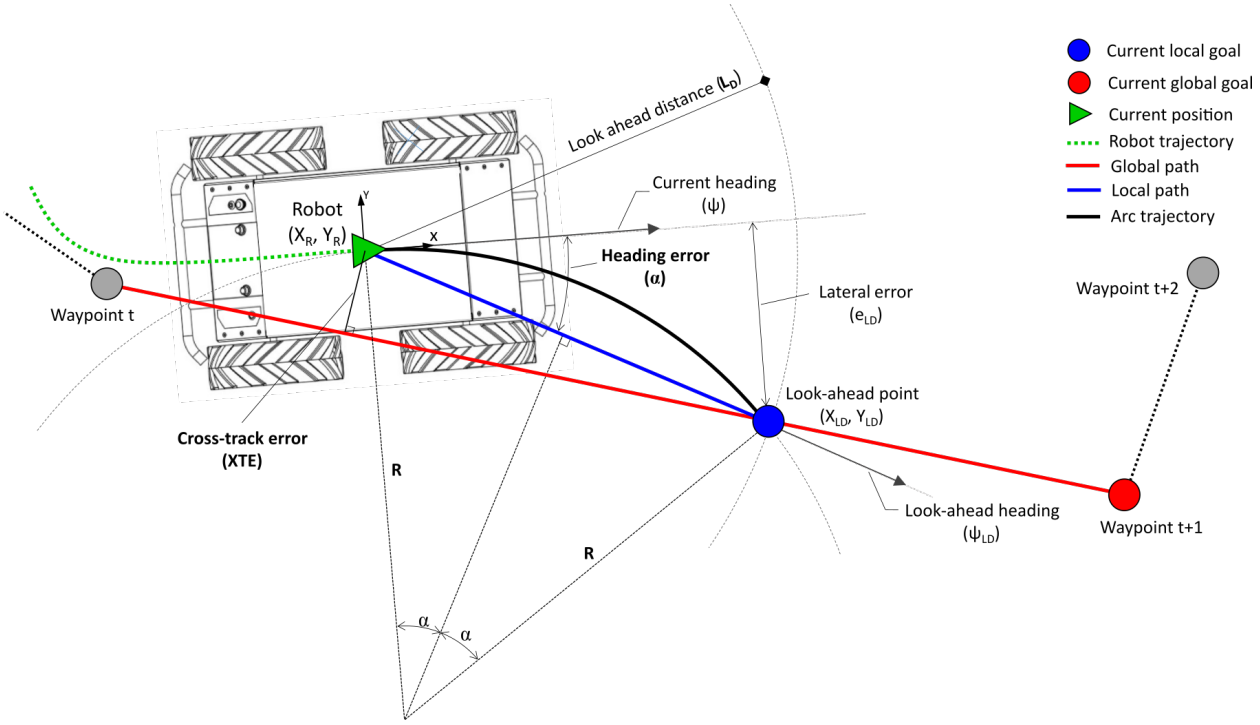

Figure 6.11: Pure Pursuit algorithm principle.

Figure 6.11 results in:

$$\frac{L_D}{\sin(2\alpha)} = \frac{R}{\sin(\frac{\pi}{2} - \alpha)}$$

$$\frac{L_D}{2 \times \sin(\alpha) \times \cos(\alpha)} = \frac{R}{\cos(\alpha)}$$

Therefore, the radius of the arc trajectory will be given by:

$$R = \frac{L_D}{2 \times \sin(\alpha)} \tag{6.10}$$

The curvature of the arc will be the reciprocal of the radius:

$$k = \frac{2 \times \sin(\alpha)}{L_D} \tag{6.11}$$

This curvature will determine the control law needed for the vehicle to follow the arc trajectory from the current location. At each control cycle, the pure pursuit planner calculated the curvature and computed the linear and angular velocities to make the robot follow the arc trajectory. The pure pursuit planner was implemented as a local planner for the *move_base* package as in Xu and Li, 2022a and adhered to the *nav_core::BaseLocalPlanner* interface. During our field experiments, we set the look-ahead parameter to 1 meter.

6.5 Performance Evaluation

6.5.1 Experimental Fields

To test and validate our autonomous phenotyping system, two different trial fields were used. The fields were part of a multi-year and multi-location cotton breeding trial and were located at the Iron Horse Farm in Greene County, Georgia, U.S. (33°43'01.3"N 83°18'29.1"W). A total of 10 different cotton genotypes were planted on the fields for genotype comparison. Two different field layouts were used to test and validate our autonomous phenotyping system (Figure 6.12).

The first field was an engineered field (ENGR) for breeding purposes. The crop was arranged in plots following a wide row (72-inch rows) planting pattern (Figure 6.12 (a). The dimensions of this field were 30 m $\times$ 20 m (length $\times$ width). The ENGR field was composed of 60 individual

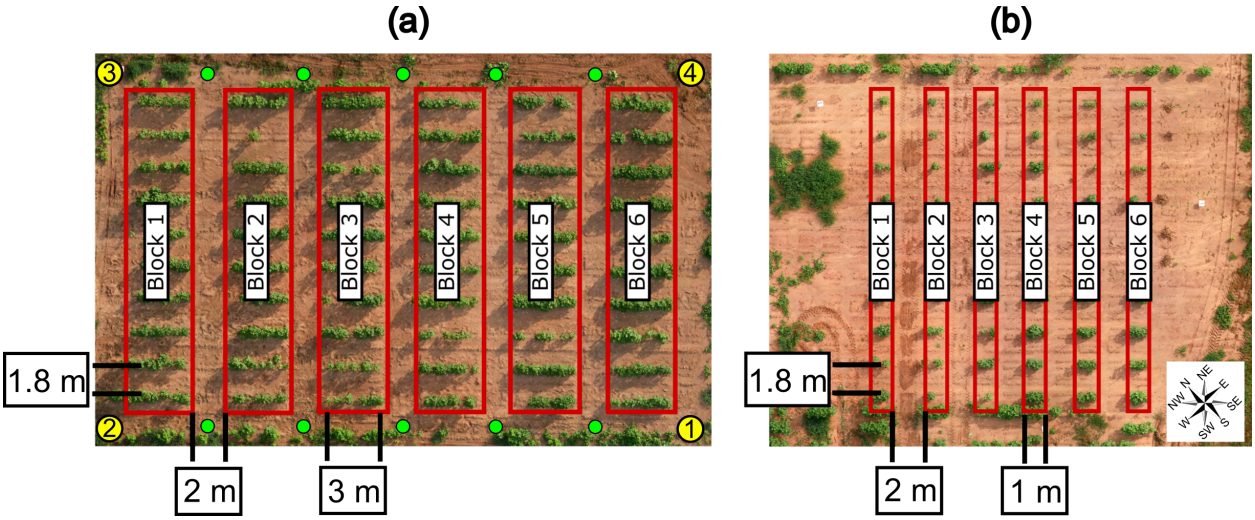

Figure 6.12: Experimental fields. (a) aerial view of the engineered (ENGR) breeding field with wide row spacing . (b) aerial view of the single plant layout (SPL) field. Numbers in yellow circles indicate waypoint sequence for border navigation experiment. Green dots indicate waypoints used for serpentine navigation experiment.

plots following a randomized block design for 10 genotypes and 6 repetitions per genotype. A total of 40 seeds of each genotype were sowed into plots of 3 meter long and thinned to less than 20 plants after crop establishment. Plots were arranged into 6 blocks with 10 plots per block. The distance between plots centers in each block was set to approximately 1.8 meters (i.e., wide-row spacing), while the distance between blocks was set to 2 meters. This field was originally intended for conducting phenotyping experiments based on tractor-mounted proximal sensors, and hence the selection of a wide-row spacing. The second field consisted of a single plant layout (SPL) field with 10 cotton genotypes and 6 repetitions arranged into blocks (Figure 6.12 (b)). The dimensions of this field were 20 m $\times$ 20 m (length $\times$ width). A total of 5 seeds were planted in 1 meter long plots and thinned to 1 plant after germination to ensure an approximate distance of 2 meters between blocks (individual plants in the same row). The distance between plant centers in each block was

set to approximately 1.8 meters. This field was intended for architectural traits analysis, where an individual plant layout can help reduce overlapping and occlusion issues between different plants.

To facilitate posterior comparisons for performance analysis, five 200 mm diameter Koppa registration spheres (Koppa Target Spheres, California, USA) were deployed throughout the field for helping co-register the point clouds collected from multiple locations into a common coordinate system. The targets were installed on top of aluminum rods with a height between 1.4 m and 2 m. At the beginning of each test the spherical targets were placed in the field prior conducting the autonomous TLS survey.

6.5.2 Navigation Performance Evaluation Experiments

To evaluate the navigation performance of our autonomous TLS-based phenotyping platform during the experiments, we made a distinction between non-stationary performance and stationary performance. Non-stationary performance refers to the performance of the platform during autonomous field navigation and accounts for the accuracy of the path-following task. Stationary performance refers to the performance of the platform while the robot is stationary during the LiDAR scanning process at each scan location.

Non-Stationary Performance

To characterize non-stationary performance during autonomous field navigation, two experiments were performed on the ENGR field (Figure 6.12 (a)). The first experiment used the corners of the field as waypoints to navigate around the field (yellow circles numbered 1 to 4 in Figure 6.12 (a)). Starting at the corner number 1, the robot moved clockwise visiting corners 2, 3 and 4 sequentially,

to finally return to the starting position. At each corner the robot executed a 90° clockwise in-place rotation to face the next waypoint. The second experiment used the alleys and headlands to navigate through the crop in a serpentine manner. Two full passes per each direction (i.e., right to left and left to right), were carried out. For this experiment, the intersections between alleys and headlands (green circles in Figure 6.12 (a)) were used as the waypoints for the navigation path. The robot traveled 12 sub-paths (i.e., path joining consecutive waypoints) and performed 12 in-place rotations per direction. For both experiments, the robot was commanded to navigate the path between waypoints following a straight trajectory based on the plan calculated by the global path planner. All ROS topics related to robot navigation, including state estimations for location (X, Y) and heading (ψ) from the *robot_localization* package, were recorded during field navigation using the *ROS bag* file format for further processing. The cross-track error (XTE), given by the perpendicular distance from the global planned path, and the heading error, which measures the angular difference between the robot's current heading and the local planned path direction, for each path, as well as the standard deviation (SD) for these two errors were computed to evaluate the navigation accuracy 6.11.

Stationary Performance

To evaluate the stationary performance of the platform during the autonomous TLS survey, we analyzed pose statistics at the LiDAR sensor level, specifically focusing on the location (X, Y) and heading (ψ) for each scan location. The primary goal of this analysis was to gain a comprehensive understanding of the accuracy and consistency of our platform's performance throughout the TLS survey.

A total of 11 scan locations were used to collect point clouds from the ENGR field. A total of 7 scan locations were used to collect TLS data from the SPL field. The distribution of scan locations was based on the optimized layout calculated by our methodology, and included both scan locations at the border of the field and inside the field. Location and orientation data were collected during the laser scanning operation while the platform was stationary at each scan location. The robot pose information was stored in a ROS *bag* file while the LiDAR scanner was performing the scan. This information was analyzed offline to extract the location and orientation of the LiDAR scanner (X, Y, Z, and heading) and to calculate positioning statistics.

To quantify the absolute positioning errors, we computed the distance between the planned scan point coordinates and the platform coordinates recorded during the scanning process at the corresponding location. Additionally, to obtain insights into the precision and variability of our system's performance on pose estimation, we examined the residuals for all three components in relation to the estimated sensor location at each scan point. This estimation was achieved by averaging the platform coordinates recorded during the scanning process at each specific location.

6.5.3 TLS Automation Experiments

To evaluate the performance of our methodology at collecting TLS data in a real field, we conducted a TLS survey session using the autonomous phenotyping platform in both the ENGR and SPL fields. We first modeled the field on MATLAB R2021a (The MathWorks Inc., Massachusetts, United States) using the parameters of the field described in Section 6.5.1 (i.e., number of rows, number of plots, row spacing, and alleys width). The dimensions of the plots (length, width, and height) were established based on a mature growth stage (i.e., near canopy closure). The ENGR

field (Figure 6.13 (a)) was composed of 10 rows with 6 plots per row. Each plot was defined by a box with dimensions 3 $\times$ 1 $\times$ 1.9 (L $\times$ W $\times$ H) given in meters. Using voxels of 0.5 $\times$ 0.5 $\times$ 0.33 meters (length $\times$ width $\times$ height) for discretizing the bounding boxes, each digitized plot was composed of 72 cells. The SPL field (Figure 6.13 (b)) was composed of 10 rows with 6 individual plants per row. Each plant was defined by a box with dimensions 1 $\times$ 1 $\times$ 1.9 (L $\times$ W $\times$ H) in meters. Again, using the same voxel size of 0.5 $\times$ 0.5 $\times$ 0.33 meters, each digitized plot in the SPL field was composed of 48 cells. Given the field layout and the dimensions of the plots, the effective free space available for robot navigation at this growth stage was 0.8 meters for row spacing and to 1.5 meters for alley width, enough space for the robot to navigate safely.

As indicated in Section 6.4.1, the potential scan locations for the TLS survey were limited to the free space were the robot can freely navigate. The plots distribution on the field and the growth stage of the crop reduced the feasible space for placing the scanner to the intersections points between row spacing, alleys and headlands. In addition, to reduce the impact of the minimum range limitation of the LiDAR scanner on the quality of the collected data, only the scan locations whose distance to the crop was greater than 0.8 meters were considered valid for the TLS survey. Therefore, only the intersections between alleys and free space between rows were considered as valid scan locations. For each field, a total of 77 field positions were defined as potential scan locations (black squares in Figure 6.13).

In order to compute crop visibility from each potential scan position, the AABB–ray intersection algorithm was implemented on MATLAB using ray casting approaches. LiDAR sensor parameters for ray casting analysis, such as start and end angles, and angular resolution were selected according to the capabilities of the FARO Focus S70 LiDAR scanner. Specifically, vertical angle was

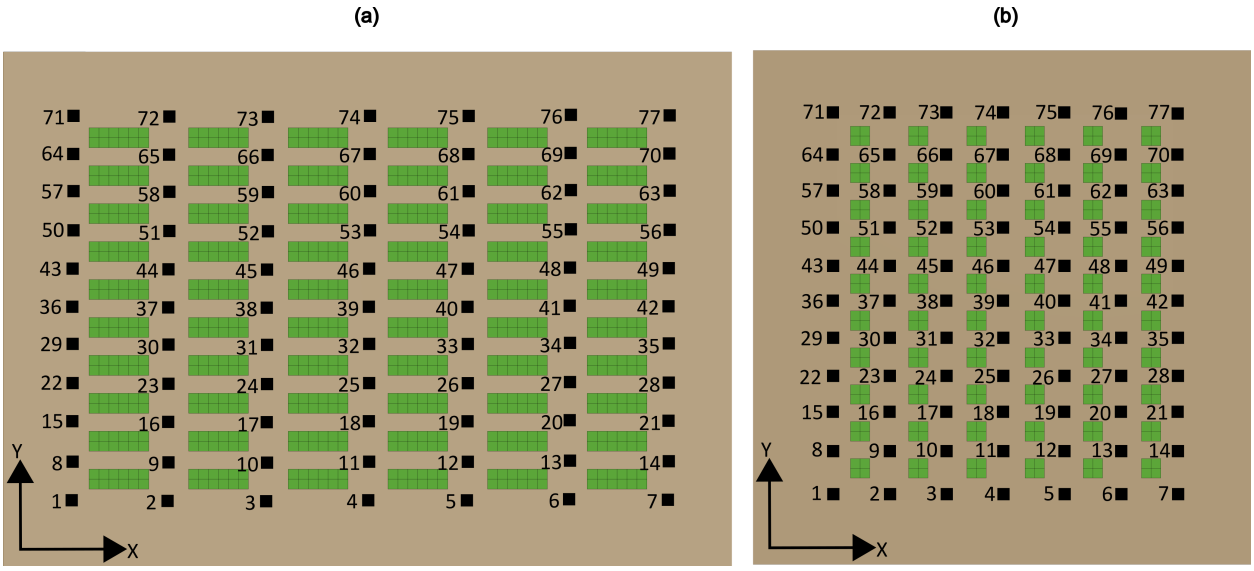

Figure 6.13: Digital model of the fields for ray-box intersection analysis. (a) ENGR field . (b) SPL field. Plots are represented as green boxes. Potential scan locations are identified as black squares

configured between -60° and 90°, and horizontal angle was configured between 0° and 360°. To accelerate code execution and avoid potential memory issues, the angular step was set to 0.36° for both the vertical and horizontal angles, which translates to a laser scanner resolution of $\frac{1}{4}$ (i.e., 6.1 mm over 10 meters). The MATLAB script provided as outputs the number of rays that impacted each cell in the field, the distance from the origin of the ray to the hitting point, the row and plot indices of the plots intercepted per each ray, and the cell index. With this information the visibility score table including the number of cells covered from each scan location was obtained. Finally, the optimal set of scan locations for the TLS survey was identified using Algorithm 2 according to the visibility score.

To optimize the route between scan location pairs from the identified set, the MATLAB Optimization Toolbox (The MathWorks Inc., 2021) was used to solve the TSP problem with subtour

elimination constraints (Section 6.4.2) for both route definition approaches (BR_{nav} and AHA_{nav}) described in Section 6.4.2.

6.5.4 Point Clouds Registration Performance Analysis

In order to evaluate the effectiveness of our system in automating the registration of point clouds, we used the data from the navigation sensors to position and align autonomously collected point clouds from multiple field locations. This involved determining the position (X_{LiDAR}, Y_{LiDAR}, Z_{LiDAR}) and the orientation (ψ_{LiDAR}) of the LiDAR sensor relative to its origin. We achieved this by computing these values through the conversion of state estimates obtained from the ROS bag files in the world frame into the LiDAR scanner frame. The homogeneous transformation described in Equation 6.1 facilitated this transformation. Additionally, the pitch and roll angles, required to fully characterize the orientation of the LiDAR scanner at each scan location, were directly acquired from the device's internal dual-axis compensator.

To achieve a consistent coordinate system for the collected scans from different locations, the pose information at the LiDAR sensor level was associated with each scan using FARO SCENE software (FARO Technologies, Florida, US). Subsequently, a cloud-to-cloud (C2C) registration was performed using the same software. C2C registration is an automated procedure that enables the alignment of point clouds based solely on overlapping points, without the need for artificial targets.

Following the C2C registration, the aligned point cloud obtained from this procedure was compared to the point cloud registered using the spherical targets (known as target-based registration), which served as the reference for benchmarking. In order to assess the accuracy of the registra-

tion, various metrics were computed. These metrics included target-based statistics, such as the Euclidean distance between corresponding targets, as well as scan point error statistics. To ensure a representative analysis, the scan point error statistics were computed on a subset of points that were uniformly subsampled from each individual scan within the complete point cloud.

In order to evaluate the performance of the automatic registration process, the Hausdorff distance (Rote, 1991) was adopted as the benchmarking metric. This distance serves as a dissimilarity measure for comparing two sets of points. Specifically, it quantifies the maximum distance between any point in one set (source) and its nearest point in the other set (reference). Given a source set of points $PC_{src} = \{a_1, a_2, ..., a_n\}$ and a reference set of points $PC_{ref} = \{b_1, b_2, ..., b_n\}$, the Hausdorff distance from the source to the reference will be given by the following equation:

$$d_H(PC_{src}, PC_{ref}) = \max_{a \in PC_{src}} \left(\min_{b \in PC_{ref}} (d(a,b)) \right), \tag{6.12}$$

where a and b represent the 3D points belonging to the point clouds PC_{src} and PC_{ref} respectively, and *d(a,b)* is the Euclidean distance between these two points.

6.6 Results and Discussion

6.6.1 Field Navigation Evaluation

Overall, the comprehensive analysis of cross-track error (XTE) and heading errors confirm the system's capability to maintain precise trajectories during field navigation, demonstrating the platform's reliability and accuracy in autonomous operation.

Non-Stationary Error Analysis

During the border navigation experiment, the robotic platform traveled a total distance of 970 meters. Throughout the test, the XTE remained below 5 cm for the majority of the path, accounting for over 86% of the path (Figure 6.14 (a)). The average XTE value recorded was 2.370 cm.

In the serpentine navigation experiment, the platform completed 170 meters per pass, accumulating a total of 680 meters after four passes. Similar to the previous navigation experiment, the XTE remained below 5 cm for most of the path. In the right-left direction (Figure 6.14 (b), left), the XTE error was below 5 cm for 78% of the experiment, between 5 cm and 10 cm for 14% of the experiment, and exceeded 10 cm for 8% of the experiment. In the left-right direction (Figure 6.14 (b), right), the XTE error was below 5 cm for 83% of the experiment, between 5 cm and 10 cm for a 13%, and exceeded 10 cm for only 4%. Across the four passes, the average XTE error measured 3.666 cm.

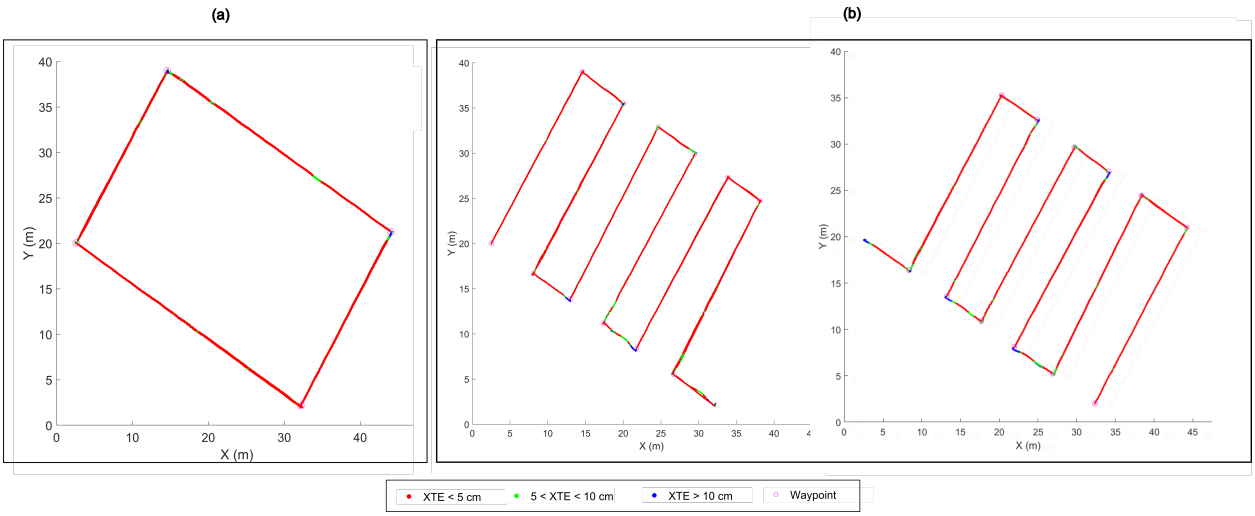

Figure 6.14: Cross-track error (XTE) observed during the navigation experiments. (a) border navigation experiment. (b) serpentine navigation experiment. The color-coded lines indicate the range of error encountered during navigation in relation to the global plan. The waypoints used for autonomous navigation were located at the headlands areas and are marked as circles.

Overall, the XTE observations depicted in Figure 6.14 underscore the system's consistent performance in maintaining a precise trajectory during field navigation. The majority of both the border and serpentine navigation experiments showcased the platform's ability to achieve reliable and accurate autonomous navigation, with XTE values consistently below the 5 cm threshold.

During the entire navigation experiment, the average XTE was approximately 3 cm, slightly higher than expected for a standard RTK-GPS positioning system. This disparity can be attributed to tracking errors observed during in-place rotations. The robot effectively followed the straight sections of the navigation paths (Figure 6.14), but the in-place rotations to align the heading towards the next waypoint introduced a lateral displacement, contributing to increased XTE. Uneven traction during rotations caused by terrain irregularities and loose soil in certain areas of the field further impacted the effective center of rotation and exacerbated cross-track error, particularly at waypoints requiring 90° turns, as can be seen on the corners of Figure 6.14.

Despite these challenges, the robotic platform demonstrated the ability to quickly return to the planned path, even in zones with XTE values exceeding 5 cm (southernmost paths in Figure 6.14 (b)). These zones were characterized by loose rocks that affected traction and caused slight slippage. However, the navigation errors in these areas were not excessive, and the platform efficiently regained the intended path within a short distance. It's important to note that our primary objective was accurate pose estimation at scan locations, rather than achieving high accuracy in field navigation (see Section 6.6.1).

Heading error analysis during field navigation revealed that the average heading error for the entire border navigation experiment was -0.281° (Figure 6.15). Once the robot completed the rotation towards the desired heading, it consistently maintained its heading within a range of $\pm$ 2.5°.

However, the serpentine navigation experiment showed an average heading error more than six times higher than that of border navigation, with an average error of -1.516°. This discrepancy can be attributed to larger errors accumulated during the in-place rotations to align the platform's heading. The significant difference between the current and objective headings during these rotations led to a temporary increase in heading error. As the platform rotated, the heading error gradually diminished until it reached the path tracking heading tolerance of 2°, allowing the platform to effectively fulfill its mission.

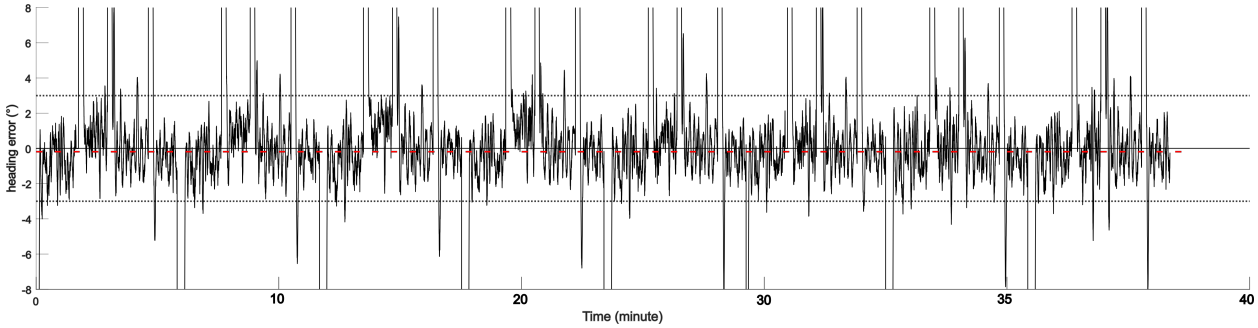

Figure 6.15: Heading error during the border navigation experiment. The red dash line indicates the average heading error value for the entire experiment (-0.281°). The black dotted lines indicate the range of error between ± 3°. High heading errors occurred when the robot was making turns at the corners of the field.

Stationary Errors Analysis

In the stationary errors analysis, we investigated the precision and accuracy of our robotic platform during the data collection process at each scan location. The robotic platform remained stationary for 7 to 10 minutes while the LiDAR scanner captured TLS data. To analyze the stationary errors, we gathered data during the laser scanning operation at each scan location and computed pose statistics at the LiDAR sensor level. The observed location errors for each scan location in the ENGR and SPL fields are depicted in Figures 6.16 and 6.17, respectively.

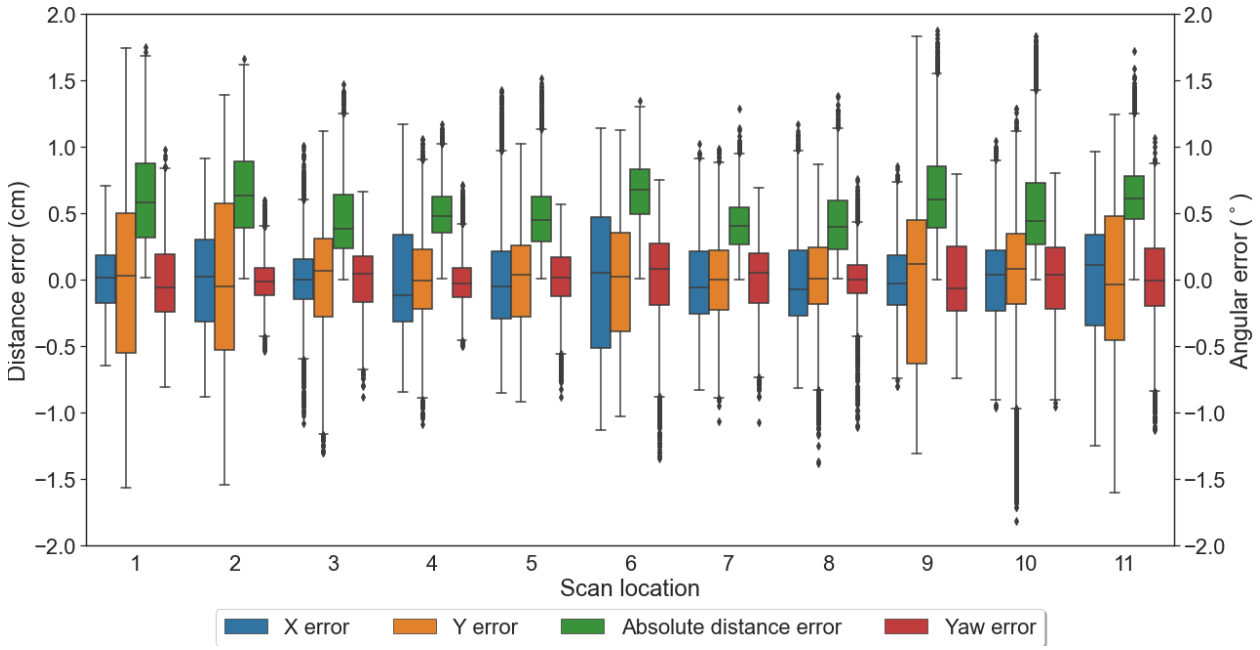

Figure 6.16: Statistics of location and orientation errors observed in the ENGR field. The distribution of residuals for the X, Y, and heading components is represented by the blue, orange, and red boxes, respectively. The green boxes indicate the absolute distance error between the planned scan location and the actual location.

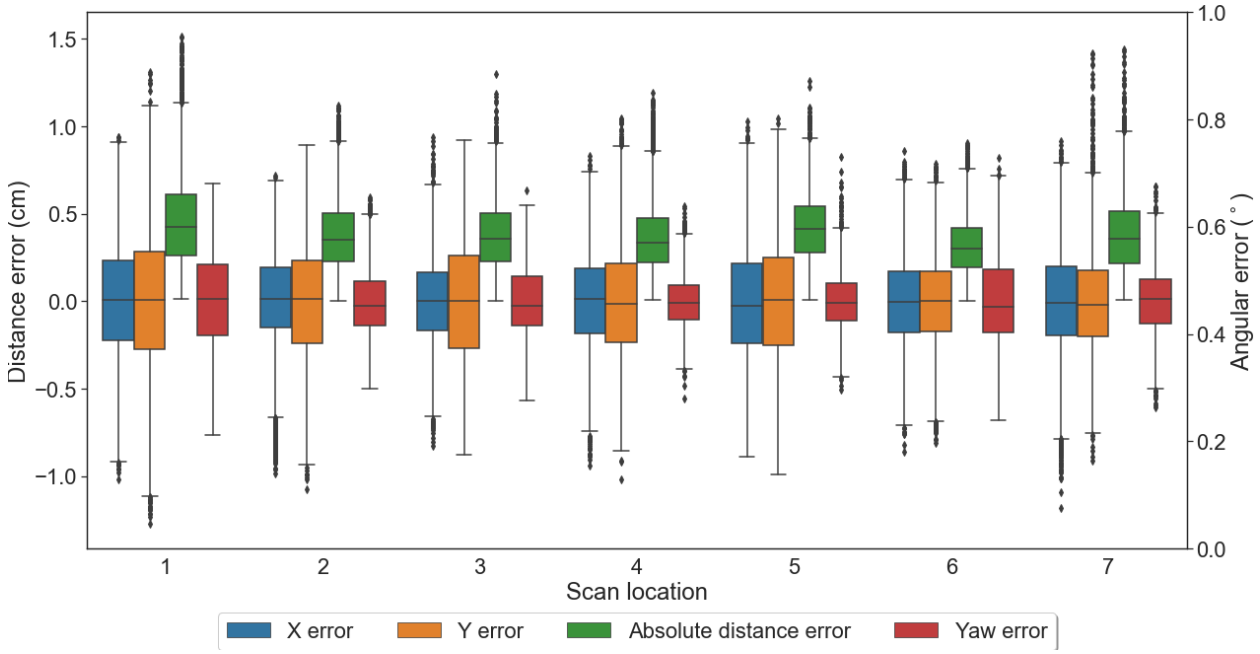

Figure 6.17: Location and orientation errors observed in the SPL field. The distribution of residuals for the X, Y, and heading components is represented by the blue, orange, and red boxes, respectively. The green boxes indicate the absolute distance error between the planned scan location and the actual location.

For the ENGR field experiment, our system exhibited a high level of precision in both location and heading estimates. The average location errors was found to be 0.565 cm, and the average heading error was 0.035°. Analyzing the residuals for X and Y coordinates, we observed a range between approximately ±1.25 cm and ±1.75 cm, respectively. Notably, the average residuals for X and Y coordinates were below 0.5 cm. The standard deviation values for all pose estimates during the scan operation remained consistently low, indicating the system's ability to provide accurate and consistent location estimates. Regarding heading estimates, the yaw error ranged from approximately ±1° throughout the entire TLS data collection process. The low standard deviation values obtained in our tests suggest that both location and heading estimates were primarily clustered around the mean value during the scanning operation, further emphasizing the accuracy and reliability of our system.

Moving on to the TLS survey conducted on the SPL field (Figure 6.17), the system continued to demonstrate precise location and heading estimates. We analyzed a total of 7 scan locations in this field. The residuals for X and Y coordinates fell within the approximate ranges of ±1 cm and ±1.25 cm, respectively. For X coordinates, the average residuals value was 0.25 cm, while for Y coordinates, it was 0.275 cm. Similar to the ENGR field trial, the spread of values for all pose estimates during the scan operation remained below 0.25 cm for location estimates, highlighting the system's consistency in providing accurate location estimates. The average location error for the entire TLS survey session in the SPL field was 0.376 cm. As for heading estimates, the yaw error ranged from approximately ±0.75° during the trial, with an average yaw error smaller than 0.005°.

Both TLS surveys exhibited low standard deviation values for location and heading estimates, indicating that the estimations were closely clustered around the mean value during the scanning operation. This analysis provides valuable insight into the accuracy and reliability of our system's positioning capabilities in both the ENGR and SPL fields, reaffirming its ability to achieve precise location and orientation during data collection in two different field layouts.

6.6.2 Autonomous TLS Survey Results

The optimization process, combining the visibility score and the greedy algorithm (Algorithm 2), resulted in a significant reduction in the required number of scan locations. This reduction ranged from 85% to 90%. For instance, in the ENGR field, only 11 scan locations were needed to cover all the cells in the digitized field, compared to the initial 77 potential scan locations that were analyzed. Similarly, for the SPL field, the number of scan locations was reduced to 7. Figure 6.18 shows the optimized layout of scan locations for both fields.

To determine the optimal route for the TLS survey, we assumed that the robotic platform would start from the bottom right corner of the field (Origin). The pairwise distances between scan locations were represented by the undirected weighted graph depicted in Figure 6.19. For simplicity, the weight of the edges have been drawn using lines with variable thickness according to the distance between scan locations.

By solving the graph using the TSP solver, we obtained the optimal route for the ENGR field, as illustrated in red in Figure 6.19. The optimal route can be traversed in either direction: Origin-14-26-4-17-30-65-43-74-60-39-55-Origin, or the reverse order. Both routes optimize the collection of TLS data in the field.

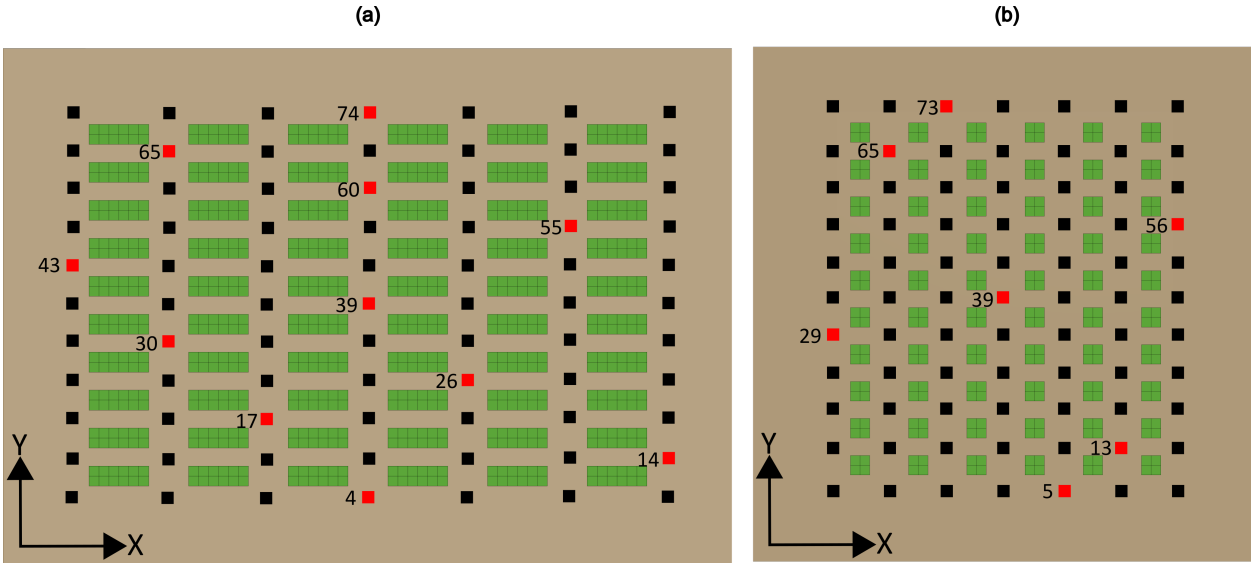

Figure 6.18: Optimized TLS layout. Layout obtained using ray casting approaches for visibility analysis on the ENGR (a) and the SPL (b) digitized fields. Plots are colored as green boxes. Scan locations are identified as black squares. Optimal scan locations are identified by red squares.

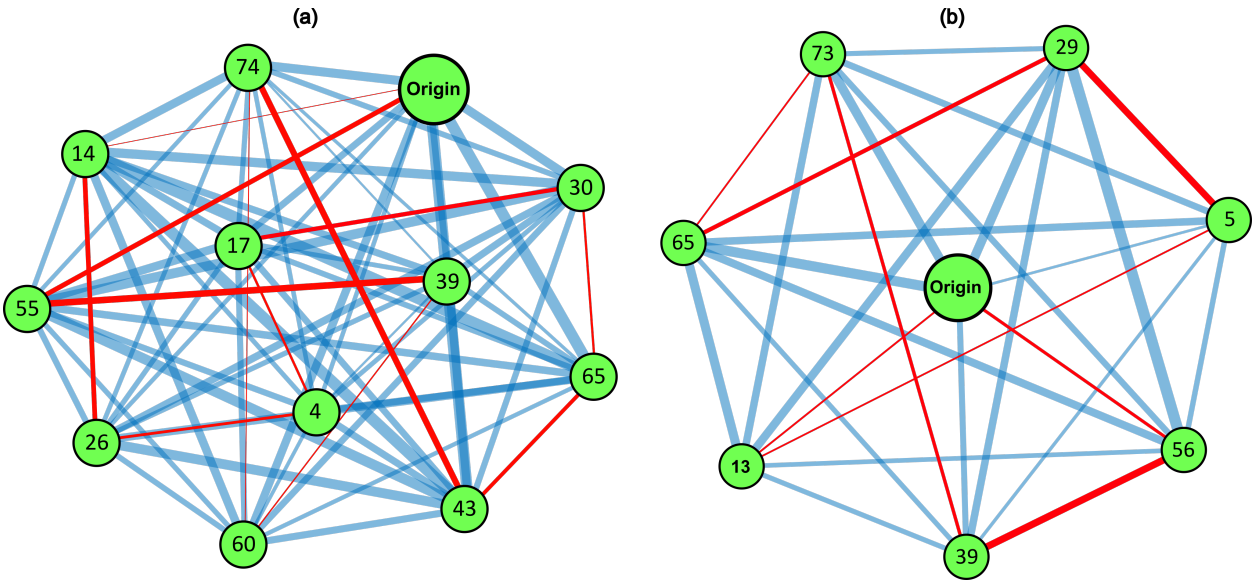

Figure 6.19: Weighted graph for route optimization. (a) ENGR field and (b) SPL field. The nodes of the graph identifying each scan location are represented as green circles. The edges of the graph are identified by blue lines joining each node pair. The thickness of the lines indicate the weight for each particular edge (i.e., distance between scan locations). The optimal route for both fields, the ENGR (Origin-14-26-4-17-30-65-43-74-60-39-55-Origin) and the SPL (Origin-13-5-29-65-73-39-56-Origin), are identified by red lines.

The total cost associated with the optimal route, i.e., the total distance that the platform needs to travel during the TLS survey, using the AHA_{nav} approach was determined to be 134.5 meters. For comparison, we also calculated the total navigation cost using the BR_{nav} approach (Section 6.4.2), which takes into account the space between rows during the early crop growth stage. After route optimization, the total distance to travel was reduced to 98 meters. A visual comparison of the optimal routes obtained by both approaches is provided in Figure 6.20.

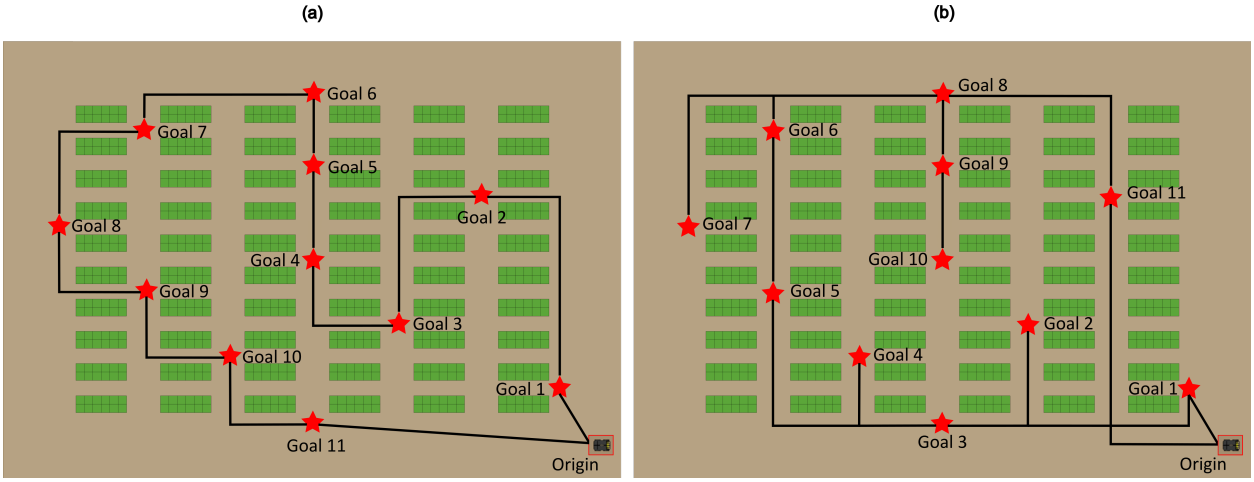

Figure 6.20: Optimal route for TLS-based field phenotyping. Optimized route for the BR_{nav} approach (a) and the AHA_{nav} approach (b). Plots are colored as green boxes. Optimal scan locations (i.e., goals for robot navigation) are identified by red stars. Black lines identified the navigation paths between scan location pairs.

Additionally, we calculated the distance required using a simpler approach based on the nearest neighbor algorithm, where the platform would visit the closest scan location from its current position. In this case, the distance traveled by the platform increased to 146 meters. As expected, optimizing the route resulted in a reduction in the total distance needed to cover the entire field. The use of the TSP formulation for route optimizing led to a 7.8% decrease in the traveled distance. This improvement increased to 33% when the platform was able to navigate between the rows of the crop.

The optimization of the route is indeed crucial in minimizing the distance traveled by the robotic platform during TLS-based field phenotyping. However, it is important to recognize that route optimization is not the sole factor impacting the overall productivity and effectiveness of the phenotyping process. Autonomous field navigation can be significantly affected by the presence of obstacles and various factors that introduce variability into the field.

6.6.3 Point Cloud Registration Results

Initially, the point clouds were positioned (pre-aligned) based only the information gathered at each scan location during the scanning operation using SCENE software. However, as illustrated in the insets of Figure 6.21, the point clouds did not align perfectly and displayed noticeable misalignments, with errors on the order of tens of centimeters. The maximum observed mismatch reached 27.3 cm. These discrepancies were primarily due to inaccuracies in pose estimation, specifically in the estimation of pitch and roll during the scan process.

The accurate registration of point clouds heavily relies on the orientation of the LiDAR scanner. To estimate pitch and roll, we utilized the information provided by the internal dual-axis compensator of the LiDAR scanner. Although the sensor's user manual (FARO Technologies, 2020) specified an accuracy of 0.019° for inclinations between $\pm 2°$, we encountered challenges in controlling the inclination of the robotic platform during autonomous data collection, leading to higher inclinations in certain areas due to variations in terrain slope, bumps, or other surface irregularities.

Using the pre-aligned point clouds, an automatic C2C registration was performed using SCENE software. To ensure efficient and accurate point clouds matching, we limited the radius to search for common points to 30 cm, given the relatively small alignment errors. The results were highly

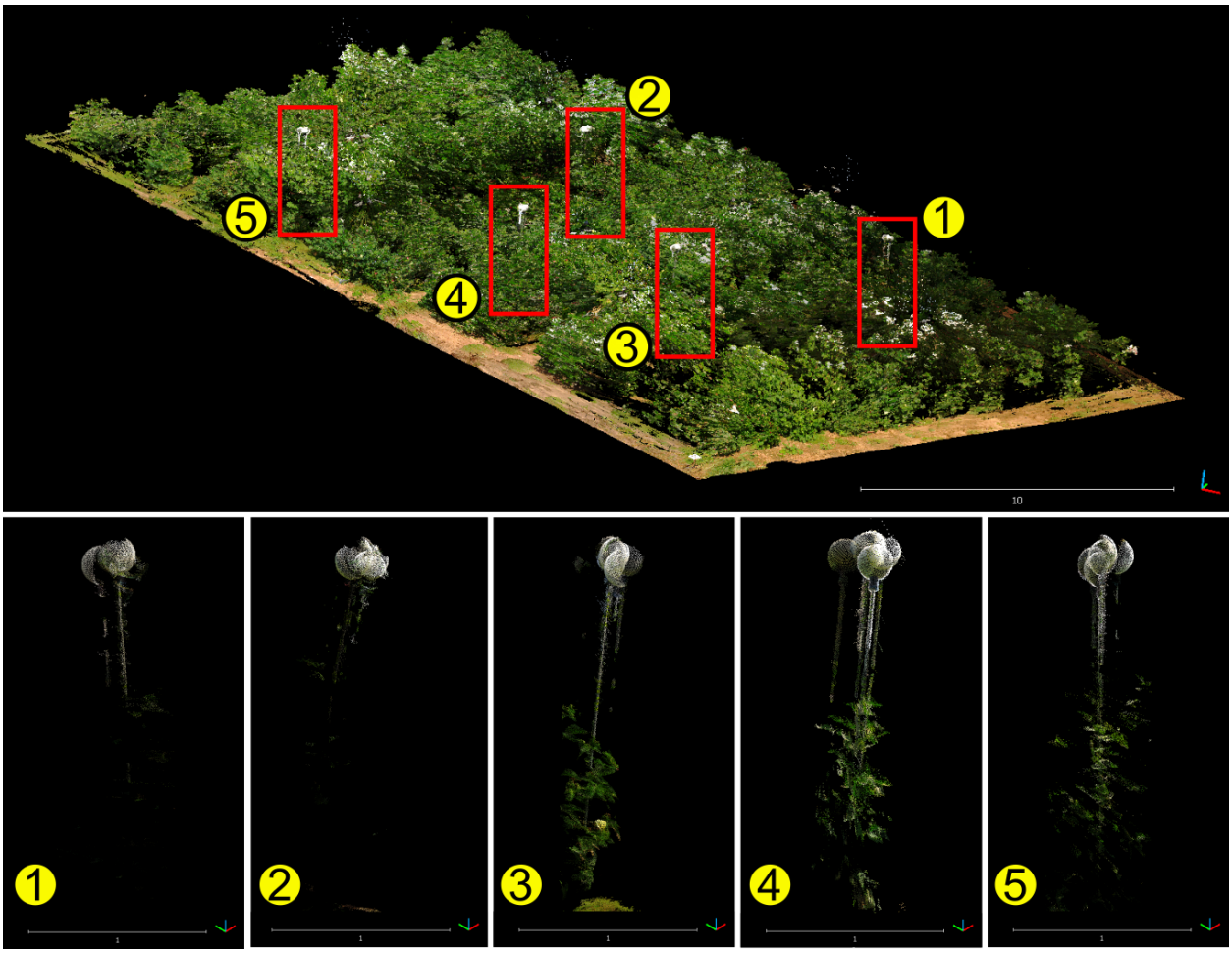

Figure 6.21: Point cloud pre-alignment results. Alignment using only the information provided by the navigation sensors during the scanning process. The numbered insets show the five spheres deployed in the field for benchmarking

promising, as demonstrated in Figure 6.22, with a significant improvement in alignment. At the spheres level, the maximum misalignment observed was reduced to 4.17 cm.

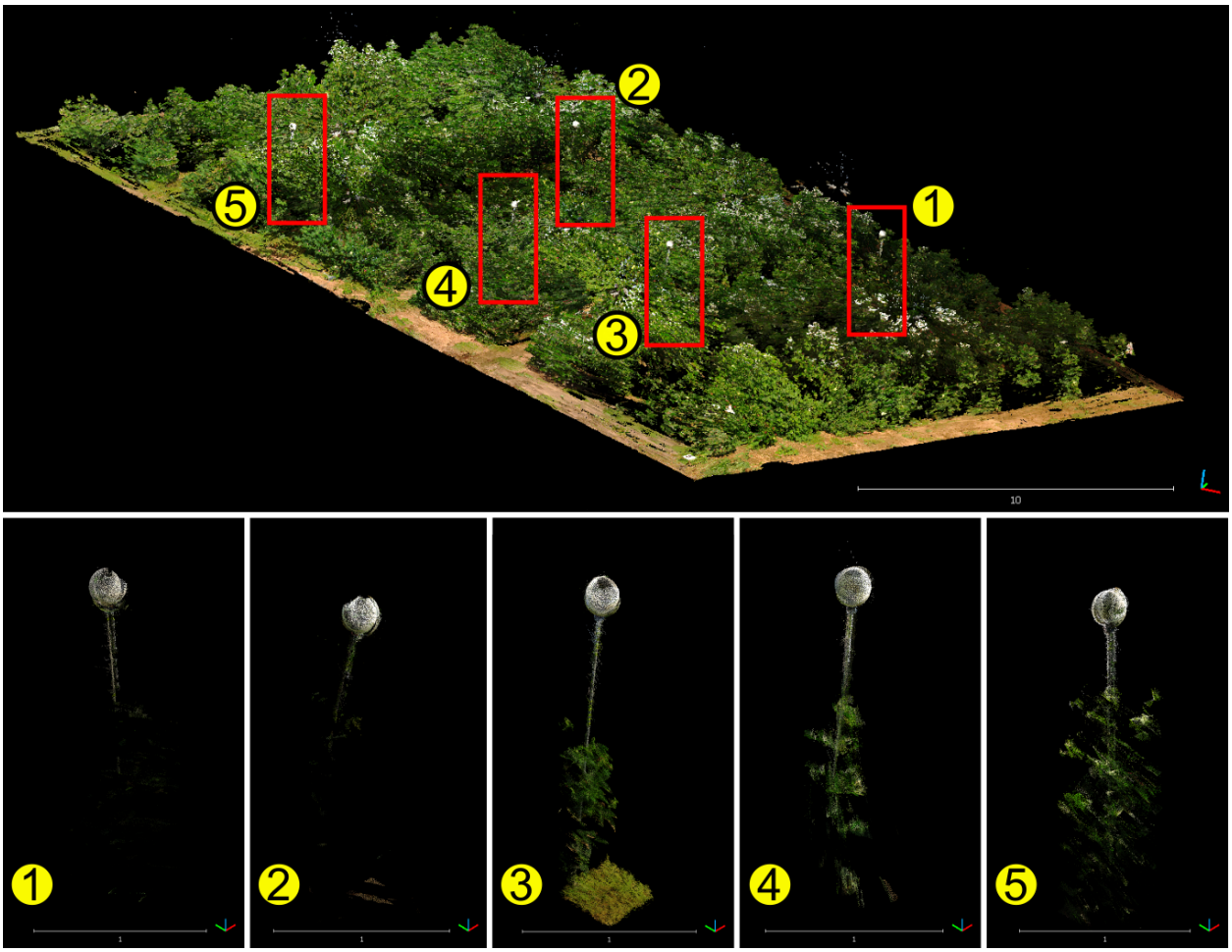

Figure 6.22: Automatic registration results. Alignment using the navigation sensors information and automatic cloud-to-cloud registration. The numbered insets show the five spheres deployed in the field for benchmarking

Despite the challenges in controlling the inclination of the robotic platform during data collection, the alignment of the point clouds proved sufficiently accurate to enable automatic registration refinement using SCENE software. Table 6.1 provides a summary of the registration results obtained using SCENE software for both the target-based registration and our autonomous system (navigation sensors + C2C).

Table 6.1: Registration errors comparison. Comparison of errors from our method using the navigation sensors and cloud-to-cloud (C2C) registration versus target-based registration.

Registration method	Target statistics (cm)			Scan point statistics (cm)	
	Mean error	Horizontal error	Vertical error	Max. point error	Mean point error
Target-based	0.59	0.53	0.22	2.10	1.37
Nav. sensors + C2C	1.72	1.34	0.82	3.02	2.07

Our autonomous point cloud registration method demonstrated high accuracy, with mean errors averaging approximately 2 cm. While target-based registration appears to outperform our autonomous system based on mean target error statistics, this metric can be misleading. It is important to note that target statistics are computed solely based on the points identified by the software as belonging to the spheres, calculating the distance between those points and the best-fitting sphere models. However, this approach may yield biased measurements, particularly when dealing with partial spheres containing only a small number of points. In such cases, the fitted model may not accurately represent the actual shape, leading to potentially misleading results.

A more comprehensive assessment of the registration performance can be obtained by considering scan point statistics. Our system consistently delivered measurements with mean errors close to 2 cm, representing a difference of only 50% compared to the mean error obtained using spherical targets. This difference is less than 1 cm, indicating that our methodology can achieve results comparable to traditional and more laborious methods for TLS survey.

Finally, we evaluated the dissimilarity between the point cloud registered using our approach and the target-based registered point cloud by computing the Hausdorff distance between them (Figure 6.23). The calculated distance for the autonomous TLS survey was 1.25 cm with a standard

deviation of 0.82 cm. Examining the distribution of distances (Figure 6.23 (b)), we observed that 85% of the points had errors below 2 cm, and 95% of the points had errors below 3 cm.

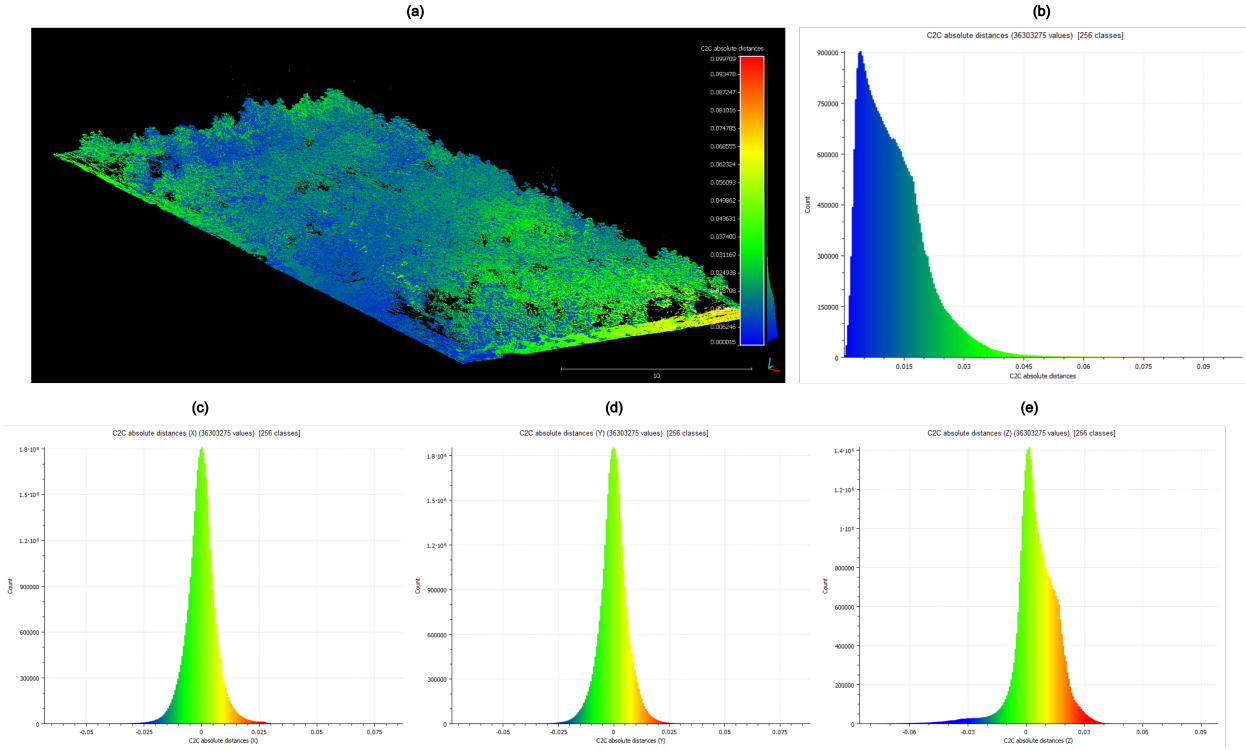

Figure 6.23: Dissimilarity results analysis. Comparison of results for the TLS data collected autonomously versus the target-based registered data. (a) autonomously reconstructed point cloud colorized according to the Hausdorff distance. (b) histogram of distances. (c) decomposition of distance for the X axis dH_X. (d) Y axis dH_Y. (e) Z axis dH_Z.

Analyzing the histograms for the X and Y axes (Figure 6.23 (c) and (d)), we found that the distances followed a Gaussian distribution, with means of -0.014 cm and 0.001 cm, and standard deviations of 0.63 cm and 0.62 cm, respectively. However, for the Z axis (Figure 6.23 (e) the distribution of distances exhibited a positive skewness, with a mean of 0.5 cm and a standard deviation of 1.08 cm. It is worth noting that the distances between point clouds along the Z axis were slightly larger compared to those along the X and Y axes. This can be attributed to the known lower accuracy in estimating altitude, typically double the accuracy of horizontal positioning.

Nonetheless, the errors remained small and fell within the expected ranges of accuracy for standard RTK-GPS positioning systems.

Our approach provides a robust and efficient alternative to target-based registration, offering accuracy comparable to conventional approaches. While the target-based method may show a smaller mean error on paper, the practical difference is minimal, and our autonomous system demonstrates impressive accuracy in point cloud registration without the need for physical targets. However, considering the advantages of improved accuracy in scanner orientation estimation, it would be beneficial to incorporate dedicated sensors such as inertial measurement units to achieve more reliable results.

6.7 Limitations and Future Work

The application of autonomous robotic systems in agricultural fields is an exciting area of research. However, several challenges arise due to the inherent complexities of real-life agricultural environments. One initial assumption we made was that all plots had the same length and the distance between them remained constant. However, real-life agricultural fields exhibit variability due to factors like unequal germination rates, planting errors, and heterogeneous plant growth. To address these challenges, we aim to investigate the use of digital twins to model the crop and the deployment of physics engines to simulate the interaction between laser beams and the plants more realistically. By doing so, we hope to enhance the system's ability to handle the complexities that arise throughout the agricultural season. This approach will allow for more precise visibility analysis, enabling the system to make informed decisions based on the current state of the field.

Despite our platform successfully navigated the field using the alleys of the field based only on pre-programmed waypoints and a 2D LiDAR to avoid immediate collisions, it is worth noting that certain paths may become obstructed as plants grow or lean, posing challenges for the navigation system as the season progresses. To address these challenges, we will integrate additional sensors like color and depth cameras for visual servoing. By leveraging real-time visual information, the platform can detect and avoid obstacles while traversing the field. Incorporating these sensor capabilities can significantly improve the safety and precision of the autonomous navigation system, enabling seamless adaptation to dynamic field conditions.

The LiDAR scanner on our robotic platform had limitations in capturing comprehensive data from the crop due to its relatively low height compared to the plants. To mitigate this, one solution could be using a taller structure, like a mast or pole, to mount the LiDAR. However, increasing the height must be carefully balanced with system stability, as placing a heavy object far from the robot's center of mass may introduce instability and pose a risk of tipping over. To address this concern, we are exploring novel approaches such as collapsible structures with auto-deployment capabilities, allowing the LiDAR to extend to a sufficient height when the robot is stable. This would optimize data collection while minimizing the risk of instability and system damage. Implementing this improvement will enhance data acquisition accuracy, facilitating better analysis and decision-making in agricultural applications.

Finally, the accurate registration results presented in our study offer the potential for estimating a wide range of morphological traits. To fully leverage the system's capabilities, we aim to explore its application in collecting 3D data over time for comprehensive 4D analysis. This approach would enable us to track trait evolution and deepen our understanding of crop development and its corre-

lation with yield traits. By continuously monitoring and quantifying structural and morphological characteristics, our autonomous system could enable breeders and researchers to gain valuable insights into the dynamic evolution of the crop, improving yield predictions and understanding trait development. The collection and analysis of 4D data have the potential to revolutionize crop research, contributing to more efficient and sustainable agricultural practices.

6.8 Conclusions

In this study, we successfully introduced an innovative phenotyping platform and autonomous data collection methodology for in-field terrestrial laser scanning (TLS) for plant phenotyping. By integrating readily available equipment within the ROS framework, we achieved efficient and accurate LiDAR data acquisition from multiple field locations without human involvement. The capability to autonomously collect TLS data both inside and outside the field boundaries provides breeders with comprehensive and accurate plant 3D models, surpassing the limitations of conventional surveying methods. This represents a significant milestone in plant phenotyping, streamlining data collection and enhancing accuracy.

Our autonomous phenotyping platform has proven to be a reliable and effective alternative for TLS surveys, offering accuracy on par with traditional approaches while eliminating the need for cumbersome target setups. The precise localization through real-time kinematic positioning and sensor fusion enabled registration of point clouds with mean errors comparable to those using artificial targets. The seamless autonomous navigation further contributed to overall efficiency,

showing the potential of our methodology in various LiDAR-based surveying applications for plant phenotyping.

CHAPTER 7

CONCLUSIONS AND FUTURE WORK

7.1 Conclusions and Key Findings

This dissertation presents significant advancements in in-field digital crop phenotyping methodologies for crop breeding using UAVs, machine learning, and a ground mobile robot, addressing critical challenges in traditional methods. Key developments include the creation of a Support Vector Machine (SVM) classifier for estimating cotton boll number, offering a reliable and efficient alternative to manual methods. In peanut breeding, the Segment Anything Model (SAM) improved plot extraction and trait estimation from UAV multispectral imagery, reducing manual labor and increasing accuracy in traits assessment, including canopy height, main stem prominence, growth habit, and TSWV incidence. For continuous crop monitoring, a methodology using terrestrial laser scanning (TLS) for spatiotemporal registration of 3D point cloud data was developed, allowing precise tracking of canopy height and volume. Additionally, an autonomous ground robotic system

for TLS-based field phenotyping was created, demonstrating reliable data collection and point cloud registration.

Both remote and proximal sensing technologies offer unique advantages for in-field phenotyping, as highlighted in this dissertation. UAVs enable rapid, large-scale data collection, efficiently covering extensive breeding fields and capturing high-resolution aerial imagery for assessing simple traits such as the number of cotton bolls or canopy height, as well as more complex morphological traits in simpler canopies such as peanut plants. In contrast, TLS-based ground systems excel in providing detailed 3D point clouds at the plot level for accurate measurement of morphological traits, as well as dynamic growth trends in smaller breeding trials and more complex crops like cotton. The autonomous ground robot developed in this research has proven to be reliable in data collection and point cloud registration, offering an efficient method for automating in-field phenotyping data acquisition. These technologies facilitate comprehensive and efficient phenotyping strategies for breeding trials, leveraging the rapid, broad assessments of UAVs and the detailed, high-precision data from ground systems.

Introducing foundation models for computer vision, such as SAM, into the aerial data processing workflow has the potential to enhance phenotyping processes for diverse crops beyond peanuts. SAM's zero-shot learning capabilities significantly reduce the necessity for manual annotations, thereby enhancing the efficiency of extracting field plot data from aerial imagery and streamlining the phenotyping process for plant breeding. Furthermore, existing data processing workflows can be seamlessly adapted by integrating a preliminary SAM-based step, expediting plot extraction and increasing accessibility for users without technical expertise.

Integrating our autonomous robot into breeding programs offers a promising approach for comprehensive in-field trait estimation and targeted selection. Automating 3D phenotyping data collection with ground platforms enables continuous crop monitoring, facilitating real-time analysis of canopy growth and biomass changes. This understanding of dynamic growth trends can significantly aid in selecting cotton genotypes with specific characteristics that maximize resource efficiency or implementing targeted management practices. For example, early canopy closure limits light penetration to the soil surface, enhancing crop competitiveness against weeds. Therefore, accurately modeling growth rate and maximum height can help identify genotypes capable of achieving rapid canopy closure, which is key for effective weed suppression.

The methodologies and technologies developed in this dissertation provide a comprehensive framework for modernizing field phenotyping. These advancements not only enhance the precision and efficiency of trait assessment but also pave the way for large-scale implementation in breeding programs, ultimately accelerating crop improvement and agricultural sustainability. The continued development and refinement of these technologies will be crucial in meeting the growing demands of global food production and ensuring the resilience of our agricultural systems.

7.2 Limitations

Despite the advancements presented in this dissertation, several limitations remain:

1. Limited testing scope: UAV-based methods were tested on a single session and field layout for specific crops like cotton and peanuts. Broader experimentation across different crops, field conditions, and seasons is necessary for wider applicability and robustness.

2. Incomplete yield assessment: While boll count is a valuable metric and can indicate potential yield, it does not account for variations in boll size and lint quality, which are critical components of the final yield. Complementing UAV-based boll count estimations with detailed field measurements of boll characteristics could provide more comprehensive yield information for plant breeders.

3. In-field yield estimation robustness: Although the SVM classifier showed good performance for cotton boll counting, more testing in varied field layouts and environmental conditions is required. Additionally, transitioning from handcrafted features to advanced methods like deep learning could improve performance and robustness.

4. Challenges in automating UAV data processing: The automation of UAV data processing in peanut breeding was based primarily on accurately distinguishing peanut plants from the soil using the excess green minus red vegetation index. Weed pressure affecting field conditions can lead to inaccuracies in plot segmentation. More advanced methods to robustly segment vegetation are needed to ensure precision and reliability of our method for UAV-based phenotyping.

5. TLS analysis constraints: Time-series analysis using TLS was limited to canopy height and volume, without linking to other yield-related traits such as biomass or light use efficiency due to a lack of field data. Enhanced communication between plant scientists and engineers is needed to develop adequate methods for validating digital crop information.

6. Ground robot navigation limitations: The ground robot for TLS automation faced challenges in navigation and data capture due to plant growth and varying field conditions. The 2D

LiDAR provided real-time path information to avoid collisions but did not actively influence navigation paths. More robust integration of exteroceptive sensing systems is needed for safe in-field operations.

7.3 Future Work

Building on the findings of this dissertation, future research should address the identified limitations and enhance high-throughput phenotyping in crop breeding. Detailed information about the future work is as follows:

1. Integrating ground robots equipped with TLS to complement UAV-based cotton boll counts can provide detailed, high-precision point clouds from sampling plots, measuring cotton boll size, and refining yield estimates. This multi-tiered approach leverages both aerial and ground-based technologies for comprehensive and precise yield predictions.

2. Applying more advanced machine learning techniques, such as artificial general intelligence systems, can enhance the accuracy of plant identification, health assessment, and yield prediction by effectively handling the complexities of diverse field conditions and crop structures.

3. Integrating foundation models such as SAM into user-friendly software tools to streamline workflows may facilitate breeders' work and enhance the phenotyping process in varying field environments.

4. Investigating novel methodologies for acquiring multispectral data at greater resolutions and applying recent deep learning techniques to improve the accuracy and robustness of detecting TSWV can contribute to early and precise disease management strategies.

5. The use of 3D deep learning techniques for plot identification and segmentation can help automate and enhance point cloud data manipulation, providing more reliable and timely insights for crop phenotyping.

6. Investigating real-time data processing and analysis for spatiotemporal registration of 3D point cloud data can enable dynamic and responsive management of crop growth and health.

7. Scaling up the autonomous ground robotic system for larger fields and integrating it with other phenotyping tools can increase the efficiency and scalability of phenotyping operations in various agricultural settings.

APPENDIX A

SUPPLEMENTARY DATA FOR CHAPTER 5

A.0.1 Data preprocessing

After each data collection session, the individual point clouds from various scan locations were co-registered using SCENE software (FARO Technologies, Florida, US), version 2019.2. The raw point cloud data, stored in .FLS files, were imported and processed in SCENE. Only the *'Edge artifact'* filter was preselected for scan processing within SCENE. This filter allows for the identification and removal of noisy scan points at the edges of objects. The *'Find Spheres'* checkbox was selected to automatically identify the registration spheres during processing. The *'Active Sphere Radii'* parameter was configured to 0.0994 meters.

To register the point clouds, the information gathered by the scanner's internal sensors, including color camera, inclinometer, compass, and GPS, were used within SCENE as initial scan

placement. A subsequent automatic registration was performed using the *'Target Based* registration method based on the detected registration spheres. The quality of the registered point cloud was assessed using both target-based and mean point error statistics. Target-based statistics included the Euclidean distance between corresponding target pairs used for registration, while mean point error statistics computed the distance between local reference points and their corresponding references. Lower values for both metrics indicate a more accurate registration.

Once the spatial registration process was completed, the SCENE software's *'Clipping box'* tool was employed to isolate and extract the 3D points within the designated study area. The dimensions of the clipping boxes were manually adjusted to encompass the field boundaries defined by the scan locations at the outermost perimeter. Points within the clipping box were saved in the LASer (.LAS) file format, while all remaining points outside this region were excluded from the final point cloud dataset.

Co-registered point clouds were preprocessed to prepare them for subsequent analysis using the CloudCompare software, version 2.11.3 (Supplementary Figure S1). The preprocessing involved point cloud denoising and subsampling. For denoising, we applied a statistical outlier removal (SOR) filter with $N = 20$ and ± 2.5 standard deviations as outlier boundaries, eliminating points significantly distant from their neighbors. To further reduce point cloud size and manage computational demands while preserving spatial information, we introduced a subsampling step based on point-to-point distances. This step selectively retained points from the cloud using a distance threshold value, resulting in a new point cloud where any two points were at a distance equal to or greater than the specified value. We tested several distance threshold (i.e., 20 mm, 10 mm, 5

mm, and 1 mm), and found that a 5 mm threshold provided sufficient point cloud size reduction to enable posterior processing.

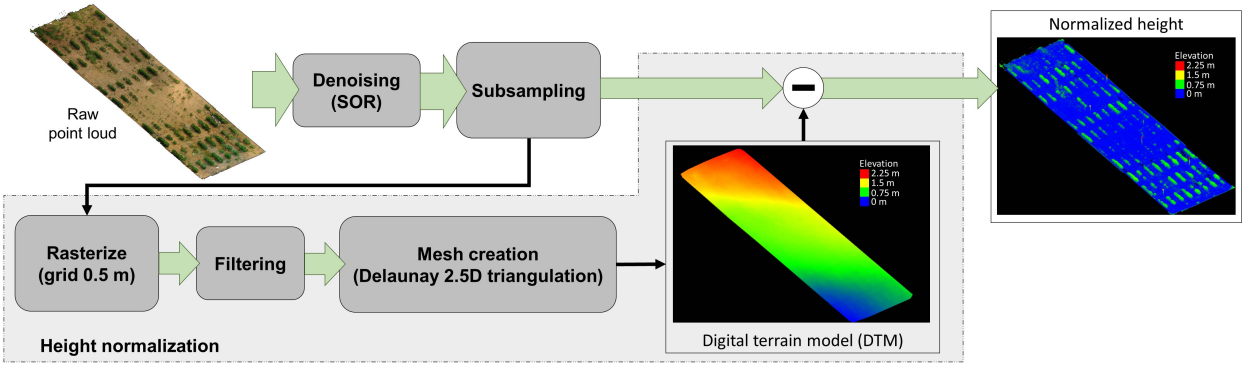

Figure S1: Steps for point cloud data preprocessing after spatial registration.

After subsampling, point cloud height was normalized with respect to the ground surface to correct for potential fluctuations in elevation within the field due to variations in terrain topography. This normalization process involved the creation of a digital terrain model (DTM) as a local reference (Supplementary Figure S1). First, the preprocessed point clouds were sampled using a grid with dimensions of 0.5 meters by 0.5 meters to obtain a rasterized sparse point cloud. Post-rasterization, any non-terrain points that may have been sampled would likely be spatially distant from their neighborhood points, facilitating their identification as outliers. Subsequently, a noise filter was applied to the sparse cloud to eliminate points that deviated significantly from the underlaying surface. Then, using the Delaunay triangulation method over the filtered sparse cloud, a mesh was reconstructed. This triangulation was executed on the local plane that best fitted the point cloud projection, leading to the creation of a DTM representing the field's surface. Finally, the height value of the DTM was subtracted from the elevation of each point in the point cloud, completing the height normalization procedure.

A.1 Tables

Table A.1: Common crop growth models parametrization. Mathematical definition of growth models of the Richards family curves for sigmoidal growth.

Model	T_i form
Logistic	$W = A\left(1 + e^{-k(t-T_i)}\right)^{-1}$
Gompertz	$W = Ae^{-e^{-k(t-T_i)}}$
3P-Richards	$W = A\left(1 + 3e^{-k(t-T_i)}\right)^{-\frac{1}{3}}$

Table A.2: Spatial registration statistics per data collection. DAP: Days after planting.

	Registration errors (mm)		Original point clouds		Processed point clouds	
DAP	Mean target error	Mean point error	#Points (M)	Size (GB)	#Points (M)	Size (GB)
35	0.9	5.0	110	2.8	6	0.24
42	1.7	3.8	106	2.7	15	0.38
49	0.9	4.6	161	4.1	16	0.42
56	1.3	4.2	224	5.7	18	0.46
62	1.3	5.1	288	7.3	17	0.44
70	2.1	6.9	361	9.1	23	0.59
77	2.2	6.4	353	8.7	25	0.65
84	2.3	8.5	348	8.8	25	0.62
98	3.2	7.9	332	8.1	23	0.58

Table A.3: Canopy height (CH) estimation results. Comparison of CH computed as the 95^{th} percentile (CH95), the 99^{th} percentile (CH99), and maximum height (CH_{max}). Subscript u indicates CH values obtained from non-temporal co-registered (unregistered) point clouds. Bold numbers indicate the best results.

Metric	CH95	$CH95_u$	CH99	$CH99_u$	CHmax	$CHmax_u$
$R^2\uparrow$	0.919	0.904	0.941	0.929	**0.945**	0.930
RMSE (cm)$\downarrow$	9.18	9.98	7.84	8.60	**7.56**	8.53
MAPE (%)$\downarrow$	6.59	7.02	5.54	5.98	**5.34**	5.92

Table A.4: Comparison of growth models performance. Degrees of freedom (df), log-likelihood (logLik), Akaike information criterion (AIC), and Bayesian information criterion (BIC) values for each model and trait combination.

		CH			CV		
	df	ΔAIC$\downarrow$	ΔBIC$\downarrow$	logLik$\uparrow$	ΔAIC$\downarrow$	ΔBIC$\downarrow$	logLik$\uparrow$
Logistic	31	0	0	786.3	0	0	-273.0
Gompertz	31	54	54.1	759.3	10.3	10.3	-278.2
3P-Richards	31	4.1	4.2	784.2	38.7	38.7	-292.4

A.2 Figures

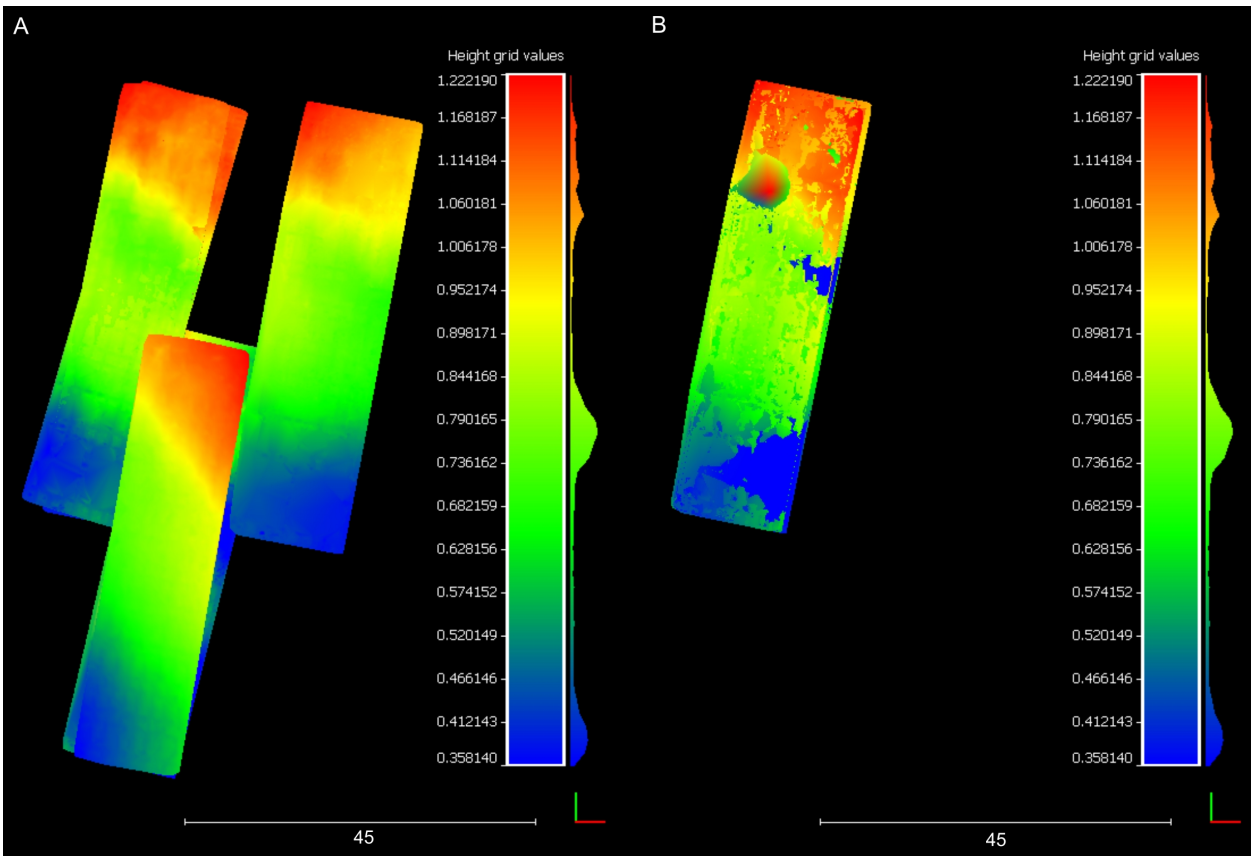

Figure S2: Results of terrain-based alignment. A) initial positions of the DTMs viewed from a top-down perspective and B) final positions of the meshes after ICP-based registration

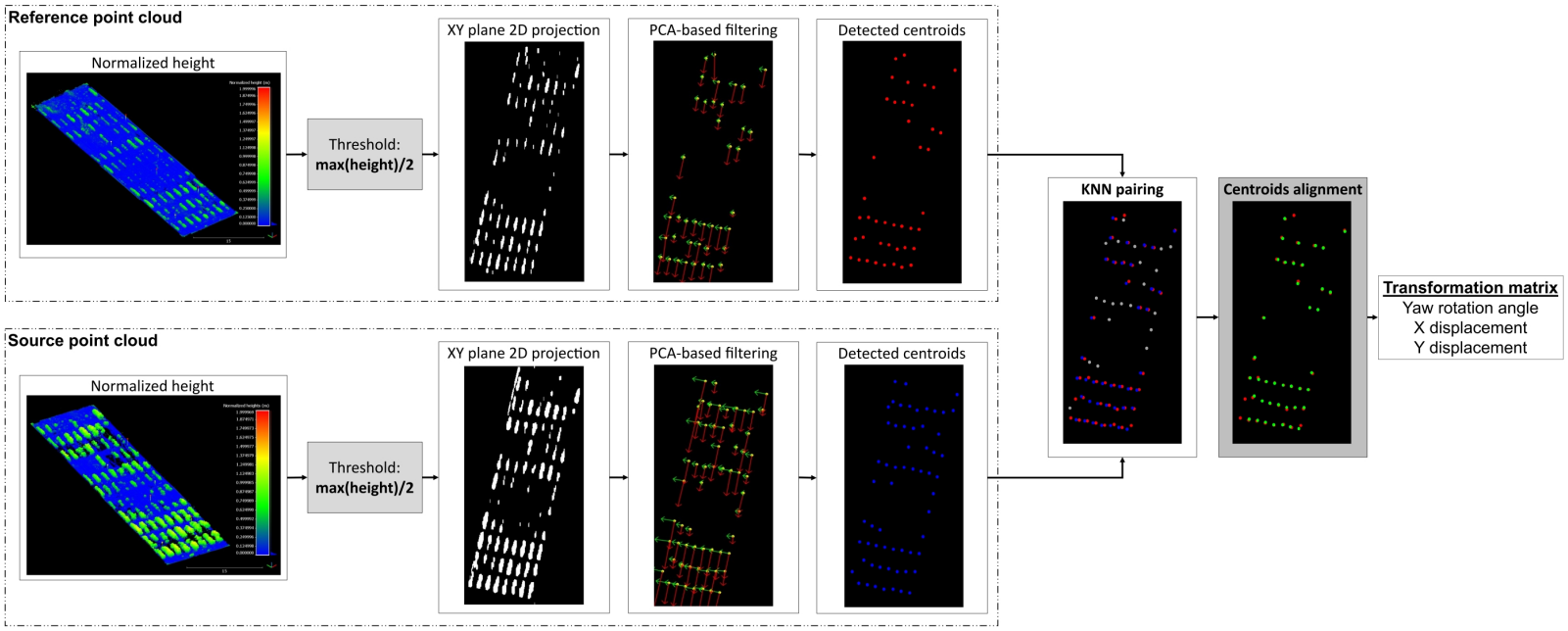

Figure S3: Fine registration of two point clouds using bird's-eye view alignment. The reference point cloud data corresponds to the data collection session conducted at 35 DAP, while the source point cloud data corresponds to 62 DAP. Point clouds are colorized based on normalized height. In the 2D projection, white pixels represent the 3D vegetation points projected onto the XY plane. Red dots indicate plot centroids from the reference point cloud, while blue dots represent plot centroids from the source point cloud to be aligned. Following alignment, green dots denote the aligned plot centroids after minimizing pairwise neighbor distance errors.

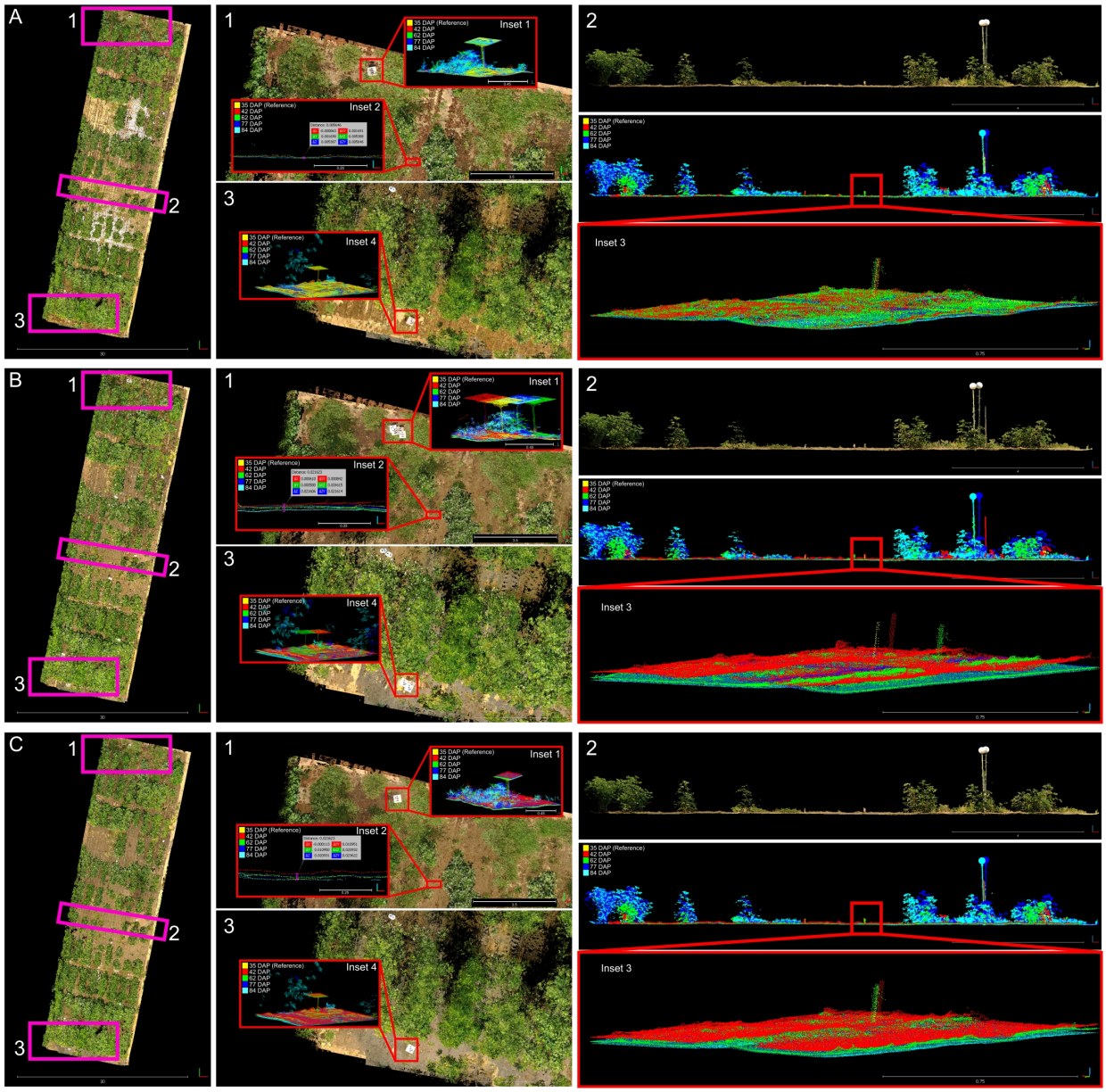

Figure S4: Comprehensive comparison of qualitative results. A) Manual alignment considered as the ground truth for performance evaluation. B) Rough alignment results after the first alignment step based on digital terrain model matching. C) Final alignment achieved after the bird's-eye view refinement. Numbered windows indicate close-ups of the respective areas of the field demarcated by pink rectangles. Insets: 1) Generalized alignment errors at the northern ground control point. 2) Errors in the Z direction at the terrain level. 3) Alignment errors in the center of the field. 4) Generalized alignment errors at the southern ground control point. Different solid colors denote point clouds collected on different dates.

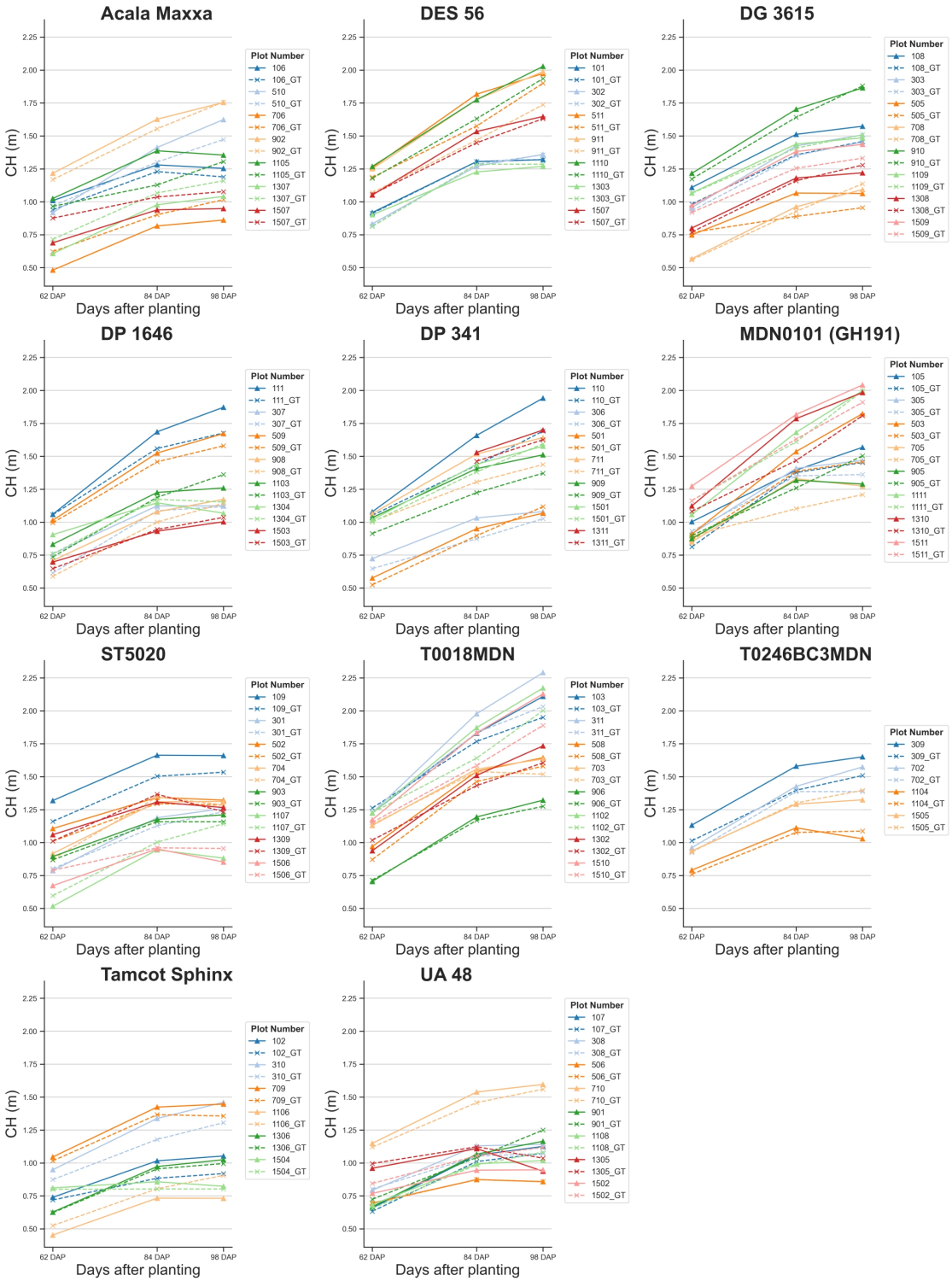

Figure S5: Temporal variation of canopy height (CH) for individual plots within genotype. Temporal variation of predicted and observed CH per each plot. Solid lines represent CH values estimated using our methodology. Dashed lines represent ground truth (GT) CH values measured manually in the field. Each color and symbol combination represents a different genotype, with corresponding pairs.

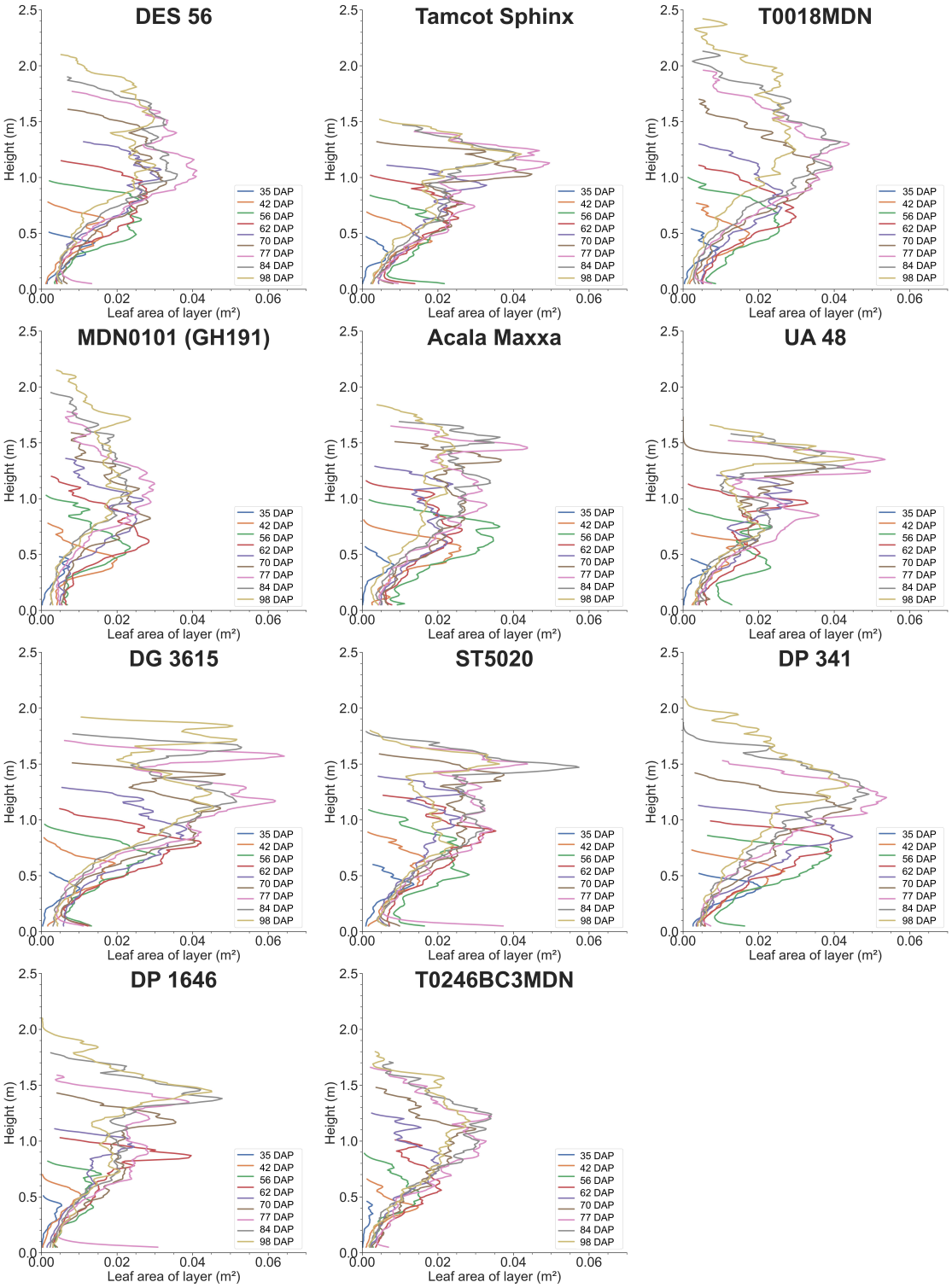

Figure S6: Evolution of the vertical distribution of leaf area over time. Colored lines distinguish different data collection sessions for each genotype (11 genotypes in total). The TLS data have been binned into 1 cm height layers and smoothed to enhance visualization.

BIBLIOGRAPHY

Abd-El Monsef, H., Smith, S. E., Rowland, D. L., & Abd El Rasol, N. (2019). Using multispectral imagery to extract a pure spectral canopy signature for predicting peanut maturity. *Computers and Electronics in Agriculture*, *162*, 561–572. https://doi.org/10.1016/j.compag.2019.04.028

Ahmed, I., Eramian, M., Ovsyannikov, I., van der Kamp, W., Nielsen, K., Duddu, H. S., Rumali, A., Shirtliffe, S., & Bett, K. (2019). Automatic detection and segmentation of lentil crop breeding plots from multi-spectral images captured by UAV-mounted camera. *2019 IEEE Winter Conference on Applications of Computer Vision (WACV)*. https://doi.org/10.1109/wacv.2019.00183

Akaike, H. (1992). Information theory and an extension of the maximum likelihood principle. In *Springer series in statistics* (pp. 610–624). Springer New York. https://doi.org/10.1007/978-1-4612-0919-5_38

Amanatides, J., & Woo, A. (1987). A fast voxel traversal algorithm for ray tracing. *EG 1987-Technical Papers*. https://doi.org/10.2312/egtp.19871000

Anderson, S. L., & Murray, S. C. (2020). R/UAStools::plotshpcreate: Create multi-polygon shapefiles for extraction of research plot scale agriculture remote sensing data. *Frontiers in Plant Science*, *11*. https://doi.org/10.3389/fpls.2020.511768

Andrade-Sanchez, P., Gore, M. A., Heun, J. T., Thorp, K. R., Carmo-Silva, A. E., French, A. N., Salvucci, M. E., & White, J. W. (2014). Development and evaluation of a field-based high-throughput phenotyping platform. *Functional Plant Biology*, *41*(1), 68–79. https://doi.org/10.1071/FP13126

Appel, A. (1968). Some techniques for shading machine renderings of solids. *Proceedings of the April 30–May 2, 1968, Spring Joint Computer Conference*, 37–45. https://doi.org/10.1145/1468075.1468082

Araus, J. L., & Cairns, J. E. (2014). Field high-throughput phenotyping: The new crop breeding frontier. *Trends in Plant Science*, *19*(1), 52–61. https://doi.org/10.1016/j.tplants.2013.09.008

Araus, J. L., Kefauver, S. C., Zaman-Allah, M., Olsen, M. S., & Cairns, J. E. (2018). Translating high-throughput phenotyping into genetic gain. *Trends in Plant Science*, *23*(5), 451–466. https://doi.org/10.1016/j.tplants.2018.02.001

Ashapure, A., Jung, J., Chang, A., Oh, S., Yeom, J., Maeda, M., Maeda, A., Dube, N., Landivar, J., Hague, S., & Smith, W. (2020). Developing a machine learning based cotton yield estimation framework using multi-temporal UAS data. *ISPRS Journal of Photogrammetry and Remote Sensing*, *169*, 180–194. https://doi.org/10.1016/j.isprsjprs.2020.09.015

Atefi, A., Ge, Y., Pitla, S. K., & Schnable, J. C. (2021). Robotic technologies for high-throughput plant phenotyping: Contemporary reviews and future perspectives. *Frontiers in Plant Science*, *12*. https://doi.org/10.3389/fpls.2021.611940

Bagherian, K., Bidese-Puhl, R., Bao, Y., Zhang, Q., Sanz-Saez, A., Dang, P. M., Lamb, M. C., & Chen, C. (2023). Phenotyping agronomic and physiological traits in peanut under mid-season drought stress using UAV-based hyperspectral imaging and machine learning. *The Plant Phenome Journal*, *6*(1). https://doi.org/10.1002/ppj2.20081

Bai, G., Ge, Y., Hussain, W., Baenziger, P. S., & Graef, G. (2016). A multi-sensor system for high throughput field phenotyping in soybean and wheat breeding. *Computers and Electronics in Agriculture*, *128*, 181–192. https://doi.org/10.1016/j.compag.2016.08.021

Bai, G., Ge, Y., Scoby, D., Leavitt, B., Stoerger, V., Kirchgessner, N., Irmak, S., Graef, G. L., Schnable, J. C., & Awada, T. (2019). NU-Spidercam: A large-scale, cable-driven, integrated sensing and robotic system for advanced phenotyping, remote sensing, and agronomic research. *Computers and Electronics in Agriculture*, *160*, 71–81. https://doi.org/10.1016/j.compag.2019.03.009

Baker, D. N., & Meyer, R. E. (1966). Influence of stand geometry on light interception and net photosynthesis in cotton. *Crop Science*, *6*(1), 15–19. https://doi.org/10.2135/cropsci1966.0011183x000600010004x

Bao, Y., Gai, J., Xiang, L., & Tang, L. (2021). Field robotic systems for high-throughput plant phenotyping: A review and a case study. *Concepts and Strategies in Plant Sciences*.

Barbedo, J. G. A. (2019). A review on the use of unmanned aerial vehicles and imaging sensors for monitoring and assessing plant stresses. *Drones*, *3*(2), 40. https://doi.org/10.3390/drones3020040

Barr, D. J., Levy, R., Scheepers, C., & Tily, H. J. (2013). Random effects structure for confirmatory hypothesis testing: Keep it maximal. *Journal of Memory and Language*, *68*(3), 255–278. https://doi.org/10.1016/j.jml.2012.11.001

Bates, D. M., Kliegl, R., Vasishth, S., & Baayen, H. (2015). Parsimonious mixed models. *arXiv: Methodology*. https://doi.org/10.48550/arXiv.1506.04967

Beauchêne, K., Leroy, F., Fournier, A., Huet, C., Bonnefoy, M., Lorgeou, J., de Solan, B., Piquemal, B., Thomas, S., & Cohan, J.-P. (2019). Management and characterization of abiotic stress via PhénoField®, a high-throughput field phenotyping platform. *Frontiers in Plant Science*, *10*. https://doi.org/10.3389/fpls.2019.00904

Bellón, B., Bégué, A., Lo Seen, D., de Almeida, C., & Simões, M. (2017). A remote sensing approach for regional-scale mapping of agricultural land-use systems based on NDVI time series. *Remote Sensing*, *9*(6), 600. https://doi.org/10.3390/rs9060600

Benet, B., Dubos, C., Maupas, F., Malatesta, G., & Lenain, R. (2018). Development of autonomous robotic platforms for sugar beet crop phenotyping using artificial vision. *AGENG Conference 2018*, 8–p.

Besl, P., & McKay, N. D. (1992). A method for registration of 3-D shapes. *IEEE Transactions on Pattern Analysis and Machine Intelligence*, *14*(2), 239–256. https://doi.org/10.1109/34.121791

Bhandari, M., Chang, A., Jung, J., Ibrahim, A. M. H., Rudd, J. C., Baker, S., Landivar, J., Liu, S., & Landivar, J. (2023). Unmanned aerial system-based high-throughput phenotyping for plant breeding. *The Plant Phenome Journal*, *6*(1). https://doi.org/10.1002/ppj2.20058

Bourland, F., & Myers, G. O. (2015). Conventional cotton breeding. In D. D. Fang & R. G. Percy (Eds.), *Cotton* (pp. 205–228). John Wiley & Sons, Ltd. https://doi.org/10.2134/agronmonogr57.2013.0025

Bowman, D. T., Bourland, F. M., Myers, G. O., Wallace, T. P., & Caldwell, D. (2004). Visual selection for yield in cotton breeding programs. *Journal of Cotton Science*, *8*(2), 62–68.

Bradski, G. (2000). The opencv library. *Dr. Dobb's Journal: Software Tools for the Professional Programmer*, *25*(11), 120–123.

Brown, N., Zhang, J., Maleski, J., Schwartz, B., & Branch, W. D. (2022). Utility of unmanned aerial systems for measuring plant height and plant vigor among several georgia runner peanut cultivars. *The Plant Phenome Journal*, *5*(1). https://doi.org/10.1002/ppj2.20053

Bruce, R. W., Rajcan, I., & Sulik, J. (2020). Plot extraction from aerial imagery: A precision agriculture approach. *The Plant Phenome Journal*, *3*(1). https://doi.org/10.1002/ppj2.20000

Buchaillot, M. L., Gracia-Romero, A., Vergara-Diaz, O., Zaman-Allah, M. A., Tarekegne, A., Cairns, J. E., Prasanna, B. M., Araus, J. L., & Kefauver, S. C. (2019). Evaluating maize genotype performance under low nitrogen conditions using RGB UAV phenotyping techniques. *Sensors*, *19*(8), 1815. https://doi.org/10.3390/s19081815

Calders, K., Adams, J., Armston, J., Bartholomeus, H., Bauwens, S., Bentley, L. P., Chave, J., Danson, F. M., Demol, M., Disney, M., Gaulton, R., Krishna Moorthy, S. M., Levick, S. R., Saarinen, N., Schaaf, C., Stovall, A., Terryn, L., Wilkes, P., & Verbeeck, H. (2020).

Terrestrial laser scanning in forest ecology: Expanding the horizon. *Remote Sensing of Environment*, *251*, 112102. https://doi.org/10.1016/j.rse.2020.112102

Carlone, L., Dong, J., Fenu, S., Rains, G., & Dellaert, F. (2015). Towards 4D crop analysis in precision agriculture: Estimating plant height and crown radius over time via expectation-maximization. *ICRA Workshop on Robotics in Agriculture*, 1–8.

Carraro, A., Sozzi, M., & Marinello, F. (2023). The Segment Anything Model (SAM) for accelerating the smart farming revolution. *Agricultural Technologies*. https://doi.org/10.1016/j.atech.2023.100367

Chapu, I., Okello, D. K., Okello, R. C. O., Odong, T. L., Sarkar, S., & Balota, M. (2022). Exploration of alternative approaches to phenotyping of late leaf spot and groundnut rosette virus disease for groundnut breeding. *Frontiers in Plant Science*, *13*. https://doi.org/10.3389/fpls.2022.912332

Chawade, A., van Ham, J., Blomquist, H., Bagge, O., Alexandersson, E., & Ortiz, R. (2019). High-throughput field-phenotyping tools for plant breeding and precision agriculture. *Agronomy*, *9*(5), 258. https://doi.org/10.3390/agronomy9050258

Chebrolu, N., Labe, T., & Stachniss, C. (2018). Robust long-term registration of UAV images of crop fields for precision agriculture. *IEEE Robotics and Automation Letters*, *3*(4), 3097–3104. https://doi.org/10.1109/lra.2018.2849603

Chebrolu, N., Labe, T., & Stachniss, C. (2020). Spatio-temporal non-rigid registration of 3d point clouds of plants. *2020 IEEE International Conference on Robotics and Automation (ICRA)*, 3112–3118. https://doi.org/10.1109/icra40945.2020.9197569

Chebrolu, N., Magistri, F., Läbe, T., & Stachniss, C. (2021). Registration of spatio-temporal point clouds of plants for phenotyping. *PLOS ONE*, *16*(2), e0247243. https://doi.org/10.1371/journal.pone.0247243

Chen, C.-J., & Zhang, Z. (2020). GRID: A Python package for field plot phenotyping using aerial images. *Remote Sensing*, *12*(11), 1697. https://doi.org/10.3390/rs12111697

Chen, D., Neumann, K., Friedel, S., Kilian, B., Chen, M., Altmann, T., & Klukas, C. (2014). Dissecting the phenotypic components of crop plant growth and drought responses based on high-throughput image analysis. *The Plant Cell*, *26*(12), 4636–4655. https://doi.org/10.1105/tpc.114.129601

Chu, T., Chen, R., Landivar, J. A., Maeda, M. M., Yang, C., & Starek, M. J. (2016). Cotton growth modeling and assessment using unmanned aircraft system visual-band imagery. *Journal of Applied Remote Sensing*, *10*(3), 1–17. https://doi.org/10.1117/1.JRS.10.036018

Chvatal, V. (1979). A greedy heuristic for the set-covering problem. *Mathematics of Operations Research*, *4*(3), 233–235. https://doi.org/10.1287/moor.4.3.233

Collard, B. C., & Mackill, D. J. (2008). Marker-assisted selection: An approach for precision plant breeding in the twenty-first century. *Philosophical Transactions of the Royal Society B: Biological Sciences*, *363*, 557–572. https://api.semanticscholar.org/CorpusID:7107714

Condorelli, G. E., Maccaferri, M., Newcomb, M., Andrade-Sanchez, P., White, J. W., French, A. N., Sciara, G., Ward, R., & Tuberosa, R. (2018). Comparative aerial and ground based high throughput phenotyping for the genetic dissection of NDVI as a proxy for drought adaptive traits in durum wheat. *Frontiers in Plant Science*, *9*, 893.

Cortes, C., & Vapnik, V. (1995). Support vector networks. *Machine Learning*, *20*, 273–297. https://doi.org/10.1007/BF00994018

Costa, J. M., Marques da Silva, J., Pinheiro, C., Barón, M., Mylona, P., Centritto, M., Haworth, M., Loreto, F., Uzilday, B., & Turkan, I. (2019). Opportunities and limitations of crop phenotyping in Southern European countries. *Frontiers in Plant Science*, *10*, 1125. https://doi.org/10.3389/fpls.2019.01125

Coulter, R. C. (1992). *Implementation of the pure pursuit path tracking algorithm* (tech. rep.). The robotic Institute, Carnegie-Mellon University. Pittsburgh, PA, USA.

Crommelinck, S., & Höfle, B. (2016). Simulating an autonomously operating low-cost static terrestrial LiDAR for multitemporal maize crop height measurements. *Remote Sensing*, *8*(3). https://doi.org/10.3390/rs8030205

Dantzig, G., Fulkerson, R., & Johnson, S. (1954). Solution of a large-scale traveling-salesman problem. *Journal of the Operations Research Society of America*, *2*(4), 393–410. https://doi.org/10.1287/opre.2.4.393

Deery, D., Jimenez-Berni, J., Jones, H., Sirault, X., & Furbank, R. (2014). Proximal remote sensing buggies and potential applications for field-based phenotyping. *Agronomy*, *4*(3), 349–379. https://doi.org/10.3390/AGRONOMY4030349

de Mendiburu, F., & Yaseen, M. (2020). *Agricolae: Statistical procedures for agricultural research* [Available online https://cran.r-project.org/package=agricolae].

Dodge, W. (2019). *Image based yield estimation in cotton using UAS* [PhD dissertation]. Texas Tech University.

Dong, J., Burnham, J. G., Boots, B., Rains, G., & Dellaert, F. (2017). 4D crop monitoring: Spatio-temporal reconstruction for agriculture. *2017 IEEE International Conference on Robotics and Automation (ICRA)*, 3878–3885. https://doi.org/10.1109/icra.2017.7989447

Drucker, H., Burges, C. J. C., Kaufman, L., Smola, A., & Vapnik, V. (1996). Support vector regression machines. In M. Mozer, M. I. Jordan, & T. Petsche (Eds.), *Proceedings of the 9th international conference on neural information processing systems (nips 1996)* (pp. 155–161). MIT Press.

Dubovyk, O., Menz, G., Lee, A., Schellberg, J., Thonfeld, F., & Khamzina, A. (2015). Spot-based sub-field level monitoring of vegetation cover dynamics: A case of irrigated croplands. *Remote Sensing*, *7*(6), 6763–6783. https://doi.org/10.3390/rs70606763

Ehlert, D., Heisig, M., & Adamek, R. (2010). Suitability of a laser rangefinder to characterize winter wheat. *Precision Agriculture*, *11*, 650–663. https://doi.org/10.1007/s11119-010-9191-4

Eitel, J. U., Magney, T. S., Vierling, L. A., Brown, T. T., & Huggins, D. R. (2014). LiDAR based biomass and crop nitrogen estimates for rapid, non-destructive assessment of wheat nitrogen status. *Field Crops Research*, *159*, 21–32. https://doi.org/10.1016/j.fcr.2014.01.008

Eitel, J. U., Magney, T. S., Vierling, L. A., Greaves, H. E., & Zheng, G. (2016). An automated method to quantify crop height and calibrate satellite-derived biomass using hypertemporal LiDAR. *Remote Sensing of Environment*, *187*, 414–422. https://doi.org/10.1016/j.rse.2016.10.044

El-Naggar, A., Jolly, B., Hedley, C., Horne, D., Roudier, P., & Clothier, B. (2021). The use of terrestrial LiDAR to monitor crop growth and account for within-field variability of

crop coefficients and water use. *Computers and Electronics in Agriculture*, *190*, 106416. https://doi.org/10.1016/j.compag.2021.106416

Ermanis, A., Gobbo, S., Snider, J. L., Cohen, Y., Liakos, V., Lacerda, L., Perry, C. D., Aaron Bruce, M., Virk, G., & Vellidis, G. (2020). Defining physiological contributions to yield loss in response to irrigation in cotton. *Journal of Agronomy and Crop Science*, *207*(2), 186–196. https://doi.org/10.1111/jac.12453

Fang, Y., Qiu, X., Guo, T., Wang, Y., Cheng, T., Zhu, Y., Chen, Q., Cao, W., Yao, X., Niu, Q., Hu, Y., & Gui, L. (2020). An automatic method for counting wheat tiller number in the field with terrestrial LiDAR. *Plant Methods*, *16*. https://doi.org/10.1186/s13007-020-00672-8

FARO Technologies. (2020, January). *Automation interface user manual*. FARO Technologies Inc.

Feng, A., Zhou, J., Vories, E. D., Sudduth, K., & Zhang, M. (2020). Yield estimation in cotton using UAV-based multi-sensor imagery. *Biosystems Engineering*, *193*, 101–114. https://doi.org/10.1016/j.biosystemseng.2020.02.014

Fiorani, F., & Schurr, U. (2013). Future scenarios for plant phenotyping. *Annual review of plant biology*, *64*, 267–291. https://doi.org/10.1146/annurev-arplant-050312-120137

Fix, E., & Hodges, J. L. (1951). Discriminatory analysis: Nonparametric discrimination: Consistency properties. https://doi.org/10.1037/e471672008-001

Friedli, M., Kirchgessner, N., Grieder, C., Liebisch, F., Mannale, M., & Walter, A. (2016). Terrestrial 3d laser scanning to track the increase in canopy height of both monocot and dicot crop species under field conditions. *Plant Methods*, *12*(1), 1–15. https://doi.org/10.1186/s13007-016-0109-7

Furbank, R. T., & Tester, M. (2011). Phenomics – technologies to relieve the phenotyping bottleneck. *Trends in Plant Science*, *16*(12), 635–644. https://doi.org/10.1016/j.tplants.2011.09.005

Gage, J. L., Richards, E., Lepak, N., Kaczmar, N., Soman, C., Chowdhary, G., Gore, M. A., & Buckler, E. S. (2019). In-field whole-plant maize architecture characterized by subcanopy rovers and latent space phenotyping. *The Plant Phenome Journal*, *2*. https://doi.org/10.2135/tppj2019.07.0011

Gano, B., Bhadra, S., Vilbig, J. M., Ahmed, N., Sagan, V., & Shakoor, N. (2024). Drone-based imaging sensors, techniques, and applications in plant phenotyping for crop breeding: A comprehensive review. *The Plant Phenome Journal*, *7*(1). https://doi.org/10.1002/ppj2.20100

Garcia-Ruiz, F., Sankaran, S., Maja, J. M., Lee, W. S., Rasmussen, J., & Ehsani, R. (2013). Comparison of two aerial imaging platforms for identification of huanglongbing-infected citrus trees. *Computers and Electronics in Agriculture*, *91*, 106–115. https://doi.org/10.1016/j.compag.2012.12.002

Gelard, W., Herbulot, A., Devy, M., & Casadebaig, P. (2018). 3d leaf tracking for plant growth monitoring. *2018 25th IEEE International Conference on Image Processing (ICIP)*, 3663–3667. https://doi.org/10.1109/icip.2018.8451553

Gill, T., Gill, S. K., Saini, D. K., Chopra, Y., de Koff, J. P., & Sandhu, K. S. (2022). A comprehensive review of high throughput phenotyping and machine learning for plant stress phenotyping. *Phenomics*, *2*(3), 156–183. https://doi.org/10.1007/s43657-022-00048-z

Goggin, F. L., Lorence, A., & Topp, C. N. (2015). Applying high-throughput phenotyping to plant–insect interactions: Picturing more resistant crops. *Current Opinion in Insect Science*, *9*, 69–76. https://doi.org/10.1016/J.COIS.2015.03.002

Gottschalk, S., Lin, M. C., & Manocha, D. (1996). OBBTree: A hierarchical structure for rapid interference detection. *Proceedings of the 23rd Annual Conference on Computer Graphics and Interactive Techniques*, 171–180. https://doi.org/10.1145/237170.237244

Gregorczyk, A. (1998). Richards plant growth model. *Journal of Agronomy and Crop Science*, *181*(4), 243–247. https://doi.org/10.1111/j.1439-037x.1998.tb00424.x

Großkinsky, D. K., Svensgaard, J., Christensen, S., & Roitsch, T. (2015). Plant phenomics and the need for physiological phenotyping across scales to narrow the genotype-to-phenotype knowledge gap. *Journal of experimental botany*, *66*(18), 5429–5440. https://doi.org/10.1093/jxb/erv345

Gui, B., Bhardwaj, A., & Sam, L. (2024). Evaluating the efficacy of Segment Anything Model for delineating agriculture and urban green spaces in multiresolution aerial and spaceborne remote sensing images. *Remote Sensing*, *16*(2), 414. https://doi.org/10.3390/rs16020414

Günder, M., Ispizua Yamati, F. R., Kierdorf, J., Roscher, R., Mahlein, A.-K., & Bauckhage, C. (2022). Agricultural plant cataloging and establishment of a data framework from UAV-based crop images by computer vision. *GigaScience*, *11*. https://doi.org/10.1093/gigascience/giac054

Guo, C., Liu, L., Zhang, K., Sun, H., Zhang, Y., Li, A., Bai, Z., Dong, H., & Li, C. (2022). High-throughput estimation of plant height and above-ground biomass of cotton using digital

image analysis and Canopeo. *Technology in Agronomy*, *2*(1), 1–10. https://doi.org/10.48130/tia-2022-0004

Guo, Q., Wu, F., Pang, S., Zhao, X., Chen, L., Liu, J., Xue, B., Xu, G., Li, L., Jing, H., & Chu, C. (2018). Crop 3D-a LiDAR based platform for 3D high-throughput crop phenotyping. *Science China. Life sciences*, *61*, 328–339. https://doi.org/10.1007/s11427-017-9056-0

Guo, T., Fang, Y., Cheng, T., Tian, Y., Zhu, Y., Chen, Q., Qiu, X., & Yao, X. (2019). Detection of wheat height using optimized multi-scan mode of LiDAR during the entire growth stages. *Computers and Electronics in Agriculture*, *165*, 104959. https://doi.org/10.1016/j.compag.2019.104959

Guo, W., Carroll, M. E., Singh, A., Swetnam, T. L., Merchant, N. C., Sarkar, S., Singh, A. K., & Ganapathysubramanian, B. (2021). UAS-based plant phenotyping for research and breeding applications. *Plant Phenomics*, *2021*.

Gurav, R., Patel, H., Shang, Z., Eldawy, A., Chen, J., Scudiero, E., & Papalexakis, E. (2023). Can SAM recognize crops? quantifying the zero-shot performance of a semantic segmentation foundation model on generating crop-type maps using satellite imagery for precision agriculture. *arXiv preprint*. https://arxiv.org/abs/2311.15138

Ha, T., Duddu, H., Bett, K., & Shirtliffe, S. J. (2021). A semi-automatic workflow to extract irregularly aligned plots and sub-plots: A case study on lentil breeding populations. *Remote Sensing*, *13*(24), 4997. https://doi.org/10.3390/rs13244997

Ha, T., Duddu, H., Vandenberg, A., & Shirtliffe, S. (2022). A semi-automatic workflow for plot boundary extraction of irregularly sized and spaced field plots from UAV imagery. *The Plant Phenome Journal*, *5*(1). https://doi.org/10.1002/ppj2.20039

Hämmerle, M., & Höfle, B. (2014). Effects of reduced terrestrial LiDAR point density on high-resolution grain crop surface models in precision agriculture. *Sensors*, *14*(12), 24212–24230. https://doi.org/10.3390/s141224212

Hdioud, B., Tirari, M. E. H., Thami, R. O. H., & Faizi, R. (2018). Detecting and shadows in the HSV color space using dynamic thresholds. *Bulletin of Electrical Engineering and Informatics*, *7*, 70–79. https://doi.org/10.11591/eei.v7i1.893

Hearst, A. A., & Cherkauer, K. A. (2015). Extraction of small spatial plots from geo-registered UAS imagery of crop fields. *Environmental Practice*, *17*(3), 178–187. https://doi.org/10.1017/s1466046615000162

Herr, A. W., Adak, A., Carroll, M. E., Elango, D., Kar, S., Li, C., Jones, S. E., Carter, A. H., Murray, S. C., Paterson, A., Sankaran, S., Singh, A., & Singh, A. K. (2023). Unoccupied aerial systems imagery for phenotyping in cotton, maize, soybean, and wheat breeding. *Crop Science*, *63*(4), 1722–1749. https://doi.org/10.1002/csc2.21028

Herrero-Huerta, M., Lindenbergh, R., & Gard, W. (2018). Leaf movements of indoor plants monitored by terrestrial LiDAR. *Frontiers in Plant Science*, *9*. https://doi.org/10.3389/fpls.2018.00189

Hoffmeister, D., Waldhoff, G., Curdt, C., Tilly, N., Bendig, J., & Bareth, G. (2013). Spatial variability detection of crop height in a single field by terrestrial laser scanning. In J. V. Stafford (Ed.), *Precision agriculture '13* (pp. 267–274). Wageningen Academic Publishers. https://doi.org/10.3920/978-90-8686-778-3

Hosoi, F., & Omasa, K. (2009). Estimating vertical plant area density profile and growth parameters of a wheat canopy at different growth stages using three-dimensional portable

LiDAR imaging. *ISPRS Journal of Photogrammetry and Remote Sensing*, *64*(2), 151–158. https://doi.org/10.1016/j.isprsjprs.2008.09.003

Hosoi, F., & Omasa, K. (2012). Estimation of vertical plant area density profiles in a rice canopy at different growth stages by high-resolution portable scanning LiDAR with a lightweight mirror. *ISPRS Journal of Photogrammetry and Remote Sensing*, *74*, 11–19. https://doi.org/10.1016/j.isprsjprs.2012.08.001

Hough, P. V. (1962). Method and means for reconizing complex patterns (U.S. Patent No. 3,069,654). https://www.osti.gov/biblio/4746348

Hu, J., Lin, J., Gong, S., & Cai, W. (2024). Relax image-specific prompt requirement in SAM: A single generic prompt for segmenting camouflaged objects. *Proceedings of the AAAI Conference on Artificial Intelligence*, *38*(11), 12511–12518. https://doi.org/10.1609/aaai.v38i11.29144

Hu, P., Guo, W., Chapman, S. C., Guo, Y., & Zheng, B. (2019). Pixel size of aerial imagery constrains the applications of unmanned aerial vehicle in crop breeding. *ISPRS Journal of Photogrammetry and Remote Sensing*, *154*, 1–9. https://doi.org/10.1016/j.isprsjprs.2019.05.008

Huang, Y., Howard, J. B., Ruixiu, S., Steven, J. T., Tomonari, F., & M.Wayne, E. (2016). Cotton yield estimation using very high-resolution digital images acquired with a low-cost small unmanned aerial vehicle. *Transactions of the ASABE*, *59*, 1563–1574. https://doi.org/10.13031/trans.59.11831

Huang, Y., Sui, R., Thomson, S., & Fisher, D. K. (2013). Estimation of cotton yield with varied irrigation and nitrogen treatments using aerial multispectral imagery. *International Journal*

of Agricultural and Biological Engineering, *6*, 37–41. https://doi.org/10.3965/j.ijabe.20130602.005

Hui, F., Zhu, J., Hu, P., Meng, L., Zhu, B., Guo, Y., Li, B., & Ma, Y. (2018). Image-based dynamic quantification and high-accuracy 3d evaluation of canopy structure of plant populations. *Annals of Botany*, *121*(5), 1079–1088. https://doi.org/10.1093/aob/mcy016

Hunter, M. C., Smith, R. G., Schipanski, M. E., Atwood, L. W., & Mortensen, D. A. (2017). Agriculture in 2050: Recalibrating targets for sustainable intensification. *Bioscience*, *67*(4), 386–391.

Ji, W., Li, J., Bi, Q., Liu, T., Li, W., & Cheng, L. (2024). Segment Anything is not always perfect: An investigation of SAM on different real-world applications. *Machine Intelligence Research*. https://doi.org/10.1007/s11633-023-1385-0

Jiang, Y., Li, C., Robertson, J. S., Sun, S., Xu, R., & Paterson, A. H. (2018). GPhenoVision: A ground mobile system with multi-modal imaging for field-based high throughput phenotyping of cotton. *Scientific reports*, *8*(1), 1–15.

Jiang, Y., Li, C., Takeda, F., Kramer, E. A., Ashrafi, H., & Hunter, J. (2019). 3D point cloud data to quantitatively characterize size and shape of shrub crops. *Horticulture Research*, *6*. https://doi.org/10.1038/s41438-019-0123-9

Jiang, Z., Chen, Z., Chen, J., Ren, J., Li, Z., & Sun, L. (2014). The estimation of regional crop yield using ensemble-based four-dimensional variational data assimilation. *Remote Sensing*, *6*(4), 2664–2681. https://doi.org/10.3390/rs6042664

Jiménez-Berni, J. A., Deery, D. M., Rozas-Larraondo, P., Condon, A. G., Rebetzke, G. J., James, R., Bovill, W. D., Furbank, R. T., & Sirault, X. (2018). High throughput determination of

plant height, ground cover, and above-ground biomass in wheat with LiDAR. *Frontiers in Plant Science*, *9*. https://doi.org/10.3389/fpls.2018.00237

Jin, S., Su, Y., Gao, S., Wu, F., Hu, T., Liu, J., Li, W., Wang, D., Chen, S., Jiang, Y., Pang, S., & Guo, Q. (2018). Deep learning: Individual maize segmentation from terrestrial LiDAR data using faster R-CNN and regional growth algorithms. *Frontiers in Plant Science*, *9*. https://doi.org/10.3389/fpls.2018.00866

Jin, S., Su, Y., Song, S., Xu, K., Hu, T., Yang, Q., Wu, F., Xu, G., Ma, Q., Guan, H., et al. (2020). Non-destructive estimation of field maize biomass using terrestrial LiDAR: An evaluation from plot level to individual leaf level. *Plant Methods*, *16*(1), 1–19. https://doi.org/10.1186/s13007-020-00613-5

Jin, S., Su, Y., Wu, F., Pang, S., Gao, S., Hu, T., Liu, J., & Guo, Q. (2019). Stem–leaf segmentation and phenotypic trait extraction of individual maize using terrestrial LiDAR data. *IEEE Transactions on Geoscience and Remote Sensing*, *57*(3), 1336–1346. https://doi.org/10.1109/TGRS.2018.2866056

Jin, S., Su, Y., Zhang, Y., Song, S., Li, Q., Liu, Z., Ma, Q., Ge, Y., Liu, L., Ding, Y., Baret, F., & Guo, Q. (2021). Exploring seasonal and circadian rhythms in structural traits of field maize from LiDAR time series. *Plant Phenomics*, *2021*. https://doi.org/10.34133/2021/9895241

Jin, S., Sun, X., Wu, F., Su, Y., Li, Y., Song, S., Xu, K., Ma, Q., Baret, F., Jiang, D., Ding, Y., & Guo, Q. (2021). LiDAR sheds new light on plant phenomics for plant breeding and management: Recent advances and future prospects. *ISPRS Journal of Photogrammetry and Remote Sensing*, *171*, 202–223. https://doi.org/10.1016/j.isprsjprs.2020.11.006

Jung, J., Maeda, M., Chang, A., Landivar, J., Yeom, J., & McGinty, J. (2018). Unmanned aerial system assisted framework for the selection of high yielding cotton genotypes. *Computers and Electronics in Agriculture*, *152*, 74–81. https://doi.org/10.1016/j.compag.2018.06.051

Kaur, N., Snider, J. L., Paterson, A. H., Grey, T. L., Li, C., Virk, G., & Parkash, V. (2023). Variation in thermotolerance of photosystem ii energy trapping, intersystem electron transport, and photosystem i electron acceptor reduction for diverse cotton genotypes. *Plant Physiology and Biochemistry*, *201*, 107868. https://doi.org/10.1016/j.plaphy.2023.107868

Kay, T. L., & Kajiya, J. T. (1986). Ray tracing complex scenes. *Proceedings of the 13th Annual Conference on Computer Graphics and Interactive Techniques*, 269–278. https://doi.org/10.1145/15922.15916

Khan, Z., & Miklavcic, S. J. (2019). An automatic field plot extraction method from aerial orthomosaic images. *Frontiers in Plant Science*, *10*. https://doi.org/10.3389/fpls.2019.00683

Kim, J. Y. (2020). Roadmap to high throughput phenotyping for plant breeding. *Journal of Biosystems Engineering*, *45*(1), 43–55. https://doi.org/10.1007/s42853-020-00043-0

Kirchgessner, N., Liebisch, F., Yu, K., Pfeifer, J., Friedli, M., Hund, A., & Walter, A. (2016). The ETH field phenotyping platform FIP: A cable-suspended multi-sensor system. *Functional Plant Biology*, *44*, 154–168. https://doi.org/10.1071/FP16165

Kirillov, A., Mintun, E., Ravi, N., Mao, H., Rolland, C., Gustafson, L., Xiao, T.-Y., Whitehead, S., Berg, A. C., Lo, W.-Y., Dollár, P., & Girshick, R. (2023). Segment Anything. *2023 IEEE/CVF International Conference on Computer Vision (ICCV)*. https://doi.org/10.1109/iccv51070.2023.00371

Koenig, K., Höfle, B., Hämmerle, M., Jarmer, T., Siegmann, B., & Lilienthal, H. (2015). Comparative classification analysis of post-harvest growth detection from terrestrial LiDAR point clouds in precision agriculture. *ISPRS Journal of Photogrammetry and Remote Sensing*, *104*, 112–125. https://doi.org/10.1016/j.isprsjprs.2015.03.003

Koranne, S. (2009). *Practical computing on the cell broadband engine* (1st). Springer Publishing Company, Incorporated. https://doi.org/10.1007/978-1-4419-0308-2

Krause, E. F. (1986). *Taxicab geometry—an adventure in non-Euclidean geometry*. Courier Corporation. https://doi.org/10.2307/3618288

Kumar, J., Pratap, A., & Kumar, S. (2015). Plant phenomics: An overview. In J. Kumar, A. Pratap, & S. Kumar (Eds.), *Phenomics in crop plants: Trends, options and limitations* (pp. 1–10). Springer India. https://doi.org/10.1007/978-81-322-2226-2_1

Kunta, S., Agmon, S., Chedvat, I., Levy, Y., Chu, Y., Ozias-Akins, P., & Hovav, R. (2021). Identification of consistent QTL for time to maturation in virginia-type peanut (Arachis hypogaea L.) *BMC Plant Biology*, *21*(1). https://doi.org/10.1186/s12870-021-02951-5

Lecun, Y., Bottou, L., Bengio, Y., & Haffner, P. (1998). Gradient-based learning applied to document recognition. *Proceedings of the IEEE*, *86*(11), 2278–2324. https://doi.org/10.1109/5.726791

Li, D., Bai, D., Tian, Y., Li, Y.-H., Zhao, C., Wang, Q., Guo, S., Gu, Y., Luan, X., Wang, R., Yang, J., Hawkesford, M. J., Schnable, J. C., Jin, X., & Qiu, L.-J. (2022). Time series canopy phenotyping enables the identification of genetic variants controlling dynamic phenotypes in soybean. *Journal of Integrative Plant Biology*, *65*(1), 117–132. https://doi.org/10.1111/jipb.13380

Li, J., Xu, M., Xiang, L., Chen, D., Zhuang, W., Yin, X., & Li, Z. (2024). Foundation models in smart agriculture: Basics, opportunities, and challenges. *Computers and Electronics in Agriculture*, *222*, 109032. https://doi.org/10.1016/j.compag.2024.109032

Li, L., Zhang, Q., & Huang, D. (2014). A review of imaging techniques for plant phenotyping. *Sensors*, *14*(11), 20078–20111. https://doi.org/10.3390/s141120078

Li, L., Yang, X., Cui, S., Meng, X., Mu, G., Hou, M., He, M., Zhang, H., Liu, L., & Chen, C. Y. (2019). Construction of high-density genetic map and mapping quantitative trait loci for growth habit-related traits of peanut (Arachis hypogaea L.) *Frontiers in Plant Science*, *10*. https://doi.org/10.3389/fpls.2019.00745

Li, P., Zhang, X., Wang, W., Zheng, H., Yao, X., Tian, Y., Zhu, Y., Cao, W., Chen, Q., & Cheng, T. (2020). Estimating aboveground and organ biomass of plant canopies across the entire season of rice growth with terrestrial laser scanning. *International Journal of Applied Earth Observation and Geoinformation*, *91*, 102132. https://doi.org/10.1016/j.jag.2020.102132

Li, Y., Fan, X., Mitra, N. J., Chamovitz, D., Cohen-Or, D., & Chen, B. (2013). Analyzing growing plants from 4D point cloud data. *ACM Transactions on Graphics*, *32*(6), 1–10. https://doi.org/10.1145/2508363.2508368

Li, Y., Wen, W., Fan, J., Gou, W., Gu, S., Lu, X., Yu, Z., Wang, X., & Guo, X. (2023). Multi-source data fusion improves time-series phenotype accuracy in maize under a field high-throughput phenotyping platform. *Plant Phenomics*, *5*. https://doi.org/10.34133/plantphenomics.0043

Li, Y., Huang, Z., Cao, Z., Lu, H., Wang, H., & Zhang, S. (2020). Performance evaluation of crop segmentation algorithms. *IEEE Access*, *8*, 36210–36225. https://doi.org/10.1109/access.2020.2969451

Li, Y., Wang, D., Yuan, C., Li, H., & Hu, J. (2023). Enhancing agricultural image segmentation with an agricultural Segment Anything Model adapter. *Sensors*, *23*(18), 7884. https://doi.org/10.3390/s23187884

Lin, C., Hu, F., Peng, J., Wang, J., & Zhai, R. (2022). Segmentation and stratification methods of field maize terrestrial LiDAR point cloud. *Agriculture*. https://doi.org/10.3390/agriculture12091450

Lin, Y. (2015). LiDAR: An important tool for next-generation phenotyping technology of high potential for plant phenomics? *Computers and Electronics in Agriculture*, *119*, 61–73. https://doi.org/10.1016/j.compag.2015.10.011

Liu, J., Zhou, Z., & Li, B. (2024). *Remote sensing for field-based crop phenotyping*. Frontiers Media SA. https://doi.org/10.3389/978-2-8325-4430-3

Liu, S., & Whitty, M. A. (2015). Automatic grape bunch detection in vineyards with an SVM classifier. *Journal of Applied Logic*, *13*, 643–653. https://doi.org/10.1016/j.jal.2015.06.001

Liu, S., Baret, F., Abichou, M., Boudon, F., Thomas, S., Zhao, K., Fournier, C., Andrieu, B., Irfan, K., Hemmerlé, M., & de Solan, B. (2017). Estimating wheat green area index from ground-based LiDAR measurement using a 3D canopy structure model. *Agricultural and Forest Meteorology*, *247*, 12–20. https://doi.org/10.1016/j.agrformet.2017.07.007

Llorens, J., Gil, E., Llop, J., & Escolà, A. (2011). Ultrasonic and LiDAR sensors for electronic canopy characterization in vineyards: Advances to improve pesticide application methods. *Sensors*, *11*(2), 2177–2194. https://doi.org/10.3390/s110202177

Loomis, R., & Williams, W. (2015). Productivity and the morphology of crop stands: Patterns with leaves. In S. C. Eastin J.D. Haskins F.A. & V. B. C.H.M. (Eds.), *Physiological aspects of*

crop yield (pp. 27–47). American Society of Agronomy, Crop Science Society of America. https://doi.org/10.2135/1969.physiologicalaspects.c3

Lu, J., Cheng, D., Geng, C., Zhang, Z., Xiang, Y., & Hu, T. (2021). Combining plant height, canopy coverage and vegetation index from UAV-based RGB images to estimate leaf nitrogen concentration of summer maize. *Biosystems Engineering*, *202*, 42–54. https://doi.org/10.1016/j.biosystemseng.2020.11.010

Ma, J., He, Y., Li, F., Han, L., You, C., & Wang, B. (2024). Segment Anything in medical images. *Nature Communications*, *15*(1). https://doi.org/10.1038/s41467-024-44824-z

Madec, S., Baret, F., de Solan, B., Thomas, S., Dutartre, D., Jezequel, S., Hemmerlé, M., Colombeau, G., & Comar, A. (2017). High-throughput phenotyping of plant height: Comparing unmanned aerial vehicles and ground LiDAR estimates. *Frontiers in Plant Science*, *8*. https://doi.org/10.3389/fpls.2017.02002

Magistri, F., Chebrolu, N., & Stachniss, C. (2020). Segmentation-based 4D registration of plants point clouds for phenotyping. *2020 IEEE/RSJ International Conference on Intelligent Robots and Systems (IROS)*, 2433–2439. https://doi.org/10.1109/iros45743.2020.9340918

Maimaitijiang, M., Sagan, V., Sidike, P., Hartling, S., Esposito, F., & Fritschi, F. B. (2020). Soybean yield prediction from UAV using multimodal data fusion and deep learning. *Remote Sensing of Environment*, *237*, 111599. https://doi.org/10.1016/j.rse.2019.111599

Maja, J. M. J., Campbell, T., Neto, J. C., & Astillo, P. (2016). Predicting cotton yield of small field plots in a cotton breeding program using UAV imagery data. In J. Valasek & J. A. Thomasson (Eds.), *Autonomous air and ground sensing systems for agricultural optimization and phenotyping* (pp. 39–45, Vol. 9866). SPIE. https://doi.org/10.1117/12.2228929

Malambo, L., Popescu, S., Horne, D., Pugh, N., & Rooney, W. (2019). Automated detection and measurement of individual sorghum panicles using density-based clustering of terrestrial LiDAR data. *ISPRS Journal of Photogrammetry and Remote Sensing*, *149*, 1–13. https://doi.org/10.1016/j.isprsjprs.2018.12.015

Malambo, L., Popescu, S., Murray, S., Putman, E., Pugh, N., Horne, D., Richardson, G., Sheridan, R., Rooney, W., Avant, R., Vidrine, M., McCutchen, B., Baltensperger, D., & Bishop, M. (2018). Multitemporal field-based plant height estimation using 3d point clouds generated from small unmanned aerial systems high-resolution imagery. *International Journal of Applied Earth Observation and Geoinformation*, *64*, 31–42. https://doi.org/10.1016/j.jag.2017.08.014

Mardanisamani, S., Ayalew, T. W., Badhon, M. A., Khan, N. A., Hasnat, G., Duddu, H., Shirtliffe, S., Vail, S., Stavness, I., & Eramian, M. (2021). Automatic microplot localization using UAV images and a hierarchical image-based optimization method. *Plant Phenomics*, *2021*. https://doi.org/10.34133/2021/9764514

Mardanisamani, S., & Eramian, M. (2022). Segmentation of vegetation and microplots in aerial agriculture images: A survey. *The Plant Phenome Journal*, *5*(1). https://doi.org/10.1002/ppj2.20042

Matias, F. I., Caraza-Harter, M. V., & Endelman, J. B. (2020). FIELDimageR: An R package to analyze orthomosaic images from agricultural field trials. *The Plant Phenome Journal*, *3*(1). https://doi.org/10.1002/ppj2.20005

McCrea, R., King, R., Graham, L., & Börger, L. (2023). Realising the promise of large data and complex models. *Methods in Ecology and Evolution*, *14*(1), 4–11. https://doi.org/10.1111/2041-210x.14050

Medic, T., Bömer, J., & Paulus, S. (2023). Challenges and recommendations for 3d plant phenotyping in agriculture using terrestrial lasers scanners. *ISPRS Annals of the Photogrammetry, Remote Sensing and Spatial Information Sciences*, *X-1/W1-2023*, 1007–1014. https://doi.org/10.5194/isprs-annals-X-1-W1-2023-1007-2023

Meyer, G., & Neto, J. C. (2008). Verification of color vegetation indices for automated crop imaging applications. *Computers and Electronics in Agriculture*, *63*, 282–293. https://doi.org/10.1016/j.compag.2008.03.009

Miao, C., Xu, Y., Liu, S., Schnable, P. S., & Schnable, J. C. (2020). Increased power and accuracy of causal locus identification in time series genome-wide association in sorghum. *Plant Physiology*, *183*(4), 1898–1909. https://doi.org/10.1104/pp.20.00277

Miller, C. E., Tucker, A. W., & Zemlin, R. A. (1960). Integer programming formulation of traveling salesman problems. *J. ACM*, *7*(4), 326–329. https://doi.org/10.1145/321043.321046

Moore, T., & Stouch, D. (2014). A generalized extended Kalman filter implementation for the robot operating system. *Proceedings of the 13th International Conference on Intelligent Autonomous Systems (IAS-13)*. https://doi.org/10.1007/978-3-319-08338-4_25

Morisse, M., Wells, D. M., Millet, E. J., Lillemo, M., Fahrner, S., Cellini, F., Lootens, P., Muller, O., Herrera, J. M., & Bentley, A. R. (2022). A European perspective on opportunities and demands for field-based crop phenotyping. *Field Crops Research*, *276*, 108371. https://doi.org/10.1016/j.fcr.2021.108371

Mozaffar, M. H., & Varshosaz, M. (2016). Optimal placement of a terrestrial laser scanner with an emphasis on reducing occlusions. *The Photogrammetric Record*, *31*. https://doi.org/10.1111/phor.12162

Nagasubramanian, K., Jones, S., Sarkar, S., Singh, A. K., Singh, A., & Ganapathysubramanian, B. (2018). Hyperspectral band selection using genetic algorithm and support vector machines for early identification of charcoal rot disease in soybean stems. *Plant Methods*, *14*(1). https://doi.org/10.1186/s13007-018-0349-9

Nigam, S. (2014). Groundnut at a glance, pp. 121.

Nobel, P. S., Forseth, I. N., & Long, S. P. (1993). Canopy structure and light interception. In D. O. Hall, J. M. O. Scurlock, H. R. Bolhàr-Nordenkampf, R. C. Leegood, & S. P. Long (Eds.), *Photosynthesis and production in a changing environment: A field and laboratory manual* (pp. 79–90). Springer Netherlands. https://doi.org/10.1007/978-94-011-1566-7_6

O'Banion, M. S., & Olsen, M. J. (2019). Efficient planning and acquisition of terrestrial laser scanning–derived digital elevation models: Proof of concept study. *Journal of Surveying Engineering*. https://doi.org/10.1061/(ASCE)SU.1943-5428.0000265

Osco, L. P., Marcato Junior, J., Marques Ramos, A. P., de Castro Jorge, L. A., Fatholahi, S. N., de Andrade Silva, J., Matsubara, E. T., Pistori, H., Gonçalves, W. N., & Li, J. (2021). A review on deep learning in UAV remote sensing. *International Journal of Applied Earth Observation and Geoinformation*, *102*, 102456. https://doi.org/10.1016/j.jag.2021.102456

Pabuayon, I. L. B., Sun, Y., Guo, W., & Ritchie, G. L. (2019). High-throughput phenotyping in cotton: A review. *Journal of Cotton Research*, *2*(1). https://doi.org/10.1186/s42397-019-0035-0

Paproki, A., Sirault, X., Berry, S., Furbank, R., & Fripp, J. (2012). A novel mesh processing based technique for 3d plant analysis. *BMC Plant Biology*, *12*(1), 63. https://doi.org/10.1186/1471-2229-12-63

Patel, J. D., Wright, R. J., Auld, D., Chandnani, R., Goff, V. H., Ingles, J., Pierce, G. J., Torres, M. J., & Paterson, A. H. (2014). Alleles conferring improved fiber quality from EMS mutagenesis of elite cotton genotypes. *Theoretical and Applied Genetics*, *127*, 821–830. https://doi.org/10.1007/s00122-013-2259-6

Patrick, A., Pelham, S., Culbreath, A., Holbrook, C. C., De Godoy, I. J., & Li, C. (2017). High throughput phenotyping of tomato spot wilt disease in peanuts using unmanned aerial systems and multispectral imaging. *IEEE Instrumentation & Measurement Magazine*, *20*(3), 4–12. https://doi.org/10.1109/mim.2017.7951684

Pauli, D., Andrade-Sanchez, P., Carmo-Silva, A. E., Gazave, E., French, A. N., Heun, J., Hunsaker, D. J., Lipka, A. E., Setter, T. L., Strand, R. J., Thorp, K. R., Wang, S., White, J. W., & Gore, M. A. (2016). Field-based high-throughput plant phenotyping reveals the temporal patterns of quantitative trait loci associated with stress-responsive traits in cotton. *G3 Genes|Genomes|Genetics*, *6*(4), 865–879. https://doi.org/10.1534/g3.115.023515

Paulus, S. (2019). Measuring crops in 3D: Using geometry for plant phenotyping. *Plant methods*, *15*(1), 1–13. https://doi.org/10.1186/s13007-019-0490-0

Paulus, S., Schumann, H., Kuhlmann, H., & Léon, J. (2014). High-precision laser scanning system for capturing 3D plant architecture and analysing growth of cereal plants. *Biosystems Engineering*, *121*, 1–11. https://doi.org/10.1016/j.biosystemseng.2014.01.010

Pawar, P. S., & Matias, F. I. (2023). FIELDimageR.Extra: Advancing user experience and computational efficiency for analysis of orthomosaic from agricultural field trials. *The Plant Phenome Journal*, *6*(1). https://doi.org/10.1002/ppj2.20083

Pedregosa, F., Varoquaux, G., Gramfort, A., Michel, V., Thirion, B., Grisel, O., Blondel, M., Louppe, G., Prettenhofer, P., Weiss, R., Weiss, R. J., Vanderplas, J., Passos, A., Cournapeau, D., Brucher, M., Perrot, M., & Duchesnay, E. (2011). Scikit-learn: Machine learning in Python. *Journal of Machine Learning Research.*, *12*, 2825–2830. https://doi.org/10.48550/arXiv.1201.0490

Pieruschka, R., & Schurr, U. (2019). Plant phenotyping: Past, present, and future. *Plant Phenomics*, *2019*. https://doi.org/10.34133/2019/7507131

Pinheiro, J. C., & Bates, D. M. (2000). *Mixed-effects models in S and S-PLUS*. Springer. https://doi.org/10.1007/b98882

Pittman, R. N. (1995). *United States peanut descriptors*. USDA, Agricultural Research Service.

Pokhrel, A., Snider, J. L., Virk, S., Sintim, H. Y., Hand, L. C., Vellidis, G., Parkash, V., Chalise, D. P., & Lee, J. M. (2023). Quantifying physiological contributions to nitrogen-induced yield variation in field-grown cotton. *Field Crops Research*, *299*, 108976. https://doi.org/10.1016/j.fcr.2023.108976

Qi, H., Wu, Z., Zhang, L., Li, J., Zhou, J., Jun, Z., & Zhu, B. (2021). Monitoring of peanut leaves chlorophyll content based on drone-based multispectral image feature extraction. *Computers and Electronics in Agriculture*, *187*, 106292. https://doi.org/10.1016/j.compag.2021.106292

Qi, H., Zhu, B., Wu, Z., Liang, Y., Li, J., Wang, L., Chen, T., Lan, Y., & Zhang, L. (2020). Estimation of peanut leaf area index from unmanned aerial vehicle multispectral images. *Sensors*, *20*(23), 6732. https://doi.org/10.3390/s20236732

Qiu, Q., Sun, N., Bai, H., Wang, N., Fan, Z., Wang, Y., Meng, Z., Li, B., & Cong, Y. (2019). Field-based high-throughput phenotyping for maize plant using 3D LiDAR point cloud generated with a "Phenomobile". *Frontiers in Plant Science*, *10*, 554. https://doi.org/10.3389/fpls.2019.00554

R Core Team. (2020). *R: A language and environment for statistical computing*. R Foundation for Statistical Computing. Vienna, Austria. https://www.R-project.org/

R Core Team. (2023). *R: A language and environment for statistical computing*. R Foundation for Statistical Computing. Vienna, Austria. https://www.R-project.org/

Raza, S.-e.-A., Prince, G., Clarkson, J. P., & Rajpoot, N. M. (2015). Automatic detection of diseased tomato plants using thermal and stereo visible light images. *PLOS ONE*, *10*(4), 1–20. https://doi.org/10.1371/journal.pone.0123262

Reynolds, M., & Langridge, P. (2016). Physiological breeding. *Current Opinion in Plant Biology*, *31*, 162–171. https://doi.org/10.1016/j.pbi.2016.04.005

Ritchie, G. L., Bednarz, C. W., Jost, P. H., & Brown, S. M. (2007). *Cotton growth and development* (Bulletin No. 1952). University of Georgia.

Robb, C., Hardy, A., Doonan, J. H., & Brook, J. (2020). Semi-automated field plot segmentation from UAS imagery for experimental agriculture. *Frontiers in Plant Science*, *11*. https://doi.org/10.3389/fpls.2020.591886

Rodriguez-Sanchez, J., Johnsen, K., & Li, C. (2024). A ground mobile robot for autonomous terrestrial laser scanning-based field phenotyping. https://doi.org/10.48550/arXiv.2404.04404

Rodriguez-Sanchez, J., & Li, C. (2022). An autonomous ground system for 3D LiDAR-based crop scouting. *2022 ASABE Annual International Meeting*, 1. https://doi.org/10.13031/aim.202200142

Rohlf, F. J., & Slice, D. (1990). Extensions of the procrustes method for the optimal superimposition of landmarks. *Systematic Zoology*, *39*(1), 40. https://doi.org/10.2307/2992207

Rosell Polo, J. R., Sanz, R., Llorens, J., Arnó, J., Escolà, A., Ribes-Dasi, M., Masip, J., Camp, F., Gràcia, F., Solanelles, F., Pallejà, T., Val, L., Planas, S., Gil, E., & Palacín, J. (2009). A tractor-mounted scanning LIDAR for the non-destructive measurement of vegetative volume and surface area of tree-row plantations: A comparison with conventional destructive measurements. *Biosystems Engineering*, *102*(2), 128–134. https://doi.org/10.1016/j.biosystemseng.2008.10.009

Rote, G. (1991). Computing the minimum Hausdorff distance between two point sets on a line under translation. *Information Processing Letters*, *38*(3), 123–127. https://doi.org/10.1016/0020-0190(91)90233-8

Rumpf, T., Mahlein, A. .-., Steiner, U., Oerke, E. .-., Dehne, H. .-., & Plümer, L. (2010). Early detection and classification of plant diseases with support vector machines based on hyperspectral reflectance. *Computers and Electronics in Agriculture*, *74*(1), 91–99. https://doi.org/10.1016/j.compag.2010.06.009

Rutkoski, J., Poland, J., Mondal, S., Autrique, E., Pérez, L. G., Crossa, J., Reynolds, M., & Singh, R. (2016). Canopy temperature and vegetation indices from high-throughput phenotyping improve accuracy of pedigree and genomic selection for grain yield in wheat. *G3 Genes|Genomes|Genetics*, *6*(9), 2799–2808. https://doi.org/10.1534/g3.116.032888

Saeys, W., Lenaerts, B., Craessaerts, G., & De Baerdemaeker, J. (2009). Estimation of the crop density of small grains using LiDAR sensors. *Biosystems Engineering*, *102*(1), 22–30. https://doi.org/10.1016/j.biosystemseng.2008.10.003

Sandhu, J., Zhu, F., Paul, P., Gao, T., Dhatt, B. K., Ge, Y., Staswick, P., Yu, H., & Walia, H. (2019). PI-Plat: A high-resolution image-based 3d reconstruction method to estimate growth dynamics of rice inflorescence traits. *Plant Methods*, *15*(1). https://doi.org/10.1186/s13007-019-0545-2

Santos, A. F., Lacerda, L. N., Rossi, C., Moreno, L. d. A., Oliveira, M. F., Pilon, C., Silva, R. P., & Vellidis, G. (2021). Using UAV and multispectral images to estimate peanut maturity variability on irrigated and rainfed fields applying linear models and artificial neural networks. *Remote Sensing*, *14*(1), 93. https://doi.org/10.3390/rs14010093

Sarkar, S., Cazenave, A. B., Oakes, J., McCall, D., Thomason, W., Abbot, L., & Balota, M. (2020). High-throughput measurement of peanut canopy height using digital surface models. *The Plant Phenome Journal*, *3*(1). https://doi.org/10.1002/ppj2.20003

Sarkar, S., Cazenave, A. B., & Oakes, J. e. a. (2021). Aerial high-throughput phenotyping of peanut leaf area index and lateral growth. *Scientific Reports*, *11*(21661). https://doi.org/10.1038/s41598-021-00936-w

Sarkar, S., Ramsey, A. F., Cazenave, A. B., & Balota, M. (2021). Peanut leaf wilting estimation from RGB color indices and logistic models. *Frontiers in Plant Science*, *12*. https://doi.org/10.3389/fpls.2021.658621

Schneider, P. J., & Eberly, D. (2002). *Geometric tools for computer graphics*. Elsevier Science Inc. https://doi.org/10.1016/b978-1-55860-594-7.x5000-0

Schwarz, G. (1978). Estimating the dimension of a model. *The Annals of Statistics*, *6*(2). https://doi.org/10.1214/aos/1176344136

Seedorff, M., Oleson, J., & McMurray, B. (2019). Maybe maximal: Good enough mixed models optimize power while controlling type I error. *PsyArXiv Preprints*. https://doi.org/10.31234/osf.io/xmhfr

Shafiekhani, A., Kadam, S., Fritschi, F., & DeSouza, G. (2017). Vinobot and Vinoculer: Two robotic platforms for high-throughput field phenotyping. *Sensors*, *17*(1), 214. https://doi.org/10.3390/s17010214

Singh, A., Ganapathysubramanian, B., Singh, A. K., & Sarkar, S. (2016). Machine learning for high-throughput stress phenotyping in plants. *Trends in Plant Science*, *21*(2), 110–124. https://doi.org/10.1016/j.tplants.2015.10.015

Slavík, P. (1997). A tight analysis of the greedy algorithm for set cover. *Journal of Algorithms*, *25*(2), 237–254. https://doi.org/10.1006/jagm.1997.0887

Smits, B. (1998). Efficiency issues for ray tracing. *Journal of Graphical Tools*, *3*(2), 1–14. https://doi.org/10.1080/10867651.1998.10487488

Sneath, P. H. A. (1967). Trend-surface analysis of transformation grids. *Journal of Zoology*, *151*(1), 65–122. https://doi.org/10.1111/j.1469-7998.1967.tb02866.x

Snider, J., Bange, M., & Heitholt, J. (2021). Cotton. In *Crop physiology case histories for major crops* (pp. 714–746). Elsevier. https://doi.org/10.1016/b978-0-12-819194-1.00022-0

Song, Y., Glasbey, C. A., Horgan, G. W., Polder, G., Dieleman, J. A., & van der Heijden, G. (2014). Automatic fruit recognition and counting from multiple images. *Biosystems Engineering*, *118*, 203–215. https://doi.org/10.1016/j.biosystemseng.2013.12.008

Souza, J. B. C., de Almeida, S. L. H., Freire de Oliveira, M., Santos, A. F. d., Filho, A. L. B., Meneses, M. D., & Silva, R. P. d. (2022). Integrating satellite and UAV data to predict peanut maturity upon artificial neural networks. *Agronomy*, *12*(1512). https://doi.org/10.3390/agronomy12071512

Starek, M. J., Chu, T., Mitasova, H., & Harmon, R. S. (2020). Viewshed simulation and optimization for digital terrain modelling with terrestrial laser scanning. *International Journal of Remote Sensing*, *41*(16), 6409–6426. https://doi.org/10.1080/01431161.2020.1752952

Su, Y., Wu, F., Ao, Z., Jin, S., Qin, F., Liu, B., Pang, S., Liu, L., & Guo, Q. (2019). Evaluating maize phenotype dynamics under drought stress using terrestrial LiDAR. *Plant Methods*, *15*. https://doi.org/10.1186/s13007-019-0396-x

Sugiura, R., Tsuda, S., Tamiya, S., Itoh, A., Nishiwaki, K., Murakami, N., Shibuya, Y., Hirafuji, M., & Nuske, S. (2016). Field phenotyping system for the assessment of potato late blight resistance using RGB imagery from an unmanned aerial vehicle. *Biosystems Engineering*, *148*, 1–10. https://doi.org/10.1016/j.biosystemseng.2016.04.010

Sun, G., Lu, H., Zhao, Y., Zhou, J., Jackson, R., Wang, Y., Xu, L., Wang, A., Colmer, J., Ober, E., Zhao, Q., Han, B., & Zhou, J. (2022). Air Measurer: Open-source software to quantify static and dynamic traits derived from multiseason aerial phenotyping to empower genetic

mapping studies in rice. *New Phytologist*, *236*(4), 1584–1604. https://doi.org/10.1111/nph.18314

Sun, J., Yan, S., Alexandridis, T., Yao, X., Zhou, H., Gao, B., Huang, J., Yang, J., & Li, Y. (2024). Enhancing crop mapping through automated sample generation based on Segment Anything Model with medium-resolution satellite imagery. *Remote Sensing*, *16*(9), 1505. https://doi.org/10.3390/rs16091505

Sun, S., Li, C., Chee, P. W., Paterson, A. H., Meng, C., Zhang, J., Ma, P., Robertson, J. S., & Adhikari, J. (2021). High resolution 3D terrestrial LiDAR for cotton plant main stalk and node detection. *Computers and Electronics in Agriculture*, *187*, 106276. https://doi.org/10.1016/j.compag.2021.106276

Sun, S., Li, C., & Paterson, A. H. (2017). In-field high-throughput phenotyping of cotton plant height using LiDAR. *Remote Sensing*, *9*(4), 377. https://doi.org/10.3390/rs9040377

Sun, S., Li, C., Paterson, A. H., Jiang, Y., Xu, R., Robertson, J. S., Snider, J. L., & Chee, P. W. (2018). In-field high throughput phenotyping and cotton plant growth analysis using LiDAR. *Frontiers in Plant Science*, *9*. https://doi.org/10.3389/fpls.2018.00016

Sweet, D. D., Tirado, S. B., Springer, N. M., Hirsch, C. N., & Hirsch, C. D. (2022). Opportunities and challenges in phenotyping row crops using drone-based RGB imaging. *The Plant Phenome Journal*, *5*(1). https://doi.org/10.1002/ppj2.20044

Tang, Z., Wang, M., Schirrmann, M., Dammer, K.-H., Li, X., Brueggeman, R., Sankaran, S., Carter, A., Pumphrey, M., Hu, Y., Chen, X., & Zhang, Z. (2022). Affordable high throughput field detection of wheat stripe rust using deep learning with semi-automated image labeling. https://doi.org/10.20944/preprints202204.0177.v1

Tao, H., Xu, S., Tian, Y., Li, Z., Ge, Y., Zhang, J., Wang, Y., Zhou, G., Deng, X., Zhang, Z., Ding, Y., Jiang, D., Guo, Q., & Jin, S. (2022). Proximal and remote sensing in plant phenomics: 20 years of progress, challenges, and perspectives. *Plant Communications*, 100344. https://doi.org/10.1016/j.xplc.2022.100344

Tardieu, F., Cabrera-Bosquet, L., Pridmore, T., & Bennett, M. (2017). Plant phenomics, from sensors to knowledge. *Current Biology*, *27*(15), R770–R783. https://doi.org/10.1016/j.cub.2017.05.055

The MathWorks Inc. (2021). Matlab optimization toolbox.

Thulasiraman, K., Arumugam, S., Brandstädt, A., & Nishizeki, T. (Eds.). (2016). *Handbook of graph theory, combinatorial optimization, and algorithms*. CRC Press. https://doi.org/10.1201/b19163

Tilly, N., Hoffmeister, D., Cao, Q., Huang, S., Lenz-Wiedemann, V., Miao, Y., & Bareth, G. (2014). Multitemporal crop surface models: Accurate plant height measurement and biomass estimation with terrestrial laser scanning in paddy rice. *Journal of Applied Remote Sensing*, *8*(1), 083671. https://doi.org/10.1117/1.jrs.8.083671

Tilly, N., Hoffmeister, D., Cao, Q., Lenz-Wiedemann, V., Miao, Y., & Bareth, G. (2015). Transferability of models for estimating paddy rice biomass from spatial plant height data. *Agriculture*, *5*(3), 538–560. https://doi.org/10.3390/agriculture5030538

Tjørve, E., & Tjørve, K. M. (2010). A unified approach to the Richards-model family for use in growth analyses: Why we need only two model forms. *Journal of Theoretical Biology*, *267*(3), 417–425. https://doi.org/10.1016/j.jtbi.2010.09.008

Torres-Sánchez, J., López-Granados, F., Serrano, N., Arquero, O., & Peña, J. M. (2015). High-throughput 3-D monitoring of agricultural-tree plantations with unmanned aerial vehicle (UAV) technology (Q. K. Hassan, Ed.). *PLOS ONE*, *10*(6), e0130479. https://doi.org/10.1371/journal.pone.0130479

Townsend, T., & Sette, J. (2016). Natural fibres and the world economy. In R. Fangueiro & S. Rana (Eds.), *Natural fibres: Advances in science and technology towards industrial applications* (pp. 381–390). Springer Netherlands. https://doi.org/10.1007/978-94-017-7515-1_30

Tresch, L., Müller, M. C., Itoh, A., Kaga, A., Taguchi, K., Hirafuji, M., Ninomiya, S., & Guo, W. (2019). Easy MPE: Extraction of quality microplot images for UAV-based high-throughput field phenotyping. *Plant Phenomics*, *2019*, 2591849. https://doi.org/10.34133/2019/2591849

van Iersel, W., Straatsma, M., Addink, E., & Middelkoop, H. (2018). Monitoring height and greenness of non-woody floodplain vegetation with UAV time series. *ISPRS Journal of Photogrammetry and Remote Sensing*, *141*, 112–123. https://doi.org/10.1016/j.isprsjprs.2018.04.011

Vapnik, V., Golowich, S. E., & Smola, A. (1996). Support vector method for function approximation, regression estimation and signal processing. In M. Mozer, M. I. Jordan, & T. Petsche (Eds.), *Proceedings of the 9th international conference on neural information processing systems (nips 1996)* (pp. 281–287). MIT Press.

Vinces, R. F. (2011). Phenomics : Genotype to phenotype. https://api.semanticscholar.org/CorpusID:16431896

Virlet, N., Sabermanesh, K., Sadeghi-Tehran, P., & Hawkesford, M. J. (2016). Field Scanalyzer: An automated robotic field phenotyping platform for detailed crop monitoring. *Functional Plant Biology*, *44*, 143–153. https://doi.org/10.1071/FP16163

Volpato, L., Pinto, F., González-Pérez, L., Thompson, I. G., Borém, A., Reynolds, M., Gérard, B., Molero, G., & Rodrigues, F. A. (2021). High throughput field phenotyping for plant height using UAV-based RGB imagery in wheat breeding lines: Feasibility and validation. *Frontiers in Plant Science*, *12*. https://doi.org/10.3389/fpls.2021.591587

Vosselman, G., & Maas, H. (Eds.). (2010). *Airborne and terrestrial laser scanning*. CRC Press (Taylor & Francis).

Voss-Fels, K. P., Stahl, A., & Hickey, L. T. (2019). Q&A: Modern crop breeding for future food security. *BMC biology*, *17*(1), 1–7. https://doi.org/10.1186/s12915-019-0638-4

Wada, K. (2018). Labelme: Image polygonal annotation with Python. https://doi.org/10.5281/zenodo.5711226

Walter, A., Liebisch, F., & Hund, A. (2015). Plant phenotyping: From bean weighing to image analysis. *Plant Methods*, *11*(1), 14. https://doi.org/10.1186/s13007-015-0056-8

Walter, J., Edwards, J., McDonald, G. K., & Kuchel, H. (2019). Estimating biomass and canopy height with LiDAR for field crop breeding. *Frontiers in Plant Science*, *10*. https://doi.org/10.3389/fpls.2019.01145

Wang, X., Singh, D., Marla, S., Morris, G., & Poland, J. (2018). Field-based high-throughput phenotyping of plant height in sorghum using different sensing technologies. *Plant Methods*, *14*(1). https://doi.org/10.1186/s13007-018-0324-5

Wang, X., Singh, D. S. K., Marla, S. R., Morris, G. P., & Poland, J. A. (2018). Field-based high-throughput phenotyping of plant height in sorghum using different sensing technologies. *Plant Methods*, *14*. https://doi.org/10.1186/s13007-018-0324-5

Watanabe, K., Guo, W., Arai, K., Takanashi, H., Kajiya-Kanegae, H., Kobayashi, M., Yano, K., Tokunaga, T., Fujiwara, T., Tsutsumi, N., & Iwata, H. (2017). High-throughput phenotyping of sorghum plant height using an unmanned aerial vehicle and its application to genomic prediction modeling. *Frontiers in Plant Science*, *8*. https://doi.org/10.3389/fpls.2017.00421

Watt, M., Fiorani, F., Usadel, B., Rascher, U., Muller, O., & Schurr, U. (2020). Phenotyping: New windows into the plant for breeders. *Annual review of plant biology*, *71*, 689–712. https://doi.org/10.1146/annurev-arplant-042916-041124

White, J. W., Andrade-Sanchez, P., Gore, M. A., Bronson, K. F., Coffelt, T. A., Conley, M. M., Feldmann, K. A., French, A. N., Heun, J. T., Hunsaker, D. J., Jenks, M. A., Kimball, B. A., Roth, R. L., Strand, R. J., Thorp, K. R., Wall, G. W., & Wang, G. (2012). Field-based phenomics for plant genetics research. *Field Crops Research*, *133*, 101–112. https://doi.org/10.1016/j.fcr.2012.04.003

Williams, A., Barrus, S., Morley, R. K., & Shirley, P. (2005). An efficient and robust ray-box intersection algorithm. *ACM SIGGRAPH 2005 Courses*, 9–es. https://doi.org/10.1145/1198555.1198748

Williams, D., MacFarlane, F., & Britten, A. (2023). Leaf only SAM: A segment anything pipeline for zero-shot automated leaf segmentation. *arXiv preprint*. https://arxiv.org/abs/2305.09418

Wood, S. E., Poudel, B., Wright, G. C., Dieters, M. I., Pandey, M. K., & Ash, G. (2023). Development of a rapid phenotyping method to screen for Didymella arachidicola resistance in peanuts. *PhytoFrontiers*™. https://doi.org/10.1094/phytofr-07-22-0078-r

Xavier, A., Hall, B., Hearst, A. A., Cherkauer, K. A., & Rainey, K. M. (2017). Genetic architecture of phenomic-enabled canopy coverage in Glycine max. *Genetics*, *206*(2), 1081–1089. https://doi.org/10.1534/genetics.116.198713

Xia, L., Zhang, R., Chen, L., Huang, Y., Xu, G., Wen, Y., & Yi, T. (2019). Monitor cotton budding using SVM and UAV images. *Applied Sciences*, *9*(20), 4312. https://doi.org/10.3390/app9204312

Xie, C., & Yang, C. (2020). A review on plant high-throughput phenotyping traits using UAV-based sensors. *Computers and Electronics in Agriculture*, *178*, 105731. https://doi.org/10.1016/j.compag.2020.105731

Xu, R., & Li, C. (2022a). A modular agricultural robotic system (MARS) for precision farming: Concept and implementation. *Journal of Field Robotics*, *39*(4), 387–409. https://doi.org/10.1002/rob.22056

Xu, R., & Li, C. (2022b). A review of high-throughput field phenotyping systems: Focusing on ground robots. *Plant Phenomics*. https://doi.org/10.34133/2022/9760269

Xu, R., Li, C., & Paterson, A. H. (2019). Multispectral imaging and unmanned aerial systems for cotton plant phenotyping. *PLOS ONE*, *14*(2), 1–20. https://doi.org/10.1371/journal.pone.0205083

Yang, G., Liu, J., Zhao, C., Li, Z., Huang, Y., Yu, H., Xu, B., Yang, X., Zhu, D., Zhang, X., Zhang, R., Feng, H., Zhao, X., Li, Z., Li, H., & Yang, H. (2017). Unmanned aerial vehicle remote

sensing for field-based crop phenotyping: Current status and perspectives. *Frontiers in Plant Science*, *8*. https://doi.org/10.3389/fpls.2017.01111

Yeom, J., Jung, J., Chang, A., Maeda, M., & Landivar, J. (2018). Automated open cotton boll detection for yield estimation using unmanned aircraft vehicle (UAV) data. *Remote Sensing*, *10*, 1895. https://doi.org/10.3390/rs10121895

Yoosefzadeh-Najafabadi, M., Singh, K. D., Pourreza, A., Sandhu, K. S., Adak, A., Murray, S. C., Eskandari, M., & Rajcan, I. (2023). Remote and proximal sensing: How far has it come to help plant breeders? In *Advances in agronomy* (pp. 279–315). Elsevier. https://doi.org/10.1016/bs.agron.2023.05.004

Yuan, H., Bennett, R. S., Wang, N., & Chamberlin, K. D. (2019). Development of a peanut canopy measurement system using a ground-based LiDAR sensor. *Frontiers in plant science*, *10*, 203. https://doi.org/10.3389/fpls.2019.00203

Zhang, M., Wu, B., Yu, M., Zou, W., & Zheng, Y. (2014). Crop condition assessment with adjusted NDVI using the uncropped arable land ratio. *Remote Sensing*, *6*(6), 5774–5794. https://doi.org/10.3390/rs6065774

Zhang, X., Zhao, J., Yang, G., Liu, J., Cao, J., Li, C., Zhao, X., & Gai, J. (2019). Establishment of plot-yield prediction models in soybean breeding programs using UAV-based hyperspectral remote sensing. *Remote Sensing*, *11*(23), 2752. https://doi.org/10.3390/rs11232752

Zhang, X., Pourreza, A., Cheung, K. H., Zuniga-Ramirez, G., Lampinen, B. D., & Shackel, K. A. (2021). Estimation of fractional photosynthetically active radiation from a canopy 3D model; Case study: Almond yield prediction. *Frontiers in Plant Science*, *12*. https://doi.org/10.3389/fpls.2021.715361

Zhou, X., Wang, P., Tansey, K., Zhang, S., Li, H., & Tian, H. (2020). Reconstruction of time series leaf area index for improving wheat yield estimates at field scales by fusion of sentinel-2, -3 and MODIS imagery. *Computers and Electronics in Agriculture*, *177*, 105692. https://doi.org/10.1016/j.compag.2020.105692

Zhu, L., Suomalainen, J., Liu, J., Hyyppä, J., Kaartinen, H., & Haggren, H. (2018). A review: Remote sensing sensors. In *Multi-purposeful application of geospatial data*. InTech. https://doi.org/10.5772/intechopen.71049

Zhu, Y., Sun, G., Ding, G., Zhou, J., Wen, M., Jin, S., Zhao, Q., Colmer, J., Ding, Y., Ober, E. S., & Zhou, J. (2021). Large-scale field phenotyping using backpack LiDAR and GUI-based CropQuant-3D to measure structural responses to different nitrogen treatments in wheat. *bioRxiv*. https://doi.org/10.1101/2021.05.19.444842